Chris Freeman

Control System Design for Electrical Stimulation in Upper Limb Rehabilitation

Modelling, Identification and Robust Performance

Springer

Control System Design for Electrical Stimulation in Upper Limb Rehabilitation

Chris Freeman

Control System Design for Electrical Stimulation in Upper Limb Rehabilitation

Modelling, Identification and Robust Performance

Springer

Chris Freeman
University of Southampton
Southampton
UK

ISBN 978-3-319-25704-4 ISBN 978-3-319-25706-8 (eBook)
DOI 10.1007/978-3-319-25706-8

Library of Congress Control Number: 2015952996

Springer Cham Heidelberg New York Dordrecht London

Printed on acid-free paper

Springer International Publishing AG Switzerland is part of Springer Science+Business Media (www.springer.com)

To Kathryn

Preface

Assisting human movement using electrical stimulation and mechanical support is a challenging task. It must balance the demands of controlling highly complex, non-linear, time-varying dynamics with the practical requirements that exist when performing tests with neurologically impaired users. These demands naturally compete since the process of model identification and controller tuning is labour intensive, time-consuming, and may therefore fatigue or demotivate the user. This has led researchers in the field to focus on simplicity at the expense of performance and functional scope.

The motivation for this book is to develop a comprehensive control design framework to enable performance and pragmatism to be transparently balanced. Emphasis is placed on applying and translating robust performance results into intuitive procedures that are suitable for application in practice with users. These are illustrated by case studies demonstrating how the control approaches have been applied in a clinical setting, and the outcomes that have been achieved.

The rehabilitation systems developed and clinically evaluated in this book are a result of a decade of collaboration with my colleagues Dr. Ann-Marie Hughes and Professor Jane Burridge, both of the Faculty of Health Sciences at the University of Southampton. It is their clinical expertise that has driven the engineering component of this research, ensuring that it is strongly focused on solving real-world problems that meet users' needs. Clinical evaluation of the technology reported in this book has also involved substantial input from Dr. Katie Meadmore, Trish Sampson and Emma Hallewell. In terms of engineering contribution to the rehabilitation systems developed at Southampton, both Mustafa Kutlu and Dr. Tim Exell have provided critical input into the hardware development of the systems reported in Chaps. 7 and 9, respectively. In addition, Dr. Kai Yang and Dr. John Tudor developed the fabric electrodes described in Chap. 10, and Professor Mark

French has provided significant input to the estimation-based multiple model iterative learning control framework summarised in the same chapter. My sincere thanks to them all.

Southampton Chris Freeman
September 2015

Contents

Acronyms

9HPT	Nine Hole Peg Test
ANN	Artificial Neural Network
ARAT	Action Research Arm Test
CMC	Carpometacarpal
DALY	Disability-Adjusted Life Year
EEG	Electroencephalography
EMG	Electromyography
EMMILC	Estimation-based Multiple Model Iterative Learning Control
EMMSAC	Estimation-based Multiple Model Switched Adaptive Control
ES	Electrical Stimulation
FEA	Fabric Electrode Array
FMA	Fugl-Meyer Assessment
GUI	Graphical User Interface
ILC	Iterative Learning Control
LTI	Linear Time-Invariant
LTV	Linear Time-Varying
MAM	Manual Ability Measure
MCP	Metacarpophalangeal
MIMO	Multiple Input, Multiple Output
MS	Multiple Sclerosis
NOILC	Norm Optimal Iterative Learning Control
PD	Proportional-Derivative
PID	Proportional-Integral-Derivative
PIP	Proximal Interphalangeal
PWM	Pulse-Width Modulated
PVC	Polyvinyl Chloride
pwMS	People with MS
RGB	Red, Green, Blue
SCI	Spinal Cord Injury
SISO	Single Input, Single Output
VR	Virtual Reality

Chapter 1
Introduction

Fifteen million people annually experience a stroke, and every two seconds someone in the world will have a stroke for the first time [1]. During a stroke, tissues in the brain are damaged because their blood supply is obstructed by a blood clot or by a narrowing or bursting of blood vessels. A third of people who experience a stroke are left permanently disabled, and require care. Since stroke is an age-related disease, the number of strokes worldwide is expected to increase. The burden of stroke is often measured using disability-adjusted life years (DALYs), which combine years of potential life lost due to premature death with years of productive life lost due to disability. Using this measure, stroke burden is projected to rise from 38 million DALYs globally in 1990 to 61 million DALYs in 2020.

A common result of stroke is an impaired ability to control movement. For example, half of all acute stroke patients starting rehabilitation have a marked impairment of function of one arm, of whom only about 14 % will regain sensory-motor function. This is particularly detrimental since it has also been argued that arm and hand function is more important than mobility in achieving independence after stroke.

The brain's ability to reorganize itself by forming new neural connections means that it is possible to 're-learn' lost movement capability through intense practice of functional tasks. As with learning any new skill, this process requires sensory feedback (e.g. visual, proprioceptive or haptic) to promote the necessary reorganization of pathways in the motor cortex of the brain. The problem facing the stroke patient is that they are unable to practice moving their impaired limb and therefore are unable to receive feedback. The longer this disuse continues, the less likely recovery becomes because surrounding areas of the motor cortex are gradually taken over by other functions still under the patient's voluntary control.

1.1 Rehabilitation Technologies

Conventional therapy consists of performing movement exercises using the impaired arm, with assistance provided by a physiotherapist. Unfortunately, conventional treatments have been found to have a very limited effect on recovery of useful function, and there is hence a pressing need for novel rehabilitation technologies to support

C. Freeman, *Control System Design for Electrical Stimulation in Upper Limb Rehabilitation*, DOI 10.1007/978-3-319-25706-8_1

recovery of arm function post-stroke. Governments around the world are urging health and social care services to adopt innovative technology that patients can use at home to support independent living. For example, the UK government termed the situation a 'ticking time bomb' in a recent report, and in 2014 introduced the 'Care Bill' calling on health and social services to adopt innovative technology that patients can use at home to support independent living.

In recent years new assistive technologies have emerged to reduce impairment post-stroke, including electrical stimulation [2–5] and rehabilitation robots [6], which facilitate intense practice of movement in a motivating environment. These technologies have potential to provide the motivation, assistance, range and duration of task practice required for effective rehabilitation of functional movement.

Electrical stimulation (ES) uses electric impulses to artificially contract muscles and has become an area of intense engineering and clinical research over the last few years. By directly activating weak or paralyzed muscles, ES is able to drive neuroplastic cortical changes to enable recovery. ES is supported by a growing body of clinical evidence [7–9]. For example, meta-analysis of 22 randomized control trials involving 894 participants in [8] found that neuromuscular stimulation of the wrist/finger flexors/extensors had a significant beneficial effect on motor function (impairment) and muscle strength. This body of clinical evidence has theoretical support from neurophysiology [10] and motor learning [11] which shows that the therapeutic benefit increases when it is applied co-incidently with a patient's own voluntary intention [12]. Hence ES must precisely assist the patient's own voluntary task completion in order to maximize functional recovery. Its inherent affordability means there is also intense commercial interest in ES technology, with numerous products available on the market. Use of ES has also gained recognition from bodies such as The Royal College of Physicians (RCP), National Institute for Health and Care Excellence (NICE), and Evidence-Based Review of Stroke Rehabilitation (EBRSR). The latter concludes that 'there is strong evidence that ES treatment improves upper extremity function'.

Increasingly ES is being combined with mechanical support, taking the form of either passive orthoses or active robots. These devices help support the affected limb, and may resist or assist movement through various training modalities. They can therefore help reduce muscle fatigue or provide functionality that ES cannot (e.g. to assist with forearm supination or help stabilze the scapula).

Although systematic reviews support the use of robots [13] and electrical stimulation [8, 9] to reduce impairments and in some cases improve function, translation into clinical practice remains poor. A recent survey has found that removal of key barriers limiting translation requires improvements in assistive technology design, pragmatic clinical evaluation, better knowledge and awareness and improvement in provision of services [14].

1.2 Role of Control Systems

ES and robotic technologies both have rich potential to help people with impaired movement perform the tasks they need for every-day living. Their performance in doing so is governed by the ability of their control systems to accurately support the intended movement. Model-based control is critical to enable any dynamic system performing a tracking or regulation task to maximize performance in the presence of measurement noise and exogenous disturbances. However few model-based upper limb ES approaches have been implemented within clinical ES systems and none in commercial products. The controllers typically employed are open-loop or triggered by switches or external events, and therefore do not adjust the supplied ES according to the movement produced. This not only means that the resulting movements are generally crude and inaccurate, but they also do not adequately promote voluntary contribution from the user. Current systems are therefore limited in terms of the type of tasks they train, and the amount and manner in which they assist movement. This severely limits the quality of the assistance they provide, and hence the effectiveness of treatment when used therapeutically for the purpose of rehabilitation. Principal reasons for this are the difficulties in:

- modeling the movement produced by ES,
- identifying the dynamic model effectively and efficiently in practice,
- defining and assisting complex tasks involving many muscles and joints,
- sensing the positions of relevant joints in real-time, and
- designing control systems that allow the user to perform the task accurately despite physiological changes in their response to ES, exogenous disturbances and measurement error.

Therefore, this book focuses on constructing a control design framework with the necessary generality and scope to address all these modeling, identification, task specification and control design issues. Its aim is to provide a systematic set of theoretical results, procedures and illustrative case-studies that together provide a comprehensive and widely applicable framework for upper limb ES control design. Although the analysis is necessarily theoretical, results are tied to practical design considerations intended to maximize the effectiveness of ES technology (combined if necessary with mechanical support) to assist impaired people to complete functional activities such as reaching, pressing buttons, grasping and manipulating objects.

The book will primarily focus on rehabilitation with the assumption that the task is presented to the user during a training paradigm, and is therefore known a priori and is repetitive in nature. However, extensions are outlined to more general assistive utility, in which ES is employed as an orthosis (i.e. to assist people in performing movements during their day-to-day lives without an intended therapeutic re-learning effect). It will also outline extensions to incorporate increased sensor data, emerging hardware, and address pertinent challenges in the field.

1.3 Book Structure

Chapter 2 introduces the dynamic structures that comprise the control problem: the stimulated human arm combined with a robotic or passive support. Identification methods are also presented and exemplified.

Chapter 3 presents control design procedures for a general class of feedback controllers, leading to explicit stability guarantees for both actuated and unactuated joint variable sets.

Chapter 4 extends the control framework to include an additional update mechanism termed 'iterative learning control' that enables the system to learn from previous attempts at the task. Results provide a transparent separation between the feedback controller and the learning update with respect to both tracking performance and robust stability margins.

Chapter 5 presents results from a clinical feasibility trial undertaken with people with multiple sclerosis, in which the dual feedback and iterative learning control framework is implemented and assessed.

Chapter 6 extends the previous control strategies by embedding principles from human motor control so that they can support fully functional tasks. Results are then presented from an experimental study to confirm accuracy of the proposed human motor control models.

Chapter 7 describes how the controller extensions are used in a further clinical feasibility study with stroke participants. The system is described, and clinical feasibility results are presented and discussed.

Chapter 8 applies the earlier control framework to the emerging field of ES electrode arrays, and provides design procedures that address the difficulty in obtaining an accurate model when using these arrays. Design freedoms embedded in both controller structures are exploited to meet this challenge, together with mechanisms with which to make identification feasible in clinical practice.

Chapter 9 develops a general procedure which integrates both arrays and single-pad electrodes within a comprehensive, overarching design framework. This framework is then employed within an upper limb rehabilitation system which embeds novel hardware, including depth cameras, arrays and a touch table. Experimental results from a usability study with stroke participants are then presented and discussed.

Chapter 10 outlines conclusions and future research directions which focus on the translation of technology into patients' homes. These include extensions to the framework which remove the need to perform identification tests, and the development of wearable electrode array prototypes.

References

1. Stroke Association, *State of the nation—stroke statistics*. Technical report, Stroke.org.uk (2015)
2. N. Foley, R.W. Teasell, J. Jutai, S. Bhogal, E. Kruger, Evidence-based review of stroke rehabilitation: upper extremity interventions, version 11 (2008), http://www.ebrsr.com/uploads/Upper_Extremity.pdf
3. T. Pelton, P. van Vliet, K. Hollands, Interventions for improving coordination of reach to grasp following stroke: a systematic review. Int. J. Evid.-Based Healthc. **10**(2), 89–102 (2012)
4. K. Hayward, R. Barker, S. Brauer, Interventions to promote upper limb recovery in stroke survivors with severe paresis: a systematic review. Disabil. Rehabil. **32**(24), 1973–1986 (2010)
5. F. Quandt, F.C. Hummel, The influence of functional electrical stimulation on hand motor recovery in stroke patients: a review. Exp. Transl. Stroke Med. **6**(1), 9 (2014)
6. G.B. Prange, M.A. Jannick, C.G.M. Groothuis-Oudshoorn, H. Hermens, M.J. Ijzerman, Systematic review of the effect of robot-aided therapy on recovery of the hemiparetic arm after stroke. J. Rehabil. Res. Dev. **43**, 171–184 (2006)
7. J.R. de Kroon, J.H. van der Lee, M.J. Ijzerman, G.J. Lankhorst, Therapeutic electrical stimulation to improve motor control and functional abilities of the upper extremity after stroke: a systematic review. Clin. Rehabil. **16**, 350–360 (2002)
8. J.M. Veerbeek, E. van Wegen, R. van Peppen, P.J. van der Wees, E. Hendriks, M. Rietberg, G. Kwakkel, What is the evidence for physical therapy poststroke? A systematic review and meta-analysis. PLoS One **9**(2), e87987 (2014)
9. O.A. Howlett, N.A. Lannin, L. Ada, C. McKinstry, Functional electrical stimulation improves activity after stroke: a systematic review with meta-analysis. Arch. Phys. Med. Rehabil. **96**(5), 934–943 (2015)
10. J.H. Burridge, M. Ladouceur, Clinical and therapeutic applications of neuromuscular stimulation: a review of current use and speculation into future developments. Neuromodulation **4**(4), 147–154 (2001)
11. R.A. Schmidt, T.D. Lee, *Motor Control and Learning: A Behavioural Emphasis*, 4th edn. (Human Kinetics Europe Ltd, Champaign, 2005)
12. D.N. Rushton, Functional electrical stimulation and rehabilitation—an hypothesis. Med. Eng. Phys. **25**(1), 75–78 (2003)
13. J. Mehrholz, A. Hadrich, T. Platz, M. Pohl, Electromechanical and robot-assisted arm training for improving generic activities of daily living, arm function, and arm muscle strength after stroke. Cochrane Database Syst. Rev. **6**, CD006876 (2012)
14. A.-M. Hughes, J.H. Burridge, S.H. Demain, C.E. Ellis-Hill, C. Meagher, L. Tedesco-Triccas, R. Turk, I. Swain, Translation of evidence-based assistive technologies into stroke rehabilitation: users' perceptions of the barriers and opportunities. BMC Health Serv. Res. **14**, 124 (2014)

Chapter 2
Modeling and Identification

Assistive upper limb technologies must be applied within a controlled environment in order to ensure safety and comfort across a broad spectrum of patient ability. When using electrical stimulation to assist completion of upper limb reaching movements, this environment may be provided by a passive/orthotic support device such as a simple sling or hinged 'de-weighting' structure, or an active robotic mechanism of which many designs are available [1]. In this chapter a suitable model of the combined human arm and mechanical support is developed that has widespread application across upper limb rehabilitation. This representation will then be used in subsequent chapters for model-based controller development.

2.1 Modeling of the Mechanically Supported Human Arm

Spasticity (velocity-dependent stiffness) is common in stroke and typically produces resistance to arm extension due to overactivity of biceps, wrist and finger flexors, and loss of activity of triceps, anterior deltoid, wrist and finger extensors [2]. For effective upper limb stroke rehabilitation, ES should therefore be provided to assist muscles that have experienced a loss of activity, such as the triceps, anterior deltoid, wrist and finger extensors [2–4]. This is in contrast to overactivity of muscles such as the biceps, wrist and finger flexors, which typically produce a resistance to arm extension as a result of spasticity. Triceps and anterior deltoid are hence often selected for stimulation because they align with the clinical need to increase muscle tone and restore motor control of weakened muscles.

C. Freeman, *Control System Design for Electrical Stimulation in Upper Limb Rehabilitation*, DOI 10.1007/978-3-319-25706-8_2

The relationship between muscle stimulation and subsequent movement is well explored, and sophisticated muscle models exist with multiple attachment points across more than one joint, and movement over complex sliding surfaces [5]. Clear divisions exist between modeling for analysis and for direct model-based control application. The former encompass muscles with multiple attachment points, often biarticular structure, and movement over pre-defined sliding surfaces [5, 6]. However, dynamic models used for experimental motion control must be identifiable and assumptions such as muscles eliciting moments about a single fixed axis offer practical routes for parameter identification. A pragmatic approach appropriate to clinical implementation is therefore taken, with additional simplifications discussed in Sect. 2.2. This opens up routes for both parameter identification and controller derivation that have not yet been possible for more complex models [7].

2.1.1 Human Arm Dynamics

A general dynamic model of the human arm is given by

$$\boldsymbol{B}_h(\boldsymbol{\Phi})\ddot{\boldsymbol{\Phi}} + \boldsymbol{C}_h(\boldsymbol{\Phi}, \dot{\boldsymbol{\Phi}})\dot{\boldsymbol{\Phi}} + \boldsymbol{F}_h(\boldsymbol{\Phi}, \dot{\boldsymbol{\Phi}}) + \boldsymbol{G}_h(\boldsymbol{\Phi}) = \boldsymbol{\tau}(\boldsymbol{u}, \boldsymbol{\Phi}, \dot{\boldsymbol{\Phi}}) \tag{2.1}$$

in which $\boldsymbol{\Phi} = [\phi_1, \ldots, \phi_p]^\top$ is the vector of p joint angles, $\boldsymbol{B}_h(\cdot)$ and $\boldsymbol{C}_h(\cdot)$ are inertial and Coriolis $p \times p$ matrices respectively, and $\boldsymbol{F}_h$ and $\boldsymbol{G}_h$ are frictional and gravitational $p \times 1$ vectors respectively. The term $\boldsymbol{\tau}(\boldsymbol{u}, \boldsymbol{\Phi}, \dot{\boldsymbol{\Phi}})$ comprises the moments generated through application of ES, so that if m muscles are assumed to actuate the upper limb system, $\boldsymbol{u}(t) = [u_1(t), \ldots, u_m(t)]^\top$. The ith element of the muscle torque vector $\boldsymbol{\tau}(\cdot)$ is the sum of moments generated by each of the m muscles that may each impart a moment about the ith joint.

2.1.2 Muscle Selection and Modeling

A well-established model of the moment, $\tau(t)$, generated by applying stimulation, $u(t)$, to a muscle acting about a single joint, $\phi(t)$, is

$$\boldsymbol{\tau}\big(u(t), \phi(t), \dot{\phi}(t)\big) = h(u(t), t) \times \tilde{F}_M\big(\phi(t), \dot{\phi}(t)\big) \tag{2.2}$$

where $h(u(t), t)$ is a Hammerstein structure incorporating a static non-linearity, $h_{IRC}(u(t))$, representing the isometric recruitment curve, cascaded with linear activation dynamics, $h_{LAD}(t)$. The multiplicative term $\tilde{F}_M(\cdot)$ captures the effect of joint angle and angular velocity on the force generated. When multiple joints are actuated by multiple muscles and/or tendons which may each span any subset of joints, then the general expression for the total moment generated about the ith joint is

$$\tau_i = \sum_j^m \left\{ r_{i,j}(\phi_i) \times \tau_{i,j}\left(u_j(t), \phi_i(t), \dot{\phi}_i(t)\right) \right\}, \quad i = 1, \ldots, p$$

$$= \Bigg[\underbrace{r_{i,1}(\phi_i)\tilde{F}_{M,i,1}\left(\boldsymbol{\Phi}(t), \dot{\boldsymbol{\Phi}}(t)\right)}_{F_{M,i,1}\left(\boldsymbol{\Phi}(t), \dot{\boldsymbol{\Phi}}(t)\right)}, \ldots, \underbrace{r_{i,m}(\phi_i)\tilde{F}_{M,i,m}\left(\boldsymbol{\Phi}(t), \dot{\boldsymbol{\Phi}}(t)\right)}_{F_{M,i,m}\left(\boldsymbol{\Phi}(t), \dot{\boldsymbol{\Phi}}(t)\right)} \Bigg] \begin{bmatrix} h_1(u_1(t), t) \\ \vdots \\ h_m(u_m(t), t) \end{bmatrix} \tag{2.3}$$

Here $r_{i,j}(\phi_i) = \frac{\partial E_j(\phi_i)}{\partial \phi_i}$ is the moment arm of the jth muscle with respect to the ith joint, where E is the associated excursion (displacement) [8]. If each muscle length is primarily dependent on a single joint angle, the form $\tilde{F}_{M,i,j}(\boldsymbol{\Phi}, \dot{\boldsymbol{\Phi}}) = \tilde{F}_{M,i,j}(\phi_i, \dot{\phi}_i)$ can be taken, leading to the simplified structure

$$\tau_i = \Bigg[\underbrace{r_{i,1}(\phi_i)\tilde{F}_{M,i,1}\left(\phi_i(t), \dot{\phi}_i(t)\right)}_{F_{M,i,1}\left(\phi_i(t), \dot{\phi}_i(t)\right)}, \ldots, \underbrace{r_{i,m}(\phi_i)\tilde{F}_{M,i,m}\left(\phi_i(t), \dot{\phi}_i(t)\right)}_{F_{M,i,m}\left(\phi_i(t), \dot{\phi}_i(t)\right)} \Bigg] \begin{bmatrix} h_1(u_1(t), t) \\ \vdots \\ h_m(u_m(t), t) \end{bmatrix}. \tag{2.4}$$

It is also possible to include the neuromuscular reflex in the form of an additional dynamic function placed in series with the muscle model. However it is neglected here since ES produces negligible effect on the reflex loop when applied on a macroscopic scale as in the transcutaneous case considered in [9, 10]. It is also worth noting that recent works have shown that Hill-Huxley models [11–13] may be at least as accurate as a Hammerstein structure in representing the activation dynamics [14]. The drawback that their complexity undermines application to control has been countered by the proposal of a Hammerstein-Wiener structure [15], but as yet Hill-Huxley models have not been shown to extend to non-isometric conditions, and have not been used in controller derivation.

2.1.3 Mechanical Support

As stated, the human arm is often supported by a mechanical device during ES assisted task practice in order to reduce fatigue and provide additional assistance. A general dynamic model of the support structure which assumes rigid links is

$$\boldsymbol{B}_a(\boldsymbol{\Theta})\ddot{\boldsymbol{\Theta}} + \boldsymbol{C}_a(\boldsymbol{\Theta}, \dot{\boldsymbol{\Theta}})\dot{\boldsymbol{\Theta}} + \boldsymbol{F}_a(\boldsymbol{\Theta}, \dot{\boldsymbol{\Theta}}) + \boldsymbol{G}_a(\boldsymbol{\Theta}) + \boldsymbol{K}_a(\boldsymbol{\Theta}) = -\boldsymbol{J}_a^\top(\boldsymbol{\Theta})\boldsymbol{h} \tag{2.5}$$

where $\boldsymbol{\Theta} = [\theta_1, \ldots, \theta_q]^\top$ is a vector of q joint angles, $\boldsymbol{h}$ is a $q \times 1$ vector of externally applied force, and $\boldsymbol{B}_a(\cdot)$ and $\boldsymbol{C}_a(\cdot)$ are $q \times q$ inertial and Coriolis matrices respectively. In addition, $\boldsymbol{J}_a(\cdot)$ is the system Jacobian, and $\boldsymbol{F}_a(\cdot)$ and $\boldsymbol{G}_a(\cdot)$ are friction and gravitational $q \times 1$ vectors respectively. Finally, vector $\boldsymbol{K}_a(\cdot)$ comprises the $q \times 1$

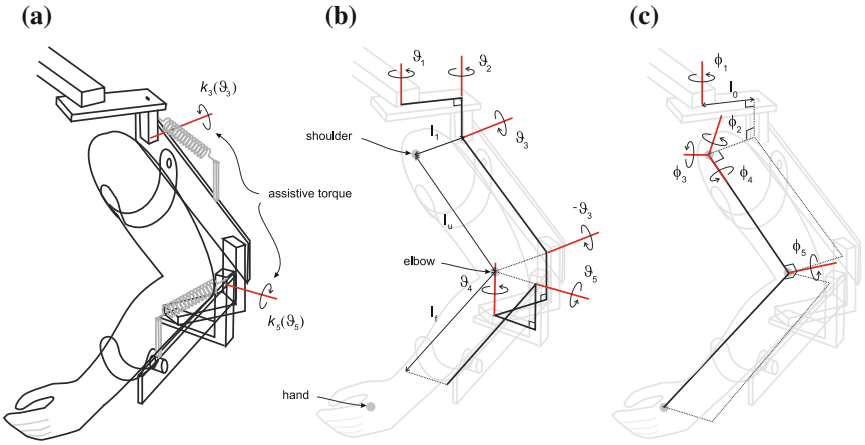

Fig. 2.1 ArmeoSpring: **a** mechanical support, **b** kinematic relationships, and **c** human arm

moments produced by the assistive action of the support mechanism. This may be passive, via springs or counter-balances, or active, as in the case of a robotic structure supplying active torque to assist, or even resist, the intended movement.

A popular form of support is an exoskeletal structure which enables assistance to be applied about individual joints. An example is the commercial ArmeoSpring (Hocoma AG) which provides adjustable force against gravity via two springs. Each joint is aligned in either the horizontal or vertical plane, as shown in Fig. 2.1a, with measured joint variables $\boldsymbol{\Theta} = [\theta_1, \theta_2, \theta_3, \theta_4, \theta_5]^\top$. The patient's arm is rigidly strapped to the exoskeleton support with lengths l_0, l_1 relating the shoulder joint to a fixed base frame.

Hence for the ArmeoSpring $\boldsymbol{B}_a(\cdot)$ and $\boldsymbol{C}_a(\cdot)$ are 5-by-5 inertial and Corelis matrices, and moments produced through gravity compensation provided by each spring yield the form $\boldsymbol{K}_a(\cdot) = [0, 0, k_3(\theta_3), 0, k_5(\theta_5)]^\top$. Figure 2.1c shows the axes corresponding to anthropomorphic joints.

Another common structure is the end-effector type where support is only supplied at a single attachment point. An example is the SaeboMAS (Saebo, Charlotte, USA) shown in Fig. 2.2. Here the support takes the form $\boldsymbol{K}_a(\cdot) = [k_1(\theta_1), 0, 0, 0]^\top$.

2.1.4 Combined Dynamics

It is now assumed that within the necessary joint ranges there exists a unique bijective transformation between coordinate sets, given by $\boldsymbol{\Theta} = \boldsymbol{k}(\boldsymbol{\Phi})$, which allows the mechanical support and human arm models to be combined. This explicitly holds for exoskeletal passive or robotic structures (where $q = p$), and can be extended to

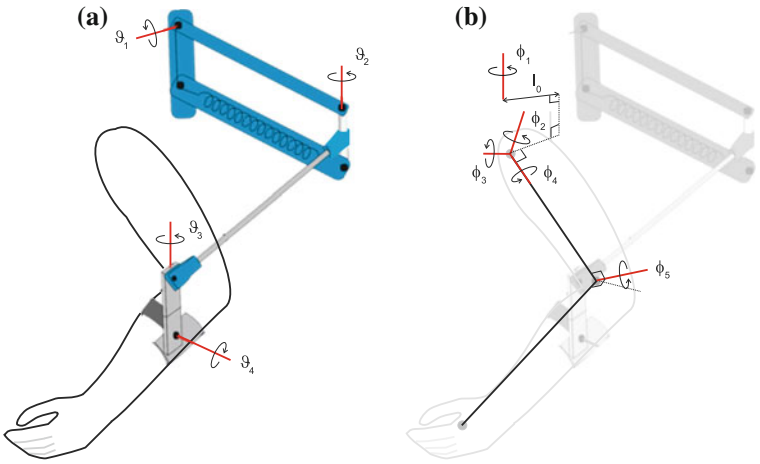

Fig. 2.2 SaeboMAS: **a** mechanical support and kinematic relationships, and **b** human arm

end-effector robot devices developed for rehabilitation. The Lagrangian equation in one variable can be expressed in terms of the other through application of the chain rule, and the results added to produce the combined model

$$\boldsymbol{B}(\boldsymbol{\Phi})\ddot{\boldsymbol{\Phi}} + \boldsymbol{C}(\boldsymbol{\Phi}, \dot{\boldsymbol{\Phi}})\dot{\boldsymbol{\Phi}} + \boldsymbol{F}(\boldsymbol{\Phi}, \dot{\boldsymbol{\Phi}}) + \boldsymbol{G}(\boldsymbol{\Phi}) + \boldsymbol{K}(\boldsymbol{\Phi}) = \boldsymbol{\tau}(\boldsymbol{u}, \boldsymbol{\Phi}, \dot{\boldsymbol{\Phi}}) - \boldsymbol{J}^{\top}(\boldsymbol{\Phi})\boldsymbol{h} \tag{2.6}$$

where

$$\begin{aligned}
\boldsymbol{B}(\boldsymbol{\Phi}) &= \boldsymbol{B}_h(\boldsymbol{\Phi}) + \boldsymbol{k}_1(\boldsymbol{\Phi})^{\top}\boldsymbol{B}_a(\boldsymbol{k}(\boldsymbol{\Phi}))\boldsymbol{k}_1(\boldsymbol{\Phi}), \quad \boldsymbol{J}^{\top}(\boldsymbol{\Phi}) = \boldsymbol{k}_1(\boldsymbol{\Phi})^{\top}\boldsymbol{J}_a^{\top}(\boldsymbol{k}(\boldsymbol{\Phi})), \\
\boldsymbol{C}(\boldsymbol{\Phi}, \dot{\boldsymbol{\Phi}}) &= \boldsymbol{C}_h(\boldsymbol{\Phi}, \dot{\boldsymbol{\Phi}}) + \boldsymbol{k}_1(\boldsymbol{\Phi})^{\top}\boldsymbol{C}_a(\boldsymbol{k}(\boldsymbol{\Phi}), \boldsymbol{k}_1(\boldsymbol{\Phi})\dot{\boldsymbol{\Phi}})\boldsymbol{k}_1(\boldsymbol{\Phi}) \\
&\quad + \boldsymbol{k}_1(\boldsymbol{\Phi})^{\top}\boldsymbol{B}_a(\boldsymbol{k}(\boldsymbol{\Phi}))\boldsymbol{k}_2(\boldsymbol{\Phi}, \dot{\boldsymbol{\Phi}}), \\
\boldsymbol{F}(\boldsymbol{\Phi}, \dot{\boldsymbol{\Phi}}) &= \boldsymbol{F}_h(\boldsymbol{\Phi}, \dot{\boldsymbol{\Phi}}) + \boldsymbol{k}_1(\boldsymbol{\Phi})^{\top}\boldsymbol{F}_a(\boldsymbol{k}(\boldsymbol{\Phi}), \boldsymbol{k}_1(\boldsymbol{\Phi})\dot{\boldsymbol{\Phi}}), \quad \boldsymbol{K}(\boldsymbol{\Phi}) = \boldsymbol{k}_1(\boldsymbol{\Phi})^{\top}\boldsymbol{K}_a(\boldsymbol{k}(\boldsymbol{\Phi})), \\
\boldsymbol{G}(\boldsymbol{\Phi}) &= \boldsymbol{G}_h(\boldsymbol{\Phi}) + \boldsymbol{k}_1(\boldsymbol{\Phi})^{\top}\boldsymbol{G}_a(\boldsymbol{k}(\boldsymbol{\Phi})),
\end{aligned}$$

with $\boldsymbol{k}_1(\boldsymbol{\Phi}) = \dfrac{d\boldsymbol{k}(\boldsymbol{\Phi})}{d\boldsymbol{\Phi}}$ and $\boldsymbol{k}_2(\boldsymbol{\Phi}, \dot{\boldsymbol{\Phi}}) = \dfrac{d}{dt}\left(\dfrac{d\boldsymbol{k}(\boldsymbol{\Phi})}{d\boldsymbol{\Phi}}\right)$.

Now let each $h_{LAD,j}(t)$ be realized using continuous-time state-space model matrices $\{\boldsymbol{M}_{A,j}, \boldsymbol{M}_{B,j}, \boldsymbol{M}_{C,j}\}$ (state, input and output respectively), with corresponding states $\boldsymbol{x}_j(t)$. The system (2.6) can then be expressed over time interval $t \geq 0$ in the following state-space form

$$\dot{\boldsymbol{x}}_s(t) = \underbrace{\begin{bmatrix} \dot{\boldsymbol{\Phi}}(t) \\ \boldsymbol{B}(\boldsymbol{\Phi}(t))^{-1}\boldsymbol{X}\left(\boldsymbol{\Phi}(t), \dot{\boldsymbol{\Phi}}(t)\right) \\ \boldsymbol{M}_{A,1}\boldsymbol{x}_1 \\ \vdots \\ \boldsymbol{M}_{A,m}\boldsymbol{x}_m \end{bmatrix}}_{\boldsymbol{f}_s(\boldsymbol{x}_s(t))} + \underbrace{\begin{bmatrix} \boldsymbol{0} \\ \boldsymbol{0} \\ \boldsymbol{M}_{B,1}h_{IRC,1}(u_1(t)) \\ \vdots \\ \boldsymbol{M}_{B,m}h_{IRC,m}(u_m(t)) \end{bmatrix}}_{\boldsymbol{g}_s(\boldsymbol{u}(t))},$$

$$\boldsymbol{\Phi}(t) = \underbrace{\begin{bmatrix} \boldsymbol{I} & \boldsymbol{0} & \cdots & \boldsymbol{0} \end{bmatrix}\boldsymbol{x}_s(t)}_{\boldsymbol{h}_s(\boldsymbol{x}_s(t))}, \quad \boldsymbol{\Phi}(0) = \boldsymbol{\Phi}_0, \tag{2.7}$$

where $\boldsymbol{x}_s(t) = [\boldsymbol{\Phi}(t)^\top, \ \dot{\boldsymbol{\Phi}}(t)^\top, \ \boldsymbol{x}_1(t)^\top \ \cdots \ \boldsymbol{x}_m(t)^\top]^\top$, and the ith row of $\boldsymbol{X}\left(\boldsymbol{\Phi}(t), \dot{\boldsymbol{\Phi}}(t)\right)$ is given by

$$\begin{aligned} X_i\left(\boldsymbol{\Phi}(t), \dot{\boldsymbol{\Phi}}(t)\right) = &\sum_j^m \left(\boldsymbol{M}_{C,j}\boldsymbol{x}_j(t)F_{M,i,j}\left(\boldsymbol{\Phi}(t), \dot{\boldsymbol{\Phi}}(t)\right)\right) - \left(\boldsymbol{J}^\top(\boldsymbol{\Phi}(t))\right)_i \boldsymbol{h}(t) \\ &- \boldsymbol{C}_i\left(\boldsymbol{\Phi}(t), \dot{\boldsymbol{\Phi}}(t)\right)\dot{\boldsymbol{\Phi}}(t) - \boldsymbol{F}_i\left(\boldsymbol{\Phi}(t), \dot{\boldsymbol{\Phi}}(t)\right) - \boldsymbol{G}_i(\boldsymbol{\Phi}(t)) - \boldsymbol{K}_i(\boldsymbol{\Phi}(t)). \end{aligned}$$

2.2 Model Identification

We next develop procedures to identify parameters in composite model (2.6) that can be used in a clinical setting. We first assume it is possible to manipulate each joint individually while measuring and recording the resulting joint angle and applied force signals. This is clearly not possible for all joints in the wrist and hand, and so alternative identification approaches for these structures are presented in Chap. 8.

Depending on the underlying musculo-tendon structure, it is often possible to set terms within (2.3) or (2.4) to zero by defining joint axes which align with the axes about which muscles generate moments. This is discussed next, before an illustrative example is presented in Sect. 2.2.5.

2.2.1 Muscle Axis Identification

After measuring rigid body lengths, the next step is to define the position and orientation of each joint in the kinematic chain of the anthropomorphic system. In some cases these axes are uniquely defined (e.g. the elbow joint) and in others multiple choices are possible (e.g. the glenohumeral joint). In the latter case joints can be specified to align with the one or more axes about which ES produces movement (e.g. motion about the glenohumeral joint due to anterior deltoid stimulation). Identification of these axes is simplified if they can be assumed to be fixed with respect to a rigid link, and a suitable procedure is described in the appendix of [16]. This involves applying stimulation followed by the least squares fitting of a three dimen-

sional plane to the arc traced out by a point attached to the link. Fixed rotations are introduced into the kinematic chain to align the axis with a vector orthogonal to this plane. This procedure results in components of $F_M(\cdot)$ within (2.3) being set to zero. For example, if muscle j is aniarticular (i.e. acts about a single joint axis) and the above approach is applied to identify corresponding joint axis i, this produces the simplified form

$$F_{M,i,j}(\boldsymbol{\Phi}(t), \dot{\boldsymbol{\Phi}}(t)) \begin{cases} =0, & j \neq i \\ \neq 0, & j = i. \end{cases} \tag{2.8}$$

2.2.2 Passive Parameter Identification

With no applied ES, system (2.6) simplifies to

$$\boldsymbol{B}(\boldsymbol{\Phi})\ddot{\boldsymbol{\Phi}} + \boldsymbol{C}(\boldsymbol{\Phi}, \dot{\boldsymbol{\Phi}})\dot{\boldsymbol{\Phi}} + \boldsymbol{F}(\boldsymbol{\Phi}, \dot{\boldsymbol{\Phi}}) + \boldsymbol{G}(\boldsymbol{\Phi}) + \boldsymbol{K}(\boldsymbol{\Phi}) = -\boldsymbol{J}_h^\top(\boldsymbol{\Phi})\boldsymbol{h} \tag{2.9}$$

and can be written in a linear-in-parameter form. First introduce matrix $\boldsymbol{Y}_B$ containing kinematic data, and vector $\boldsymbol{\pi}_B$ containing a minimal parameter set, such that

$$\begin{aligned} &\boldsymbol{Y}_B\left(\boldsymbol{\Phi}(t), \dot{\boldsymbol{\Phi}}(t), \ddot{\boldsymbol{\Phi}}(t)\right)\boldsymbol{\pi}_B \\ &\quad = \boldsymbol{B}(\boldsymbol{\Phi}(t))\ddot{\boldsymbol{\Phi}}(t) + \boldsymbol{C}(\boldsymbol{\Phi}(t), \dot{\boldsymbol{\Phi}}(t))\dot{\boldsymbol{\Phi}}(t) + \boldsymbol{G}(\boldsymbol{\Phi}(t)) + \boldsymbol{K}(\boldsymbol{\Phi}(t)). \end{aligned}$$

Similarly represent $\boldsymbol{F}(\boldsymbol{\Phi}, \dot{\boldsymbol{\Phi}})$ using piecewise linear functions by introducing matrix $\boldsymbol{Y}_F$ containing kinematic data, and vector $\boldsymbol{\pi}_F$ containing a minimal parameter set, such that

$$\boldsymbol{Y}_F\left(\boldsymbol{\Phi}(t), \dot{\boldsymbol{\Phi}}(t)\right)\boldsymbol{\pi}_F = \boldsymbol{F}(\boldsymbol{\Phi}(t), \dot{\boldsymbol{\Phi}}(t)). \tag{2.10}$$

Using these (2.9) is written as

$$\underbrace{[\boldsymbol{Y}_B(t),\ \boldsymbol{Y}_F(t)]}_{\boldsymbol{Y}(t)} \underbrace{\left[\boldsymbol{\pi}_B^\top,\ \boldsymbol{\pi}_F^\top\right]^\top}_{\boldsymbol{\pi}} = \underbrace{-\boldsymbol{J}_h^\top(\boldsymbol{\Phi}(t))\boldsymbol{h}(t)}_{\hat{\boldsymbol{\tau}}(t)}. \tag{2.11}$$

A 6-axis force/torque sensor is attached to the extreme link of the mechanical support to provide externally applied force and torque vector $\boldsymbol{h}$. This can be done using a handle attached to the sensor which is used to kinematically excite the system, during which the kinematic variables $\boldsymbol{Y}(t)$ and forces $\hat{\boldsymbol{\tau}}(t)$ are recorded at discrete times $t = \{t_1, \ldots, t_N\}$. For structures with multiple degrees of freedom, this process may need to be repeated with different attachment points to provide sufficient kinematic excitation to all joints. From these assemble the matrices

$$\bar{\boldsymbol{Y}} = \left[\boldsymbol{Y}(t_1)^\top \cdots \boldsymbol{Y}(t_N)^\top\right]^\top, \quad \bar{\boldsymbol{\tau}} = \left[\hat{\boldsymbol{\tau}}(t_1)^\top \cdots \hat{\boldsymbol{\tau}}(t_N)^\top\right]^\top.$$

The least squares solution to the problem $\min_{\boldsymbol{\pi}} \|\bar{\boldsymbol{Y}}\boldsymbol{\pi} - \bar{\boldsymbol{\tau}}\|^2$ for the parameter vector is $\boldsymbol{\pi} = \bar{\boldsymbol{Y}}^{\dagger}\bar{\boldsymbol{\tau}}$ where $\boldsymbol{A}^{\dagger} = (\boldsymbol{A}^{\top}\boldsymbol{A})^{-1}\boldsymbol{A}^{\top}$ denotes the pseudoinverse of $\boldsymbol{A}$.

There is always a compromise between accuracy and repeatability in practice, and hence the simplest realistic structure should be used to represent unknown functional forms appearing in (2.6). For example, biomechanical coupling between anthropomorphic joints can be omitted to give the form

$$\boldsymbol{F}(\boldsymbol{\Phi}, \dot{\boldsymbol{\Phi}}) = [F_{e,1}(\phi_1) + F_{v,1}(\dot{\phi}_1), \ldots, F_{e,p}(\phi_p) + F_{v,p}(\dot{\phi}_p)]^{\top}, \tag{2.12}$$

provided effects such as spasticity in bi-articular elbow/shoulder muscles are sufficiently mild [17, 18]. The form (2.12) requires p instances of the structure

$$\sum_{n=1}^{N_e} a_n X_n(\phi_i) + \sum_{n=1}^{N_v} b_n X_n(\dot{\phi}_i), \quad i = 1, \ldots, p \tag{2.13}$$

with basis function $X_n(\dot{)}$, and N_e, N_v denoting the number of parameters appearing in each functional form. This gives rise to vector $[a_1, \ldots, a_{N_e}, b_1, \ldots, b_{N_v}]$ appearing in $\boldsymbol{\pi}_F$ for each instance, and a total of $p \times (N_e + N_v)$ parameters. Taking the more general form

$$\boldsymbol{F}(\boldsymbol{\Phi}, \dot{\boldsymbol{\Phi}}) = [F_{ev,1}(\phi_1, \dot{\phi}_1), \ldots, F_{ev,p}(\phi_p, \dot{\phi}_p)]^{\top}, \tag{2.14}$$

requires p instances of the form

$$\sum_{n=1}^{N_e \times N_v} c_n X_n(\phi_i, \dot{\phi}_i), \quad i = 1, \ldots, p \tag{2.15}$$

and hence a total of $p \times (N_e \times N_v)$ parameters appear in $\boldsymbol{\pi}_F$. More general functional forms therefore require far more data to identify, with the most general structure requiring $p^2 \times N_e \times N_v$ parameters. The simpler form of (2.12) has been found to be accurate provided effects such as spasticity in bi-articular elbow/shoulder muscles, which introduce biomechanical coupling between joints, are sufficiently mild [17]. Further information on constructing basis functions appears in [18].

2.2.3 Muscle Identification

Next consider the Hammerstein structures $h_j(u_j, t)$, $j = 1, \ldots, m$ appearing in torque vector $\boldsymbol{\tau}(t)$, defined by (2.2). These are identified by fixing the sensor handle and applying ES inputs, $u_j(t)$, to each muscle in turn. Vector $\hat{\boldsymbol{\tau}}(t)$ is recorded and the torque generated about the ith joint axis is extracted using

$$\tau_{i,j}(u_j(t), \boldsymbol{\Phi}, \dot{\boldsymbol{\Phi}}) = \boldsymbol{Y}_i(t)\hat{\boldsymbol{\pi}} - \hat{\tau}_i, \quad i = 1, \ldots, p \tag{2.16}$$

where $\hat{\boldsymbol{\pi}}$ is provided by the previous tests. Here $\boldsymbol{Y}_i(t)$ corresponds to static operating conditions $\boldsymbol{\Phi} = \bar{\boldsymbol{\Phi}}$, $\dot{\boldsymbol{\Phi}}, \ddot{\boldsymbol{\Phi}} = \boldsymbol{0}$, and taking without loss of generality $F_{M,i,j}(\bar{\boldsymbol{\Phi}}, \boldsymbol{0}) = 1$,

$$\tau_{i,j}(u_j(t), \bar{\boldsymbol{\Phi}}, \boldsymbol{0}) = h_j(u_j, t) \times F_{M,i,j}(\bar{\boldsymbol{\Phi}}, \boldsymbol{0}) = h_j(u_j, t). \tag{2.17}$$

Algorithms developed specifically for stroke patients appear in [19], and can be applied to data sets $\{u_j, \tau_{i,j}(\cdot)\}_{i=1,\ldots,p}$ to identify the Hammerstein structures $h_j(u_j, t)$, $j = 1, \ldots, m$. Each of these comprises static nonlinearity $h_{IRC,j}(\cdot)$ and linear activation dynamics $h_{LAD,j}(\cdot)$. The latter is then expressed using state-space matrices $\boldsymbol{M}_{A,j}, \boldsymbol{M}_{B,j}, \boldsymbol{M}_{C,j}$ for inclusion in state-space form (2.7).

2.2.4 Multiplicative Muscle Function Identification

To identify the general form of muscle function $F_{M,i,j}(\boldsymbol{\Phi}(t), \dot{\boldsymbol{\Phi}}(t))$, kinematic excitation is again applied and $\boldsymbol{Y}(t)$ and $\hat{\boldsymbol{\tau}}(t)$ recorded at samples $t = \{t_1, \ldots, t_N\}$. However now ES sequences $u_j(t)$ are applied and using the Hammerstein models previously identified, the isometric muscle torque is calculated using $h_j(u_j, t)$, so that

$$F_{M,i,j}(\boldsymbol{\Phi}(t), \dot{\boldsymbol{\Phi}}(t)) = \frac{\tau_i^*(t) - \hat{\tau}_i(t)}{h_j(u_j(t), t)}, \quad j = 1, \ldots, m. \tag{2.18}$$

Here $\boldsymbol{\tau}^*(t) = \boldsymbol{Y}(t)\hat{\boldsymbol{\pi}}$ is the passive torque, with $\hat{\boldsymbol{\pi}}$ provided by previous tests. $F_{M,i,j}(\cdot)$ is now represented as $\boldsymbol{Y}_{F_M}(t)\boldsymbol{\pi}_{F_m}$, with an optimal parameter set $\boldsymbol{\pi}_{F_M} = \bar{\boldsymbol{Y}}^{\dagger}\bar{\boldsymbol{\tau}}$, where

$$\bar{\boldsymbol{Y}} = \begin{bmatrix} \boldsymbol{Y}_{F_M}(t_1) \\ \vdots \\ \boldsymbol{Y}_{F_M}(t_N) \end{bmatrix}, \quad \bar{\boldsymbol{\tau}} = \begin{bmatrix} \dfrac{\tau_i^*(t_1) - \hat{\tau}_i(t_1)}{h_j(u_j(t_1), t_1)} \\ \vdots \\ \dfrac{\tau_i^*(t_N) - \hat{\tau}_i(t_N)}{h_j(u_j(t_N), t_N)} \end{bmatrix}.$$

Given the limited time available for identification in a clinical setting, accuracy can be improved by taking the simplest structure capable of capturing the underlying relationship. For example, if muscle length can be assumed to predominantly depend on a single joint angle, structure (2.4) yields

$$F_{M,i,j}(\boldsymbol{\Phi}(t), \dot{\boldsymbol{\Phi}}(t)) = F_{M,i,j}(\phi_i(t), \dot{\phi}_i(t)), \quad j = 1, \ldots, m \tag{2.19}$$

giving rise to m instances of the form (2.15), and a total of $m \times (N_e \times N_v)$ parameters, each associated with kinematic excitation of a single variable. To produce more

repeatable muscle functions, it has been proposed in [20] that the muscle model function takes the form

$$F_{M,i,j}(\boldsymbol{\Phi}(t), \dot{\boldsymbol{\Phi}}(t)) = F_{M1,i,j}(\phi_i(t)) \times F_{M2,i,j}(\dot{\phi}_i(t)), \quad j = 1, \ldots, m \tag{2.20}$$

and taking logarithms produces the identifiable form

$$\log\left(F_{M1,i,j}(\phi_i(t))\right) + \log\left(F_{M2,i,j}(\dot{\phi}_i(t))\right) = \log\left(\frac{\tau_i^*(t) - \hat{\tau}_i(t)}{h_j(u_j(t), t)}\right) \tag{2.21}$$

reducing the number of parameters to m instances of form (2.13) with a total of only $m \times (N_e + N_v)$ parameters. After identification, functions $F_{M1,i,j}(\phi_i(t))$ and $F_{M2,i,j}(\dot{\phi}_i(t))$ are retrieved through application of the exponential function.

2.2.5 *Case Study: Triceps and Anterior Deltoid with ArmeoSpring*

Consider the combined anthropomorphic and mechanical support structure shown in Fig. 2.1 and assume that ES is applied to the triceps and the anterior deltoid muscles. Following the procedure of Sect. 2.2.1, we assume the triceps generates a moment about an axis orthogonal to both the forearm and upper arm, and that the anterior deltoid generates a moment about an axis that is fixed with respect to the shoulder. These axes are shown in Fig. 2.3.

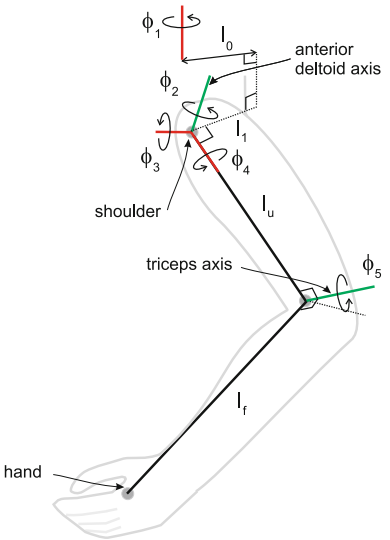

Fig. 2.3 Human arm kinematic relatioships ($m = 2$, $p = 5$)

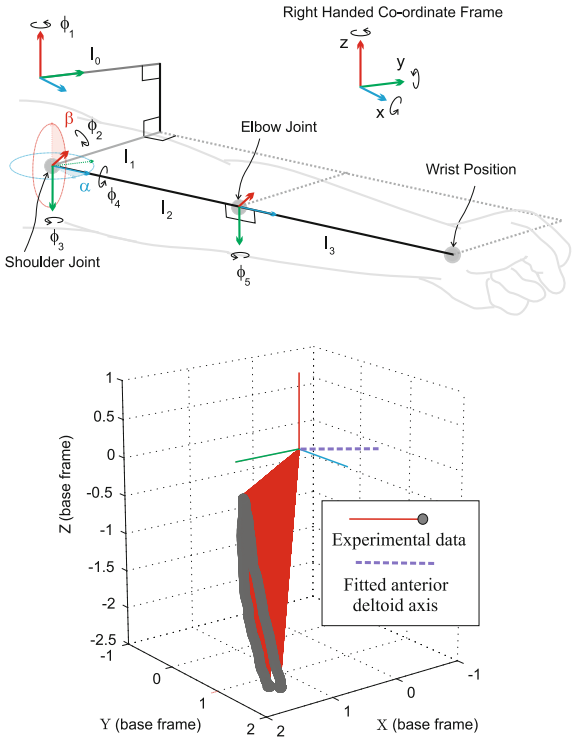

Fig. 2.4 Kinematic model with α and β defining the anterior deltoid axis, together with fitted experimental data. Experimental values $\alpha = 8°$, $\beta = -87°$, are shown together with $\phi_1 = \phi_2 = \phi_3 = \phi_4 = \phi_5 = 0$

To identify the anterior deltoid axis experimentally, the participant is seated in the ArmeoSpring, which is adjusted to their individual arm dimensions. The level of support in each spring is modified so that their arm is raised above their lap. Surface electrodes are placed on the anterior deltoid and triceps muscles and adjusted to elicit the maximum appropriate movement. ES is then applied to the anterior deltoid using a trapezoidal profile to slowly lift the arm, and then lower it back to the starting position. To orientate the ϕ_2 axis to correspond with the stimulated anterior deltoid, two additional rotations, with variables α and β, are introduced as shown in Fig. 2.4. After initial rotation of the base frame by ϕ_1, it is rotated about the z-axis by α and about the x-axis by β. The identification procedure described in the appendix of [16] yields values of α and β which are then substituted into the augmented dynamic model. An example of the fitted axis is shown in Fig. 2.4.

Next the passive identification procedure of Sect. 2.2.2 is applied using the functional form (2.12), yielding the parameter vector $\boldsymbol{\pi}$ appearing in (2.11). Examples of resulting frictional parameters relating to joint ϕ_2 are shown in Fig. 2.5.

The muscle identification procedure described in Sect. 2.2.3 is then applied. Experimental results are shown in Fig. 2.6 where the forms

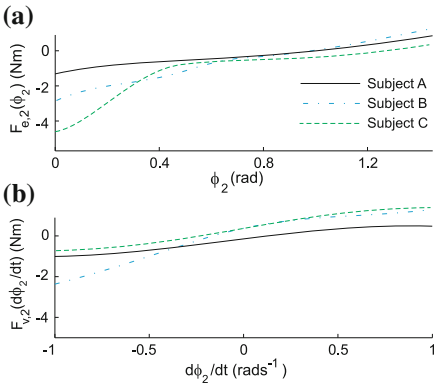

Fig. 2.5 Identified forms **a** $F_{e2}(\phi_2)$ and **b** $F_{v2}(\dot{\phi}_2)$

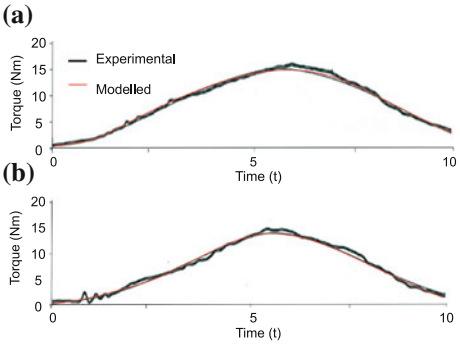

Fig. 2.6 Fitting results for: **a** torque component $\tau_{2,1}$ and modelled $h_1(u_1, t)$ corresponding to isometric anterior deltoid muscle, and **b** torque component $\tau_{5,2}$ and modelled $h_2(u_2, t)$ corresponding to isometric triceps muscle

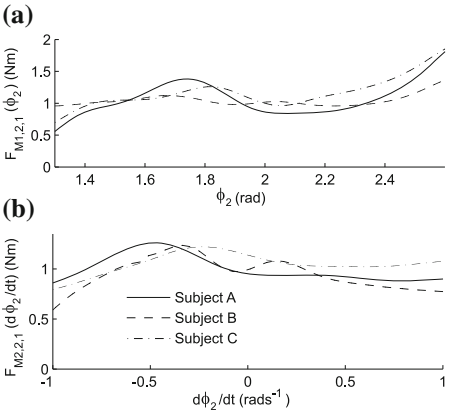

Fig. 2.7 Fitting results for: **a** $F_{M1,2,2}(\phi_2)$ and **b** $F_{M2,2,2}(\dot{\phi}_2)$

$$h_{IRC,1}(u_1) = a_{1,i}\frac{\exp(a_{2,i}u_1) - 1}{\exp(a_{2,i}u_1) + a_{3,i}}, \quad \text{and } h_{LAD,1}(t) = \mathscr{L}^{-1}\left\{\frac{w_{n,i}^2}{s^2 + 2w_{n,i}s + w_{n,i}^2}\right\}$$

have been taken for $i = 1, 2$.

Finally, multiplicative muscle functions of the form (2.20) have been identified through application of the procedure of Sect. 2.2.4. Results are given in Fig. 2.7. Note that since axes are aligned with muscle moments, all components of $F_M(\cdot)$ are zero apart from $F_{M,2,1}(\cdot)$ and $F_{M,5,2}(\cdot)$. Further results and fitting accuracy data can be found in [18, 21] for the case of both unimpaired and stroke participants.

2.3 Conclusions

This chapter has introduced general structures that model the dynamic response of the mechanically supported, electrically stimulated, upper limb. Identification procedures have been proposed and representative experimental results presented for the case of a passive exoskeletal support. In the next two chapters the general model form of (2.6) is used to design controllers which enable a reference tracking task to be completed. Chapter 5 then employs these model and controller structures within a clinical intervention to assist stroke patients' completion of upper limb reaching tasks.

References

1. J. Mehrholz, A. Hadrich, T. Platz, M. Pohl, Electromechanical and robot-assisted arm training for improving generic activities of daily living, arm function, and arm muscle strength after stroke. Cochrane Database Syst. Rev. **6**, CD006876 (2012)
2. P.S. Lum, C.G. Burgar, P.C. Shor, Evidence for improved muscle activation patterns after retraining of reaching movements with the mime robotic system in subjects with post-stroke hemiparesis. IEEE Trans. Neural Syst. Rehabil. Eng. **12**(2), 186–194 (2004)
3. J.R. de Kroon, J.H. van der Lee, M.J. Ijzerman, G.J. Lankhorst, Therapeutic electrical stimulation to improve motor control and functional abilities of the upper extremity after stroke: a systematic review. Clin. Rehabil. **16**, 350–360 (2002)
4. J.H. Burridge, M. Ladouceur, Clinical and therapeutic applications of neuromuscular stimulation: a review of current use and speculation into future developments. Neuromodulation **4**(4), 147–154 (2001)
5. E.K. Chadwick, D. Blana, A.J. van den Bogert, R.F. Kirsch, A real-time, 3-d musculoskeletal model for dynamic simulation of arm movements. IEEE Trans. Biomed. Eng. **56**(4), 941–948 (2009)
6. D. Blana, J.G. Hincapie, E.K. Chadwick, R.F. Kirsch, A musculoskeletal model of the upper extremity for use in the development of neuroprosthetic systems. J. Biomech. **41**, 1714–1721 (2008)
7. D. Zhang, T.H. Guan, F. Widjaja, W.T. Ang, Functional electrical stimulation in rehabilitation engineering: a survey, in *Proceedings of the 1st International Convention on Rehabilitation Engineering and Assistive Technology*. ACM (2007), pp. 221–226
8. F.J. Valero-Cuevas, A mathematical approach to the mechanical capabilities of limbs and fingers. Prog. Mot. Control **629**, 619–633 (2009)
9. B. Doran, A.K. Thompson, R.B. Stein, Short-term effects of functional electrical stimulation on spinal excitatory and inhibitory reflexes in ankle extensor and flexor muscles. Exp. Brain Res. **170**(2), 216–226 (2006)

10. D. Zhang, W.T. Ang, Musculoskeletal models of tremor (chapter 5), *Mechanisms and Emerging Therapies in Tremor Disorders* (Springer Science & Business Media, Berlin, 2012), pp. 79–107
11. J. Bobet, E. Gossen, R. Stein, A comparison of models of force production during stimulated isometric ankle dorsiflexion in humans. IEEE Trans. Neural Syst. Rehabil. Eng. **13**(4), 444–451 (2005)
12. J. Bobet, R. Stein, A simple model of force generation by skeletal muscle during dynamic isometric contractions. IEEE Trans. Biomed. Eng. **45**(8), 1010–1016 (1998)
13. J. Ding, A.S. Wexler, S.A. Binder-Macleod, A mathematical model that predicts the force frequency relationship of human skeletal muscle. Muscle Nerve **26**(4), 477–485 (2002)
14. L.A. Law, R.K. Shields, Mathematical models of human paralyzed muscle after long-term training. J. Biomech. **40**(12), 2587–2595 (2007)
15. E.-W. Bai, Z. Cai, S. Dudley-Javoroskv, R.K. Shields, Identification of a modified Wiener-Hammerstein system and its application in electrically stimulated paralyzed skeletal muscle modeling. Automatica **45**, 736–743 (2009)
16. C.T. Freeman, Upper limb electrical stimulation using input-output linearization and iterative learning control. IEEE Trans. Control Syst. Technol. **23**(4), 1546–1554 (2015)
17. J. Yu, D.C. Ackland, M.G. Pandy, Shoulder muscle function depends on elbow joint position: an illustration of dynamic coupling in the upper limb. J. Biomech. **44**(10), 1859–1868 (2011)
18. C.T. Freeman, A.M. Hughes, J.H. Burridge, P.H. Chappell, P.L. Lewin, E. Rogers, A model of the upper extremity using FES for stroke rehabilitation. ASME J. Biomech. Eng. **131**(3), 031006–1–031006–10 (2009)
19. F. Le, I. Markovsky, C.T. Freeman, E. Rogers, Identification of electrically stimulated muscle models of stroke patients. Control Eng. Pract. **18**(4), 396–407 (2010)
20. W.K. Durfee, K.I. Palmer, Estimation of force-activation, force-length and force-velocity properties in isolated, electrically stimulated muscle. IEEE Trans. Biomed. Eng. **41**(3), 205–216 (1994)
21. D. Tong, Upper limb rehabilitation system using FES mediated by ILC. Ph.D. thesis, University of Southampton (2013)

Chapter 3
Feedback Control Design

Many control techniques have been applied to assist upper limb movement using electrical stimulation. However in clinical trials with neurologically impaired participants the applied control schemes remain mostly open-loop, triggered [1], or based on electromyographic (EMG) [2, 3] or electroencephalographic (EEG) feedback [4, 5] to provide a measure of the users' voluntary intention. Used mainly with spinal cord injured participants, another approach involves employing artificial neural networks (ANNs) to create a mapping between muscle activity and kinematic variables [6–10]. However limitations include a lack of robust performance analysis, transparent parameter tuning, and the need to re-train for use with different movements or physiological changes.

Feedback approaches which employ a model of the relationship between applied stimulation and resulting movement are crucial to address the complex, time-varying dynamics. However, such approaches have transferred to clinical practice with neurological participants in only a small number of cases and fewer still benefit from a model. This is due to difficulties in obtaining an accurate model since the identification time available is restricted by the onset of fatigue and the time constraints of the impaired participant, carer, physiotherapist and/or engineer. Time-varying physiological effects also mean that models should ideally be re-identified at the start of, and even during, each treatment session. A further feature of the rehabilitation problem is that ES is applied only to a subset of weak or paralyzed muscles, and hence the controller must ensure stability of the joints that are not supported by ES. It is also beneficial that control parameters may be tuned in a transparent manner so that performance can be maintained despite changes in underlying dynamics.

This chapter addresses the design of feedback controllers to stabilize all joints in the upper limb system. Moreover, robust stability margins are derived to ensure that changes in the dynamics do not destabilize the system. To maximize practical utility, these are employed to derive bounds on the most significant sources of model

C. Freeman, *Control System Design for Electrical Stimulation in Upper Limb Rehabilitation*, DOI 10.1007/978-3-319-25706-8_3

inaccuracy, with explicit focus on muscle fatigue. In the next chapter a feedforward control action will be combined with the feedback controllers developed here in order to further improve tracking accuracy and hence ensure successful task completion.

3.1 General Feedback Control Framework

The combined mechanical and anthropomorphic system was shown to take the form

$$M : \begin{cases} \dot{\boldsymbol{x}}_s(t) = \boldsymbol{f}_s(\boldsymbol{x}_s(t)) + \boldsymbol{g}_s(\boldsymbol{u}(t)) \\ \boldsymbol{\Phi}(t) = \boldsymbol{h}_s(\boldsymbol{x}_s(t)), \end{cases} \qquad t \geq 0 \tag{3.1}$$

with components given by (2.7). Since $\boldsymbol{f}_s(\cdot), \boldsymbol{g}_s(\cdot), \boldsymbol{h}_s(\cdot)$ are continuously differentiable, M has the properties of uniqueness and continuity [11]. In this chapter we consider a general feedback control structure given by

$$K : \begin{cases} \dot{\boldsymbol{x}}_c(t) = \boldsymbol{f}_c(\boldsymbol{x}_c(t), \boldsymbol{e}(t)) \\ \boldsymbol{u}(t) = \boldsymbol{h}_c(\boldsymbol{x}_c(t), \boldsymbol{e}(t)), \end{cases} \qquad t \geq 0 \tag{3.2}$$

where functions $\boldsymbol{f}_c(\cdot), \boldsymbol{h}_c(\cdot)$ are continuously differentiable, so that K also has the properties of uniqueness and continuity. Figure 3.1 shows the combined structure, where the reference vector is denoted $\hat{\boldsymbol{\Phi}} \in \mathscr{L}_2^p$ and the tracking error is $\boldsymbol{e} = \hat{\boldsymbol{\Phi}} - \boldsymbol{\Phi}$. This must be designed to embed robustness to model uncertainty and disturbance, together with baseline tracking performance of the resulting closed-loop system

$$\underbrace{\begin{bmatrix} \dot{\boldsymbol{x}}_s(t) \\ \dot{\boldsymbol{x}}_c(t) \end{bmatrix}}_{\dot{\boldsymbol{x}}(t)} = \underbrace{\begin{bmatrix} \boldsymbol{f}_s(\boldsymbol{x}_s(t)) + \boldsymbol{g}_s(\boldsymbol{h}_c(\boldsymbol{x}_c(t), \hat{\boldsymbol{\Phi}}(t) - \boldsymbol{h}_s(\boldsymbol{x}_s(t)))) \\ \boldsymbol{f}_c(\boldsymbol{x}_c(t), \hat{\boldsymbol{\Phi}}(t) - \boldsymbol{h}_s(\boldsymbol{x}_s(t))) \end{bmatrix}}_{\boldsymbol{f}(\boldsymbol{x}(t), \hat{\boldsymbol{\Phi}}(t))}$$

$$\boldsymbol{\Phi}(t) = \underbrace{\boldsymbol{h}_s(\boldsymbol{x}_s(t))}_{\boldsymbol{h}(\boldsymbol{x}(t))}, \qquad t \geq 0. \tag{3.3}$$

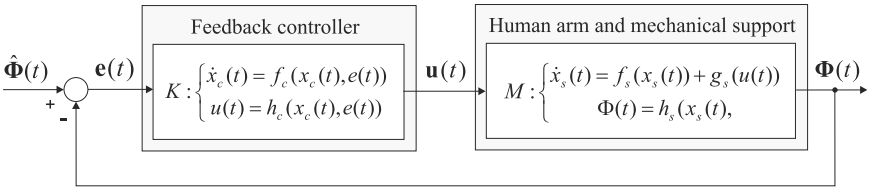

Fig. 3.1 Feedback control scheme with $K : \boldsymbol{e} \mapsto \boldsymbol{u} : \mathscr{L}_2^p \to \mathscr{L}_2^m$

The functional movements used in rehabilitation may not involve all joint axes. Equally movement about certain joints may need to be actively avoided, due to the presence of subluxations, stiffness, or limited angular range of movement for example. To embed this flexibility in controlled joint selection, we define the set $\mathscr{P}$ containing the controlled joint indices, with elements $\mathscr{P} = \{p_1, \ldots, p_{n_p}\}$, $n_p \leq p$. We denote the complement of $\mathscr{P}$ by $\bar{\mathscr{P}} = \{1, \ldots p\} \setminus \mathscr{P}$. For signal $\boldsymbol{x}$ and set of distinct indices $\mathscr{S}$ we use notation $\boldsymbol{x}_{\mathscr{S}}(t) = [\boldsymbol{x}_{\mathscr{S}(1)}(t), \ldots \boldsymbol{x}_{\mathscr{S}_{|\mathscr{S}|}}(t)]^\top$ where $\mathscr{S}(i)$ is the ith smallest element of $\mathscr{S}$. With this notation, the controlled and uncontrolled joint angle signals are $\boldsymbol{\Phi}_{\mathscr{P}} \in \mathscr{L}_2^{n_p}$ and $\boldsymbol{\Phi}_{\bar{\mathscr{P}}} \in \mathscr{L}_2^{p-n_p}$ respectively. Armed with this notation, we can now introduce a definition of stability for use in control design:

Definition 3.1 Feedback controller (3.2) is said to stabilize the closed-loop system $[M, K]$ about operating-point $\bar{\boldsymbol{\Phi}} \in \mathscr{L}_2^{n_p}$ if it achieves global asymptotic stability of the controlled joints, $\boldsymbol{\Phi}_{\mathscr{P}}$, about $\bar{\boldsymbol{\Phi}}$.

Satisfying the condition of Definition 3.1 stabilizes joints with indices in set $\mathscr{P}$, but musculo-tendon interaction and dynamic rigid body coupling cause movement in the remaining joints. We therefore next derive conditions to ensure stability of the uncontrolled joints, ϕ_i, $i \in \bar{\mathscr{P}}$.

3.1.1 Stability of Unactuated Joints

To examine stability of uncontrolled joints, ϕ_i, $i \in \bar{\mathscr{P}}$, first express components of $\boldsymbol{C}(\boldsymbol{\Phi}, \dot{\boldsymbol{\Phi}})$ in standard form as

$$c_{i,j} = \sum_{k=1}^{p} c_{i,j,k}\dot{\phi}_k, \quad c_{i,j,k} = \frac{1}{2}\left(\frac{\partial b_{i,j}}{\partial \phi_k} + \frac{\partial b_{i,k}}{\partial \phi_j} - \frac{\partial b_{j,k}}{\partial \phi_i}\right), \quad i,j = 1, \ldots, p \tag{3.4}$$

where $b_{i,j}$ are components of $\boldsymbol{B}(\boldsymbol{\Phi})$. Then using $\boldsymbol{\eta}_1 = \boldsymbol{\Phi}_{\bar{\mathscr{P}}}$, $\boldsymbol{\eta} = [\boldsymbol{\eta}_1^\top,\ \boldsymbol{\eta}_2^\top]^\top$, $\boldsymbol{\xi} = [\boldsymbol{\xi}_1^\top,\ \boldsymbol{\xi}_2^\top,\ \boldsymbol{\xi}_3^\top]^\top$, the system (2.7) and controller (3.2) can be represented as

$$\dot{\boldsymbol{x}} = \boldsymbol{f}(\boldsymbol{x}), \tag{3.5}$$

$$\dot{\boldsymbol{\eta}} = \boldsymbol{\omega}(\boldsymbol{\xi}, \boldsymbol{\eta}, t), \tag{3.6}$$

$$\boldsymbol{\xi}(\boldsymbol{x}) = \begin{bmatrix} \bar{\boldsymbol{\Phi}} - \boldsymbol{\Phi}_{\mathscr{P}} \\ \bar{\boldsymbol{\Phi}}^{(1)} - \boldsymbol{\Phi}_{\mathscr{P}}^{(1)} \\ \bar{\boldsymbol{\Phi}}^{(2)} - \boldsymbol{\Phi}_{\mathscr{P}}^{(2)} \end{bmatrix} = \begin{bmatrix} \bar{\boldsymbol{\Phi}} - \boldsymbol{h}_{\mathscr{P}}(\boldsymbol{x}(t)) \\ \bar{\boldsymbol{\Phi}}^{(1)} - \boldsymbol{h}_{\mathscr{P}}(\boldsymbol{f}(\boldsymbol{x}(t))) \\ \bar{\boldsymbol{\Phi}}^{(2)} - \boldsymbol{h}_{\mathscr{P}}(\boldsymbol{f}'(\boldsymbol{x}(t))\boldsymbol{f}(\boldsymbol{x}(t))) \end{bmatrix}, \tag{3.7}$$

where $\boldsymbol{\Phi} = [\boldsymbol{\eta}_1^\top, \bar{\boldsymbol{\Phi}}^\top - \boldsymbol{\xi}_1^\top]^\top$, $\dot{\boldsymbol{\Phi}} = [\boldsymbol{\eta}_2^\top, (\bar{\boldsymbol{\Phi}}^{(1)})^\top - \boldsymbol{\xi}_2^\top]^\top$, and the uncontrolled joint dynamics are

$$\boldsymbol{\omega}(\boldsymbol{\xi}, \boldsymbol{\eta}, t) = \begin{pmatrix} \boldsymbol{\eta}_2 \\ \boldsymbol{B}_{\bar{\mathscr{P}}}^{-1}(\boldsymbol{\Phi})\Big(\boldsymbol{\tau}_{\bar{\mathscr{P}}}\big(K(\hat{\boldsymbol{\Phi}}_{\mathscr{P}} - \bar{\boldsymbol{\Phi}} + \boldsymbol{\xi}_1), \bar{\boldsymbol{\Phi}} - \boldsymbol{\xi}_1, \bar{\boldsymbol{\Phi}}^{(1)} - \boldsymbol{\xi}_2\big) - \boldsymbol{C}_{\bar{\mathscr{P}}}(\boldsymbol{\Phi}, \dot{\boldsymbol{\Phi}})\boldsymbol{\eta}_2 - \boldsymbol{G}_{\bar{\mathscr{P}}}(\boldsymbol{\Phi}) \\ -\boldsymbol{C}_{\bar{\mathscr{P}}\mathscr{P}}(\boldsymbol{\Phi}, \dot{\boldsymbol{\Phi}})\big(\bar{\boldsymbol{\Phi}}^{(1)} - \boldsymbol{\xi}_2\big) - \boldsymbol{F}_{\bar{\mathscr{P}}}(\boldsymbol{\Phi}, \dot{\boldsymbol{\Phi}}) - \boldsymbol{K}_{\bar{\mathscr{P}}}(\boldsymbol{\Phi}) - \boldsymbol{B}_{\bar{\mathscr{P}}\mathscr{P}}(\boldsymbol{\Phi})\big(\bar{\boldsymbol{\Phi}}^{(2)} - \boldsymbol{\xi}_3\big)\Big) \end{pmatrix}.$$

Terms $\boldsymbol{C}_{\bar{\mathscr{P}}}(\boldsymbol{\Phi}, \dot{\boldsymbol{\Phi}})$ and $\boldsymbol{C}_{\bar{\mathscr{P}}\mathscr{P}}(\boldsymbol{\Phi}, \dot{\boldsymbol{\Phi}})$ respectively have elements

$$C_{\bar{\mathscr{P}},i,j} = \sum_{k=1}^{n} c_{\bar{\mathscr{P}}(i),\bar{\mathscr{P}}(j),k}\dot{\phi}_k, \quad C_{\bar{\mathscr{P}}\mathscr{P},i,j} = \sum_{k=1}^{n} c_{\bar{\mathscr{P}}(i),\mathscr{P}(j),k}\dot{\phi}_k$$

and likewise $\boldsymbol{B}_{\bar{\mathscr{P}}}(\boldsymbol{\Phi})$ and $\boldsymbol{B}_{\bar{\mathscr{P}}\mathscr{P}}(\boldsymbol{\Phi})$ have elements

$$B_{\bar{\mathscr{P}},i,j} = b_{\bar{\mathscr{P}}(i),\bar{\mathscr{P}}(j)}, \quad B_{\bar{\mathscr{P}}\mathscr{P},i,j} = b_{\bar{\mathscr{P}}(i),\mathscr{P}(j)}. \tag{3.8}$$

Assuming the passive parameter form (2.12), $\boldsymbol{F}_{\bar{\mathscr{P}}}(\boldsymbol{\Phi}, \dot{\boldsymbol{\Phi}})$ has elements

$$\begin{aligned} F_{\bar{\mathscr{P}},i}(\boldsymbol{\Phi}, \dot{\boldsymbol{\Phi}}) &= F_{e,\bar{\mathscr{P}}(i)}(\phi_{\bar{\mathscr{P}}(i)}) + F_{v,\bar{\mathscr{P}}(i)}(\dot{\phi}_{\bar{\mathscr{P}}(i)}) \\ &:= F_{e,i}(\boldsymbol{\Phi}_{\bar{\mathscr{P}}}) + F_{v,i}(\dot{\boldsymbol{\Phi}}_{\bar{\mathscr{P}}}), \qquad i = 1, \cdots p - n_p \end{aligned}$$

From (3.5)–(3.7) the surface $\boldsymbol{\xi} = \mathbf{0}$ defines an integral manifold for the system

$$\dot{\boldsymbol{\eta}} = \boldsymbol{\omega}(\mathbf{0}, \boldsymbol{\eta}, t). \tag{3.9}$$

Since the controlled joints are assumed to be stable about this surface via Definition 3.1, system (3.9) is globally attractive and defines the zero dynamics relative to the controlled output $\boldsymbol{\Phi}_{\mathscr{P}} = \bar{\boldsymbol{\Phi}}$. We next state the Center Manifold Theorem, see [12].

Theorem 3.1 *Suppose that $\boldsymbol{\omega}(\mathbf{0}, \boldsymbol{\eta}_1^*, t) = \mathbf{0}$ for $t \geq 0$, i.e. $(\mathbf{0}, \boldsymbol{\eta}_1^*)$ is an equilibrium of the full system (3.5)–(3.7), and $\boldsymbol{\eta}_1^*$ is an equilibrium of the zero dynamics (3.9), and that Definition 3.1 is satisfied. Then $(\mathbf{0}, \boldsymbol{\eta}_1^*)$ of the full system (3.5)–(3.7) is locally stable if $\boldsymbol{\eta}_1^*$ is locally stable for dynamics (3.9).*

Stability of all joints, $\boldsymbol{\Phi}$, is hence assured if both the controlled and uncontrolled joints are independently stable. The former is guaranteed via Definition 3.1, and the following theorem gives conditions for the latter.

Theorem 3.2 *Let feedback controller K satisfy Definition 3.1 and uncontrolled joints, $\boldsymbol{\Phi}_{\bar{\mathscr{P}}}$, be passive with respect to $(\boldsymbol{\tau}^*_{\bar{\mathscr{P}}}(\boldsymbol{\Phi}^*_{\bar{\mathscr{P}}}), \boldsymbol{\Phi}^*_{\bar{\mathscr{P}}})$, i.e.*

$$(\boldsymbol{\Phi}_{\bar{\mathscr{P}}} - \boldsymbol{\Phi}^*_{\bar{\mathscr{P}}})^\top \left(\boldsymbol{F}_e(\boldsymbol{\Phi}_{\bar{\mathscr{P}}}) + \boldsymbol{G}_{\bar{\mathscr{P}}}(\boldsymbol{\Phi}_{\bar{\mathscr{P}}}) + \boldsymbol{K}_{\bar{\mathscr{P}}}(\boldsymbol{\Phi}_{\bar{\mathscr{P}}}) - \boldsymbol{\tau}^*_{\bar{\mathscr{P}}}(\boldsymbol{\Phi}_{\bar{\mathscr{P}}})\right) \geq 0 \quad (3.10)$$

where $\boldsymbol{\Phi}^*_{\bar{\mathscr{P}}}$ satisfies $\boldsymbol{F}_e(\boldsymbol{\Phi}^*_{\bar{\mathscr{P}}}) + \boldsymbol{G}_{\bar{\mathscr{P}}}(\boldsymbol{\Phi}^*_{\bar{\mathscr{P}}}) + \boldsymbol{K}_{\bar{\mathscr{P}}}(\boldsymbol{\Phi}^*_{\bar{\mathscr{P}}}) = \boldsymbol{\tau}^*_{\bar{\mathscr{P}}}(\boldsymbol{\Phi}^*_{\bar{\mathscr{P}}})$, with $\boldsymbol{\tau}^*_{\bar{\mathscr{P}}}(\boldsymbol{\Phi}^*_{\bar{\mathscr{P}}}) = \boldsymbol{\tau}_{\bar{\mathscr{P}}}\left(K(\hat{\boldsymbol{\Phi}}_{\mathscr{P}} - \bar{\boldsymbol{\Phi}}), \bar{\boldsymbol{\Phi}}, \dot{\bar{\boldsymbol{\Phi}}}\right) - \bar{\boldsymbol{C}}_{\bar{\mathscr{P}}\mathscr{P}}(\boldsymbol{\Phi}^*_{\bar{\mathscr{P}}})\dot{\bar{\boldsymbol{\Phi}}} - \boldsymbol{B}_{\bar{\mathscr{P}}\mathscr{P}}(\boldsymbol{\Phi}^*_{\bar{\mathscr{P}}})\ddot{\bar{\boldsymbol{\Phi}}}$ the moment transferred from controlled to uncontrolled joints, and let the uncontrolled joint damping function satisfy the sector bounds

$$F_{v,i}(\dot{\phi}) \begin{cases} > \bar{F}_{v,i}\dot{\phi}_i & \text{if } \dot{\phi} > 0, \\ < \bar{F}_{v,i}\dot{\phi}_i & \text{otherwise.} \end{cases} \quad i \in \bar{\mathscr{P}} \quad \text{where} \quad \bar{F}_{v,i} = \sum_{i,k \notin \mathscr{P},\, i \neq k} \left| \sum_{j \in \mathscr{P}} c_{i,j,k}\dot{\bar{\phi}}_j \right| \quad (3.11)$$

Then the uncontrolled joints are locally stable about $(\boldsymbol{\tau}^*_{\bar{\mathscr{P}}}(\boldsymbol{\Phi}^*_{\bar{\mathscr{P}}}), \boldsymbol{\Phi}^*_{\bar{\mathscr{P}}})$.

Proof From (2.7) the uncontrolled system dynamics are given by

$$\begin{aligned} &\boldsymbol{B}_{\bar{\mathscr{P}}}(\boldsymbol{\Phi})\ddot{\boldsymbol{\Phi}}_{\bar{\mathscr{P}}} + \boldsymbol{C}_{\bar{\mathscr{P}}}(\boldsymbol{\Phi}, \dot{\boldsymbol{\Phi}})\dot{\boldsymbol{\Phi}}_{\bar{\mathscr{P}}} + \boldsymbol{C}_{\bar{\mathscr{P}}\mathscr{P}}(\boldsymbol{\Phi}, \dot{\boldsymbol{\Phi}})\dot{\boldsymbol{\Phi}}_{\mathscr{P}} + \boldsymbol{F}_{\bar{\mathscr{P}}}(\boldsymbol{\Phi}, \dot{\boldsymbol{\Phi}}) + \boldsymbol{G}_{\bar{\mathscr{P}}}(\boldsymbol{\Phi}) + \boldsymbol{K}_{\bar{\mathscr{P}}}(\boldsymbol{\Phi}) \\ &\quad + \boldsymbol{B}_{\bar{\mathscr{P}}\mathscr{P}}(\boldsymbol{\Phi})\ddot{\boldsymbol{\Phi}}_{\mathscr{P}} = \boldsymbol{\tau}_{\bar{\mathscr{P}}}\left(K(\boldsymbol{\xi}_1 + \hat{\boldsymbol{\Phi}}_{\mathscr{P}} - \bar{\boldsymbol{\Phi}}), \bar{\boldsymbol{\Phi}} - \boldsymbol{\xi}_1, \bar{\boldsymbol{\Phi}}^{(1)} - \boldsymbol{\xi}_2\right). \end{aligned} \quad (3.12)$$

The term $\boldsymbol{C}_{\bar{\mathscr{P}}\mathscr{P}}(\boldsymbol{\Phi}, \dot{\boldsymbol{\Phi}})$ can be partitioned as $\overline{\boldsymbol{C}}_{\bar{\mathscr{P}}\mathscr{P}}(\boldsymbol{\Phi}, \dot{\boldsymbol{\Phi}}_{\mathscr{P}}) + \underline{\boldsymbol{C}}_{\bar{\mathscr{P}}\mathscr{P}}(\boldsymbol{\Phi}, \dot{\boldsymbol{\Phi}}_{\bar{\mathscr{P}}})$, where

$$\overline{C}_{\bar{\mathscr{P}}\mathscr{P},i,j} = \sum_{k=1}^{n_p} c_{\bar{\mathscr{P}}(i),\mathscr{P}(j),\mathscr{P}(k)}\dot{\phi}_{\mathscr{P}(k)} \quad \text{and} \quad \underline{C}_{\bar{\mathscr{P}}\mathscr{P},i,j} = \sum_{k=1}^{p-n_p} c_{\bar{\mathscr{P}}(i),\mathscr{P}(j),\bar{\mathscr{P}}(k)}\dot{\phi}_{\bar{\mathscr{P}}(k)}.$$

Furthermore $\underline{\boldsymbol{C}}_{\bar{\mathscr{P}}\mathscr{P}}(\boldsymbol{\Phi}, \dot{\boldsymbol{\Phi}}_{\bar{\mathscr{P}}})\dot{\boldsymbol{\Phi}}_{\mathscr{P}}$ can be written as $\underline{\boldsymbol{C}}_{\bar{\mathscr{P}}}(\boldsymbol{\Phi}, \dot{\boldsymbol{\Phi}}_{\mathscr{P}})\dot{\boldsymbol{\Phi}}_{\bar{\mathscr{P}}}$ with

$$\underline{C}_{\bar{\mathscr{P}},i,j} = \sum_{k=1}^{n_p} c_{\bar{\mathscr{P}}(i),\mathscr{P}(k),\bar{\mathscr{P}}(j)}\dot{\phi}_{\mathscr{P}(k)}.$$

This enables (3.12) to be rewritten using substitutions $\boldsymbol{C}_{\bar{\mathscr{P}}\mathscr{P}} \Leftrightarrow \overline{\boldsymbol{C}}_{\bar{\mathscr{P}}\mathscr{P}}$ and $\boldsymbol{C}_{\bar{\mathscr{P}}} \Leftrightarrow \overline{\boldsymbol{C}}_{\bar{\mathscr{P}}}$, where $\overline{\boldsymbol{C}}_{\bar{\mathscr{P}}} = \boldsymbol{C}_{\bar{\mathscr{P}}} + \underline{\boldsymbol{C}}_{\bar{\mathscr{P}}}$, to give

$$\begin{aligned} &\boldsymbol{B}_{\bar{\mathscr{P}}}(\boldsymbol{\Phi})\ddot{\boldsymbol{\Phi}}_{\bar{\mathscr{P}}} + \overline{\boldsymbol{C}}_{\bar{\mathscr{P}}}(\boldsymbol{\Phi}, \dot{\boldsymbol{\Phi}})\dot{\boldsymbol{\Phi}}_{\bar{\mathscr{P}}} + \overline{\boldsymbol{C}}_{\bar{\mathscr{P}}\mathscr{P}}(\boldsymbol{\Phi}, \dot{\boldsymbol{\Phi}}_{\mathscr{P}})\dot{\boldsymbol{\Phi}}_{\mathscr{P}} + \boldsymbol{F}_{\bar{\mathscr{P}}}(\boldsymbol{\Phi}, \dot{\boldsymbol{\Phi}}) + \boldsymbol{G}_{\bar{\mathscr{P}}}(\boldsymbol{\Phi}) \\ &\quad + \boldsymbol{K}_{\bar{\mathscr{P}}}(\boldsymbol{\Phi}) + \boldsymbol{B}_{\bar{\mathscr{P}}\mathscr{P}}(\boldsymbol{\Phi})\ddot{\boldsymbol{\Phi}}_{\mathscr{P}} = \boldsymbol{\tau}_{\bar{\mathscr{P}}}\left(K(\boldsymbol{\xi}_1 + \hat{\boldsymbol{\Phi}}_{\mathscr{P}} - \bar{\boldsymbol{\Phi}}), \bar{\boldsymbol{\Phi}} - \boldsymbol{\xi}_1, \bar{\boldsymbol{\Phi}}^{(1)} - \boldsymbol{\xi}_2\right). \end{aligned} \quad (3.13)$$

When $\boldsymbol{\xi} = \mathbf{0}$ the zero dynamics correspond to the system

$$\begin{aligned}\boldsymbol{B}_{\bar{\mathscr{P}}}(\boldsymbol{\eta}_1)\dot{\boldsymbol{\eta}}_2 + \overline{\boldsymbol{C}}_{\bar{\mathscr{P}}}(\boldsymbol{\eta}_1, \boldsymbol{\eta}_2)\boldsymbol{\eta}_2 + \overline{\boldsymbol{C}}_{\bar{\mathscr{P}}\mathscr{P}}(\boldsymbol{\eta}_1)\bar{\boldsymbol{\Phi}}^{(1)} + \boldsymbol{F}_{\bar{\mathscr{P}}}(\boldsymbol{\eta}_1, \boldsymbol{\eta}_2) + \boldsymbol{G}_{\bar{\mathscr{P}}}(\boldsymbol{\eta}_1) + \boldsymbol{K}_{\bar{\mathscr{P}}}(\boldsymbol{\eta}_1) \\ + \boldsymbol{B}_{\bar{\mathscr{P}}\mathscr{P}}(\boldsymbol{\eta}_1)\bar{\boldsymbol{\Phi}}^{(2)} = \boldsymbol{\tau}_{\bar{\mathscr{P}}}\big(K(\hat{\boldsymbol{\Phi}}_{\mathscr{P}} - \bar{\boldsymbol{\Phi}}), \bar{\boldsymbol{\Phi}}, \bar{\boldsymbol{\Phi}}^{(1)}\big)\end{aligned} \tag{3.14}$$

where the muscle dynamic forms (2.2)–(2.4) mean $\boldsymbol{\tau}_{\bar{\mathscr{P}}}(\cdot)$ is bounded input, bounded output stable, and functional dependence on $\bar{\boldsymbol{\Phi}}, \bar{\boldsymbol{\Phi}}^{(1)}$ has been omitted. System (3.14) equates to $\dot{\boldsymbol{\eta}}_2 = -\boldsymbol{h}(\boldsymbol{\eta}_1, \boldsymbol{\eta}_2) - \boldsymbol{g}(\boldsymbol{\eta}_1)$ where

$$\begin{aligned}\boldsymbol{h}(\boldsymbol{\eta}_1, \boldsymbol{\eta}_2) &= \boldsymbol{B}_{\bar{\mathscr{P}}}(\boldsymbol{\eta}_1)^{-1}\Big(\overline{\boldsymbol{C}}_{\bar{\mathscr{P}}}(\boldsymbol{\eta}_1, \boldsymbol{\eta}_2)\boldsymbol{\eta}_2 + \boldsymbol{F}_e(\boldsymbol{\eta}_1) + \boldsymbol{F}_v(\boldsymbol{\eta}_2) + \boldsymbol{G}_{\bar{\mathscr{P}}}(\boldsymbol{\eta}_1) + \boldsymbol{K}_{\bar{\mathscr{P}}}(\boldsymbol{\eta}_1)\Big), \\ \boldsymbol{g}(\boldsymbol{\eta}_1) &= \boldsymbol{B}_{\bar{\mathscr{P}}}(\boldsymbol{\eta}_1)^{-1}\Big(\overline{\boldsymbol{C}}_{\bar{\mathscr{P}}\mathscr{P}}(\boldsymbol{\eta}_1)\bar{\boldsymbol{\Phi}}^{(1)} + \boldsymbol{B}_{\bar{\mathscr{P}}\mathscr{P}}(\boldsymbol{\eta}_1)\bar{\boldsymbol{\Phi}}^{(2)} - \boldsymbol{\tau}_{\bar{\mathscr{P}}}\big(K(\hat{\boldsymbol{\Phi}}_{\mathscr{P}} - \bar{\boldsymbol{\Phi}}), \bar{\boldsymbol{\Phi}}, \bar{\boldsymbol{\Phi}}^{(1)}\big)\Big).\end{aligned}$$

The equilibrium point of the uncontrolled joints satisfies $\boldsymbol{h}(\boldsymbol{\eta}_1^*, \mathbf{0}) + \boldsymbol{g}(\boldsymbol{\eta}_1^*) = \mathbf{0}$, and, following [13], the system can be interpreted as conservative system $\dot{\boldsymbol{\eta}}_2 + \boldsymbol{g}(\tilde{\boldsymbol{\eta}}_1 + \boldsymbol{\eta}_1^*) = \mathbf{0}$ acted on by external force $-\boldsymbol{h}(\tilde{\boldsymbol{\eta}}_1 + \boldsymbol{\eta}_1^*, \boldsymbol{\eta}_2)$ where $\tilde{\boldsymbol{\eta}}_1 = \boldsymbol{\eta}_1 - \boldsymbol{\eta}_1^*$. Accordingly, introduce energy function

$$\begin{aligned}V(\tilde{\boldsymbol{\eta}}_1, \boldsymbol{\eta}_2) = \boldsymbol{\eta}_2^\top \frac{\boldsymbol{B}_{\bar{\mathscr{P}}}(\tilde{\boldsymbol{\eta}}_1 + \boldsymbol{\eta}_1^*)}{2}\boldsymbol{\eta}_2 + \int_0^{\tilde{\boldsymbol{\eta}}_1}\big(\boldsymbol{F}_e(\boldsymbol{\sigma}) + \boldsymbol{G}_{\bar{\mathscr{P}}}(\boldsymbol{\sigma}) + \boldsymbol{K}_{\bar{\mathscr{P}}}(\boldsymbol{\sigma})\big)\delta\boldsymbol{\sigma} \\ + \int_0^{\tilde{\boldsymbol{\eta}}_1}\Big(\bar{\boldsymbol{C}}_{\bar{\mathscr{P}}\mathscr{P}}(\boldsymbol{\sigma})\bar{\boldsymbol{\Phi}}^{(1)} + \boldsymbol{B}_{\bar{\mathscr{P}}\mathscr{P}}(\boldsymbol{\sigma})\bar{\boldsymbol{\Phi}}^{(2)} - \boldsymbol{\tau}_{\bar{\mathscr{P}}}\big(K(\hat{\boldsymbol{\Phi}}_{\mathscr{P}} - \bar{\boldsymbol{\Phi}}), \bar{\boldsymbol{\Phi}}, \bar{\boldsymbol{\Phi}}^{(1)}\big)\Big)\delta\boldsymbol{\sigma}.\end{aligned}$$

The first and second terms respectively correspond to the kinetic and potential energy in the uncontrolled joint system, and the third to the potential energy transferred from the controlled joints. The rate of energy satisfies

$$\begin{aligned}\dot{V}(\tilde{\boldsymbol{\eta}}_1, \boldsymbol{\eta}_2) &= \boldsymbol{\eta}_2^\top \boldsymbol{B}_{\bar{\mathscr{P}}}(\tilde{\boldsymbol{\eta}}_1 + \boldsymbol{\eta}_1^*)\dot{\boldsymbol{\eta}}_2 + \boldsymbol{\eta}_2^\top \frac{\dot{\boldsymbol{B}}_{\bar{\mathscr{P}}}(\tilde{\boldsymbol{\eta}}_1 + \boldsymbol{\eta}_1^*)}{2}\boldsymbol{\eta}_2 \\ &\quad + \boldsymbol{\eta}_2^\top\big(\boldsymbol{F}_e(\tilde{\boldsymbol{\eta}}_1 + \boldsymbol{\eta}_1^*) + \boldsymbol{G}_{\bar{\mathscr{P}}}(\tilde{\boldsymbol{\eta}}_1 + \boldsymbol{\eta}_1^*) + \boldsymbol{K}_{\bar{\mathscr{P}}}(\tilde{\boldsymbol{\eta}}_1 + \boldsymbol{\eta}_1^*)\big) \\ &\quad + \boldsymbol{\eta}_2^\top\Big(\bar{\boldsymbol{C}}_{\bar{\mathscr{P}}\mathscr{P}}(\tilde{\boldsymbol{\eta}}_1 + \boldsymbol{\eta}_1^*)\bar{\boldsymbol{\Phi}}^{(1)} + \boldsymbol{B}_{\bar{\mathscr{P}}\mathscr{P}}(\tilde{\boldsymbol{\eta}}_1 + \boldsymbol{\eta}_1^*)\bar{\boldsymbol{\Phi}}^{(2)} \\ &\qquad - \boldsymbol{\tau}_{\bar{\mathscr{P}}}\big(K(\bar{\boldsymbol{\Phi}}_{\mathscr{P}} - \bar{\boldsymbol{\Phi}}), \bar{\boldsymbol{\Phi}}, \bar{\boldsymbol{\Phi}}^{(1)}\big)\Big) \\ &= \boldsymbol{\eta}_2^\top\left(\frac{\dot{\boldsymbol{B}}_{\bar{\mathscr{P}}}(\boldsymbol{\eta}_1)}{2} - \overline{\boldsymbol{C}}_{\bar{\mathscr{P}}}(\boldsymbol{\eta}_1, \boldsymbol{\eta}_2)\right)\boldsymbol{\eta}_2 - \boldsymbol{\eta}_2^T\boldsymbol{F}_v(\boldsymbol{\eta}_2) \\ &\leq \boldsymbol{\eta}_2^\top\left(\frac{1}{2}\dot{\boldsymbol{B}}_{\bar{\mathscr{P}}}(\boldsymbol{\eta}_1) - \overline{\boldsymbol{C}}_{\bar{\mathscr{P}}}(\boldsymbol{\eta}_1, \boldsymbol{\eta}_2) - \bar{\boldsymbol{F}}_v\right)\boldsymbol{\eta}_2.\end{aligned}$$

Hence the system converges to $\boldsymbol{\eta}_1 = \boldsymbol{\eta}_1^*$, $\boldsymbol{\eta}_2 = \dot{\boldsymbol{\eta}}_1 = \mathbf{0}$ if

$$\min_i \Re\left(\lambda_i\left(\frac{\dot{\boldsymbol{B}}_{\bar{\mathscr{P}}}(\boldsymbol{\eta}_1)}{2} - \boldsymbol{C}_{\bar{\mathscr{P}}}(\boldsymbol{\eta}_1, \boldsymbol{\eta}_2) - \underline{\boldsymbol{C}}_{\bar{\mathscr{P}}}(\boldsymbol{\eta}_1, \boldsymbol{\eta}_2) - \bar{\boldsymbol{F}}_v\right)\right) < 0.$$

As $\frac{1}{2}\dot{\boldsymbol{B}}_{\bar{\mathscr{P}}}(\boldsymbol{\eta}_1) - \boldsymbol{C}_{\bar{\mathscr{P}}}(\boldsymbol{\eta}_1, \boldsymbol{\eta}_2)$ is skew-symmetric, a sufficient condition is that the term $\underline{\boldsymbol{C}}_{\bar{\mathscr{P}}}(\boldsymbol{\eta}_1, \boldsymbol{\eta}_2) + \bar{\boldsymbol{F}}_v$ is diagonally dominant with positive diagonal entries, which is satisfied by (3.11). □

The conditions of Theorem 3.2 motivate the following intuitive guidelines for ensuring stability of the uncontrolled joints:

Procedure 1 (Design guidelines for stabilizing uncontrolled joints)

Add damping: The condition on $\boldsymbol{F}_v(\dot{\phi})$, given by (3.11), can always be met by adding viscous damping to the uncontrolled joints.
Feedback controller tuning: Bounds on $\boldsymbol{F}_v$ scale with $|\bar{\Phi}^{(1)}|$, and hence (3.10) and (3.11) are easy to satisfy if the controlled joint equilibrium trajectory is smooth. This motivates (de)-tuning of feedback controller (3.2).
Reference selection: The controlled joint equilibrium trajectory can also be made smoother through selection of the reference trajectory $\hat{\boldsymbol{\Phi}}_{\mathscr{P}}$.
Arm structure selection: The amount of damping required for stability is dictated by the degree of axis coupling which is reflected in the magnitude of elements $\underline{\boldsymbol{C}}_{\bar{\mathscr{P}}}(\cdot)$. The components of $\underline{\boldsymbol{C}}_{\bar{\mathscr{P}}}(\cdot)$ are related to the elements of $\boldsymbol{B}(\boldsymbol{\Phi})$ via (3.4). Note that they do not involve components on the principal diagonal of $\boldsymbol{B}(\boldsymbol{\Phi})$ and hence the bound is solely dependent on the amount of interaction between the system joints. With no interaction $\overline{F}_{v,i} = 0$, reducing to the requirement that $\boldsymbol{F}_v(\cdot)$ is passive.
Stimulated muscle selection: Musculo-tendon coupling produces moments $\boldsymbol{\tau}_{\bar{\mathscr{P}}}(\cdot)$ about uncontrolled joints due to applied ES. This solely has the effect of displacing the equilibrium point $\boldsymbol{\Phi}^*_{\bar{\mathscr{P}}}$.
Mechanical support: This also displaces the equilibrium point $\boldsymbol{\Phi}^*_{\bar{\mathscr{P}}}$, but can also be used to satisfy passivity condition (3.10). Note that the mechanical support must provide sufficient support such that an equilibrium point, $\boldsymbol{\Phi}^*_{\bar{\mathscr{P}}}$, exists for the uncontrolled joints.

3.2 Case Study: Input-Output Linearizing Controller

The feedback control design approach is next illustrated by applying it to the clinically relevant system that was introduced in Sect. 2.2.5. Here ES is applied to the anterior deltoid and triceps muscles using inputs $u_1(t)$ and $u_2(t)$ respectively. The kinematics

are shown in Fig. 2.3, and the clinical objective is to ensure $\phi_2(t)$ and $\phi_5(t)$ track reference signals $\hat{\phi}_2(t)$ and $\hat{\phi}_5(t)$ respectively, with the remaining joint angles stable [14, 15]. Hence we set $m = 2$, $p = 5$, $n_p = 2$ and $\mathscr{P} = \{2, 5\}$.

The linear actuation dynamics $h_{LAD,i}(t)$, $i = 1, 2$ appearing in dynamic model (2.7) can be assumed to be second order [16], so that without loss of generality $\mathscr{L}\left\{h_{LAD,i}(t)\right\} = \frac{n_{i,1}s+n_{i,2}}{s^2+d_{i,1}s+d_{i,2}}$. This gives rise to the Hammerstein structures

$$\begin{aligned}\dot{\boldsymbol{x}}_i(t) &= \underbrace{\begin{bmatrix} -d_{i,1} & -d_{i,2} \\ 1 & 0 \end{bmatrix}}_{\boldsymbol{M}_{A,i}} \boldsymbol{x}_i(t) + \underbrace{\begin{bmatrix} 1 \\ 0 \end{bmatrix}}_{\boldsymbol{M}_{B,i}} h_{IRC,i}(u_i(t)), \\ h_i(u_i, t) &= \underbrace{[\, n_{i,1} \;\; n_{i,2} \,]}_{\boldsymbol{M}_{C,i}} \boldsymbol{x}_i(t), \qquad\qquad i \in \{1, 2\}. \end{aligned} \tag{3.15}$$

We employ musclo-tendon mapping (2.4) and since muscles are aligned with joints

$$\begin{gathered}\boldsymbol{\tau}_1 = 0, \;\; \boldsymbol{\tau}_2(\boldsymbol{u}, \boldsymbol{\Phi}, \dot{\boldsymbol{\Phi}}) = F_{M,2,1}(\phi_2(t), \dot{\phi}_2(t))h_1(u_1, t), \;\; \boldsymbol{\tau}_3 = 0, \;\; \boldsymbol{\tau}_4 = 0, \\ \boldsymbol{\tau}_5(\boldsymbol{u}, \boldsymbol{\Phi}, \dot{\boldsymbol{\Phi}}) = F_{M,5,2}(\phi_5(t), \dot{\phi}_5(t))h_2(u_2, t).\end{gathered}$$

Using $\boldsymbol{x}_s = [\boldsymbol{\Phi}^\top, \dot{\boldsymbol{\Phi}}^\top, \boldsymbol{x}_2^\top, \boldsymbol{x}_5^\top]^\top$ the controlled dynamics, M, of system (3.1) are hence

$$\begin{aligned}\dot{\boldsymbol{x}}_s &= \underbrace{\begin{bmatrix} \dot{\boldsymbol{\Phi}} \\ \boldsymbol{B}(\boldsymbol{\Phi})^{-1} \left(\begin{bmatrix} 0 \\ F_{M,2,1}(\phi_2, \dot{\phi}_2)\boldsymbol{M}_{C,1}\boldsymbol{x}_1 \\ 0 \\ F_{M,5,2}(\phi_5, \dot{\phi}_5)\boldsymbol{M}_{C,2}\boldsymbol{x}_2 \end{bmatrix} - \boldsymbol{X}(\boldsymbol{\Phi}, \dot{\boldsymbol{\Phi}}) \right) \\ \boldsymbol{M}_{A,1}\boldsymbol{x}_1 \\ \boldsymbol{M}_{A,2}\boldsymbol{x}_2 \end{bmatrix}}_{f_s(\boldsymbol{x}_s)} + \underbrace{\overbrace{[g_1(\boldsymbol{x}_s), \; g_2(\boldsymbol{x}_s)]}^{} \begin{bmatrix} 0 & 0 \\ 0 & 0 \\ 0 & 0 \\ 0 & 0 \\ 0 & 0 \\ \boldsymbol{M}_{B,1} & 0 \\ 0 & \boldsymbol{M}_{B,2} \end{bmatrix}}_{g_s(\boldsymbol{u})} \begin{bmatrix} h_{IRC,1}(u_1) \\ h_{IRC,2}(u_2) \end{bmatrix} \\ \boldsymbol{\Phi}_{\mathscr{P}} &= \begin{bmatrix} \phi_2 \\ \phi_5 \end{bmatrix} = \begin{bmatrix} h_1(\boldsymbol{x}_s) \\ h_2(\boldsymbol{x}_s) \end{bmatrix} \end{aligned} \tag{3.16}$$

where

$$\boldsymbol{X}(\boldsymbol{\Phi}, \dot{\boldsymbol{\Phi}}) = \boldsymbol{C}(\boldsymbol{\Phi}, \dot{\boldsymbol{\Phi}})\dot{\boldsymbol{\Phi}} + \boldsymbol{F}(\boldsymbol{\Phi}, \dot{\boldsymbol{\Phi}}) + \boldsymbol{G}(\boldsymbol{\Phi}) + \boldsymbol{K}(\boldsymbol{\Phi}).$$

To satisfy Definition 3.1, we next design K using input-output linearization in order to control $\boldsymbol{\Phi}_{\mathscr{P}}$ using $\boldsymbol{u} = [u_1, u_2]^\top$. As described in [12], for an $m \times m$ system the control action is

$$\begin{bmatrix} h_{IRC,1}(u_1) \\ h_{IRC,2}(u_2) \end{bmatrix} = \boldsymbol{\chi}(\boldsymbol{x}_s)^{-1}\big(\boldsymbol{v} - \boldsymbol{\mu}(\boldsymbol{x}_s)\big) \tag{3.17}$$

with control input demand $\boldsymbol{v} = [v_1, v_2]^\top$. The components of $\boldsymbol{\mu}$, $\boldsymbol{\chi}$ are

$$\mu_i(\boldsymbol{x}_s) = L_f^{k_i} h_i(\boldsymbol{x}_s), \qquad \chi_{ij}(\boldsymbol{x}_s) = L_{g_j} L_f^{k_i - 1} h_i(\boldsymbol{x}_s)$$

respectively, with $i, j = 1, \ldots, 2$, and k_i the relative degree of output i. The Lie derivatives of $h_i(\boldsymbol{x}_s)$ are defined by

$$L_f h_i(\boldsymbol{x}_s) = \frac{\delta h_i}{\delta \boldsymbol{x}_s} \boldsymbol{f}_s(\boldsymbol{x}_s), \qquad L_{g_i} h_i(\boldsymbol{x}_s) = \frac{\delta h_i}{\delta \boldsymbol{x}_s} g_i(\boldsymbol{x}_s) \tag{3.18}$$

and $L_f^j h_i(\boldsymbol{x}_s)$ and $L_{g_i} L_f^{j-1} h_i(\boldsymbol{x}_s)$ are respectively given by

$$L_f\big(L_f^{j-1} h_i(\boldsymbol{x}_s)\big) \quad \text{and} \quad L_{g_i}\big(L_f^{j-1} h_i(\boldsymbol{x}_s)\big).$$

Relative degree k_i satisfies $L_{g_i} L_f^{k_i - 1} h_i(\boldsymbol{x}_s) \neq 0$, and $L_{g_i} L_f^n h_i(\boldsymbol{x}_s) = 0$ for $n = 1, 2, \ldots (k_i - 2)$. Hence (3.17) becomes

$$\begin{bmatrix} h_{IRC,1}(u_1) \\ h_{IRC,2}(u_2) \end{bmatrix} = \begin{bmatrix} L_{g_1} L_f^{k_1 - 1} h_1(\boldsymbol{x}_s) & L_{g_2} L_f^{k_1 - 1} h_1(\boldsymbol{x}_s) \\ L_{g_1} L_f^{k_2 - 1} h_2(\boldsymbol{x}_s) & L_{g_2} L_f^{k_2 - 1} h_2(\boldsymbol{x}_s) \end{bmatrix}^{-1} \left(\boldsymbol{v} - \begin{bmatrix} L_f^{k_1} h_1(\boldsymbol{x}_s) \\ L_f^{k_2} h_2(\boldsymbol{x}_s) \end{bmatrix} \right)$$

with $k_1 = 3$ if $n_{1,1} = 0$, and $k_1 = 4$ otherwise, and $k_2 = 3$ if $n_{2,1} = 0$, and $k_2 = 4$ otherwise. Applied to (3.16) this yields

$$u_1 = \begin{cases} h_{IRC,1}^{-1}\left(\dfrac{\frac{\delta}{\delta \boldsymbol{x}_s}\left(\frac{\delta f_{s,7}(\boldsymbol{x}_s)}{\delta \boldsymbol{x}_s} \boldsymbol{f}_s(\boldsymbol{x}_s)\right) \boldsymbol{f}_s(\boldsymbol{x}_s) - v_1}{(\boldsymbol{B}(\boldsymbol{\Phi})^{-1})_{2,2} F_{M,2,1}(\phi_2, \dot{\phi}_2) n_{1,2}} \right) & \text{if } n_{1,1} = 0 \\ h_{IRC,1}^{-1}\left(\dfrac{\frac{\delta f_{s,7}(\boldsymbol{x}_s)}{\delta \boldsymbol{x}_s} \boldsymbol{f}_s(\boldsymbol{x}_s) - v_1}{(\boldsymbol{B}(\boldsymbol{\Phi})^{-1})_{2,2} F_{M,2,1}(\phi_2, \dot{\phi}_2) n_{1,1}} \right) & \text{otherwise} \end{cases} \tag{3.19}$$

$$u_2 = \begin{cases} h_{IRC,2}^{-1}\left(\dfrac{\frac{\delta}{\delta \boldsymbol{x}_s}\left(\frac{\delta f_{s,10}(\boldsymbol{x}_s)}{\delta \boldsymbol{x}_s} \boldsymbol{f}_s(\boldsymbol{x}_s)\right) \boldsymbol{f}_s(\boldsymbol{x}_s) - v_2}{(\boldsymbol{B}(\boldsymbol{\Phi})^{-1})_{5,5} F_{M,5,2}(\phi_5, \dot{\phi}_5) n_{2,2}} \right) & \text{if } n_{2,1} = 0 \\ h_{IRC,2}^{-1}\left(\dfrac{\frac{\delta f_{s,10}(\boldsymbol{x}_s)}{\delta \boldsymbol{x}_s} \boldsymbol{f}_s(\boldsymbol{x}_s) - v_2}{(\boldsymbol{B}(\boldsymbol{\Phi})^{-1})_{5,5} F_{M,5,2}(\phi_5, \dot{\phi}_5) n_{2,1}} \right) & \text{otherwise.} \end{cases} \tag{3.20}$$

The case $n_{i,1} \neq 0$, $i \in \{1, 2\}$ is now assumed, however similar analysis applies if $n_{i,1} = 0$. Inputs (3.19) and (3.20) yield the decoupled signals

$$\phi_2^{(4)} = v_1, \qquad \phi_5^{(4)} = v_2 \qquad \text{where} \qquad \phi_i^{(k)} = \frac{\delta^k}{\delta t^k}\phi_i. \tag{3.21}$$

3.2.1 Optimal Tracking Controller

Having decoupled and linearized the controlled joints $\boldsymbol{\Phi}_{\mathscr{P}}$, an optimal tracking controller is next designed to achieve global stability, as required by Definition 3.1. We select the control demand, $\boldsymbol{v}$, as

$$\boldsymbol{v} = \hat{\boldsymbol{\Phi}}_{\mathscr{P}}^{(4)} - \Lambda \begin{bmatrix} \hat{\boldsymbol{\Phi}}_{\mathscr{P}} - \boldsymbol{\Phi}_{\mathscr{P}} \\ \hat{\boldsymbol{\Phi}}_{\mathscr{P}}^{(1)} - \boldsymbol{\Phi}_{\mathscr{P}}^{(1)} \\ \hat{\boldsymbol{\Phi}}_{\mathscr{P}}^{(2)} - \boldsymbol{\Phi}_{\mathscr{P}}^{(2)} \\ \hat{\boldsymbol{\Phi}}_{\mathscr{P}}^{(3)} - \boldsymbol{\Phi}_{\mathscr{P}}^{(3)} \end{bmatrix} \tag{3.22}$$

with $\Lambda = [A_0, A_1, A_2, A_3]$. From (3.21), $\boldsymbol{v} = \boldsymbol{\Phi}_{\mathscr{P}}^{(4)}$, so the resulting closed-loop joint dynamics (3.5) and (3.7) are then given by

$$\underbrace{\frac{d}{dt}\begin{bmatrix} \hat{\boldsymbol{\Phi}}_{\mathscr{P}} - \boldsymbol{\Phi}_{\mathscr{P}} \\ \hat{\boldsymbol{\Phi}}_{\mathscr{P}}^{(1)} - \boldsymbol{\Phi}_{\mathscr{P}}^{(1)} \\ \hat{\boldsymbol{\Phi}}_{\mathscr{P}}^{(2)} - \boldsymbol{\Phi}_{\mathscr{P}}^{(2)} \\ \hat{\boldsymbol{\Phi}}_{\mathscr{P}}^{(3)} - \boldsymbol{\Phi}_{\mathscr{P}}^{(3)} \end{bmatrix}}_{\dot{\boldsymbol{x}}} = \underbrace{\begin{bmatrix} 0 & I & 0 & 0 \\ 0 & 0 & I & 0 \\ 0 & 0 & 0 & I \\ -A_0 & -A_1 & -A_2 & -A_3 \end{bmatrix}}_{A} \underbrace{\begin{bmatrix} \hat{\boldsymbol{\Phi}}_{\mathscr{P}} - \boldsymbol{\Phi}_{\mathscr{P}} \\ \hat{\boldsymbol{\Phi}}_{\mathscr{P}}^{(1)} - \boldsymbol{\Phi}_{\mathscr{P}}^{(1)} \\ \hat{\boldsymbol{\Phi}}_{\mathscr{P}}^{(2)} - \boldsymbol{\Phi}_{\mathscr{P}}^{(2)} \\ \hat{\boldsymbol{\Phi}}_{\mathscr{P}}^{(3)} - \boldsymbol{\Phi}_{\mathscr{P}}^{(3)} \end{bmatrix}}_{\boldsymbol{x}}, \tag{3.23}$$

$$\boldsymbol{\xi}(\boldsymbol{x}) = \begin{bmatrix} I, & 0 \end{bmatrix} \boldsymbol{x}. \tag{3.24}$$

Selecting elements of matrix Λ which ensure the eigenvalues of matrix A are stable can be achieved by computing Λ to minimize the cost

$$J(\boldsymbol{v}) = \int_0^\infty \left(\boldsymbol{v}^\top \tilde{R} \boldsymbol{v} + \boldsymbol{x}^\top \tilde{Q} \boldsymbol{x} \right) \mathrm{d}t \tag{3.25}$$

which weights error and input energy norms, subject to $\boldsymbol{v} - \hat{\boldsymbol{\Phi}}_{\mathscr{P}}^{(4)} = -\Lambda \boldsymbol{x}$ and

$$\dot{\boldsymbol{x}} = \begin{bmatrix} 0 & I & 0 & 0 \\ 0 & 0 & I & 0 \\ 0 & 0 & 0 & I \\ 0 & 0 & 0 & 0 \end{bmatrix} \boldsymbol{x} + \begin{bmatrix} 0 & 0 & 0 & I \end{bmatrix}^\top \left(\boldsymbol{v} - \hat{\boldsymbol{\Phi}}_{\mathscr{P}}^{(4)} \right). \tag{3.26}$$

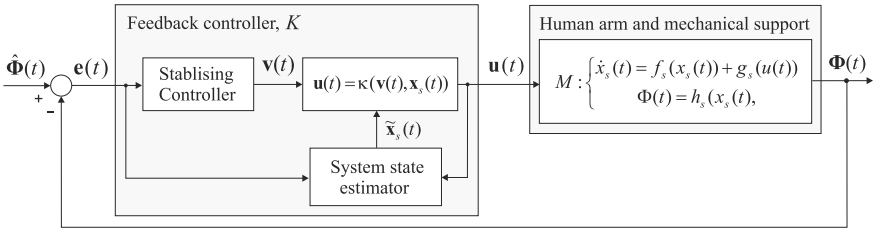

Fig. 3.2 Input-output linearizing control scheme with stabilizing feedback

Writing mappings (3.19) and (3.20) as $\boldsymbol{u} = \boldsymbol{\kappa}(\boldsymbol{v}, \boldsymbol{x}_s)$ then yields the overall control action

$$K := \begin{cases} \dot{\boldsymbol{x}}_c = \underbrace{\begin{bmatrix} 0 & 0 & 0 & 0 \\ 0 & 0 & I & 0 \\ 0 & 0 & 0 & I \\ -A_0 & -A_1 & -A_2 & -A_3 \end{bmatrix} \boldsymbol{x}_c + \begin{bmatrix} I \\ 0 \\ 0 \\ 0 \end{bmatrix} \underbrace{\begin{bmatrix} 0\,1\,0\,0\,0 \\ 0\,0\,0\,0\,I \end{bmatrix} \boldsymbol{e}}_{\boldsymbol{e}_{\mathscr{P}}}}_{\boldsymbol{f}_c(\boldsymbol{x}_c, \boldsymbol{e})}, \\ \boldsymbol{u} = \underbrace{\boldsymbol{\kappa}\left(\hat{\boldsymbol{\Phi}}^{(4)}_{\mathscr{P}} - K\boldsymbol{x}_c, \boldsymbol{x}_s\right)}_{\boldsymbol{h}_c(\boldsymbol{x}_c, \boldsymbol{e})} \end{cases} \tag{3.27}$$

which hence satisfies Definition 3.1 with equilibrium point $\bar{\boldsymbol{\Phi}} = \hat{\boldsymbol{\Phi}}_{\mathscr{P}}$. Note that (3.25) can also be solved over a finite range $[0, T]$, $T < \infty$ resulting in a time-varying Λ which also provides stability of the error dynamics.

In practice an observer may also be required to provide estimates of system states $\boldsymbol{x}_s$, comprising the system joint angles and angular velocities, together with the muscle states $\boldsymbol{x}_1, \boldsymbol{x}_2$. The resulting augmented feedback structure is shown in Fig. 3.2. Experimental results using this control scheme appear in Sect. 4.2, where it is also combined with an ILC feedforward action.

3.3 Robust Performance

Design of feedback controller K to satisfy Definition 3.1 requires stabilizing nominal system model M. However, in practice all such models possess uncertainty so stabilization is not guaranteed when the feedback action is subsequently applied to the true plant. Theorem 3.2 showed that stability of uncontrolled joints can be addressed despite model uncertainty simply by increasing damping and stiffness, but still requires that Definition 3.1 holds. Therefore a comprehensive treatment is required to examine the robust stability of the full closed-loop system incorporating both controlled and uncontrolled joints. A powerful framework is now developed to address this, and will yield practical design guidelines.

We first consider the openloop nominal plant, and derive stability conditions for all joints. These will then be used by the subsequent robust performance analysis.

Proposition 3.1 *Let passive function* $\boldsymbol{F}(\boldsymbol{\Phi}, \dot{\boldsymbol{\Phi}})$ *have form (2.12), then the rigid body system*

$$\boldsymbol{B}(\boldsymbol{\Phi})\ddot{\boldsymbol{\Phi}} + \boldsymbol{C}(\boldsymbol{\Phi}, \dot{\boldsymbol{\Phi}})\dot{\boldsymbol{\Phi}} + \boldsymbol{F}(\boldsymbol{\Phi}, \dot{\boldsymbol{\Phi}}) + \boldsymbol{G}(\boldsymbol{\Phi}) + \boldsymbol{K}(\boldsymbol{\Phi}) = \boldsymbol{\tau}, \tag{3.28}$$

with input $\boldsymbol{\tau}$ *and output* $\boldsymbol{\Phi}$*, is bounded-input, bounded-output (BIBO) stable about operating point* $(\bar{\boldsymbol{\tau}}, \bar{\boldsymbol{\Phi}})$ *if it satisfies the passivity condition*

$$(\boldsymbol{\Phi} - \bar{\boldsymbol{\Phi}})^\top \left(\boldsymbol{F}_e(\boldsymbol{\Phi}) + \boldsymbol{G}(\boldsymbol{\Phi}) + \boldsymbol{K}(\boldsymbol{\Phi}) - \bar{\boldsymbol{\tau}}\right) \geq 0 \tag{3.29}$$

Proof Following [17] we impose additional conditions on a suitable system Liapunov function to enable asymptotic stability to be exchanged for the stricter condition of BIBO stability. Assuming for simplicity $\dot{\bar{\boldsymbol{\Phi}}} = \boldsymbol{0}$, operating point $\bar{\boldsymbol{\Phi}}$ satisfies

$$\boldsymbol{K}(\bar{\boldsymbol{\Phi}}) + \boldsymbol{G}(\bar{\boldsymbol{\Phi}}) + \boldsymbol{F}_e(\bar{\boldsymbol{\Phi}}) = \bar{\boldsymbol{\tau}}, \tag{3.30}$$

hence the system dynamics can be represented about the equilibrium point by

$$\begin{aligned}\boldsymbol{B}(\tilde{\boldsymbol{\Phi}} + \bar{\boldsymbol{\Phi}})\ddot{\boldsymbol{\Phi}} + \boldsymbol{C}(\tilde{\boldsymbol{\Phi}} + \bar{\boldsymbol{\Phi}}, \dot{\boldsymbol{\Phi}})\dot{\boldsymbol{\Phi}} + \boldsymbol{K}(\tilde{\boldsymbol{\Phi}} + \bar{\boldsymbol{\Phi}}) + \boldsymbol{G}(\tilde{\boldsymbol{\Phi}} + \bar{\boldsymbol{\Phi}}) + \boldsymbol{F}_v\dot{\boldsymbol{\Phi}} + \boldsymbol{F}_e(\tilde{\boldsymbol{\Phi}} + \bar{\boldsymbol{\Phi}}) \\ - \boldsymbol{K}(\bar{\boldsymbol{\Phi}}) - \boldsymbol{G}(\bar{\boldsymbol{\Phi}}) - \boldsymbol{F}_e(\bar{\boldsymbol{\Phi}}) = \boldsymbol{\tau} - \bar{\boldsymbol{\tau}}\end{aligned} \tag{3.31}$$

where $\tilde{\boldsymbol{\Phi}} = \boldsymbol{\Phi} - \bar{\boldsymbol{\Phi}}$, with $\dot{\tilde{\boldsymbol{\Phi}}} = \dot{\boldsymbol{\Phi}}$, $\ddot{\tilde{\boldsymbol{\Phi}}} = \ddot{\boldsymbol{\Phi}}$. Since (3.29) holds we can select the symmetric positive-definite Liapunov function

$$\begin{aligned}V(\tilde{\boldsymbol{\Phi}}, \dot{\boldsymbol{\Phi}}) = \dot{\boldsymbol{\Phi}}^\top \frac{\boldsymbol{B}(\tilde{\boldsymbol{\Phi}} + \bar{\boldsymbol{\Phi}})}{2}\dot{\boldsymbol{\Phi}} + \int_0^{\tilde{\boldsymbol{\Phi}}} \big(\boldsymbol{F}_e(\boldsymbol{\sigma}) + \boldsymbol{G}(\boldsymbol{\sigma}) + \boldsymbol{K}(\boldsymbol{\sigma}) \\ - \boldsymbol{F}_e(\bar{\boldsymbol{\Phi}}) - \boldsymbol{K}(\bar{\boldsymbol{\Phi}}) - \boldsymbol{G}(\bar{\boldsymbol{\Phi}})\big)\delta\boldsymbol{\sigma}\end{aligned} \tag{3.32}$$

so that

$$\begin{aligned}\dot{V}(\tilde{\boldsymbol{\Phi}}(t), \dot{\boldsymbol{\Phi}}(t)) &= \dot{\boldsymbol{\Phi}}(t)^\top \boldsymbol{B}(\tilde{\boldsymbol{\Phi}}(t) + \bar{\boldsymbol{\Phi}}(t))\ddot{\boldsymbol{\Phi}}(t) + \dot{\boldsymbol{\Phi}}(t)^\top \frac{\dot{\boldsymbol{B}}(\tilde{\boldsymbol{\Phi}}(t) + \bar{\boldsymbol{\Phi}}(t))}{2}\dot{\boldsymbol{\Phi}}(t) \\ &\quad + \dot{\boldsymbol{\Phi}}(t)^\top \big(\boldsymbol{F}_e(\tilde{\boldsymbol{\Phi}}(t) + \bar{\boldsymbol{\Phi}}(t)) + \boldsymbol{G}(\tilde{\boldsymbol{\Phi}}(t) + \bar{\boldsymbol{\Phi}}(t)) \\ &\quad + \boldsymbol{K}(\tilde{\boldsymbol{\Phi}}(t) + \bar{\boldsymbol{\Phi}}(t))\big) - \dot{\boldsymbol{\Phi}}(t)^\top \big(\boldsymbol{F}_e(\bar{\boldsymbol{\Phi}}(t)) + \boldsymbol{G}(\bar{\boldsymbol{\Phi}}(t)) + \boldsymbol{K}(\bar{\boldsymbol{\Phi}}(t))\big) \\ &= \dot{\boldsymbol{\Phi}}(t)^\top \left(\frac{\dot{\boldsymbol{B}}(\boldsymbol{\Phi}(t))}{2} - \boldsymbol{C}(\boldsymbol{\Phi}(t), \dot{\boldsymbol{\Phi}}(t)) - \boldsymbol{F}_v\right)\dot{\boldsymbol{\Phi}}(t) \\ &\quad + \dot{\boldsymbol{\Phi}}(t)^\top(\boldsymbol{\tau}(t) - \bar{\boldsymbol{\tau}}(t)).\end{aligned}$$

Since $\frac{1}{2}\dot{\boldsymbol{B}}(\boldsymbol{\Phi}(t)) - \boldsymbol{C}(\boldsymbol{\Phi}(t), \dot{\boldsymbol{\Phi}}(t))$ is skew-symmetric, $\frac{\dot{\boldsymbol{B}}(\boldsymbol{\Phi}(t))}{2} - \boldsymbol{C}(\boldsymbol{\Phi}(t), \dot{\boldsymbol{\Phi}}(t)) - \boldsymbol{F}_v$ is negative definite since $\boldsymbol{F}_v$ has positive diagonal entries. Hence $\exists\, \alpha > 0$ such that

$$\dot{\boldsymbol{\Phi}}(t)^\top \left(\frac{\dot{\boldsymbol{B}}(\boldsymbol{\Phi}(t))}{2} - \boldsymbol{C}(\boldsymbol{\Phi}(t), \dot{\boldsymbol{\Phi}}(t)) - \boldsymbol{F}_v \right) \dot{\boldsymbol{\Phi}}(t) \leq -\alpha \left\| \dot{\boldsymbol{\Phi}}(t) \right\|^2 \tag{3.33}$$

which gives the bound

$$\begin{aligned} \dot{V}(\tilde{\boldsymbol{\Phi}}(t), \dot{\boldsymbol{\Phi}}(t)) &\leq -\alpha \left\| \dot{\boldsymbol{\Phi}}(t) \right\|^2 + \left\| \dot{\boldsymbol{\Phi}}(t) \right\| \left\| \boldsymbol{\tau}(t) \right\|_{\bar{\boldsymbol{\tau}}} \\ &\leq -\left\| \dot{\boldsymbol{\Phi}}(t) \right\| \left(\alpha \left\| \dot{\boldsymbol{\Phi}}(t) \right\| - \left\| \boldsymbol{\tau}(t) \right\|_{\bar{\boldsymbol{\tau}}} \right). \end{aligned} \tag{3.34}$$

Following the approach of [17], we now show that there exists a finite β such that $\left\| \tilde{\boldsymbol{\Phi}}(t) \right\| \leq \beta \left\| \boldsymbol{\tau}(t) \right\|_{\bar{\boldsymbol{\tau}}}$. First note that for all bounded $\boldsymbol{\tau}(t)$

$$\left\| \dot{\boldsymbol{\Phi}}(t) \right\| \geq \frac{\|\boldsymbol{\tau}(t)\|_{\bar{\boldsymbol{\tau}}}}{\alpha} \Rightarrow \dot{V}(\tilde{\boldsymbol{\Phi}}(t), \dot{\boldsymbol{\Phi}}(t)) \leq 0 \tag{3.35}$$

and since $\boldsymbol{B}(\cdot)$ and $\boldsymbol{C}(\cdot)$ are bounded and continuous, $\left\| \tilde{\boldsymbol{\Phi}}(t) \right\|$ is bounded when $\left\| \dot{\boldsymbol{\Phi}}(t) \right\| < \frac{\|\boldsymbol{\tau}(t)\|_{\bar{\boldsymbol{\tau}}}}{\alpha}$, with $\|\boldsymbol{\tau}\|_{\bar{\boldsymbol{\tau}}} = \boldsymbol{0} \Rightarrow \boldsymbol{\Phi} = \bar{\boldsymbol{\Phi}}$ so that $\left\| \boldsymbol{\Phi} - \bar{\boldsymbol{\Phi}} \right\| \leq \gamma_1 \|\boldsymbol{\tau}\|_{\bar{\boldsymbol{\tau}}}$ for some finite γ_1. Then through application of LaSalle's Invariance Principle we note that for the system (3.31) to maintain $\dot{V}(\tilde{\boldsymbol{\Phi}}(t), \dot{\boldsymbol{\Phi}}(t)) = 0$ for fixed $\boldsymbol{\tau}$ the trajectory must be confined to the line given by (3.28) with $\dot{\tilde{\boldsymbol{\Phi}}} = \boldsymbol{0}, \ddot{\tilde{\boldsymbol{\Phi}}} = \boldsymbol{0} \Rightarrow \ddot{\boldsymbol{\Phi}} = \ddot{\bar{\boldsymbol{\Phi}}}, \dot{\boldsymbol{\Phi}} = \dot{\bar{\boldsymbol{\Phi}}}$. This can only be satisfied when $\boldsymbol{\tau} = \bar{\boldsymbol{\tau}}$ which hence corresponds to the set-point dynamics given by (3.30). Therefore for each $\boldsymbol{\tau}$ there exists a finite γ_2 such that

$$\left\| \dot{\boldsymbol{\Phi}} \right\| \geq \frac{\|\boldsymbol{\tau}\|_{\bar{\boldsymbol{\tau}}}}{\alpha} \Rightarrow \left\| \tilde{\boldsymbol{\Phi}} \right\| \leq \gamma_2 \|\boldsymbol{\tau}\|_{\bar{\boldsymbol{\tau}}}\,. \tag{3.36}$$

Combining the above cases guarantees $\forall \boldsymbol{\tau}$

$$\|\boldsymbol{\Phi}\|_{\bar{\boldsymbol{\Phi}}} \leq \max\{\gamma_1, \gamma_2\} \|\boldsymbol{\tau}\|_{\bar{\boldsymbol{\tau}}} \tag{3.37}$$

and it follows that system (3.28) is BIBO stable about equilibrium $(\bar{\boldsymbol{\tau}}, \bar{\boldsymbol{\Phi}})$. □

Proposition 3.1 shows that the map $\boldsymbol{\tau} \mapsto \boldsymbol{\Phi}$ is BIBO stable if all joints are passive about the operating point $(\bar{\boldsymbol{\tau}}, \bar{\boldsymbol{\Phi}})$. Compared with the closed-loop stability conditions of Definition 3.1 and Theorem 3.2, it imposes extra conditions on the joints ϕ_i, $i \in \mathscr{P}$, but relaxes conditions on joints ϕ_i, $i \in \bar{\mathscr{P}}$.

The map $\boldsymbol{\tau} \mapsto \boldsymbol{\Phi}$ corresponds to the rigid body dynamics component of the system M, which can be written in operator form using the following representations:

$$M : \mathscr{L}_2^m \to \mathscr{L}_2^p : \boldsymbol{u} \mapsto \boldsymbol{\Phi} : \begin{cases} \boldsymbol{\Phi} = \boldsymbol{h}_s(\boldsymbol{x}_s), \\ \dot{\boldsymbol{x}}_s = \boldsymbol{f}_s(\boldsymbol{x}_s) + \boldsymbol{g}_s(\boldsymbol{u}) \end{cases}$$
$$: \boldsymbol{\Phi} = H_{RB} F_m(\boldsymbol{\Phi}, \dot{\boldsymbol{\Phi}}) H_{LAD} \boldsymbol{h}_{IRC} \boldsymbol{u} \tag{3.38}$$

where, from (2.2), (2.3) and (2.6), components H_{RB}, $F_m(\boldsymbol{\Phi}, \dot{\boldsymbol{\Phi}})$, H_{LAD} and $\boldsymbol{h}_{IRC}$ are

$$H_{RB} : \mathscr{L}_2^p \to \mathscr{L}_2^p : \boldsymbol{\tau} \mapsto \boldsymbol{\Phi}$$
$$: \begin{cases} \boldsymbol{\Phi} = [\boldsymbol{I}, \boldsymbol{0}] \begin{bmatrix} \boldsymbol{\Phi} \\ \dot{\boldsymbol{\Phi}} \end{bmatrix}, \\ \frac{d}{dt} \begin{bmatrix} \boldsymbol{\Phi} \\ \dot{\boldsymbol{\Phi}} \end{bmatrix} = \begin{bmatrix} \dot{\boldsymbol{\Phi}} \\ \boldsymbol{B}(\boldsymbol{\Phi})^{-1} (\boldsymbol{\tau} - \boldsymbol{C}(\boldsymbol{\Phi}, \dot{\boldsymbol{\Phi}}) \dot{\boldsymbol{\Phi}}) - \boldsymbol{F}(\boldsymbol{\Phi}, \dot{\boldsymbol{\Phi}}) - \boldsymbol{G}(\boldsymbol{\Phi}) - \boldsymbol{K}(\boldsymbol{\Phi})) \end{bmatrix} \end{cases} \tag{3.39}$$

$$F_m(\boldsymbol{\Phi}, \dot{\boldsymbol{\Phi}}) : \mathscr{L}_2^m \to \mathscr{L}_2^p : \boldsymbol{w} \mapsto \boldsymbol{\tau} : \boldsymbol{\tau} = \begin{bmatrix} F_{M,1,1}(\phi_1, \dot{\phi}_1) & \cdots & F_{M,1,m}(\phi_1, \dot{\phi}_1) \\ \vdots & \ddots & \vdots \\ F_{M,p,1}(\phi_p, \dot{\phi}_p) & \cdots & F_{M,p,m}(\phi_p, \dot{\phi}_p) \end{bmatrix} \boldsymbol{w} \tag{3.40}$$

$$H_{LAD} : \mathscr{L}_2^m \to \mathscr{L}_2^m : \boldsymbol{v} \mapsto \boldsymbol{w} : \boldsymbol{w} = \text{diag}\{H_{LAD,1}, \cdots, H_{LAD,m}\} \boldsymbol{v},$$
$$H_{LAD,j} : \boldsymbol{v}_j \mapsto \boldsymbol{w}_j : \begin{cases} \dot{\boldsymbol{x}}_j = \boldsymbol{M}_{A,j} \boldsymbol{x}_j + \boldsymbol{M}_{B,j} \boldsymbol{v}_j \\ \boldsymbol{w}_j = \boldsymbol{M}_{C,j} \boldsymbol{x}_j \end{cases}, \quad j = 1, \cdots m \tag{3.41}$$

$$\boldsymbol{h}_{IRC} : \mathscr{L}_2^m \to \mathscr{L}_2^m : \boldsymbol{u} \mapsto \boldsymbol{v} : \boldsymbol{v} = \begin{bmatrix} h_{IRC,1}(\boldsymbol{u}_1(t)) \\ \vdots \\ h_{IRC,m}(\boldsymbol{u}_m(t)) \end{bmatrix}. \tag{3.42}$$

We now expand our analysis to consider the closed-loop system shown in Fig. 3.3a, where $\boldsymbol{u}_0$ and $\boldsymbol{y}_0$ are external disturbances. We introduce the projection operator from external to internal dynamics $\Pi_{M//K} : \begin{pmatrix} \boldsymbol{u}_0 \\ \boldsymbol{y}_0 + \hat{\boldsymbol{\Phi}} \end{pmatrix} \mapsto \begin{pmatrix} \boldsymbol{u} \\ \boldsymbol{\Phi} \end{pmatrix}$, where it follows that the plant operating point satisfies $\begin{pmatrix} \bar{\boldsymbol{u}} \\ \bar{\boldsymbol{\Phi}} \end{pmatrix} = \Pi_{M//K} \begin{pmatrix} \boldsymbol{0} \\ \hat{\boldsymbol{\Phi}} \end{pmatrix}$. We next

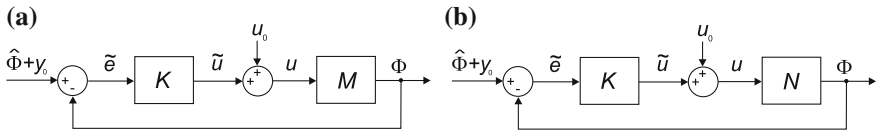

Fig. 3.3 Feedback system incorporating control action $K : \tilde{\boldsymbol{e}} \mapsto \tilde{\boldsymbol{u}}$ given by (3.2), with external disturbances $\boldsymbol{u}_0, \boldsymbol{y}_0$ and: **a** nominal plant dynamics $M : \boldsymbol{u} \mapsto \boldsymbol{\Phi}$, **b** true plant dynamics $N : \boldsymbol{u} \mapsto \boldsymbol{\Phi}$

represent the true plant by operator N as shown in Fig. 3.3b and define its projection $\Pi_{N//K} : \begin{pmatrix} \boldsymbol{u}_0 \\ \boldsymbol{y}_0 + \hat{\boldsymbol{\Phi}} \end{pmatrix} \mapsto \begin{pmatrix} \boldsymbol{u} \\ \boldsymbol{\Phi} \end{pmatrix}$, with the operating point $\begin{pmatrix} \bar{\boldsymbol{u}}_1 \\ \bar{\boldsymbol{\Phi}}_1 \end{pmatrix} = \Pi_{N//K} \begin{pmatrix} \boldsymbol{0} \\ \hat{\boldsymbol{\Phi}} \end{pmatrix}$. To obtain conditions for stability of the true closed-loop system $[N, K]$, we need the following property linking the two plant descriptions.

Proposition 3.2 *Let closed-loop systems $[M, K]$ and $[N, K]$ have respective operating points $(\bar{\boldsymbol{u}}, \bar{\boldsymbol{\Phi}})$, $(\bar{\boldsymbol{u}}_1, \bar{\boldsymbol{\Phi}}_1)$. Let $(\bar{\boldsymbol{\tau}}, \bar{\boldsymbol{\Phi}})$ and $(\bar{\boldsymbol{\tau}}_1, \bar{\boldsymbol{\Phi}}_1)$ satisfy Proposition 3.1 with bounded $\bar{\boldsymbol{\tau}} = \boldsymbol{\tau}(\bar{\boldsymbol{u}}, \bar{\boldsymbol{\Phi}}, \dot{\bar{\boldsymbol{\Phi}}})$ and $\bar{\boldsymbol{\tau}}_1 = \boldsymbol{\tau}(\bar{\boldsymbol{u}}_1, \bar{\boldsymbol{\Phi}}_1, \dot{\bar{\boldsymbol{\Phi}}}_1)$. Then there exists a surjective map between the graph of $\mathcal{G}_M$ and the graph of $\mathcal{G}_N$, defined by*

$$\mathcal{G}_M := \left\{ \begin{pmatrix} \boldsymbol{u} \\ \boldsymbol{\Phi} \end{pmatrix} : \left\| \begin{matrix} \boldsymbol{u} \\ \boldsymbol{\Phi} \end{matrix} \right\|_{\begin{pmatrix} \bar{\boldsymbol{u}} \\ \bar{\boldsymbol{\Phi}} \end{pmatrix}} < \infty, \boldsymbol{\Phi} = M\boldsymbol{u} \right\}, \quad \mathcal{G}_N := \left\{ \begin{pmatrix} \boldsymbol{u} \\ \boldsymbol{\Phi} \end{pmatrix} : \left\| \begin{matrix} \boldsymbol{u} \\ \boldsymbol{\Phi} \end{matrix} \right\|_{\begin{pmatrix} \bar{\boldsymbol{u}}_1 \\ \bar{\boldsymbol{\Phi}}_1 \end{pmatrix}} < \infty, \boldsymbol{\Phi} = N\boldsymbol{u} \right\}.$$

Proof A map $\Psi : \mathcal{G}_M \mapsto \mathcal{G}_N$ is surjective if $\forall\, \boldsymbol{y} \in \mathcal{G}_N \; \exists\, \boldsymbol{x} \in \mathcal{G}_M$ such that $\Psi(\boldsymbol{x}) = \boldsymbol{y}$. Let us choose an element $\boldsymbol{y} \in \mathcal{G}_N$ where $\boldsymbol{y} = \begin{pmatrix} \boldsymbol{u} + \bar{\boldsymbol{u}}_1 \\ N(\boldsymbol{u} + \bar{\boldsymbol{u}}_1) \end{pmatrix}$ for some $\|\boldsymbol{u}\| < \infty$. It follows that $\|\boldsymbol{u} + \bar{\boldsymbol{u}}_1\|_{\bar{\boldsymbol{u}}_1} < \infty$. As Proposition 3.1 is satisfied, the map $\boldsymbol{\tau} + \bar{\boldsymbol{\tau}}_1 \mapsto \boldsymbol{\Phi} + \bar{\boldsymbol{\Phi}}_1$ is bounded, and since $\boldsymbol{u} + \bar{\boldsymbol{u}}_1 \mapsto \boldsymbol{\tau} + \bar{\boldsymbol{\tau}}_1$ is bounded (due to bounded $\boldsymbol{h}_{IRC}$, H_{LAD} and F_m), $\boldsymbol{u} + \bar{\boldsymbol{u}}_1 \mapsto \boldsymbol{\Phi} + \bar{\boldsymbol{\Phi}}_1$ is bounded. Hence $\|N(\boldsymbol{u} + \bar{\boldsymbol{u}}_1)\|_{\bar{\boldsymbol{u}}_1} = \|\boldsymbol{\Phi} + \bar{\boldsymbol{\Phi}}_1)\|_{\bar{\boldsymbol{\Phi}}_1} < \infty$. Define: $\boldsymbol{x} = \begin{pmatrix} \boldsymbol{u} + \bar{\boldsymbol{u}} \\ M(\boldsymbol{u} + \bar{\boldsymbol{u}}) \end{pmatrix}$. Since $\|\boldsymbol{u}\| < \infty$ it follows that $\|\boldsymbol{u} + \bar{\boldsymbol{u}}\|_{\bar{\boldsymbol{u}}} < \infty$. As Proposition 3.1 is satisfied, the map $\boldsymbol{\tau} + \bar{\boldsymbol{\tau}} \mapsto \boldsymbol{\Phi} + \bar{\boldsymbol{\Phi}}$ is bounded, and since $\boldsymbol{u} + \bar{\boldsymbol{u}} \mapsto \boldsymbol{\tau} + \bar{\boldsymbol{\tau}}$ is bounded, $\boldsymbol{u} + \bar{\boldsymbol{u}} \mapsto \boldsymbol{\Phi} + \bar{\boldsymbol{\Phi}}$ is bounded. Hence $\|M(\boldsymbol{u} + \bar{\boldsymbol{u}})\|_{\bar{\boldsymbol{u}}} = \|\boldsymbol{\Phi} + \bar{\boldsymbol{\Phi}})\|_{\bar{\boldsymbol{\Phi}}} < \infty$ and $\boldsymbol{x} \in \mathcal{G}_M$ which means the mapping: $\Psi(\boldsymbol{x}) = \Psi \begin{pmatrix} \boldsymbol{u} + \bar{\boldsymbol{u}} \\ M(\boldsymbol{u} + \bar{\boldsymbol{u}}) \end{pmatrix} = \begin{pmatrix} \boldsymbol{u} + \bar{\boldsymbol{u}}_1 \\ N(\boldsymbol{u} + \bar{\boldsymbol{u}}_1) \end{pmatrix} = \boldsymbol{y}$ is surjective. Finally, note that $\Psi \begin{pmatrix} \bar{\boldsymbol{u}} \\ \bar{\boldsymbol{\Phi}} \end{pmatrix} = \begin{pmatrix} \bar{\boldsymbol{u}}_1 \\ \bar{\boldsymbol{\Phi}}_1 \end{pmatrix}$. □

Proposition 3.2 enables us to use a well-established measure of the difference between the true plant, N, and the nominal plant model, M, as follows:

Definition 3.2 The non-linear biased gap metric measures the mismatch between the plant model M and the true system N. It is defined as

$$\boldsymbol{\delta}(M, N) := \inf \left\{ \|(\Psi - I)_{\mathcal{G}_M}\|_{\begin{pmatrix} \bar{\boldsymbol{u}} \\ \bar{\boldsymbol{\Psi}} \end{pmatrix}} : \Psi \text{ is a causal, surjective map from } \mathcal{G}_M \text{ to } \mathcal{G}_N \text{ with } \Psi \begin{pmatrix} \bar{\boldsymbol{u}} \\ \bar{\boldsymbol{\Phi}} \end{pmatrix} = \begin{pmatrix} \bar{\boldsymbol{u}}_1 \\ \bar{\boldsymbol{\Phi}}_1 \end{pmatrix} \right\}, \quad (3.43)$$

and if the conditions of Proposition 3.2 are satisfied, it can be bounded as

$$\boldsymbol{\delta}(M,N) \leq \sup_{\|\boldsymbol{u}\|\neq 0} \frac{\|(N|_{\bar{\boldsymbol{u}}_1} - M|_{\bar{\boldsymbol{u}}})\boldsymbol{u}\|}{\|\boldsymbol{u}\|} \tag{3.44}$$

where $P|_{\boldsymbol{x}}\boldsymbol{u} = P(\boldsymbol{u}+\boldsymbol{x}) - P\boldsymbol{x}$ for an operator P and set-point $\boldsymbol{x}$.

Proof Proposition 3.2 guarantees existence of subjective map $\Psi\begin{pmatrix}\boldsymbol{u}+\bar{\boldsymbol{u}}\\ M(\boldsymbol{u}+\bar{\boldsymbol{u}})\end{pmatrix} = \begin{pmatrix}\boldsymbol{u}+\bar{\boldsymbol{u}}_1\\ N(\boldsymbol{u}+\bar{\boldsymbol{u}}_1)\end{pmatrix}$. Hence insertion in definition (3.43) yields

$$\begin{aligned}
\boldsymbol{\delta}(M,N) &\leq \|(\Psi - I)_{\mathscr{G}_M}\|_{\begin{pmatrix}\bar{\boldsymbol{u}}\\ \bar{\boldsymbol{\Phi}}\end{pmatrix}} \\
&= \sup_{\boldsymbol{x}\in\mathscr{G}_M\setminus\{\boldsymbol{0}\}} \frac{\left\|(\Psi - I)\boldsymbol{x} - (\Psi - I)\begin{pmatrix}\bar{\boldsymbol{u}}\\ \bar{\boldsymbol{\Phi}}\end{pmatrix}\right\|}{\left\|\boldsymbol{x} - \begin{pmatrix}\bar{\boldsymbol{u}}\\ \bar{\boldsymbol{\Phi}}\end{pmatrix}\right\|} \\
&\leq \sup_{\begin{pmatrix}\boldsymbol{u}+\bar{\boldsymbol{u}}\\ M(\boldsymbol{u}+\bar{\boldsymbol{u}})\end{pmatrix}\in\mathscr{G}_M\setminus\{\boldsymbol{0}\}} \frac{\left\|(\Psi - I)\begin{pmatrix}\boldsymbol{u}+\bar{\boldsymbol{u}}\\ M(\boldsymbol{u}+\bar{\boldsymbol{u}})\end{pmatrix} - (\Psi - I)\begin{pmatrix}\bar{\boldsymbol{u}}\\ \bar{\boldsymbol{\Phi}}\end{pmatrix}\right\|}{\left\|\begin{pmatrix}\boldsymbol{u}+\bar{\boldsymbol{u}}\\ M(\boldsymbol{u}+\bar{\boldsymbol{u}})\end{pmatrix} - \begin{pmatrix}\bar{\boldsymbol{u}}\\ \bar{\boldsymbol{\Phi}}\end{pmatrix}\right\|} \\
&= \sup_{\begin{pmatrix}\boldsymbol{u}+\bar{\boldsymbol{u}}\\ M(\boldsymbol{u}+\bar{\boldsymbol{u}})\end{pmatrix}\in\mathscr{G}_M\setminus\{\boldsymbol{0}\}} \frac{\left\|\begin{pmatrix}\boldsymbol{u}+\bar{\boldsymbol{u}}_1\\ N(\boldsymbol{u}+\bar{\boldsymbol{u}}_1)\end{pmatrix} - \begin{pmatrix}\boldsymbol{u}+\bar{\boldsymbol{u}}\\ M(\boldsymbol{u}+\bar{\boldsymbol{u}})\end{pmatrix} - \left(\begin{pmatrix}\bar{\boldsymbol{u}}_1\\ N\bar{\boldsymbol{u}}_1\end{pmatrix} - \begin{pmatrix}\bar{\boldsymbol{u}}\\ M\bar{\boldsymbol{u}}\end{pmatrix}\right)\right\|}{\left\|\begin{pmatrix}\boldsymbol{u}\\ M(\boldsymbol{u}+\bar{\boldsymbol{u}}) - M\bar{\boldsymbol{u}}\end{pmatrix}\right\|} \\
&= \sup_{\|\boldsymbol{u}\|\neq 0} \frac{\left\|\begin{pmatrix}\boldsymbol{0}\\ (N(\boldsymbol{u}+\bar{\boldsymbol{u}}_1) - N\bar{\boldsymbol{u}}_1) - (M(\boldsymbol{u}+\bar{\boldsymbol{u}}) - M\bar{\boldsymbol{u}})\end{pmatrix}\right\|}{\left\|\begin{pmatrix}\boldsymbol{u}\\ M(\boldsymbol{u}+\bar{\boldsymbol{u}}) - M\bar{\boldsymbol{u}}\end{pmatrix}\right\|} \\
&\leq \sup_{\|\boldsymbol{u}\|\neq 0} \frac{\left\|(N(\boldsymbol{u}+\bar{\boldsymbol{u}}_1) - N\bar{\boldsymbol{u}}_1) - (M(\boldsymbol{u}+\bar{\boldsymbol{u}}) - M\bar{\boldsymbol{u}})\right\|}{\|\boldsymbol{u}\|}.
\end{aligned}$$

□

We can now state the main robustness result, which provides robust performance bounds for the closed-loop system $[N, K]$ of Fig. 3.3b containing the true plant model N. This differs from the nominal feedback system $[M, K]$ of Fig. 3.3a with identified plant model M due to unmodeled dynamics and the presence of time-varying effects such as fatigue and spasticity.

Theorem 3.3 *Let K be selected to stabilize the nominal plant M by satisfying*

$$\|\Pi_{M//K}\|_{\begin{pmatrix}\mathbf{0}\\ \hat{\boldsymbol{\Phi}}\end{pmatrix}} = \sup_{\left\|\begin{pmatrix}\boldsymbol{u}_0\\ \boldsymbol{y}_0\end{pmatrix}\right\|\neq 0} \frac{\left\|\Pi_{M//K}\begin{pmatrix}\boldsymbol{u}_0\\ \boldsymbol{y}_0+\hat{\boldsymbol{\Phi}}\end{pmatrix}-\begin{pmatrix}\bar{\boldsymbol{u}}\\ \bar{\boldsymbol{\Phi}}\end{pmatrix}\right\|}{\left\|\begin{pmatrix}\boldsymbol{u}_0\\ \boldsymbol{y}_0\end{pmatrix}\right\|} \leq b_{M//K} < \infty. \tag{3.45}$$

Then the true feedback system $[N, K]$ is BIBO stable if

$$\boldsymbol{\delta}(M, N) < b_{M//K}^{-1} \tag{3.46}$$

and its performance is bounded with respect to its operating point as

$$\|\Pi_{N//K}\|_{\begin{pmatrix}\mathbf{0}\\ \hat{\boldsymbol{\Phi}}\end{pmatrix}} \leq b_{M//K}\,\frac{1+\delta(M,N)}{1-b_{M//K}\delta(M,N)} \tag{3.47}$$

Proof This theorem is proved in [18] and requires that $[M, K]$ and $[N, K]$ are well posed, which is guaranteed by structures (3.1) and (3.2). □

The bound $b_{M//K}$ in (3.45) is the familiar 'gain margin' of the nominal system with respect to its operating point. The requirement of nominal stability, $b_{M//K} < \infty$, is a generalization of Definition 3.1 and Theorem 3.2, which both comprise necessary conditions. In particular, if $K = 0$, then satisfying (3.45) reduces to the requiring that M is BIBO stable which is established by Proposition 3.1.

Theorem 3.3 together with gap bound (3.44) provides a powerful tool with which to study the effect of uncertainties on ES feedback control systems. However its practical utility is increased by localizing the most likely sources of modeling uncertainty. To do this we substitute representations (3.38)–(3.42) into Theorem 3.3 and restrict uncertainty to the most common sources of model inaccuracy. To illustrate this approach we next consider muscle fatigue which we assume to take the form of modeling inaccuracy within IRC component $\boldsymbol{h}_{IRC}$.

Proposition 3.3 *Let M and N satisfy the conditions of Proposition 3.2 and the controller be designed such that the nominal closed-loop system $[M, K]$ satisfies (3.45). Suppose a model mismatch exists between true and modeled IRC components, $\tilde{\boldsymbol{h}}_{IRC}$ and $\boldsymbol{h}_{IRC}$ respectively. Then the true system $[N, K]$ has a robust stability margin, and in particular is stable if*

$$\Delta_{IRC} < \frac{b_{M//K}^{-1} - \|H_{RB}F_m|_{\bar{\boldsymbol{w}}_1} - H_{RB}F_m|_{\bar{\boldsymbol{w}}}\|\,\|\boldsymbol{h}_{IRC}|_{\bar{\boldsymbol{u}}}\|}{\|H_{RB}F_m|_{\bar{\boldsymbol{w}}_1}\|} \tag{3.48}$$

where the model mismatch is characterized by

$$\Delta_{IRC} = \max_i \sup_{\|\boldsymbol{u}\|\neq 0} \frac{\|(\tilde{\boldsymbol{h}}_{IRC,i}|_{\bar{\boldsymbol{u}}_{1,i}} - \boldsymbol{h}_{IRC,i}|_{\bar{\boldsymbol{u}}_i})\boldsymbol{u}\|}{\|\boldsymbol{u}\|} \tag{3.49}$$

and $H_{RB}F_m|_{\bar{\boldsymbol{w}}} = H_{RB}|_{\bar{\boldsymbol{\tau}}}F_m(\boldsymbol{\Phi}, \dot{\boldsymbol{\Phi}})|_{\bar{\boldsymbol{w}}}$, $H_{RB}F_m|_{\bar{\boldsymbol{w}}_1} = H_{RB}|_{\bar{\boldsymbol{\tau}}_1}F_m(\boldsymbol{\Phi}, \dot{\boldsymbol{\Phi}})|_{\bar{\boldsymbol{w}}_1}$ *are the remaining plant components in* M *and* N *evaluated at their respective operating points. Furthermore, the gain bound for* $[N, K]$ *satisfies*

$$\|\Pi_{N//K}\|_{\begin{pmatrix}\bar{\boldsymbol{u}}_1\\ \bar{\boldsymbol{\Phi}}_1\end{pmatrix}} \leq \frac{b_{M//K}(1 + \Delta_{IRC}\|H_{RB}F_m|_{\bar{\boldsymbol{w}}_1}\| + \|H_{RB}F_m|_{\bar{\boldsymbol{w}}_1} - H_{RB}F_m|_{\bar{\boldsymbol{w}}}\|\|\boldsymbol{h}_{IRC}|_{\boldsymbol{u}}\|)}{1 - b_{M//K}(\Delta_{IRC}\|H_{RB}F_m|_{\bar{\boldsymbol{w}}_1}\| + \|H_{RB}F_m|_{\bar{\boldsymbol{w}}_1} - H_{RB}F_m|_{\bar{\boldsymbol{w}}}\|\|\boldsymbol{h}_{IRC}|_{\boldsymbol{u}}\|)} \tag{3.50}$$

Proof From Proposition 3.2 a surjective map Ψ exists from $\mathscr{G}_M$ to $\mathscr{G}_N$. Then note the expression $M|_{\bar{\boldsymbol{u}}_1}$ in (3.44) is

$$\begin{aligned} M(\boldsymbol{u} + \bar{\boldsymbol{u}}) - M\bar{\boldsymbol{u}} &= H_{RB}|_{\bar{\boldsymbol{\tau}}}F_m(\boldsymbol{\Phi}, \dot{\boldsymbol{\Phi}})|_{\bar{\boldsymbol{w}}}H_{LAD}\boldsymbol{h}_{IRC}(\bar{\boldsymbol{u}} + \boldsymbol{u}) \\ &\quad - H_{RB}|_{\bar{\boldsymbol{\tau}}}F_m(\boldsymbol{\Phi}, \dot{\boldsymbol{\Phi}})|_{\bar{\boldsymbol{w}}}H_{LAD}\boldsymbol{h}_{IRC}(\bar{\boldsymbol{u}}) \\ &= H_{RB}|_{\bar{\boldsymbol{\tau}}}F_m(\boldsymbol{\Phi}, \dot{\boldsymbol{\Phi}})|_{\bar{\boldsymbol{w}}}H_{LAD}\boldsymbol{h}_{IRC}|_{\bar{\boldsymbol{u}}}\boldsymbol{u} \end{aligned} \tag{3.51}$$

where $\bar{\boldsymbol{w}} = H_{LAD}\boldsymbol{h}_{IRC}(\bar{\boldsymbol{u}})$. Similarly, with $\bar{\boldsymbol{w}}_1 = H_{LAD}\boldsymbol{h}_{IRC}(\bar{\boldsymbol{u}}_1)$, $N|_{\bar{\boldsymbol{u}}_1}$ is given by

$$N(\boldsymbol{u} + \bar{\boldsymbol{u}}_1) - N\bar{\boldsymbol{u}}_1 = H_{RB}|_{\bar{\boldsymbol{\tau}}_1}F_m(\boldsymbol{\Phi}, \dot{\boldsymbol{\Phi}})|_{\bar{\boldsymbol{w}}_1}H_{LAD}\boldsymbol{h}_{IRC}|_{\bar{\boldsymbol{u}}_1}\boldsymbol{u}. \tag{3.52}$$

Inserting these in (3.44) and assuming without loss of generality $\|H_{LAD}\| = 1$ gives

$$\begin{aligned} \boldsymbol{\delta}(M, N) &\leq \sup_{\substack{\|\boldsymbol{u}\|\neq 0 \\ \boldsymbol{\Phi} - \bar{\boldsymbol{\Phi}}, \dot{\boldsymbol{\Phi}} - \dot{\bar{\boldsymbol{\Phi}}} \in \mathscr{L}_2^p}} \frac{\|(H_{RB}|_{\bar{\boldsymbol{\tau}}_1}F_m(\boldsymbol{\Phi}, \dot{\boldsymbol{\Phi}})|_{\bar{\boldsymbol{w}}_1}H_{LAD}\tilde{\boldsymbol{h}}_{IRC}|_{\bar{\boldsymbol{u}}_1} - H_{RB}|_{\bar{\boldsymbol{\tau}}}F_m(\boldsymbol{\Phi}, \dot{\boldsymbol{\Phi}})|_{\bar{\boldsymbol{w}}}H_{LAD}\boldsymbol{h}_{IRC}|_{\bar{\boldsymbol{u}}})\boldsymbol{u}\|}{\|\boldsymbol{u}\|} \\ &\leq \sup_{\substack{\|\boldsymbol{u}\|\neq 0 \\ \boldsymbol{\Phi} - \bar{\boldsymbol{\Phi}}, \dot{\boldsymbol{\Phi}} - \dot{\bar{\boldsymbol{\Phi}}} \in \mathscr{L}_2^p}} \frac{\|(H_{RB}|_{\bar{\boldsymbol{\tau}}_1}F_m(\boldsymbol{\Phi}, \dot{\boldsymbol{\Phi}})|_{\bar{\boldsymbol{w}}_1} - H_{RB}|_{\bar{\boldsymbol{\tau}}}F_m(\boldsymbol{\Phi}, \dot{\boldsymbol{\Phi}})|_{\bar{\boldsymbol{w}}})\boldsymbol{u}\|}{\|\boldsymbol{u}\|} \sup_{\|\boldsymbol{u}\|\neq 0} \frac{\|\boldsymbol{h}_{IRC}|_{\bar{\boldsymbol{u}}}\boldsymbol{u}\|}{\|\boldsymbol{u}\|} \\ &\quad + \sup_{\|\boldsymbol{u}\|\neq 0} \frac{\|(\tilde{\boldsymbol{h}}_{IRC}|_{\bar{\boldsymbol{u}}_1} - \boldsymbol{h}_{IRC}|_{\bar{\boldsymbol{u}}})\boldsymbol{u}\|}{\|\boldsymbol{u}\|} \sup_{\substack{\|\boldsymbol{u}\|\neq 0 \\ \boldsymbol{\Phi} - \bar{\boldsymbol{\Phi}}_1, \dot{\boldsymbol{\Phi}} - \dot{\bar{\boldsymbol{\Phi}}}_1 \in \mathscr{L}_2^p}} \frac{\|H_{RB}|_{\bar{\boldsymbol{\tau}}_1}F_m(\boldsymbol{\Phi}, \dot{\boldsymbol{\Phi}})|_{\bar{\boldsymbol{w}}_1}\boldsymbol{u}\|}{\|\boldsymbol{u}\|}. \end{aligned} \tag{3.53}$$

The decoupled form of $\boldsymbol{h}_{IRC}$ means that $\delta(M,N) \leq \Delta_{IRC}\|H_{RB}F_m|_{\bar{\boldsymbol{w}}_1}\| + \|H_{RB}F_m|_{\bar{\boldsymbol{w}}_1} - H_{RB}F_m|_{\bar{\boldsymbol{w}}}\|\|\boldsymbol{h}_{IRC}|_{\boldsymbol{u}}\|$ and it follows that

$$\Delta_{IRC}\|H_{RB}F_m|_{\bar{\boldsymbol{w}}_1}\| + \|H_{RB}F_m|_{\bar{\boldsymbol{w}}_1} - H_{RB}F_m|_{\bar{\boldsymbol{w}}}\|\|\boldsymbol{h}_{IRC}|_{\boldsymbol{u}}\| < b_{M//K}^{-1} \tag{3.54}$$

guarantees (3.46) is met which can be rearranged to give (3.48). □

Proposition 3.3 provides a condition for robust stability in a realistic situation that is highly relevant to rehabilitation. More generally it illustrates how Theorem 3.3 and gap bound (3.44) can be applied to yield stability conditions given assumptions on where the model uncertainty lies. For example, by inserting the full structure of controller K and plant M dynamics, explicit stability conditions can also be obtained for any parameter appearing in the plant description (2.6) that is subject to uncertainty. This is performed for the case of input-output linearization in [19]. The gain bound (3.50) arises by substituting the left-hand side of (3.54) into (3.47) and characterizes the true performance: the lower the right-hand side of (3.50) the closer the output of the true system follows $\bar{\boldsymbol{\Phi}}_1$.

There exist many control approaches to stabilize M. However, often a simple scheme is most appropriate if plant knowledge is limited and tuning heuristic. The next proposition gives a stability condition when only a local linear model of the dynamics $M : \boldsymbol{u} \mapsto \boldsymbol{\Phi}$ is available and is used to design feedback controller K.

Proposition 3.4 *Let N satisfy Proposition 3.2. Suppose linear approximations to the dynamics H_{RB}, tendon function F_m and muscle curve $\boldsymbol{h}_{IRC}$, given by $\overline{H_{RB}F_m}$ and $\bar{\boldsymbol{h}}_{IRC}$ respectively, are used to construct the stable nominal model $M = \overline{H_{RB}F}_m H_{LAD}\bar{\boldsymbol{h}}_{IRC}$, and then used to design K satisfying (3.45). Then the true system $[N,K]$ has a robust stability margin, and in particular is stable if*

$$\Delta_{IRC} < \frac{b_{M//K}^{-1} - \Delta_{RB}\|\bar{\boldsymbol{h}}_{IRC}\|}{\|H_{RB}F_m|_{\bar{\boldsymbol{w}}_1}\|} \quad or \quad \Delta_{IRC} < \frac{b_{M//K}^{-1} - \Delta_{RB}\|\boldsymbol{h}_{IRC}|_{\bar{\boldsymbol{u}}_1}\|}{\|\overline{H_{RB}F_m}\|} \tag{3.55}$$

where the muscle uncertainty and deviation from linearized dynamics are respectively characterized by

$$\Delta_{IRC} = \max_i \sup_{\|\boldsymbol{u}\|\neq 0} \frac{\|(\tilde{\boldsymbol{h}}_{IRC,i}|_{\bar{\boldsymbol{u}}_{1,i}} - \bar{\boldsymbol{h}}_{IRC,i})\boldsymbol{u}\|}{\|\boldsymbol{u}\|}, \quad \Delta_{RB} = \|H_{RB}F_m|_{\bar{\boldsymbol{w}}_1} - \overline{H_{RB}F_m}\|.$$

Proof This follows by inserting the form $M = \overline{H_{RB}F}_m H_{LAD}\bar{\boldsymbol{h}}_{IRC}$ into (3.53) and into the analogous expression

$$\delta(M,N) \leq \sup_{\substack{\|\boldsymbol{u}\|\neq 0 \\ \boldsymbol{\Phi},\dot{\boldsymbol{\Phi}}\in\mathscr{L}_2^p}} \frac{\|(H_{RB}|_{\bar{\boldsymbol{\tau}}_1} F_m(\boldsymbol{\Phi},\dot{\boldsymbol{\Phi}})|_{\bar{\boldsymbol{w}}_1} - H_{RB}|_{\bar{\boldsymbol{\tau}}} F_m(\boldsymbol{\Phi},\dot{\boldsymbol{\Phi}})|_{\bar{\boldsymbol{w}}})\boldsymbol{u}\|}{\|\boldsymbol{u}\|} \sup_{\|\boldsymbol{u}\|\neq 0} \frac{\|\boldsymbol{h}_{IRC}|_{\bar{\boldsymbol{u}}_1}\boldsymbol{u}\|}{\|\boldsymbol{u}\|}$$
$$+ \sup_{\|\boldsymbol{u}\|\neq 0} \frac{\|(\tilde{\boldsymbol{h}}_{IRC}|_{\bar{\boldsymbol{u}}_1} - \boldsymbol{h}_{IRC}|_{\bar{\boldsymbol{u}}})\boldsymbol{u}\|}{\|\boldsymbol{u}\|} \sup_{\substack{\|\boldsymbol{u}\|\neq 0 \\ \boldsymbol{\Phi},\dot{\boldsymbol{\Phi}}\in\mathscr{L}_2^p}} \frac{\|H_{RB}|_{\bar{\boldsymbol{\tau}}} F_m(\boldsymbol{\Phi},\dot{\boldsymbol{\Phi}})|_{\bar{\boldsymbol{w}}}\boldsymbol{u}\|}{\|\boldsymbol{u}\|}$$

□

Proposition 3.4 addresses the important case where a linear model is used for design, and provides transparent, intuitive bounds on the model inaccuracy that can be tolerated to maintain stability of the true closed-loop system. The amount of modeling inaccuracy that can be accommodated can, in principle, be made arbitrarily large by tuning feedback controller K for increased robustness rather than performance.

As well as yielding explicit robust performance bounds, the framework presented in this section directly leads to the following guidelines for feedback control design.

Procedure 2 (Design guidelines for robust stability)

Minimise $b_{M//K}$: Design feedback controller to minimize $b_{M//K}$ via (3.45). Alternatively design several feedback controllers and switch to one with a smaller $b_{M//K}$ between task attempts if the system shows signs of instability.
Reduce modeling uncertainty: This directly reduces the mismatch $\delta(M,N)$, but requires more identification tests, and cannot in practice characterize unpredictable time-varying dynamic effects such as spasticity.
Choose an appropriate linearization point: If designing K based on a linearized description of dynamics M, Δ_{RB} is minimized if the operating point corresponds to that of the true plant (i.e. $\bar{\boldsymbol{w}}_1$).
Reduce norm of H_{RB}, $F_m(\boldsymbol{\Phi},\dot{\boldsymbol{\Phi}})$, H_{LAD}, $\boldsymbol{h}_{IRC}$ **components**: These norms multiple uncertainty terms and can be reduced by, e.g. reducing stimulation levels, changing mechanical structure and applying passive/active support.

Reducing $b_{M//K}$ increases robustness but inevitably reduces tracking performance which degrades rehabilitation outcomes. This can be addressed by adding a feedforward control signal, and is the subject of the next chapter.

3.4 Case Study: Proportional-Integral-Derivative Controller

To illustrate how the previous results can be applied, we now design a feedback controller K using a linearized model of the upper arm system. To provide such a model, we take the clinically relevant system that was identified in Sect. 2.2.5, and linearize it about the set-point $\phi_2 = \frac{\pi}{4}$, $\phi_5 = \frac{\pi}{2}$. This produces the plant model (where we have restricted attention to the controlled joints, and then applied model reduction):

$$\begin{bmatrix} \frac{-0.00178s^5+0.0349s^4-0.361s^3+2.72s^2-2.11s}{s^5+2.51s^4-1.17s^3-2.87s^2-1.76s+2.55} & \frac{0.0015s^3-0.00871s^2+0.0798s}{s^3+233s^2-407s+177} \\ \frac{-0.00967s^3+0.0357s^2-0.0433s}{s^3+4.40s^2-9.91s+4.63} & \frac{-0.00293s^5+0.0577s^4-0.602s^3+4.56s^2-3.55s}{s^5+2.56s^4-1.02s^3-3.3s^2-1.51s+2.52} \end{bmatrix}. \tag{3.56}$$

Note that the strongly diagonal form reflects that the joint angles were chosen to align with stimulated muscles in order that F_m and H_{RB} are diagonalized, reducing Δ_{RB}.

We then use (3.56) to design a proportional-integral-differential (PID) controller. This controller corresponds to structure (3.2) with the terms

$$\begin{aligned} \boldsymbol{f}_c(\boldsymbol{x}_c(t), \boldsymbol{e}(t)) &= \operatorname{diag}\left\{ \begin{bmatrix} -\frac{1}{c} & 0 \\ 1 & 0 \end{bmatrix}, \begin{bmatrix} -\frac{1}{c} & 0 \\ 1 & 0 \end{bmatrix} \right\} \boldsymbol{x}_c(t) + \operatorname{diag}\left\{ \begin{bmatrix} 1 \\ 0 \end{bmatrix}, \begin{bmatrix} 1 \\ 0 \end{bmatrix} \right\} \boldsymbol{e}(t), \\ \boldsymbol{h}_c(\boldsymbol{x}_c(t), \boldsymbol{e}(t)) &= \operatorname{diag}\left\{ \begin{bmatrix} \left(k_{i1} - \frac{k_{d1}}{c^2}\right) & \frac{k_{i1}}{c} \end{bmatrix}, \begin{bmatrix} \left(k_{i2} - \frac{k_{d2}}{c^2}\right) & \frac{k_{i2}}{c} \end{bmatrix} \right\} \boldsymbol{x}_c(t) \\ &\quad + \operatorname{diag}\left\{ \left(k_{p1} + \frac{k_{d1}}{c}\right), \left(k_{p2} + \frac{k_{d2}}{c}\right) \right\} \boldsymbol{e}(t) \end{aligned}$$

where $k_{p1}, k_{p2}, k_{d1}, k_{d2}, k_{i1}$, and k_{i2} are controller gains, and c is a small positive scalar. We first choose gains $K_{p1} = 28.8$, $K_{p2} = 19.2$, $K_{i1} = 48.4$, $K_{i2} = 28.4$, $K_{d1} = 0.24$ and $K_{d2} = 0.16$ in order to achieve a response time of 2 s. This gives rise to a value of $b_{M//K} = 1.72$. When K is applied to the true upper arm dynamics N, the resultant closed loop system $[N, K]$ is therefore stable if

$$\delta(M, N) < 0.58. \tag{3.57}$$

This constrains the true plant to a 'ball' in the uncertainty space with radius 0.58, centred on M.

Next these gains are modified to achieve a response time of 1 s by setting $K_{p1} = 6.2$, $K_{p2} = 3.6$, $K_{i1} = 119$, $K_{i2} = 71.2$ and $K_{d1} = K_{d2} = 0.04$. This gives rise to a value of $b_{M//K} = 2.25$. When K is applied to the true upper arm dynamics N, stability condition (3.57) is replaced by

$$\delta(M, N) < 0.44.$$

The ball in which the true plant must belong has therefore shrunk and now has a radius of only 0.44. This illustrates the compromise between performance and robust stability. The PID control structure is tested experimentally in Sect. 4.3.

3.5 Conclusions

This chapter has developed a framework for the design of a feedback controller K to assist reference tracking using ES. The focus has been on stabilizing all joints in the mechanically supported anthropomorphic system, including those which may not be involved in the prescribed tracking task. By applying mild conditions on the

system, robust performance tools have then been employed to derive conditions for the true plant, N, to be stabilized. These conditions also quantify the performance of the closed-loop system $[N, K]$ as a function of the distance that the true plant is from the nominal model, M, used for design (as measured by the gap metric $\delta(M, N)$).

The next chapter focuses on how tracking performance can be further improved by exploiting the inherently repetitive nature of rehabilitation.

References

1. R. Davoodi, M. Hauschild, J. Lee, P.T. Montazemi, G.E. Loeb, Biomimetic control of FES reaching, in *First International Conference on Neural Interface and Control*, May (2005), pp. 177–181
2. R. Li, X.L. Hu, K.Y. Tong, Combined electromyography (EMG)-driven system with functional electrical stimulation (FES) for poststroke rehabilitation, in *Proceedings of the 2nd Biennial IEEE/RAS-EMBS International Conference on Biomedical Robotics and Biomechatronics* (2008)
3. S.O. Escobar, J.M. Reta, C.B. Tabernig, Platform for evaluation of control strategies of functional stimulators through the EMG of the same stimulated muscle. IEEE Lat. Am. Trans. **8**(1), 17–22 (2010)
4. G. Pfurtscheller, G.R. Muller-Putz, J. Pfurtscheller, R. Rupp, EEG-based asynchronous BCI controls functional electrical stimulation in a tetraplegic patient. EURASIP J. Appl. Signal Process. **19**, 3152–3155 (2005)
5. F. Meng, K. Tong, S. Chan, W. Wong, K. Lui, K. Tang, X. Gao, S. Gao, BCI-FES training system design and implementation for rehabilitation of stroke patients, in *IJCNN* (2008)
6. J.G. Hincapie, R.F. Kirsch, Feasibility of EMG-based neural network controller for an upper extremity neuroprosthesis. IEEE Trans. Neural Syst. Rehabil. Eng. **17**(1), 80–90 (2009)
7. J.P. Giuffrida, P.E. Crago, Functional restoration of elbow extension after spinal-cord injury using a neural network-based synergistic FES controller. IEEE Trans. Neural Syst. Rehabil. Eng. **13**(2), 147–152 (2005)
8. J.G. Hincapie, D. Blana, E.K. Chadwick, R.F. Kirsch, Musculoskeletal model-guided, customizable selection of shoulder and elbow muscles for a C5 SCI neuroprosthesis. Trans. Neural Syst. Rehabil. Eng. **16**(3), 255–263 (2008)
9. N. Sharma, C.M. Gregory, M. Johnson, W.E. Dixon, Closed-loop neural network-based NMES control for human limb tracking. Trans. Control Syst. Technol. **20**(3), 712–725 (2012)
10. Q. Wang, N. Sharma, M. Johnson, C.M. Gregory, W.E. Dixon, Adaptive inverse optimal neuromuscular electrical stimulation. Trans. Control Syst. Technol. **43**(6), 1710–1718 (2013)
11. P.J. Olver, Applied mathematics lecture notes. Technical report (2012)
12. A. Isidori, *Nonlinear Control Systems*, 2nd edn. (Springer, New York, 1989)
13. D.W. Jordan, P. Smith, *Nonlinear Ordinary Differential Equations, An Introduction to Dynamical Systems* (Oxford University Press, Oxford, 2006)
14. C.L. Lynch, M.R. Popovic, Functional electrical stimulation: closed-loop control of induced muscle contractions. IEEE Control Syst. Mag. **28**(2), 40–50 (2008)
15. C.T. Freeman, E. Rogers, A.M. Hughes, J.H. Burridge, K.L. Meadmore, Iterative learning control in healthcare: electrical stimulation and robotic-assisted upper limb stroke rehabilitation. IEEE Control Syst. Mag. **32**(1), 18–43 (2012)
16. F. Le, I. Markovsky, C.T. Freeman, E. Rogers, Identification of electrically stimulated muscle models of stroke patients. Control Eng. Pract. **18**(4), 396–407 (2010)
17. J. Lin, P.P. Varaiya, Bounded-input bounded-output stability of nonlinear time-varying discrete control systems. IEEE Trans. Autom. Control **12**(4), 423–427 (1967)

18. T.T. Georgiou, M.C. Smith, Robustness analysis of nonlinear feedback systems: an input-output approach. IEEE Trans. Autom. Control **42**(9), 1200–1221 (1997)
19. A. Al-Gburi, M. French, C.T. Freeman, Robustness analysis of nonlinear systems with feedback linearizing control, in *52nd IEEE Conference on Decision and Control* (2013), pp. 3055–3060

Chapter 4
Iterative Learning Control Design

Having developed tools to design robust feedback controllers that deliver guaranteed performance bounds in the presence of model uncertainty and external disturbance, we now augment the control structure to further improve tracking accuracy. To do this we exploit the inherently repetitive nature of the rehabilitation process, which involves neurologically impaired participants repeatedly performing tracking movements with their affected arm, with a rest period in between attempts during which their arm is returned to the starting position. We will use the data collected over previous task attempts to adjust the control action in order to compensate for tracking error on the subsequent task attempt.

The framework we employ is called iterative learning control (ILC), and has been used for three decades primarily for the control of industrial robots performing repeated tasks. The ILC paradigm addresses tracking of a fixed reference trajectory over a finite time interval of length T seconds. Each attempt is termed a 'trial', and the system is reset between trials to the same starting position. The tracking error is recorded during each trial, and in the reset period between trials it is used to update the control signal with the aim of reducing the error during the subsequent trial. There are a great number of methods available to compute this update, and an overview is available in [1, 2].

ILC has been successfully used by several groups to assist lower limb motion using ES, see for example [3–6]. Feasibility of using ILC for upper limb stroke rehabilitation was first established in [7] where ES was applied to the triceps muscle to assist impaired participants' completion of a reaching task. In particular, each participant's hand was strapped to a robot end-effector and they attempted to follow a target moving along an illuminated elliptical track. Each participant attempted this task six times, and between attempts the ILC algorithm updated the stimulation to be applied on the next attempt using a dynamic model of the arm [8, 9]. High levels of tracking accuracy were achieved by ILC [9, 10], which translated into statistically significant results across a range of outcome measures when used in clinical trials

C. Freeman, *Control System Design for Electrical Stimulation in Upper Limb Rehabilitation*, DOI 10.1007/978-3-319-25706-8_4

with stroke participants spanning 18–25 treatment sessions [7, 11, 12]. The models and controllers used in these feasibility studies all fit within the framework developed in this book.

4.1 General ILC Framework

Chapter 3 considered the design of feedback controller $K : \boldsymbol{e} \mapsto \boldsymbol{u}$ to stabilise the system shown in Fig. 3.1 and achieve some level of tracking performance for the controlled joints, $\boldsymbol{\Phi}_{\mathscr{P}}$. The resulting closed-loop system $[M, K]$ is represented by

$$
\begin{aligned}
G :& \mathscr{L}_2^p[0,T] \to \mathscr{L}_2^p[0,T] : \hat{\boldsymbol{\Phi}} \mapsto \boldsymbol{\Phi} \\
: & \begin{cases} \underbrace{\begin{bmatrix} \dot{\boldsymbol{x}}_s(t) \\ \dot{\boldsymbol{x}}_c(t) \end{bmatrix}}_{\dot{\boldsymbol{x}}(t)} = \underbrace{\begin{bmatrix} \boldsymbol{f}_s(\boldsymbol{x}_s(t)) + \boldsymbol{g}_s(\boldsymbol{h}_c(\boldsymbol{x}_c(t), \hat{\boldsymbol{\Phi}}(t) - \boldsymbol{h}_s(\boldsymbol{x}_s(t)))) \\ \boldsymbol{f}_c(\boldsymbol{x}_c(t), \hat{\boldsymbol{\Phi}}(t) - \boldsymbol{h}_s(\boldsymbol{x}_s(t))) \end{bmatrix}}_{\boldsymbol{f}(\boldsymbol{x}(t), \hat{\boldsymbol{\Phi}}(t))} \\ \boldsymbol{\Phi}(t) = \underbrace{\boldsymbol{h}_s(\boldsymbol{x}_s(t))}_{\boldsymbol{h}(\boldsymbol{x}(t))}, \end{cases} \qquad t \in [0,T].
\end{aligned}
\tag{4.1}
$$

where T is the task duration. The tracking error of the controlled joints is measured using $\boldsymbol{e}_{\mathscr{P}}$, which can be written in terms of G as $\boldsymbol{e}_{\mathscr{P}} = \hat{\boldsymbol{\Phi}}_{\mathscr{P}} - G_{\mathscr{P}}\hat{\boldsymbol{\Phi}}$. Here $\hat{\boldsymbol{\Phi}}_{\mathscr{P}}$ is the reference trajectory, and the following notation extracts the output associated with the controlled joints from operator G:

Lemma 4.1 *The relationship between the reference and controlled joints is defined by the map*

$$
G_{\mathscr{P}} : \mathscr{L}_2^p[0,T] \to \mathscr{L}_2^{n_p}[0,T] : \hat{\boldsymbol{\Phi}} \mapsto \boldsymbol{\Phi}_{\mathscr{P}} \tag{4.2}
$$

with components

$$
G_{\mathscr{P}}\hat{\boldsymbol{\Phi}} = (G\hat{\boldsymbol{\Phi}})_{\mathscr{P}} = \begin{bmatrix} (G\hat{\boldsymbol{\Phi}})_{\mathscr{P}(1)} \\ \vdots \\ (G\hat{\boldsymbol{\Phi}})_{\mathscr{P}(n_p)} \end{bmatrix}, \quad (G\hat{\boldsymbol{\Phi}})_{\mathscr{P}(i)} : \mathscr{L}_2^p[0,T] \to \mathscr{L}_2[0,T] : \hat{\boldsymbol{\Phi}} \mapsto \phi_{\mathscr{P}(i)}
$$

and since $\boldsymbol{f}(\cdot)$, $\boldsymbol{h}(\cdot)$ are continuous, $G_{\mathscr{P}}$ is unique and continuous [13].

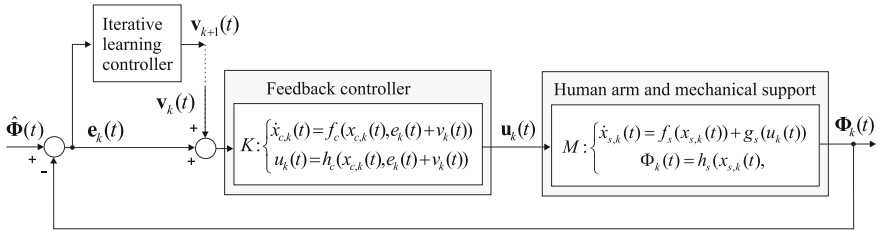

Fig. 4.1 ILC scheme added to feedback structure $[M, K]$

We now add a feedforward signal $\boldsymbol{v}$ to the previous control scheme, producing the structure shown in Fig. 4.1. Here subscript $k = 1, 2, \ldots$ denotes the trial number. Signals $\boldsymbol{v}_k \in \mathscr{L}_2^p[0, T]$ and $\boldsymbol{\Phi}_k \in \mathscr{L}_2^p[0, T]$ are the ILC input and joint angle outputs respectively on the kth trial, and the tracking error on trial k is $\boldsymbol{e}_k = \hat{\boldsymbol{\Phi}} - \boldsymbol{\Phi}_k \in \mathscr{L}_2^p[0, T]$. Note that the analysis which follows can equally be applied to the case where the ILC input is placed between the feedback controller K and the stimulated arm system M, and yields similar results.

The ILC problem is to ultimately generate a feedforward signal $\boldsymbol{v}_\infty$ which minimizes the norm of the controlled joint tracking error. This can be stated as:

$$\boldsymbol{v}_\infty := \min_{\boldsymbol{v}} J(\boldsymbol{v}), \quad J(\boldsymbol{v}) = \Big\| \underbrace{\hat{\boldsymbol{\Phi}}_{\mathscr{P}} - G_{\mathscr{P}}(\hat{\boldsymbol{\Phi}} + \boldsymbol{v})}_{\boldsymbol{e}_{\mathscr{P}}} \Big\|^2. \tag{4.3}$$

In the ILC framework this problem is solved using iterative optimization methods which employ experimental data to embed robustness against model uncertainty. When the system $G_{\mathscr{P}}$ is nonlinear, this can be accomplished using successive linear approximation of the system dynamics, as stated in the following theorem:

Theorem 4.1 *Consider the ILC update sequence*

$$\boldsymbol{v}_{k+1} = \boldsymbol{v}_k + L_k(\boldsymbol{e}_k)_{\mathscr{P}}, \quad k = 0, 1, \ldots \tag{4.4}$$

If learning operator $L_k : \mathscr{L}_2^{n_p}[0, T] \to \mathscr{L}_2^p[0, T]$ *is designed to satisfy*

$$\left\| I - \bar{G}_{\mathscr{P}}|_{\hat{\boldsymbol{\Phi}} + \boldsymbol{v}_\infty} L_k \right\| < 1 \quad \forall\, k \tag{4.5}$$

where the operator norm is induced from the inner product $\langle \cdot, \cdot \rangle$*, then*

$$\lim_{k \to \infty} (\boldsymbol{e}_k)_{\mathscr{P}} = \mathbf{0} \tag{4.6}$$

and, for $\boldsymbol{v}_0$ chosen sufficiently close to $\boldsymbol{v}_\infty$, the ILC update converges to

$$\lim_{k\to\infty}(\hat{\boldsymbol{\Phi}}+\boldsymbol{v}_k) = L_\infty(\bar{G}_{\mathscr{P}}|_{\hat{\boldsymbol{\Phi}}+\boldsymbol{v}_\infty}L_\infty)^{-1}\hat{\boldsymbol{\Phi}}_{\mathscr{P}}. \tag{4.7}$$

Alternatively, if the learning operator L_k is chosen to satisfy

$$\|I - L_k\bar{G}_{\mathscr{P}}|_{\hat{\boldsymbol{\Phi}}+\boldsymbol{v}_\infty}\| < 1 \quad \forall\, k \tag{4.8}$$

then, for $\boldsymbol{v}_0$ chosen sufficiently close to $\boldsymbol{v}_\infty$, the ILC update converges to

$$\lim_{k\to\infty}(\hat{\boldsymbol{\Phi}}+\boldsymbol{v}_k) = (L_\infty\bar{G}_{\mathscr{P}}|_{\hat{\boldsymbol{\Phi}}+\boldsymbol{v}_\infty})^{-1}L_\infty\hat{\boldsymbol{\Phi}}_{\mathscr{P}}. \tag{4.9}$$

Proof This result follows from application of conditions in [14] for solving the nonlinear equation $\hat{\boldsymbol{\Phi}}_{\mathscr{P}} - G_{\mathscr{P}}(\hat{\boldsymbol{\Phi}}+\boldsymbol{v}) = \boldsymbol{0}$ using iterative minimization. In particular, on each iteration the error dynamics locally satisfy

$$(\boldsymbol{e}_{k+1})_{\mathscr{P}} = \big(I - \bar{G}_{\mathscr{P}}|_{\hat{\boldsymbol{\Phi}}+\boldsymbol{v}_k}L_k\big)(\boldsymbol{e}_k)_{\mathscr{P}} \tag{4.10}$$

so that, if (4.5) holds, the error converges monotonically to zero since

$$\|(\boldsymbol{e}_{k+1})_{\mathscr{P}}\| \le \|I - \bar{G}_{\mathscr{P}}|_{\hat{\boldsymbol{\Phi}}+\boldsymbol{v}_k}L_k\|\|(\boldsymbol{e}_k)_{\mathscr{P}}\| < \|(\boldsymbol{e}_k)_{\mathscr{P}}\| \quad \forall\, k.$$

If $\boldsymbol{v}_0$ is sufficiently close to $\boldsymbol{v}_\infty$, then $\bar{G}_{\mathscr{P}}|_{\hat{\boldsymbol{\Phi}}+\boldsymbol{v}_k} = \bar{G}_{\mathscr{P}}|_{\hat{\boldsymbol{\Phi}}+\boldsymbol{v}_\infty}$ and $L_k = L_\infty\ \forall\, k$, so that

$$(\boldsymbol{e}_i)_{\mathscr{P}} = \prod_{j=0}^{i}\big(I - \bar{G}_{\mathscr{P}}|_{\hat{\boldsymbol{\Phi}}+\bar{\boldsymbol{v}}_j}L_j\big)(\boldsymbol{e}_0)_{\mathscr{P}} = \big(I - \bar{G}_{\mathscr{P}}|_{\hat{\boldsymbol{\Phi}}+\boldsymbol{v}_\infty}L_\infty\big)^i(\boldsymbol{e}_0)_{\mathscr{P}} \tag{4.11}$$

yielding the input expression

$$\begin{aligned}\boldsymbol{v}_{k+1} &= \boldsymbol{v}_0 + L_\infty\sum_{i=0}^{k}(\boldsymbol{e}_i)_{\mathscr{P}} = \boldsymbol{v}_0 + L_\infty\sum_{i=0}^{k}\big(I - \bar{G}_{\mathscr{P}}|_{\hat{\boldsymbol{\Phi}}+\boldsymbol{v}_\infty}L_\infty\big)^i(\boldsymbol{e}_0)_{\mathscr{P}}\\ &= \boldsymbol{v}_0 + L_\infty\sum_{i=0}^{k}(\boldsymbol{e}_i)_{\mathscr{P}} = \boldsymbol{v}_0 + L_\infty\sum_{i=0}^{k}\big(I - \bar{G}_{\mathscr{P}}|_{\hat{\boldsymbol{\Phi}}+\boldsymbol{v}_\infty}L_\infty\big)^i\\ &\quad\times\big(\hat{\boldsymbol{\Phi}}_{\mathscr{P}} - \bar{G}_{\mathscr{P}}|_{\hat{\boldsymbol{\Phi}}+\boldsymbol{v}_\infty}(\hat{\boldsymbol{\Phi}}+\boldsymbol{v}_0)\big).\end{aligned} \tag{4.12}$$

Since we have assumed that (4.5) holds, we have the limit

$$\lim_{k\to\infty} \boldsymbol{v}_k = \boldsymbol{v}_0 + L_\infty\big(I - \big(I - \bar{G}_{\mathscr{P}}|_{\hat{\boldsymbol{\Phi}}+\boldsymbol{v}_\infty} L_\infty\big)\big)^{-1}\big(\hat{\boldsymbol{\Phi}}_{\mathscr{P}} - \bar{G}_{\mathscr{P}}|_{\hat{\boldsymbol{\Phi}}+\boldsymbol{v}_\infty}(\hat{\boldsymbol{\Phi}} + \boldsymbol{v}_0)\big) \tag{4.13}$$

$$= L_\infty\big(\bar{G}_{\mathscr{P}}|_{\hat{\boldsymbol{\Phi}}+\boldsymbol{v}_\infty} L_\infty\big)^{-1}\hat{\boldsymbol{\Phi}}_{\mathscr{P}} - \hat{\boldsymbol{\Phi}}.$$

Under the same assumption, we also note that the direct input update sequence is

$$\begin{aligned}\boldsymbol{v}_{k+1} &= \boldsymbol{v}_k + L_\infty\big(\hat{\boldsymbol{\Phi}}_{\mathscr{P}} - \bar{G}_{\mathscr{P}}|_{\hat{\boldsymbol{\Phi}}+\boldsymbol{v}_\infty}(\hat{\boldsymbol{\Phi}} + \boldsymbol{v}_k)\big)\\ &= \big(I - L_\infty \bar{G}_{\mathscr{P}}|_{\hat{\boldsymbol{\Phi}}+\boldsymbol{v}_\infty}\big)\boldsymbol{v}_k + L_\infty\big(\hat{\boldsymbol{\Phi}}_{\mathscr{P}} - \bar{G}_{\mathscr{P}}|_{\hat{\boldsymbol{\Phi}}+\boldsymbol{v}_\infty}\hat{\boldsymbol{\Phi}}\big)\\ &= \big(I - L_\infty \bar{G}_{\mathscr{P}}|_{\hat{\boldsymbol{\Phi}}+\boldsymbol{v}_\infty}\big)^k \boldsymbol{v}_0 + \sum_{i=0}^{k}\big(I - L_\infty \bar{G}_{\mathscr{P}}|_{\hat{\boldsymbol{\Phi}}+\boldsymbol{v}_\infty}\big)^i L_\infty\big(\hat{\boldsymbol{\Phi}}_{\mathscr{P}} - \bar{G}_{\mathscr{P}}|_{\hat{\boldsymbol{\Phi}}+\boldsymbol{v}_\infty}\hat{\boldsymbol{\Phi}}\big)\end{aligned} \tag{4.14}$$

and if (4.8) holds we obtain the limiting input

$$\begin{aligned}\boldsymbol{v}_\infty &= \big(I - \big(I - L_\infty \bar{G}_{\mathscr{P}}|_{\hat{\boldsymbol{\Phi}}+\boldsymbol{v}_\infty}\big)\big)^{-1} L_\infty\big(\hat{\boldsymbol{\Phi}}_{\mathscr{P}} - \bar{G}_{\mathscr{P}}|_{\hat{\boldsymbol{\Phi}}+\boldsymbol{v}_\infty}\hat{\boldsymbol{\Phi}}\big)\\ &= \big(L_\infty \bar{G}_{\mathscr{P}}|_{\hat{\boldsymbol{\Phi}}+\boldsymbol{v}_\infty}\big)^{-1} L_\infty\big(\hat{\boldsymbol{\Phi}}_{\mathscr{P}} - \bar{G}_{\mathscr{P}}|_{\hat{\boldsymbol{\Phi}}+\boldsymbol{v}_\infty}\hat{\boldsymbol{\Phi}}\big) = \big(L_\infty \bar{G}_{\mathscr{P}}|_{\hat{\boldsymbol{\Phi}}+\boldsymbol{v}_\infty}\big)^{-1} L_\infty \hat{\boldsymbol{\Phi}}_{\mathscr{P}} - \hat{\boldsymbol{\Phi}}.\end{aligned}$$

Setting $\boldsymbol{v}_0 = \boldsymbol{0}$ in (4.12) and (4.14) we can also conclude

$$L_\infty \sum_{i=0}^{k}\big(I - \bar{G}_{\mathscr{P}}|_{\hat{\boldsymbol{\Phi}}+\boldsymbol{v}_\infty} L_\infty\big)^i = \sum_{i=0}^{k}\big(I - L_\infty \bar{G}_{\mathscr{P}}|_{\hat{\boldsymbol{\Phi}}+\boldsymbol{v}_\infty}\big)^i L_\infty \quad \forall\, k. \tag{4.15}$$

□

Here $\bar{G}_{\mathscr{P}}|_{\bar{\boldsymbol{v}}} : \mathscr{L}_2^p[0,T] \to \mathscr{L}_2^{n_p}[0,T]$ denotes the system obtained by linearizing $G_{\mathscr{P}}$ about operating point $\bar{\boldsymbol{v}}$, and can be computed using the following result.

Lemma 4.2 *Around operating point $\bar{\boldsymbol{v}}$, dynamics $\boldsymbol{\Phi}_{\mathscr{P}} = G_{\mathscr{P}}\boldsymbol{v}$ are represented by linear time-varying (LTV) state-space system $\tilde{\boldsymbol{\Phi}}_{\mathscr{P}} = \bar{G}|_{\bar{\boldsymbol{v}}}\tilde{\boldsymbol{v}}$, where*

$$\begin{aligned}\dot{\tilde{\boldsymbol{x}}}(t) &= A(t)\tilde{\boldsymbol{x}}(t) + B(t)\tilde{\boldsymbol{v}}(t)\\ \tilde{\boldsymbol{\Phi}}_{\mathscr{P}}(t) &= C(t)\tilde{\boldsymbol{x}}(t), \qquad\qquad \tilde{\boldsymbol{x}}(0) = \bar{\boldsymbol{x}}(0), \quad t \in [0,T]\end{aligned} \tag{4.16}$$

with

$$\begin{aligned}A(t) &= \left(\frac{\partial}{\partial \boldsymbol{x}}\boldsymbol{f}\left(\boldsymbol{x}(t), \boldsymbol{v}(t)\right)\right)_{\bar{\boldsymbol{x}}(t),\bar{\boldsymbol{v}}(t)}, \quad B(t) = \left(\frac{\partial}{\partial \boldsymbol{v}}\boldsymbol{f}\left(\boldsymbol{x}(t), \boldsymbol{v}(t)\right)\right)_{\bar{\boldsymbol{x}}(t),\bar{\boldsymbol{v}}(t)}\\ C(t) &= \left(\frac{\mathrm{d}}{\mathrm{d}\boldsymbol{x}}\boldsymbol{h}_{\mathscr{P}}\left(\boldsymbol{x}(t)\right)\right)_{\bar{\boldsymbol{x}}(t)}\end{aligned} \tag{4.17}$$

with corresponding map $\bar{G}|_{\tilde{\boldsymbol{v}}} : \mathscr{L}_2^p[0,T] \to \mathscr{L}_2^{n_p}[0,T] : \tilde{\boldsymbol{v}} \mapsto \tilde{\boldsymbol{\Phi}}_{\mathscr{P}}$ *given by*

$$(\bar{G}|_{\tilde{\boldsymbol{v}}}\tilde{\boldsymbol{v}})(t) = \int_0^t C(t)\Gamma(t,\tau)B(\tau)\tilde{\boldsymbol{v}}(\tau)\mathrm{d}\tau$$

where $\Gamma(t,\tau)$ *is the state transition matrix for system (4.16).*

Depending on the system dynamics and choice of input and output sets, problem (4.3) may have a single or an infinite number of solutions, $\boldsymbol{v}_\infty$. To examine whether perfect tracking is possible, denote the set of achievable joint motions as

$$\mathrm{im}(G_{\mathscr{P}}) := \left\{ \boldsymbol{y} = G_{\mathscr{P}}\boldsymbol{x} \mid \boldsymbol{x} \in \mathscr{L}_2^p[0,T] \right\}. \tag{4.18}$$

We next show how ILC update operator L_k can be chosen to satisfy (4.5) in the case that perfect tracking is possible, or to satisfy (4.8) in the case that it is not.

Theorem 4.2 *Within (4.4) let the ILC operator be given by*

$$L_k = (\bar{G}|_{\hat{\boldsymbol{\Phi}}+\boldsymbol{v}_k})^*\left(I + \bar{G}|_{\hat{\boldsymbol{\Phi}}+\boldsymbol{v}_k}(\bar{G}|_{\hat{\boldsymbol{\Phi}}+\boldsymbol{v}_k})^*\right)^{-1}. \tag{4.19}$$

Setting $\boldsymbol{v}_{k+1} - \boldsymbol{v}_k = \Delta\boldsymbol{v}_k$*, this is equivalent to solving*

$$\Delta\boldsymbol{v}_k := \min_{\Delta\boldsymbol{v}} \left\{ \|\Delta\boldsymbol{v}\|_R^2 + \|(\boldsymbol{e}_k)_{\mathscr{P}} - \bar{G}|_{\hat{\boldsymbol{\Phi}}+\boldsymbol{v}_k}\Delta\boldsymbol{v}\|_Q^2 \right\}, \quad \boldsymbol{v}_0 = \boldsymbol{0}. \tag{4.20}$$

with symmetric positive-definite weights R, Q, and $\|\boldsymbol{x}\|_A^2 = \int_0^T \boldsymbol{x}(t)^\top A\boldsymbol{x}(t)\delta t$*. If* $\hat{\boldsymbol{\Phi}}_{\mathscr{P}} \in \mathrm{im}(G_{\mathscr{P}})$ *this satisfies (4.5) and generates an input sequence satisfying*

$$\lim_{k\to\infty} \boldsymbol{v}_k = \boldsymbol{v}_\infty, \quad \boldsymbol{v}_\infty := \min_{\boldsymbol{v}} \|\boldsymbol{v}\|^2 \ \ s.\,t. \ \ \boldsymbol{e}_{\mathscr{P}} = \hat{\boldsymbol{\Phi}} - G_{\mathscr{P}}(\hat{\boldsymbol{\Phi}} + \boldsymbol{v}) = \boldsymbol{0}. \tag{4.21}$$

If $\hat{\boldsymbol{\Phi}}_{\mathscr{P}} \notin \mathrm{im}(G_{\mathscr{P}})$ *this satisfies (4.8) and generates an input sequence satisfying*

$$\lim_{k\to\infty} \boldsymbol{v}_k = \boldsymbol{v}_\infty, \quad \boldsymbol{v}_\infty := \min_{\boldsymbol{v}} \left\|\boldsymbol{e}_{\mathscr{P}}\right\|^2. \tag{4.22}$$

Proof A necessary condition for local error convergence on trial k is that $\exists\ \sigma > 0$ satisfying $\langle \boldsymbol{e}, \bar{G}|_{\hat{\boldsymbol{\Phi}}+\boldsymbol{v}_k}(\bar{G}|_{\hat{\boldsymbol{\Phi}}+\boldsymbol{v}_k})^*\boldsymbol{e}\rangle \geq \sigma^2\|\boldsymbol{e}\|^2, \forall\ \boldsymbol{e}$. If $\sigma > 0$ the solution to (4.20) is then $\Delta\boldsymbol{v}_k = L_k(\boldsymbol{e}_k)_{\mathscr{P}}$ with L_k given by (4.19) which satisfies (4.21) since $\|I - \bar{G}|_{\hat{\boldsymbol{\Phi}}+\boldsymbol{v}_k}L_k\| \leq (1+\sigma^2)^{-1} < 1\ \forall\ k$ so that $\|(\boldsymbol{e}_{k+1})_{\mathscr{P}}\| < \|(\boldsymbol{e}_k)_{\mathscr{P}}\| \forall\ k$. The limit (4.7) is given by

$$\begin{aligned}\boldsymbol{v}_\infty &= (\bar{G}|_{\hat{\boldsymbol{\Phi}}+\boldsymbol{v}_\infty})^*\big(I+\bar{G}|_{\hat{\boldsymbol{\Phi}}+\boldsymbol{v}_\infty}(\bar{G}|_{\hat{\boldsymbol{\Phi}}+\boldsymbol{v}_\infty})^*\big)^{-1}\\ &\quad\times\big(\bar{G}|_{\hat{\boldsymbol{\Phi}}+\boldsymbol{v}_\infty}(\bar{G}|_{\hat{\boldsymbol{\Phi}}+\boldsymbol{v}_\infty})^*\big(I+\bar{G}|_{\hat{\boldsymbol{\Phi}}+\boldsymbol{v}_\infty}(\bar{G}|_{\hat{\boldsymbol{\Phi}}+\boldsymbol{v}_\infty})^*\big)^{-1}\big)^{-1}\hat{\boldsymbol{\Phi}}_{\mathscr{P}}\\ &= (\bar{G}|_{\hat{\boldsymbol{\Phi}}+\boldsymbol{v}_\infty})^*\big(\bar{G}|_{\hat{\boldsymbol{\Phi}}+\boldsymbol{v}_\infty}(\bar{G}|_{\hat{\boldsymbol{\Phi}}+\boldsymbol{v}_\infty})^*\big)^{-1}\hat{\boldsymbol{\Phi}}_{\mathscr{P}}.\end{aligned}\tag{4.23}$$

If $\sigma = 0$ then (4.19), which can also be written as

$$L_k = \big(I+(\bar{G}|_{\hat{\boldsymbol{\Phi}}+\boldsymbol{v}_k})^*\bar{G}|_{\hat{\boldsymbol{\Phi}}+\boldsymbol{v}_k}\big)^{-1}(\bar{G}|_{\hat{\boldsymbol{\Phi}}+\boldsymbol{v}_k})^*,\tag{4.24}$$

gives $\|I-\bar{G}|_{\hat{\boldsymbol{\Phi}}+\boldsymbol{v}_k}L_k\| = 1$, however if $\exists\ \varepsilon > 0$ satisfying $\langle \boldsymbol{e}, (\bar{G}|_{\hat{\boldsymbol{\Phi}}+\boldsymbol{v}_k})^*\bar{G}|_{\hat{\boldsymbol{\Phi}}+\boldsymbol{v}_k}\boldsymbol{e}\rangle \geq \varepsilon^2\|\boldsymbol{e}\|^2, \forall\ \boldsymbol{e}$, then

$$\begin{aligned}\|I-L_k\bar{G}|_{\hat{\boldsymbol{\Phi}}+\boldsymbol{v}_k}\| &= \|I-\big(I+(\bar{G}|_{\hat{\boldsymbol{\Phi}}+\boldsymbol{v}_k})^*\bar{G}|_{\hat{\boldsymbol{\Phi}}+\boldsymbol{v}_k}\big)^{-1}(\bar{G}|_{\hat{\boldsymbol{\Phi}}+\boldsymbol{v}_k})^*\bar{G}|_{\hat{\boldsymbol{\Phi}}+\boldsymbol{v}_k}\|\\ &= \|\big(I+(\bar{G}|_{\hat{\boldsymbol{\Phi}}+\boldsymbol{v}_k})^*\bar{G}|_{\hat{\boldsymbol{\Phi}}+\boldsymbol{v}_k}\big)^{-1}\| = (1+\varepsilon^2)^{-1} < 1,\end{aligned}$$

and from (4.14), with $\boldsymbol{v}_0 = \mathbf{0}$,

$$\begin{aligned}\boldsymbol{v}_\infty &= \sum_{i=0}^{k}\big(I-L_\infty\bar{G}_{\mathscr{P}}|_{\hat{\boldsymbol{\Phi}}+\boldsymbol{v}_\infty}\big)^i L_\infty\hat{\boldsymbol{\Phi}}_{\mathscr{P}}\\ &= I-\big(I+(\bar{G}|_{\hat{\boldsymbol{\Phi}}+\boldsymbol{v}_k})^*\bar{G}|_{\hat{\boldsymbol{\Phi}}+\boldsymbol{v}_k}\big)^{-1}\big(I+(\bar{G}|_{\hat{\boldsymbol{\Phi}}+\boldsymbol{v}_k})^*\bar{G}|_{\hat{\boldsymbol{\Phi}}+\boldsymbol{v}_k}\big)^{-1}(\bar{G}|_{\hat{\boldsymbol{\Phi}}+\boldsymbol{v}_k})^*\hat{\boldsymbol{\Phi}}_{\mathscr{P}}\\ &= \big((\bar{G}|_{\hat{\boldsymbol{\Phi}}+\boldsymbol{v}_k})^*\bar{G}|_{\hat{\boldsymbol{\Phi}}+\boldsymbol{v}_k}\big)^{-1}(\bar{G}|_{\hat{\boldsymbol{\Phi}}+\boldsymbol{v}_k})^*\hat{\boldsymbol{\Phi}}_{\mathscr{P}}\end{aligned}\tag{4.25}$$

locally satisfying condition (4.22). In (4.19) and (4.24) cases adjoint operator $(\bar{G}|_{\hat{\boldsymbol{\Phi}}+\boldsymbol{v}_k})^* : \mathscr{L}_2^{n_p}[0,T] \to \mathscr{L}_2^{p}[0,T]$ is given by

$$((\bar{G}|_{\hat{\boldsymbol{\Phi}}+\boldsymbol{v}_k})^*z)(t) = \int_0^t R^{-1}(t)B^\top(t)\Gamma(t,\tau)C^\top(\tau)Q(\tau)z(\tau)\mathrm{d}\tau$$

with $\Gamma(t,\tau)$ the state transition matrix for state space system $\{A^\top(t), C^\top(t), B^\top(t)\}$, and hence can be computed efficiently using the adjoint system

$$\begin{aligned}\dot{\tilde{\boldsymbol{x}}}(t) &= -A^\top(t)\tilde{\boldsymbol{x}}(t) - C^\top(t)Q(t)z(t)\\ ((\bar{G}|_{\hat{\boldsymbol{\Phi}}+\boldsymbol{v}_k})^*z)(t) &= R^{-1}(t)B^\top(t)\tilde{\boldsymbol{x}}(t), \quad \tilde{\boldsymbol{x}}(T) = \mathbf{0}, \quad 0 \leq t \leq T.\end{aligned}\tag{4.26}$$

□

The update of Theorem 4.2 corresponds to the well-known norm optimal ILC update [15–18], and addresses the demands of rehabilitation by allowing the designer to balance change in control input from trial-to-trial and the corresponding error reduction. As more weight is applied to the right-hand term in (4.20), the algorithm corresponds to Newton method based ILC [19], which can be implemented using the simple procedure outlined next:

Lemma 4.3 *Choosing $R = rI$, $Q = qI$, $q/r \to \infty$, the ILC update (4.19) realizes minimizing solutions (4.23) or (4.25) respectively in a single iteration. In both cases the required term $L_k(\boldsymbol{e}_k)_{\mathscr{P}}$ in (4.4) can be efficiently computed off-line between experimental trials as the outcome, $\Delta \boldsymbol{v}^J$, of J iterations of*

$$\begin{aligned} \dot{\boldsymbol{z}}(t) &= -A^\top(t)\boldsymbol{z}(t) - C^\top(t)\big((\boldsymbol{e}_k)_{\mathscr{P}}(t) - \bar{G}|_{\hat{\boldsymbol{\Phi}}+\boldsymbol{v}_k}\Delta \boldsymbol{v}_k^j(t)\big), \\ \Delta \boldsymbol{v}_k^{j+1}(t) &= \Delta \boldsymbol{v}_k^j(t) + \alpha B^\top(t)\boldsymbol{z}(t), \quad \boldsymbol{z}(T) = \boldsymbol{0}, \quad 0 \le t \le T. \end{aligned} \tag{4.27}$$

where J and $\alpha > 0$ are sufficiently large and small values respectively.

Proof As $q/r \to \infty$, updates (4.19) and (4.24) respectively converge to

$$L_k = (\bar{G}|_{\hat{\boldsymbol{\Phi}}+\boldsymbol{v}_k})^*\big(\bar{G}|_{\hat{\boldsymbol{\Phi}}+\boldsymbol{v}_k}(\bar{G}|_{\hat{\boldsymbol{\Phi}}+\boldsymbol{v}_k})^*\big)^{-1}, \quad L_k = \big((\bar{G}|_{\hat{\boldsymbol{\Phi}}+\boldsymbol{v}_k})^*\bar{G}|_{\hat{\boldsymbol{\Phi}}+\boldsymbol{v}_k}\big)^{-1}(\bar{G}|_{\hat{\boldsymbol{\Phi}}+\boldsymbol{v}_k})^*$$

which it is shown in [20] correspond to solutions of the minimum energy problem

$$\min_{\Delta \boldsymbol{v}_k} \big\|(\boldsymbol{e}_k)_{\mathscr{P}} - \bar{G}|_{\hat{\boldsymbol{\Phi}}+\boldsymbol{v}_k}\Delta \boldsymbol{v}_k\big\|^2, \quad \boldsymbol{v}_0 = \boldsymbol{0}. \tag{4.28}$$

using gradient ILC [21]. This equates to $j = 1, 2, \ldots, J$ inter-trial iterations of update

$$\Delta \boldsymbol{v}_k^{j+1} = \Delta \boldsymbol{v}_k^j + \alpha(\bar{G}|_{\hat{\boldsymbol{\Phi}}+\boldsymbol{v}_k})^*\big((\boldsymbol{e}_k)_{\mathscr{P}} - \bar{G}|_{\hat{\boldsymbol{\Phi}}+\boldsymbol{v}_k}\Delta \boldsymbol{v}_k^j\big), \quad \Delta \boldsymbol{v}_k^0 = \boldsymbol{0}. \tag{4.29}$$

Scalar $\alpha \in \mathbb{R}_+$ must satisfy $0 < \alpha < \frac{2}{\overline{\sigma}}$, where $\overline{\sigma}$ is the smallest $\overline{\sigma} > 0$ that satisfies $\langle \boldsymbol{e}, \bar{G}_{\hat{\boldsymbol{\Phi}}+\boldsymbol{v}_k}\bar{G}^*_{\hat{\boldsymbol{\Phi}}+\boldsymbol{v}_k}\boldsymbol{e}\rangle \le \overline{\sigma}^2\|\boldsymbol{e}\|^2, \forall \boldsymbol{e}$. Using (4.26), update (4.29) yields (4.27). □

Whatever ILC update operator L_k is chosen, bounds on the convergence rate of the approach of Theorem 4.1 follow from properties of iterative minimization techniques established in [14]. These provide an upper bound on the convergence rate as a function of the magnitude of the linearized system, nonlinearity, and proximity of the initial input to the solution. However, these are only valid locally around the operating point of each trial and therefore we will undertake a comprehensive analysis of robustness in Sect. 4.4.

The convergence of ILC to a fixed solution, $\boldsymbol{v}_\infty$, of problem (4.3), enables us to update our initial stability result of Theorem 3.2 as follows:

Theorem 4.3 *Let ILC operator L_k satisfy (4.5). Then the controlled joints converge to reference $\hat{\boldsymbol{\Phi}}_{\mathscr{P}}$, and the uncontrolled joints are locally stable if Theorem 3.2 is satisfied using operating-point $(\boldsymbol{\tau}^*_{\bar{\mathscr{P}}}(\boldsymbol{\Phi}^*_{\bar{\mathscr{P}}}), \boldsymbol{\Phi}^*_{\bar{\mathscr{P}}})$*

where

$$\boldsymbol{F}_e(\boldsymbol{\Phi}^*_{\bar{\mathscr{P}}}) + \boldsymbol{G}_{\bar{\mathscr{P}}}(\boldsymbol{\Phi}^*_{\bar{\mathscr{P}}}) + \boldsymbol{K}_{\bar{\mathscr{P}}}(\boldsymbol{\Phi}^*_{\bar{\mathscr{P}}}) = \boldsymbol{\tau}^*_{\bar{\mathscr{P}}}(\boldsymbol{\Phi}^*_{\bar{\mathscr{P}}})$$

with

$$\boldsymbol{\tau}^*_{\bar{\mathscr{P}}}(\boldsymbol{\Phi}^*_{\bar{\mathscr{P}}}) = \boldsymbol{\tau}_{\bar{\mathscr{P}}}\big(K\boldsymbol{v}_\infty, \hat{\boldsymbol{\Phi}}_{\mathscr{P}}, \hat{\boldsymbol{\Phi}}^{(1)}_{\mathscr{P}}\big) - \overline{\boldsymbol{C}}_{\bar{\mathscr{P}}\mathscr{P}}(\boldsymbol{\Phi}^*_{\bar{\mathscr{P}}})\hat{\boldsymbol{\Phi}}^{(1)}_{\mathscr{P}} - \boldsymbol{B}_{\bar{\mathscr{P}}\mathscr{P}}(\boldsymbol{\Phi}^*_{\bar{\mathscr{P}}})\hat{\boldsymbol{\Phi}}^{(2)}_{\mathscr{P}}.$$

Proof Follows from Theorem 4.1, with substitution of resulting operating point $\bar{\boldsymbol{\Phi}} = \hat{\boldsymbol{\Phi}}_{\mathscr{P}}$ into Definition 3.1, Theorems 3.1 and 3.2. □

4.2 Case Study: ILC Applied to Input-Output Linearized System

In the special case that feedback controller K is selected to linearize the system dynamics, the relationship $G_{\mathscr{P}} : \hat{\boldsymbol{\Phi}} \mapsto \boldsymbol{\Phi}_{\mathscr{P}}$ is linear. It follows that system $\bar{G}|_{\hat{\boldsymbol{\phi}}+\boldsymbol{v}_k} = G_{\mathscr{P}}\ \forall\ k$ and the properties of Theorem 4.1 hold globally.

To illustrate this, consider the electrically stimulated, mechanically assisted arm system that was introduced in Sect. 2.2.5, and let feedback controller K be chosen as the input-output linearizing controller of (3.27) developed in Sect. 3.2. About any operating point, $\bar{\boldsymbol{v}}$, system $\bar{G}|_{\bar{\boldsymbol{v}}}$ then corresponds to the LTI system given in transfer-function form

$$G_{\mathscr{P}}(s) = \bar{G}|_{\hat{\boldsymbol{\phi}}+\boldsymbol{v}_k} = C(sI - A)^{-1}B \quad \forall\ k \tag{4.30}$$

with A, B and C matrices defined by:

$$A = \begin{bmatrix} 0 & I & 0 & 0 \\ 0 & 0 & I & 0 \\ 0 & 0 & 0 & I \\ -A_0 & -A_1 & -A_2 & -A_3 \end{bmatrix}, \quad B = \begin{bmatrix} 0 \\ 0 \\ 0 \\ A_0 \end{bmatrix}, \quad C = [\, I \;\; 0 \;\; \cdots \;\; 0 \,],$$

which writing $A_j = \mathrm{diag}\{a_{1,j}, a_{2j}\}$, $j = 0, \ldots, 3$, gives rise to the form

$$G_{\mathscr{P}}(s) = \begin{bmatrix} \dfrac{a_{10}}{s^4 + a_{13}s^3 + a_{12}s^2 + a_{11}s + a_{10}} & 0 \\ 0 & \dfrac{a_{20}}{s^4 + a_{23}s^3 + a_{22}s^2 + a_{21}s + a_{20}} \end{bmatrix}.$$

To design an ILC operator L_k for this system which satisfies (4.5), we will employ Theorem 4.2. This involves minimizing the quadratic objective function of (4.20), which since $\begin{bmatrix} (\boldsymbol{e}_k(t))_2 \\ (\boldsymbol{e}_k(t))_5 \end{bmatrix} - G_{\mathscr{P}}\Delta\boldsymbol{v} = \begin{bmatrix} (\boldsymbol{e}_{k+1}(t))_2 \\ (\boldsymbol{e}_{k+1}(t))_5 \end{bmatrix}$, specifies in the current case to

$$\int_{t=0}^{T} \Big\{ (\boldsymbol{v}_{k+1}(t) - \boldsymbol{v}_k(t))^\top R(\boldsymbol{v}_{k+1}(t) - \boldsymbol{v}_k(t)) + \big[(\boldsymbol{e}_{k+1}(t))_2,\ (\boldsymbol{e}_{k+1}(t))_5\big] Q \begin{bmatrix} (\boldsymbol{e}_{k+1}(t))_2 \\ (\boldsymbol{e}_{k+1}(t))_5 \end{bmatrix} \Big\} dt \tag{4.31}$$

where T is the duration of the task. Through selection of symmetric positive-definite weighting matrices R and Q, this objective function allows the designer to balance accuracy of task completion with the amount of ES applied to assist the impaired participant's movement. The solution to minimizing (4.31) is given by (4.19), which specifies in the current case to the update

$$\boldsymbol{v}_{k+1} = \boldsymbol{v}_k + \underbrace{G^*(s)(I + G(s)G^*(s))^{-1}}_{L_k(s)} \overbrace{\begin{bmatrix} (\boldsymbol{e}_k)_2 \\ (\boldsymbol{e}_k)_5 \end{bmatrix}}^{(\boldsymbol{e}_k)_{\mathscr{P}}}. \tag{4.32}$$

This can be implemented efficiently using Lemma 4.3. Alternatively, implementation in discrete-time follows immediately from the matrix representation of operators $G(s)$ and $(G^*(s))^{-1}$. A further alternative is the equivalent optimal state feedback plus predictive feedforward action implementation of [22].

4.2.1 Test Procedure

Following ethical approval, feedback controller (3.27) and ILC update (4.32) were experimentally implemented with three unimpaired subjects. Nine clinically relevant reference trajectory pairs $\{\hat{\phi}_2, \hat{\phi}_5\}$ were calculated to lift and extend the upper arm and forearm in three directions, over three distances, as shown in Fig. 4.2. The duration of each trajectory, T, was set at 20 s. All tests used sampling frequencies of 1000 and 40 Hz for signal capture and computation respectively.

Each unimpaired subject was seated in the ArmeoSpring, which was adjusted to their individual arm dimensions. The level of support in each spring was modified so that their arm was raised 5 cm above their lap. The identification procedure described in Sect. 2.2.5 was conducted to produce the system model of (2.7) relating stimulation $\boldsymbol{u}$ to angular movement $\boldsymbol{\Phi}$. The optimal weights used in (3.25) to compute matrices $A_i, i = 0, \ldots, 3$ were $\tilde{R} = 0.01$ and $\tilde{Q} = I$, as these were found to achieve a satisfactory balance between tracking accuracy and oscillatory behavior across all subjects. Similarly, weights of $R = I$, $Q = 5I$ were found to achieve a satisfactory compromise between convergence rate and robustness of the ILC update (4.32).

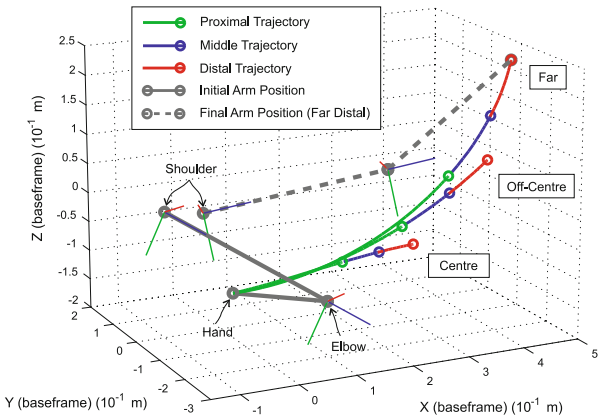

Fig. 4.2 The arm's location, axis and the nine possible participant-specific reference trajectories: made up of direction (centre, off centre, far) and distance (proximal, middle and distal)

4.2.2 Experimental Results

Tests with each subject comprised 10 trials of the far-distal and far-middle trajectories, and summary data are shown in Table 4.1. Representative tracking results for joints ϕ_2 and ϕ_5 are shown in Fig. 4.3, together with the applied stimulation pulsewidth signals u_1 and u_2. Corresponding error norm results are shown in Fig. 4.4. The results confirm error convergence to low levels in a small number of trials, and an input signal which is within comfortable limits.

To assess the stability of the unactuated joints, their movement from their initial position, $\phi_{i,k} - \phi_{i,k}(0), i \in \bar{\mathscr{P}} = \{1, 3, 4\}$ is also quantified. The results confirm the

Table 4.1 Mean (standard deviation) error norms for unimpaired tracking task

		I-O linearization + NOILC		PID + Newton ILC	
		Far middle	Far distal	Far middle	Far distal
$\|e_{2,k}\|^2$	Best trial only	3.5 (4.0)	4.2 (4.0)	3.4 (2.8)	3.3 (3.1)
	Mean of first 6 trials	6.1 (8.1)	21.8 (20.9)	9.0 (8.2)	28.6 (25.9)
$\|e_{5,k}\|^2$	Best trial only	4.7 (4.3)	5.2 (4.9)	5.2 (4.9)	7.0 (6.1)
	Mean of first 6 trials	15.1 (12.5)	30.5 (18.3)	21.9 (17.6)	47.9 (29.7)
$\|\phi_{1,k} - \phi_{1,k}(0)\|^2$	Mean of all trials	7.4 (5.4)	8.8 (6.3)	12.3 (10.1)	16.6 (13.9)
	Mean of first 6 trials	19.9 (15.1)	20.3 (17.5)	36.7 (25.6)	44.8 (34.7)
$\|\phi_{3,k} - \phi_{3,k}(0)\|^2$	Mean of all trials	14.5 (10.8)	11.6 (9.2)	16.5 (12.7)	19.8 (16.1)
	Mean of first 6 trials	28.3 (16.7)	33.0 (21.7)	42.2 (37.2)	51.6 (40.8)
$\|\phi_{4,k} - \phi_{4,k}(0)\|^2$	Mean of all trials	11.0 (8.4)	16.3 (10.8)	15.7 (12.9)	18.7 (14.6)
	Mean of first 6 trials	25.2 (22.1)	24.6 (23.8)	33.4 (26.5)	49.3 (37.0)

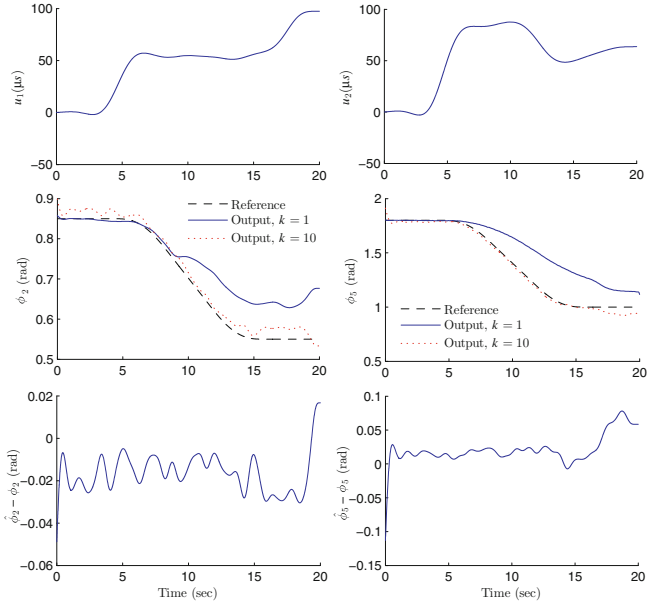

Fig. 4.3 Trial $k = 1, 10$ signals for unimpaired Subject A using NOILC with $Q = I$, $R = 5I$

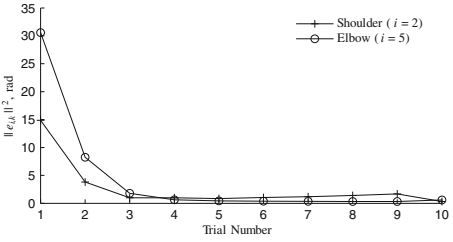

Fig. 4.4 Error norm results for unimpaired Subject A using NOILC with $Q = I$, $R = 5I$

efficacy of the separate linearization and ILC actions, and confirm that a high level of tracking accuracy is possible. They also support the analysis of Theorem 3.2 that oscillation in the uncontrolled joints is reduced by adding damping and appropriate support about the operating point.

4.3 Case Study: ILC Applied to Non-linearized System

We next implement the ILC design procedure of Theorem 4.1 with a feedback controller that does not realise global linearization of the controlled joint dynamics. We select the PID feedback controller that was considered in Sect. 3.4, and which has previously yielded satisfactory performance within the rehabilitation domain [9].

This controller corresponds to

$$K : \begin{cases} \dot{\boldsymbol{x}}_{c,k}(t) = \boldsymbol{f}_c(\boldsymbol{x}_{c,k}(t), \boldsymbol{e}_k(t) + \boldsymbol{v}_k(t)) \\ \boldsymbol{u}_k(t) = \boldsymbol{h}_c(\boldsymbol{x}_{c,k}(t), \boldsymbol{e}_k(t) + \boldsymbol{v}_k(t)), \end{cases} \qquad t \in [0, T]$$

with the functional forms

$$\begin{aligned} \boldsymbol{f}_c(\boldsymbol{x}_{c,k}(t), \boldsymbol{e}_k(t) + \boldsymbol{v}_k(t)) &= \operatorname{diag}\left\{\begin{bmatrix} -\frac{1}{c} & 0 \\ 1 & 0 \end{bmatrix}, \begin{bmatrix} -\frac{1}{c} & 0 \\ 1 & 0 \end{bmatrix}\right\} \boldsymbol{x}_{c,k}(t) \\ &\quad + \operatorname{diag}\left\{\begin{bmatrix} 1 \\ 0 \end{bmatrix}, \begin{bmatrix} 1 \\ 0 \end{bmatrix}\right\} \big(\boldsymbol{e}_k(t) + \boldsymbol{v}_k(t)\big), \\ \boldsymbol{h}_c(\boldsymbol{x}_{c,k}(t), \boldsymbol{e}_k(t) + \boldsymbol{v}_k(t)) &= \operatorname{diag}\left\{\begin{bmatrix} \left(k_{i1} - \frac{k_{d1}}{c^2}\right) & \frac{k_{i1}}{c} \end{bmatrix}, \begin{bmatrix} \left(k_{i2} - \frac{k_{d2}}{c^2}\right) & \frac{k_{i2}}{c} \end{bmatrix}\right\} \boldsymbol{x}_{c,k}(t) \\ &\quad + \operatorname{diag}\left\{\left(k_{p1} + \frac{k_{d1}}{c}\right), \left(k_{p2} + \frac{k_{d2}}{c}\right)\right\} \big(\boldsymbol{e}_k(t) + \boldsymbol{v}_k(t)\big) \end{aligned} \tag{4.33}$$

where k_{p1}, k_{p2}, k_{d1}, k_{d2}, k_{i1}, and k_{i2} are controller gains, and c is a positive scalar. Combined with identified arm model, this then yields closed-loop system (4.1).

Following Theorem 4.1, the ILC update is given by (4.4) with learning operator L_k computed after each task attempt using the linearized system description $\bar{G}_{\mathscr{P}}|_{\hat{\boldsymbol{\Phi}}+\boldsymbol{v}_k}$. Here Lemma 4.2 is used to compute $\bar{G}_{\mathscr{P}}|_{\hat{\boldsymbol{\Phi}}+\boldsymbol{v}_k}$ using functions $\boldsymbol{f}(\cdot)$, $\boldsymbol{h}(\cdot)$ of the controller dynamics (4.1).

We select L_k to correspond to the NOILC update of Theorem 4.2, and use the efficient implementation provided by Lemma 4.3. Accordingly, system (4.27) is run $J = 100$ times in between trials using a suitably small gain α, to provide the descent term $L_k(\boldsymbol{e}_k)_{\mathscr{P}} = \Delta \boldsymbol{v}_k$ which is then used in ILC update (4.4).

4.3.1 Experimental Results

The control scheme has been tested with six unimpaired subjects, employing the same test procedure as in Sect. 4.2.1. These subjects undertook the far middle and far distal tasks shown in Fig. 4.2. Figure 4.5 shows representative tracking performance

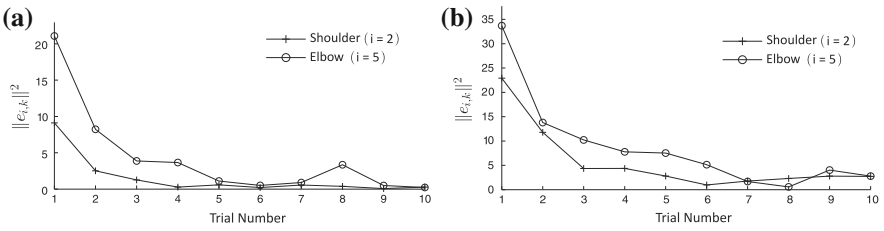

Fig. 4.5 Far middle error norm plots for unimpaired **a** Subject B and **b** Subject C

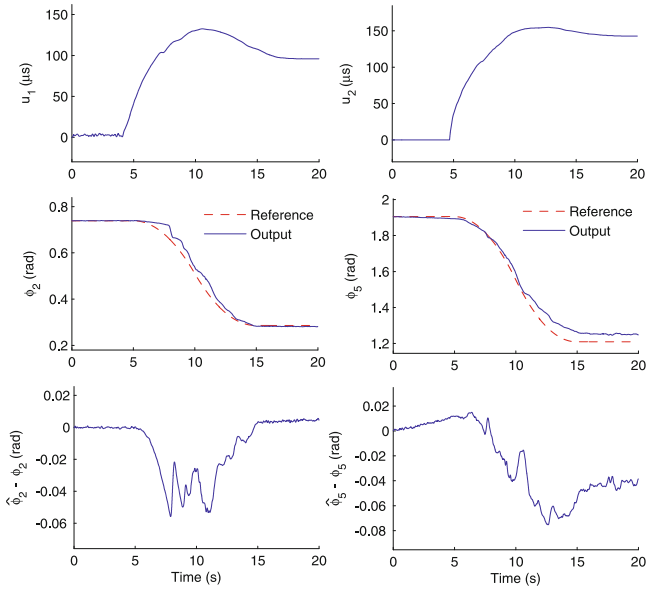

Fig. 4.6 Far middle tracking performance for unimpaired Subject B (trial 10)

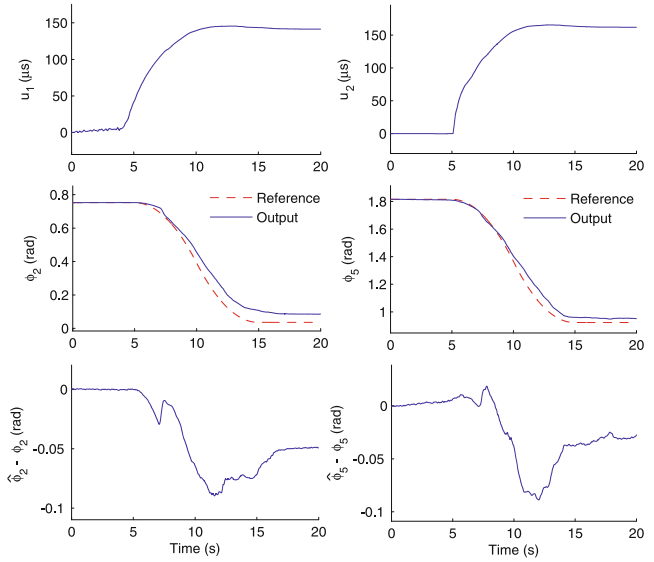

Fig. 4.7 Far middle tracking performance for unimpaired Subject C (trial 10)

results for two subjects (denoted B and C). The controller gains used with Subject B are $k_{p1} = k_{p2} = 20$, $k_{i1} = k_{i2} = 30$, $k_{d1} = k_{d2} = 2$ and $c = 0.01$. The gains used with Subject C are $k_{p1} = k_{p2} = 5$, $k_{i1} = k_{i2} = 8$, $k_{d1} = k_{d2} = 1$ and $c = 0.01$.

The tracking error reduces quickly and maintains a low level over latter trials. In some cases the error norm increases slightly in later trials because the subject's triceps started to suffer from fatigue. However, ILC was quickly able to modify the stimulation to maintain a low error. Figures 4.6 and 4.7 show tracking performance over trial 10 for the same two subjects. These illustrate close reference tracking for both controlled angles. Table 4.1 includes summary statistics for all subjects, which confirm high performance when applied to unimpaired subjects. In comparison with the case-study of Sect. 4.2, it can be seen that the lack of decoupling action in the Newton method based ILC scheme of Lemma 4.3 causes transients which lead to greater oscillation in the unactuated joint axes. Since the Newton based method is designed without consideration of the unactuated joint dynamics, these degrade the tracking performance of the actuated joints, leading to greater norms $||e_{i,k}||^2, i \in \mathscr{P}$.

4.4 Robust Performance

In Chap. 3 we derived robust stability conditions when feedback controller K is employed with the true plant N. These required calculation of bound $b_{M//K}$ on the map between external and internal signals when K is applied on the nominal plant model M. This bound was then used to calculate the maximum mismatch than can be tolerated between the nominal and true plant while preserving closed-loop stability. We now extend this analysis to include the ILC update loop that was introduced in Sect. 4.1, and defined by (4.4) of Theorem 4.1. To do this, we first embed the ILC trial-to-trial update dynamics and the feedback controller 'along the trial' dynamics within a single system description.

Since ILC runs over $t \in [0, T]$ during rehabilitation task attempts $k = 0, 1, \ldots$, we can express the dynamics of the kth trial as a single time instant of a so-called 'lifted' system [23]. To do this we first write the signals appearing in Fig. 4.1 as

$$\begin{aligned} \boldsymbol{v}_k = \boldsymbol{v}(k) \in \mathscr{L}_2^p[0, T], \quad \boldsymbol{e}_k = \boldsymbol{e}(k) \in \mathscr{L}_2^p[0, T], \\ \boldsymbol{\Phi}_k = \boldsymbol{\Phi}(k) \in \mathscr{L}_2^p[0, T], \quad \boldsymbol{u}_k = \boldsymbol{u}(k) \in \mathscr{L}_2^m[0, T], \end{aligned}$$

and then define the corresponding lifted signal spaces

$$\boldsymbol{v} \in \mathscr{L}_2^p[0, T] \times \mathbb{N}, \quad \boldsymbol{e} \in \mathscr{L}_2^p[0, T] \times \mathbb{N}, \quad \boldsymbol{\Phi} \in \mathscr{L}_2^p[0, T] \times \mathbb{N}, \quad \boldsymbol{u} \in \mathscr{L}_2^m[0, T] \times \mathbb{N}.$$

The lifted representation of the plant, feedback controller, and ILC operators are then directly inherited from their non-lifted counterparts as:

$$\bar{M} : \mathscr{L}_2^m[0, T] \times \mathbb{N} \to \mathscr{L}_2^p[0, T] \times \mathbb{N} : \boldsymbol{u} \mapsto \boldsymbol{\Phi} : \boldsymbol{\Phi}(k) = M\boldsymbol{u}(k), \tag{4.34}$$

$$\bar{K} : \mathscr{L}_2^p[0, T] \times \mathbb{N} \to \mathscr{L}_2^m[0, T] \times \mathbb{N} : (\boldsymbol{v} + \boldsymbol{e}) \mapsto \boldsymbol{u} : \boldsymbol{u}(k) = K(\boldsymbol{v}(k) + \boldsymbol{e}(k)), \tag{4.35}$$

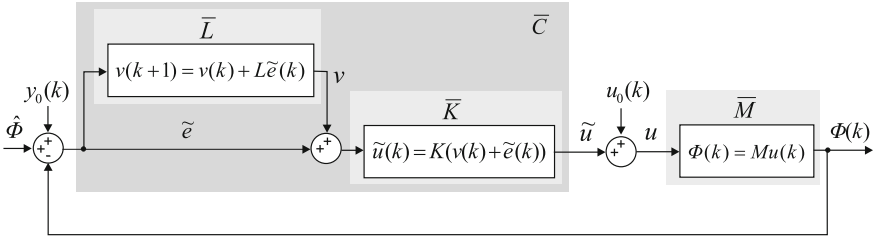

Fig. 4.8 ILC and feedback control scheme in lifted form (equivalent to Fig. 4.1 when $\boldsymbol{u}_0 = \boldsymbol{y}_0 = \boldsymbol{0}$)

$$\bar{L} : \mathscr{L}_2^p[0, T] \times \mathbb{N} \to \mathscr{L}_2^p[0, T] \times \mathbb{N} : \boldsymbol{e} \mapsto \boldsymbol{v} : \boldsymbol{v}(k+1) = \boldsymbol{v}(k) + L\boldsymbol{e}(k), \boldsymbol{v}(0) = \boldsymbol{0} \tag{4.36}$$

for $k \in \mathbb{N}_+$. Here M and K are respectively defined by (3.1) and (3.2) over $t \in [0, T]$, and L is defined by (4.4) in Theorem 4.1 with trial-dependence omitted for notational simplicity. These definitions allow the nominal system of Fig. 4.1 to be equivalently represented as in Fig. 4.8 which includes the external disturbances $\boldsymbol{u}_0$, $\boldsymbol{y}_0$. Here $\bar{C} : \tilde{\boldsymbol{e}} \mapsto \tilde{\boldsymbol{u}} : \tilde{\boldsymbol{u}} = \bar{K}(\bar{L} + I)\tilde{\boldsymbol{e}}, \boldsymbol{u}(k) = \boldsymbol{u}_0(k) - \tilde{\boldsymbol{u}}(k), \tilde{\boldsymbol{e}}(k) = \hat{\boldsymbol{\Phi}} + \boldsymbol{y}_0(k) - \boldsymbol{\Phi}(k)$. The lifted projection operator from external to internal signals, $\Pi_{\bar{M}//\bar{C}} : \begin{pmatrix} \boldsymbol{u}_0 \\ \boldsymbol{y}_0 + \hat{\boldsymbol{\Phi}} \end{pmatrix} \mapsto \begin{pmatrix} \boldsymbol{u} \\ \boldsymbol{\Phi} \end{pmatrix}$, can then be used to bound the allowable mismatch between $\bar{M}$ and true lifted system $\bar{N}$ defined by

$$\bar{N} : \mathscr{L}_2^m[0, T] \times \mathbb{N} \to \mathscr{L}_2^p[0, T] \times \mathbb{N} : \boldsymbol{u} \mapsto \boldsymbol{\Phi} : \boldsymbol{\Phi}(k) = N\boldsymbol{u}(k). \tag{4.37}$$

with associated projection operator $\Pi_{\bar{N}//\bar{C}} : \begin{pmatrix} \boldsymbol{u}_0 \\ \boldsymbol{y}_0 + \hat{\boldsymbol{\Phi}} \end{pmatrix} \mapsto \begin{pmatrix} \boldsymbol{u} \\ \boldsymbol{\Phi} \end{pmatrix}$. Using these definitions, we can directly apply Theorem 3.3 to the lifted system simply by replacing M by its lifted counterpart $\bar{M}$, and K by its lifted ILC counterpart $\bar{C}$. However to produce a more useful result we first need to relate the gap metric between lifted plants $\bar{M}$, $\bar{N}$ to the gap metric between the original unlifted plants M, N that was defined in Definition 3.2.

Theorem 4.4 *The gap metric measure of mismatch between lifted plant operators $\bar{M}$ and $\bar{N}$ can be related to the mismatch between their respective unlifted counterparts M and N via*

$$\delta(\bar{M}, \bar{N}) \leq \sup_{k \in \mathbb{N}_+} \delta_k(M, N) \tag{4.38}$$

where the unlifted gap with respect to the kth trial operating point satisfies

$$\delta_k(M, N) \leq \sup_{\|\boldsymbol{u}\| \neq 0} \frac{\|(N|_{\tilde{\boldsymbol{u}}_1(k)} - M|_{\tilde{\boldsymbol{u}}(k)})\boldsymbol{u}\|}{\|\boldsymbol{u}\|}. \tag{4.39}$$

If M is linear $M|_{\bar{\boldsymbol{u}}(k)} = M \ \forall\ k$, and likewise for N. If both M and N are linear operators then $\delta_k(M, N) = \delta(M, N) \ \forall\ k$ and

$$\delta(\bar{M}, \bar{N}) \leq \delta(M, N) \leq \sup_{\|\boldsymbol{u}\| \neq 0} \frac{\|(N - M)\boldsymbol{u}\|}{\|\boldsymbol{u}\|}. \tag{4.40}$$

Proof First note that $\{\bar{\boldsymbol{u}}(k), \bar{\boldsymbol{\Phi}}(k)\}_{k=0,\ldots,\infty}$, with $\begin{pmatrix} \bar{\boldsymbol{u}} \\ \bar{\boldsymbol{\Phi}} \end{pmatrix} = \Pi_{\bar{M}//\bar{C}} \begin{pmatrix} \mathbf{0} \\ \hat{\boldsymbol{\Phi}} \end{pmatrix}$, is the sequence of operating point trajectories generated by $[\bar{M}, \bar{C}]$ in the absence of disturbance, and likewise $\{\bar{\boldsymbol{u}}_1(k), \bar{\boldsymbol{\Phi}}_1(k)\}_{k=0,\ldots,\infty}$, with $\begin{pmatrix} \bar{\boldsymbol{u}}_1 \\ \bar{\boldsymbol{\Phi}}_1 \end{pmatrix} = \Pi_{\bar{N}//\bar{C}} \begin{pmatrix} \mathbf{0} \\ \hat{\boldsymbol{\Phi}} \end{pmatrix}$, is the sequence of operating point trajectories generated by $[\bar{N}, \bar{C}]$ in the absence of disturbance. From Proposition 3.2, the lifted graphs then are

$$\mathscr{G}_{\bar{M}} := \left\{ \begin{pmatrix} \boldsymbol{u} \\ \boldsymbol{\Phi} \end{pmatrix} : \left\| \begin{pmatrix} \boldsymbol{u} \\ \boldsymbol{\Phi} \end{pmatrix} \right\|_{\begin{pmatrix} \bar{\boldsymbol{u}} \\ \bar{\boldsymbol{\Phi}} \end{pmatrix}} = \left(\sum_{k=0}^{\infty} \left\| \begin{pmatrix} \boldsymbol{u}(k) \\ \boldsymbol{\Phi}(k) \end{pmatrix} \right\|^2_{\begin{pmatrix} \bar{\boldsymbol{u}}(k) \\ \bar{\boldsymbol{\Phi}}(k) \end{pmatrix}} \right)^{\frac{1}{2}} < \infty, \boldsymbol{\Phi}(k) = M\boldsymbol{u}(k) \right\},$$

$$\mathscr{G}_{\bar{N}} := \left\{ \begin{pmatrix} \boldsymbol{u} \\ \boldsymbol{\Phi} \end{pmatrix} : \left\| \begin{pmatrix} \boldsymbol{u} \\ \boldsymbol{\Phi} \end{pmatrix} \right\|_{\begin{pmatrix} \bar{\boldsymbol{u}}_1 \\ \bar{\boldsymbol{\Phi}}_1 \end{pmatrix}} = \left(\sum_{k=0}^{\infty} \left\| \begin{pmatrix} \boldsymbol{u}(k) \\ \boldsymbol{\Phi}(k) \end{pmatrix} \right\|^2_{\begin{pmatrix} \bar{\boldsymbol{u}}_1(k) \\ \bar{\boldsymbol{\Phi}}_1(k) \end{pmatrix}} \right)^{\frac{1}{2}} < \infty, \boldsymbol{\Phi}(k) = N\boldsymbol{u}(k) \right\}.$$

Map $\bar{\Psi} : \mathscr{G}_{\bar{M}} \mapsto \mathscr{G}_{\bar{N}}$ is surjective if $\forall\ \boldsymbol{y} \in \mathscr{G}_{\bar{N}}\ \exists\ \boldsymbol{x} \in \mathscr{G}_{\bar{M}}$ such that $\bar{\Psi}(\boldsymbol{x}) = \boldsymbol{y}$. We therefore define the map $\boldsymbol{y}(k) = (\bar{\Psi}\boldsymbol{x})(k) = \Psi_k(\boldsymbol{x}(k)) = \Psi_k \begin{pmatrix} \boldsymbol{u}(k) + \bar{\boldsymbol{u}}(k) \\ M(\boldsymbol{u}(k) + \bar{\boldsymbol{u}}(k)) \end{pmatrix} = \begin{pmatrix} \boldsymbol{u}(k) + \bar{\boldsymbol{u}}_1(k) \\ N(\boldsymbol{u}(k) + \bar{\boldsymbol{u}}_1(k)) \end{pmatrix} = \boldsymbol{y}(k)$. From the proof of Proposition 3.2 $\|\boldsymbol{x}(k)\|_{\begin{pmatrix} \bar{\boldsymbol{u}}(k) \\ \bar{\boldsymbol{\Phi}}(k) \end{pmatrix}} = \left\| \begin{pmatrix} \boldsymbol{u}(k) + \bar{\boldsymbol{u}}(k) \\ M(\boldsymbol{u}(k) + \bar{\boldsymbol{u}}(k)) \end{pmatrix} \right\|_{\begin{pmatrix} \bar{\boldsymbol{u}}(k) \\ \bar{\boldsymbol{\Phi}}(k) \end{pmatrix}} = \left\| \begin{pmatrix} \boldsymbol{u}(k) \\ \boldsymbol{\Phi}(k) \end{pmatrix} \right\| < \infty\ \forall\ k$. Hence $\boldsymbol{x} \in \mathscr{G}_{\bar{M}}$ and we note $\bar{\Psi} \begin{pmatrix} \bar{\boldsymbol{u}} \\ \bar{\boldsymbol{\Phi}} \end{pmatrix} = \begin{pmatrix} \bar{\boldsymbol{u}}_1 \\ \bar{\boldsymbol{\Phi}}_1 \end{pmatrix}$. From Definition 3.2,

$$\begin{aligned}
\delta(\bar{M}, \bar{N}) &\leq \|(\bar{\Psi} - I)_{\mathscr{G}_{\bar{M}}}\|_{\begin{pmatrix} \bar{\boldsymbol{u}} \\ \bar{\boldsymbol{\Phi}} \end{pmatrix}} \\
&= \sup_{\boldsymbol{x} \in \mathscr{G}_{\bar{M}} \setminus \{\mathbf{0}\}} \frac{\left(\sum_{k=0}^{\infty} \left\| (\Psi_k - I)\boldsymbol{x}(k) - (\Psi_k - I) \begin{pmatrix} \bar{\boldsymbol{u}}(k) \\ \bar{\boldsymbol{\Phi}}(k) \end{pmatrix} \right\|^2 \right)^{\frac{1}{2}}}{\left(\sum_{k=0}^{\infty} \left\| \boldsymbol{x}(k) - \begin{pmatrix} \bar{\boldsymbol{u}}(k) \\ \bar{\boldsymbol{\Phi}}(k) \end{pmatrix} \right\|^2 \right)^{\frac{1}{2}}} \\
&\leq \sup_{\|\boldsymbol{u}\| \neq \mathbf{0}} \frac{(\sum_{k=0}^{\infty} \|(N(\boldsymbol{u}(k) + \bar{\boldsymbol{u}}_1(k)) - N\bar{\boldsymbol{u}}_1(k)) - (M(\boldsymbol{u}(k) + \bar{\boldsymbol{u}}(k)) - M\bar{\boldsymbol{u}}(k))\|^2)^{\frac{1}{2}}}{\|\boldsymbol{u}\|}
\end{aligned}$$

$$
\begin{aligned}
&= \sup_{\|\boldsymbol{u}\|\neq\mathbf{0}} \frac{(\sum_{k=0}^{\infty} \|\left(N|_{\bar{\boldsymbol{u}}_1(k)} - M|_{\bar{\boldsymbol{u}}(k)}\right)\boldsymbol{u}(k)\|^2)^{\frac{1}{2}}}{\|\boldsymbol{u}\|} \\
&\leq \sup_{\|\boldsymbol{u}\|\neq\mathbf{0}} \frac{\left(\sum_{k=0}^{\infty}\left(\sup_{\|\boldsymbol{u}(k)\|\neq\mathbf{0}} \frac{\left\|\left(N|_{\bar{\boldsymbol{u}}_1(k)} - M|_{\bar{\boldsymbol{u}}(k)}\right)\boldsymbol{u}(k)\right\|^2}{\|\boldsymbol{u}(k)\|^2}\right)\|\boldsymbol{u}(k)\|^2\right)^{\frac{1}{2}}}{\|\boldsymbol{u}\|} \\
&\leq \sup_{\|\boldsymbol{u}\|\neq\mathbf{0}} \frac{\left(\sup\limits_{\substack{\|\boldsymbol{v}\|\neq\mathbf{0} \\ k\in\mathbb{N}_+}} \frac{\left\|\left(N|_{\bar{\boldsymbol{u}}_1(k)} - M|_{\bar{\boldsymbol{u}}(k)}\right)\boldsymbol{v}\right\|}{\|\boldsymbol{v}\|}\right)\left(\sum_{k=0}^{\infty}\|\boldsymbol{u}(k)\|^2\right)^{\frac{1}{2}}}{\|\boldsymbol{u}\|} \\
&= \sup_{k\in\mathbb{N}_+}\left(\sup_{\|\boldsymbol{v}\|\neq\mathbf{0}} \frac{\left\|\left(N|_{\bar{\boldsymbol{u}}_1(k)} - M|_{\bar{\boldsymbol{u}}(k)}\right)\boldsymbol{v}\right\|}{\|\boldsymbol{v}\|}\right).
\end{aligned}
$$

□

Further properties relating lifted and non-lifted gap metrics appear in [23]. We can generalise Theorem 3.3 as follows:

Theorem 4.5 *Let K and L be selected such that there exists $b_{\bar{M}//\bar{C}}$ satisfying:*

$$
\|\Pi_{\bar{M}//\bar{C}}\|_{\begin{pmatrix}\mathbf{0}\\ \hat{\boldsymbol{\Phi}}\end{pmatrix}} = \sup_{\left\|\begin{pmatrix}\boldsymbol{u}_0\\ \boldsymbol{y}_0\end{pmatrix}\right\|\neq 0} \frac{\left\|\Pi_{\bar{M}//\bar{C}}\begin{pmatrix}\boldsymbol{u}_0\\ \boldsymbol{y}_0+\hat{\boldsymbol{\Phi}}\end{pmatrix} - \Pi_{\bar{M}//\bar{C}}\begin{pmatrix}\mathbf{0}\\ \hat{\boldsymbol{\Phi}}\end{pmatrix}\right\|}{\left\|\begin{pmatrix}\boldsymbol{u}_0\\ \boldsymbol{y}_0\end{pmatrix}\right\|} \leq b_{\bar{M}//\bar{C}} < \infty. \tag{4.41}
$$

Then the true combined feedback and ILC system $[\bar{N}, \bar{C}]$ is BIBO stable if

$$
\sup_{k\in\mathbb{N}_+} \|N|_{\bar{\boldsymbol{u}}_1(k)} - M|_{\bar{\boldsymbol{u}}(k)}\| < b^{-1}_{\bar{M}//\bar{C}} \tag{4.42}
$$

and its performance is bounded with respect to its operating point as

$$
\|\Pi_{\bar{N}//\bar{C}}\|_{\begin{pmatrix}\mathbf{0}\\ \hat{\boldsymbol{\Phi}}\end{pmatrix}} \leq b_{\bar{M}//\bar{C}} \frac{1+\sup_{k\in\mathbb{N}_+}\|N|_{\bar{\boldsymbol{u}}_1(k)} - M|_{\bar{\boldsymbol{u}}(k)}\|}{1 - b_{\bar{M}//\bar{C}}\sup_{k\in\mathbb{N}_+}\|N|_{\bar{\boldsymbol{u}}_1(k)} - M|_{\bar{\boldsymbol{u}}(k)}\|}. \tag{4.43}
$$

Like our previous analysis in Theorem 3.3, Theorem 4.5 bounds the allowable mismatch between the true and nominal plants, but now $b_{M//K}$ is replaced by $b_{\bar{M}//\bar{C}}$. In the special case that M and K are linear operators, the lifted bound $b_{\bar{M}//\bar{C}}$ can be directly related to the bound, $b_{M//K}$ for the feedback controller alone, thereby enabling transparent design of feedback and feedforward control actions.

Theorem 4.6 *Let plant model M and controller K be linear, and ILC operator L be designed to satisfy either (4.5) or (4.8) of Theorem 4.1. Then*

$$b_{\bar{M}//\bar{C}} = b_{M//K} + \frac{\left\| \begin{pmatrix} I \\ M \end{pmatrix} K(I+MK)^{-1} \right\| \|L\| \left\| (I+MK)^{-1}(-M, I) \right\|}{1-\gamma} \tag{4.44}$$

where the gain bound for the feedback controller alone (i.e. with $L = 0$) is

$$b_{M//K} = b_{\bar{M}//\bar{K}} = \left\| \begin{pmatrix} I \\ M \end{pmatrix} (I+KM)^{-1}(I, K) \right\| \tag{4.45}$$

and $\gamma = \|I - \bar{G}_{\mathscr{P}} L\|$ or $\|I - L\bar{G}_{\mathscr{P}}\|$ depending on whether it is condition (4.5) or (4.8) of Theorem 4.1 that is satisfied.

Proof With the inclusion of disturbances $\boldsymbol{u}_0 \in \mathscr{L}_2^m[0,T] \times \mathbb{N}$, $\boldsymbol{y}_0 \in \mathscr{L}_2^p[0,T] \times \mathbb{N}$, the signals in Fig. 4.8 satisfy

$$\begin{aligned}
\tilde{\boldsymbol{e}}(i) &= \boldsymbol{y}_0(i) + \hat{\boldsymbol{\Phi}} - M\big(\boldsymbol{u}_0(i) + K(\boldsymbol{v}(i) + \tilde{\boldsymbol{e}}(i))\big) \\
\Rightarrow (I+MK)\tilde{\boldsymbol{e}}(i) &= \boldsymbol{y}_0(i) + \hat{\boldsymbol{\Phi}} - M\boldsymbol{u}_0(i) - MK\boldsymbol{v}(i) \\
\Rightarrow (I+MK)\tilde{\boldsymbol{e}}(i+1) &= \boldsymbol{y}_0(i+1) + \hat{\boldsymbol{\Phi}} - M\boldsymbol{u}_0(i+1) - MK\boldsymbol{v}(i+1) \\
\Rightarrow (I+MK)\big(\tilde{\boldsymbol{e}}(i+1) - \tilde{\boldsymbol{e}}(i)\big) &= \big(\boldsymbol{y}_0(i+1) - \boldsymbol{y}_0(i)\big) - M\big(\boldsymbol{u}_0(i+1) - \boldsymbol{u}_0(i)\big) \\
&\quad - MK\big(\underbrace{\boldsymbol{v}(i+1) - \boldsymbol{v}(i)}_{L\tilde{\boldsymbol{e}}(i)}\big).
\end{aligned}$$

Since M and K are linear $\bar{G}_{\mathscr{P}} = G_{\mathscr{P}} = G := (I+MK)^{-1}MK$, so that

$$\begin{aligned}
\tilde{\boldsymbol{e}}(i+1) &= \big(I - \underbrace{(I+MK)^{-1}MK}_{G} L\big)\tilde{\boldsymbol{e}}(i) + (I+MK)^{-1}\big(\boldsymbol{y}_0(i+1) - \boldsymbol{y}_0(i)\big) \\
&\quad - (I+MK)^{-1}M\big(\boldsymbol{u}_0(i+1) - \boldsymbol{u}_0(i)\big)
\end{aligned} \tag{4.46}$$

which we can express recursively as

$$\begin{aligned}
\tilde{\boldsymbol{e}}(i+1) &= (I - GL)^{i+1}\tilde{\boldsymbol{e}}(0) \\
&\quad + \sum_{j=0}^{i} (I - GL)^j (I+MK)^{-1}(-M, I)\big(\boldsymbol{w}_0(i+1-j) - \boldsymbol{w}_0(i-j)\big)
\end{aligned}$$

where $\boldsymbol{w}_0(i) = \begin{pmatrix} \boldsymbol{u}_0(i) \\ \boldsymbol{y}_0(i) \end{pmatrix}$. It can be shown

$$\begin{aligned}
\sum_{i=0}^{k} \tilde{\boldsymbol{e}}(i) &= \tilde{\boldsymbol{e}}(0) + \sum_{i=0}^{k-1} \tilde{\boldsymbol{e}}(i+1) \\
&= \tilde{\boldsymbol{e}}(0) + \sum_{i=0}^{k-1} (I - GL)^{i+1} \tilde{\boldsymbol{e}}(0) \\
&\quad + \sum_{i=0}^{k-1} \sum_{j=0}^{i} (I - GL)^{j} (I + MK)^{-1} (-M, I) \big(\boldsymbol{w}_0(i+1-j) - \boldsymbol{w}_0(i-j) \big) \\
&= \sum_{i=0}^{k} (I - GL)^{i} \tilde{\boldsymbol{e}}(0) \\
&\quad + \sum_{i=0}^{k-1} \sum_{j=0}^{i} (I - GL)^{j} (I + MK)^{-1} (-M, I) \big(\boldsymbol{w}_0(i+1-j) - \boldsymbol{w}_0(i-j) \big) \\
&= \sum_{i=0}^{k} (I - GL)^{i} \tilde{\boldsymbol{e}}(0) \\
&\quad + \sum_{j=0}^{k-1} \Big\{ (I - GL)^{j} (I + MK)^{-1} (-M, I) \sum_{i=j}^{k-1} \big(\boldsymbol{w}_0(i+1-j) - \boldsymbol{w}_0(i-j) \big) \Big\} \\
&= \sum_{i=0}^{k} (I - GL)^{i} \tilde{\boldsymbol{e}}(0) \\
&\quad + \sum_{j=0}^{k-1} \Big\{ (I - GL)^{j} (I + MK)^{-1} (-M, I) \big(\boldsymbol{w}_0(k-j) - \boldsymbol{w}_0(0) \big) \Big\}
\end{aligned}$$

where we have used the identity

$$\sum_{i=0}^{k} \sum_{j=0}^{i} A^j y(i-j) = \sum_{j=0}^{k} A^j \sum_{i=0}^{k-j} y(i) = \sum_{j=0}^{k} A^j \sum_{i=j}^{k} y(i-j). \tag{4.47}$$

So that, taking $\boldsymbol{v}(0) = \boldsymbol{0}$, $\tilde{\boldsymbol{e}}(0) = (I + MK)^{-1} \big(\hat{\boldsymbol{\Phi}} + (-M, I) \boldsymbol{w}_0(0) \big)$,

$$\begin{aligned}
\boldsymbol{v}(k+1) = \boldsymbol{v}(0) + L \sum_{i=0}^{k} \tilde{\boldsymbol{e}}(i) &= L \sum_{i=0}^{k} (I - GL)^{i} (I + MK)^{-1} \hat{\boldsymbol{\Phi}} \\
&\quad + L \sum_{i=0}^{k-1} (I - GL)^{i} (I + MK)^{-1} (-M, I) \boldsymbol{w}_0(k-i).
\end{aligned}$$

Now

$$\begin{aligned}\tilde{\boldsymbol{e}}(k+1) &= \boldsymbol{y}_0(k+1) + \hat{\boldsymbol{\Phi}} - M\big(\boldsymbol{u}_0(k+1) + K\big(\boldsymbol{v}(k+1) + \tilde{\boldsymbol{e}}(k+1)\big)\big)\\ &= (I+MK)^{-1}\hat{\boldsymbol{\Phi}} + (I+MK)^{-1} \times (-M, I)\boldsymbol{w}_0(k+1) - (I+MK)^{-1}MK\boldsymbol{v}(k+1)\end{aligned} \tag{4.48}$$

Therefore

$$\boldsymbol{v}(k+1) + \tilde{\boldsymbol{e}}(k+1) = (I-G)\boldsymbol{v}(k+1) + (I+MK)^{-1}\big(\hat{\boldsymbol{\Phi}} + (-M, I)\boldsymbol{w}_0(k+1)\big).$$

We can then produce the plant input

$$\begin{aligned}\boldsymbol{u}(k+1) &= \boldsymbol{u}_0(k+1) + K\big(\boldsymbol{v}(k+1) + \tilde{\boldsymbol{e}}(k+1)\big)\\ &= \boldsymbol{u}_0(k+1) + K(I+MK)^{-1}\big(\hat{\boldsymbol{\Phi}} + (-M, I)\boldsymbol{w}_0(k+1)\big) + K(I-G)L\\ &\quad \times \Bigg(\sum_{i=0}^{k}(I-GL)^i(I+MK)^{-1}\hat{\boldsymbol{\Phi}}\\ &\qquad + \sum_{i=0}^{k-1}(I-GL)^i(I+MK)^{-1}(-M, I)\boldsymbol{w}_0(k-i)\Bigg)\\ &= (I+KM)^{-1}(I, K)\boldsymbol{w}_0(k+1) + K(I+MK)^{-1}\hat{\boldsymbol{\Phi}} + K(I+MK)^{-1}L\\ &\quad \times \Bigg(\sum_{i=0}^{k}(I-GL)^i(I+MK)^{-1}\hat{\boldsymbol{\Phi}} + \sum_{i=0}^{k-1}(I-GL)^i(I+MK)^{-1}(-M, I)\boldsymbol{w}_0(k-i)\Bigg)\end{aligned} \tag{4.49}$$

and if we use our earlier expression (4.15)

$$\begin{aligned}\boldsymbol{u}(k+1) &= (I+KM)^{-1}(I, K)\boldsymbol{w}_0(k+1)\\ &\quad + K(I+MK)^{-1}\hat{\boldsymbol{\Phi}} + K(I+MK)^{-1}\\ &\quad \times \Bigg(\sum_{i=0}^{k}(I-LG)^iL(I+MK)^{-1}\hat{\boldsymbol{\Phi}}\\ &\qquad + \sum_{i=0}^{k-1}(I-LG)^iL(I+MK)^{-1}(-M, I)\boldsymbol{w}_0(k-i)\Bigg).\end{aligned}$$

Hence we can define the following maps

$$\begin{aligned}&\left[\Pi_{\bar{M}//\bar{C}}\begin{pmatrix}\boldsymbol{u}_0\\ \hat{\boldsymbol{\Phi}} + \boldsymbol{y}_0\end{pmatrix}\right](k+1)\\ &= \begin{pmatrix}I\\ M\end{pmatrix}\Big((I+KM)^{-1}(I, K)\boldsymbol{w}_0(k+1) + K(I+MK)^{-1}\hat{\boldsymbol{\Phi}} + K(I+MK)^{-1}\end{aligned}$$

$$L\Bigg(\sum_{i=0}^{k}(I-GL)^i(I+MK)^{-1}\hat{\boldsymbol{\Phi}} + \sum_{i=0}^{k-1}(I-GL)^i(I+MK)^{-1}(-M,I)\times \boldsymbol{w}_0(k-i)\Bigg)\Bigg),$$

$$\left[\Pi_{\bar{M}//\bar{C}}\begin{pmatrix}\mathbf{0}\\ \hat{\boldsymbol{\Phi}}\end{pmatrix}\right](k+1) = \begin{pmatrix}I\\ M\end{pmatrix}K(I+MK)^{-1}\left(I+L\sum_{i=0}^{k}(I-GL)^i(I+MK)^{-1}\right)\hat{\boldsymbol{\Phi}}. \tag{4.50}$$

Therefore if (4.5) holds

$$\lim_{k\to\infty}\left[\Pi_{\bar{M}//\bar{C}}\begin{pmatrix}\mathbf{0}\\ \hat{\boldsymbol{\Phi}}\end{pmatrix}\right](k) = \begin{pmatrix}I\\ M\end{pmatrix}K(I+MK)^{-1}\big(I+L(GL)^{-1}(I+MK)^{-1}\big)\hat{\boldsymbol{\Phi}} = \begin{pmatrix}I\\ M\end{pmatrix}K(I+MK)^{-1}L(GL)^{-1}\hat{\boldsymbol{\Phi}}. \tag{4.51}$$

It follows that $\|\Pi_{\bar{M}//\bar{C}}\|_{\begin{pmatrix}\mathbf{0}\\ \hat{\boldsymbol{\Phi}}\end{pmatrix}}$ is given by

$$\sup_{\substack{\boldsymbol{w}_0\\ \|\boldsymbol{w}_0\|\neq 0}} \frac{\Big(\sum_{k=-1}^{\infty}\Big\|\begin{pmatrix}I\\ M\end{pmatrix}\Big(K(I+MK)^{-1}L\sum_{i=0}^{k-1}(I-GL)^i(I+MK)^{-1}(-M,I)\boldsymbol{w}_0(k-i) + (I+KM)^{-1}(I,K)\boldsymbol{w}_0(k+1)\Big)\Big\|^2\Big)^{1/2}}{\Big(\sum_{k=0}^{\infty}\|\boldsymbol{w}_0(k)\|^2\Big)^{1/2}} \tag{4.52}$$

Hence an upper bound on $\|\Pi_{\bar{M}//\bar{C}}\|_{\begin{pmatrix}\mathbf{0}\\ \hat{\boldsymbol{\Phi}}\end{pmatrix}}$ is

$$\sup_{\substack{\boldsymbol{w}_0\\ \|\boldsymbol{w}_0\|\neq 0}} \frac{\Big(\sum_{k=0}^{\infty}\Big\|\begin{pmatrix}I\\ M\end{pmatrix}K(I+MK)^{-1}L\sum_{i=0}^{k}(I-GL)^i(I+MK)^{-1}(-M,I)\boldsymbol{w}_0(k-i)\Big\|^2\Big)^{1/2}}{\Big(\sum_{k=0}^{\infty}\|\boldsymbol{w}_0(k)\|^2\Big)^{1/2}} + \sup_{\substack{\boldsymbol{w}_0\\ \|\boldsymbol{w}_0\|\neq 0}} \frac{\Big(\sum_{k=0}^{\infty}\Big\|\begin{pmatrix}I\\ M\end{pmatrix}(I+KM)^{-1}(I,K)\boldsymbol{w}_0(k)\Big\|^2\Big)^{1/2}}{\Big(\sum_{k=0}^{\infty}\|\boldsymbol{w}_0(k)\|^2\Big)^{1/2}}. \tag{4.53}$$

Consider the lifted gain bound $\|\Pi_{\bar{M}//\bar{K}}\|_{\begin{pmatrix}\mathbf{0}\\ \hat{\boldsymbol{\Phi}}\end{pmatrix}}$, corresponding to $L = 0$. From (4.50)

$$\left[\Pi_{\bar{M}//\bar{K}}\begin{pmatrix}\boldsymbol{u}_0\\ \hat{\boldsymbol{\Phi}}+\boldsymbol{y}_0\end{pmatrix}\right](k+1) = \begin{pmatrix}I\\ M\end{pmatrix}\left((I+KM)^{-1}(I,K)\boldsymbol{w}_0(k+1) + K(I+MK)^{-1}\hat{\boldsymbol{\Phi}}\right)$$
$$\left[\Pi_{\bar{M}//\bar{K}}\begin{pmatrix}\mathbf{0}\\ \hat{\boldsymbol{\Phi}}\end{pmatrix}\right](k+1) = \begin{pmatrix}I\\ M\end{pmatrix}K(I+MK)^{-1}\hat{\boldsymbol{\Phi}} \tag{4.54}$$

so that, recalling the definition of $b_{M//K}$ from Theorem 3.3

$$\begin{aligned}
\|\Pi_{\bar{M}//\bar{K}}\|_{\begin{pmatrix}\mathbf{0}\\ \hat{\boldsymbol{\Phi}}\end{pmatrix}} &= \sup_{\substack{\boldsymbol{w}_0\\ \|\boldsymbol{w}_0\|\neq 0}} \frac{\left(\sum_{k=0}^{\infty}\left\|\begin{pmatrix}I\\ M\end{pmatrix}(I+KM)^{-1}(I,K)\boldsymbol{w}_0(k)\right\|^2\right)^{1/2}}{\left(\sum_{k=0}^{\infty}\|\boldsymbol{w}_0(k)\|^2\right)^{1/2}}\\
&\leq \sup_{\substack{\boldsymbol{w}_0\\ \|\boldsymbol{w}_0\|\neq 0}} \frac{\left\|\begin{pmatrix}I\\ M\end{pmatrix}(I+KM)^{-1}(I,K)\right\|\left(\sum_{k=0}^{\infty}\|\boldsymbol{w}_0(k)\|^2\right)^{1/2}}{\left(\sum_{k=0}^{\infty}\|\boldsymbol{w}_0(k)\|^2\right)^{1/2}}\\
&= \left\|\begin{pmatrix}I\\ M\end{pmatrix}(I+KM)^{-1}(I,K)\right\|\\
&= \sup_{\|\boldsymbol{w}_0(k)\|\neq 0} \frac{\left\|\Pi_{M//K}\begin{pmatrix}\boldsymbol{u}_0(k)\\ \hat{\boldsymbol{\Phi}}+\boldsymbol{y}_0(k)\end{pmatrix} - \Pi_{M//K}\begin{pmatrix}\mathbf{0}\\ \hat{\boldsymbol{\Phi}}\end{pmatrix}\right\|}{\|\boldsymbol{w}_0(k)\|}\\
&= \|\Pi_{M//K}\|_{\begin{pmatrix}\mathbf{0}\\ \hat{\boldsymbol{\Phi}}\end{pmatrix}}\\
&= b_{M//K}.
\end{aligned} \tag{4.55}$$

Now consider the numerator of the left-hand term in (4.53)

$$\begin{aligned}
&\left(\sum_{k=0}^{\infty}\left\|\begin{pmatrix}I\\ M\end{pmatrix}K(I+MK)^{-1}L\sum_{i=1}^{k}(I-GL)^{i-1}(I+MK)^{-1}(-M,I)\boldsymbol{w}_0(k+1-i)\right\|^2\right)^{1/2}\\
&\leq \left\|\begin{pmatrix}I\\ M\end{pmatrix}K(I+MK)^{-1}L\right\|\left(\sum_{k=0}^{\infty}\sum_{n=0}^{k-1}\left\|(I-GL)^{k-n-1}(I+MK)^{-1}(-M,I)\boldsymbol{w}_0(n)\right\|^2\right)^{1/2}\\
&\leq \left\|\begin{pmatrix}I\\ M\end{pmatrix}K(I+MK)^{-1}L\right\|\left(\sum_{n=0}^{\infty}\sum_{k=n+1}^{\infty}\left\|(I-GL)^{k-n-1}(I+MK)^{-1}(-M,I)\boldsymbol{w}_0(n)\right\|^2\right)^{1/2}\\
&\leq \left\|\begin{pmatrix}I\\ M\end{pmatrix}K(I+MK)^{-1}L\right\|\|(I+MK)^{-1}(-M,I)\|\left(\sum_{j=0}^{\infty}\|(I-GL)^{j}\|^2\right)^{\frac{1}{2}}\left(\sum_{n=0}^{\infty}\|\boldsymbol{w}_0(n)\|^2\right)^{\frac{1}{2}}
\end{aligned}$$

Provided $\|I - GL\| < 1$, it follows that $\left\|(I-GL)^j\right\| \leq \|I - GL\|^j$ for $0 \leq j \leq \infty$. Hence an upper bound for the left-hand term in (4.53) is

$$\left\|\begin{pmatrix} I \\ M \end{pmatrix} K(I+MK)^{-1}L\right\| \|(I+MK)^{-1}(-M, I)\| \left(\sum_{j=0}^{\infty} \left\|(I-GL)^j\right\|^2\right)^{1/2}$$

$$\leq \frac{\left\|\begin{pmatrix} I \\ M \end{pmatrix} K(I+MK)^{-1}L\right\| \|(I+MK)^{-1}(-M, I)\|}{1 - \|I - GL\|}. \tag{4.56}$$

Combining (4.53), (4.55) and (4.56) results in the final expression

$$\|\Pi_{\bar{M}//\bar{C}}\|_{\begin{pmatrix} \mathbf{0} \\ \hat{\boldsymbol{\Phi}} \end{pmatrix}} \leq b_{M//K} + \frac{\left\|\begin{pmatrix} I \\ M \end{pmatrix} K(I+MK)^{-1}L\right\| \|(I+MK)^{-1}(-M, I)\|}{1 - \|I - GL\|}. \tag{4.57}$$

Note that if instead of $\|I - GL\| < 1$, we have $\|I - LG\| < 1$, (4.57) is exchanged for

$$\|\Pi_{\bar{M}//\bar{C}}\|_{\begin{pmatrix} \mathbf{0} \\ \hat{\boldsymbol{\Phi}} \end{pmatrix}} \leq b_{M//K} + \frac{\left\|\begin{pmatrix} I \\ M \end{pmatrix} K(I+MK)^{-1}\right\| \|L(I+MK)^{-1}(-M, I)\|}{1 - \|I - LG\|}.$$

□

If the true plant N is also linear, then condition (4.42) simplifies to $\|N - M\| < b^{-1}_{\bar{M}//\bar{C}}$ which means the proposed controller stabilizes a 'ball' of plants in the uncertainty space centred about M. The radius of this ball is $b^{-1}_{M//K}$ in the case of feedback action alone, but reduces when ILC action is added (due to the introduction of the additional term on the right hand side of (4.44)). Note that the right hand side of (4.44) is always finite if $\|L\|$ is bounded, so the radius of this ball is always greater than zero and increases in size as $\|L\|$ reduces to zero. This means that Theorem 4.6 provides a transparent method of weighting performance against robustness. Theorem 4.6 can also be applied to the case of a nonlinear feedback controller K as follows:

Theorem 4.7 *Let K be a stable nonlinear operator, then the true system $[\bar{N}, \bar{C}]$ is stable if*

$$\sup_{k \in \mathbb{N}_+} \|N|_{\bar{\boldsymbol{u}}_1(k)} - M|_{\bar{\boldsymbol{u}}(k)}\| < b^{-1}_{\bar{C}_{lin}, \bar{M}} \left(1 - b_{\bar{M}, \bar{C}_{lin}} \sup_{k \in \mathbb{N}_+} \|K|_{\boldsymbol{e}_k + \boldsymbol{v}_k} - K_{lin}\|\right) \tag{4.58}$$

where $b_{\bar{M}, \bar{C}_{lin}}$, $b_{\bar{C}_{lin}, \bar{M}}$ are the gain bounds for $[M, K_{lin}]$, which is obtained by linearizing the system about operating point $\boldsymbol{v}_k$. In particular, $b_{\bar{M}, \bar{C}_{lin}}$ is

computed using (4.44), and

$$b_{\bar{C}_{lin},\bar{M}} = b_{\bar{M},\bar{C}_{lin}} - b_{M//K} + b_{K//M} \tag{4.59}$$

with

$$b_{K//M} = b_{\bar{K}//\bar{M}} = \left\| \begin{pmatrix} K \\ I \end{pmatrix} (I + MK)^{-1}(-M, I) \right\|. \tag{4.60}$$

Proof Since L is designed using a linearized system model $G_{\mathscr{P}}|_{\hat{\boldsymbol{\Phi}}+\boldsymbol{v}_k}$ corresponding to $[\bar{M}, \bar{C}_{lin}]$, this motivates using the linear components of $\bar{C}_{lin}$, denoted M and K_{lin}, within Theorem 4.6 to provide a robust stability bound computed using (4.44). However, in this case the robustness result of Theorem 3.3 is no longer valid as there is also a mismatch between K and K_{lin}. We therefore apply the more general stability condition of [24] which results in

$$\delta(\bar{C}_{lin}, \bar{C})\|\Pi_{\bar{C}//\bar{M}}\| + \delta(\bar{M}, \bar{N})\|\Pi_{\bar{M}//\bar{C}}\| < 1. \tag{4.61}$$

As K is bounded it can be shown that

$$\delta(\bar{C}_{lin}, \bar{C}) \leq \sup_{\|\boldsymbol{u}\|\neq 0} \frac{\|(K|_{\boldsymbol{e}_k+\boldsymbol{v}_k} - K_{lin})\boldsymbol{u}\|}{\|\boldsymbol{u}\|} \tag{4.62}$$

and $\Pi_{\bar{C}//\bar{M}} : \begin{pmatrix} \boldsymbol{u}_0 \\ \boldsymbol{y}_0 + \hat{\boldsymbol{\Phi}} \end{pmatrix} \mapsto \begin{pmatrix} \tilde{\boldsymbol{u}} \\ \tilde{\boldsymbol{e}} \end{pmatrix}$ can be calculated using (4.48) and $\tilde{\boldsymbol{u}}(k+1) = K(\tilde{\boldsymbol{e}}(k+1) + \boldsymbol{v}(k+1))$ to give

$$\begin{pmatrix} \tilde{\boldsymbol{u}} \\ \tilde{\boldsymbol{e}} \end{pmatrix} = \begin{pmatrix} K \\ I \end{pmatrix} (I + KM)^{-1}\left(\hat{\boldsymbol{\Phi}} + (-M, I)\boldsymbol{w}_0(k+1)\right) + \begin{pmatrix} K(I+MK)^{-1} \\ -(I+MK)^{-1}MK \end{pmatrix} \boldsymbol{v}(k+1)$$

Proceeding as in the proof of Theorem 4.6, we result in

$$\|\Pi_{\bar{C}//\bar{M}}\|_{\begin{pmatrix} \boldsymbol{0} \\ \hat{\boldsymbol{\Phi}} \end{pmatrix}} \leq b_{K//M} + \frac{\left\| \begin{pmatrix} I \\ -M \end{pmatrix} K(I+MK)^{-1} \right\| \|L\| \left\| (I+MK)^{-1}(-M, I) \right\|}{1-\gamma}$$

where the gain bound for the feedback controller alone (i.e. with $L = 0$) is given by (4.60). We then use (4.44) to give $\|\Pi_{\bar{C}//\bar{M}}\|_{\begin{pmatrix} \boldsymbol{0} \\ \hat{\boldsymbol{\Phi}} \end{pmatrix}} \leq b_{\bar{C}_{lin}//\bar{M}} = b_{K//M} + (b_{\bar{M}//\bar{C}_{lin}} - b_{M//K})$ which produces (4.58). □

The previous results provide explicit conditions guaranteeing robust performance, but also motivate the following design procedure:

Procedure 3 (Design guidelines for robust stability)

Feedback controller design: Design stabilizing feedback controller K to minimize $b_{M//K}$ using the procedure of Chap. 3, if necessary sacrificing performance for stability. Note that if M and K are linear then $b_{M//K}$ is given by (4.45).

ILC design: Design L to satisfy condition (4.5) or (4.8) of Theorem 4.1, the former guaranteeing nominal convergence to zero error. To maximize overall robustness requires minimizing the right hand side of (4.44). This requires balancing the minimization of $\|L\|$ and $\|I - \bar{G}_{\mathscr{P}} L\|$ (or $\|I - L\bar{G}_{\mathscr{P}}\|$).

Add robustness filter: A robustness filter, F, can be added to update (4.4), giving

$$\boldsymbol{v}_{k+1} = F(\boldsymbol{v}_k + L_k(\boldsymbol{e}_k)_{\mathscr{P}}), \quad k = 0, 1, \ldots$$

in order to restrict learning to below a frequency cut-off, so that the competing objectives above are easier to satisfy. This results in only minor modification of the bound $b_{\bar{M}//\bar{C}}$ in Theorems 4.6 and 4.7.

Minimize model uncertainty: All stabilizing K and L satisfying (4.41) can tolerate a degree of plant uncertainty (since $b_{\bar{M}//\bar{C}}$ is finite). This means that if the true plant is contained within a ball of radius $b^{-1}_{\bar{M}//\bar{C}}$ centred on M in the uncertainty space, then the true closed-loop system $[N, K]$ will be stable. It is therefore important to obtain the most accurate model possible (or most appropriate linearization point) for use in control design.

Using a nonlinear K: If K is nonlinear then Theorem 4.7 shows that the requirements of reducing both model uncertainty, $\delta_k(M, N)$, and nominal gain bound, $b_{\bar{M},\bar{C}}$, do not change. A nonlinear K may enable $b_{\bar{M},\bar{C}}$ to be reduced, but adds conservatism to the robust stability result (via (4.58)). Therefore the most appropriate linearization point to compute K_{lin} is required.

Theorems 4.6 and 4.7 provide precise robust performance guarantees which confirm that ILC can utilize the available robustness margins to significantly improve tracking capability. Having specified a general bound on the allowable difference between the unlifted model M and true plant N, we can now apply these to the most common sources of modeling uncertainty. The next result illustrates this approach, and is an extension of Proposition 3.4.

Proposition 4.1 *Let the plant satisfy Proposition 3.2, and suppose linear approximations to the dynamics H_{RB}, tendon function F_m and muscle curve $\boldsymbol{h}_{IRC}$, given by $\overline{H_{RB}F_m}$ and $\bar{\boldsymbol{h}}_{IRC}$ respectively, are used to construct the nominal model $M = \overline{H_{RB}F_m}H_{LAD}\bar{\boldsymbol{h}}_{IRC}$, which is subsequently used to design feedback controller K and ILC operator L satisfying Theorem 4.5. Then the system has a robust stability margin, and in particular is stable if*

$$\Delta_{IRC} < \sup_{k\in\mathbb{N}_+} \frac{b_{\bar{M}//\bar{C}}^{-1} - \Delta_{RB}\|\bar{\boldsymbol{h}}_{IRC}\|}{\|H_{RB}F_m|_{\bar{\boldsymbol{w}}_1(k)}\|} \tag{4.63}$$

where the model mismatch is characterised by

$$\Delta_{IRC} = \max_i \sup_{\substack{\|\boldsymbol{u}\|\neq 0\\ k\in\mathbb{N}_+}} \frac{\|(\boldsymbol{h}_{IRC,i}|_{(\bar{\boldsymbol{u}}_1(k))_i} - \bar{\boldsymbol{h}}_{IRC,i})\boldsymbol{u}\|}{\|\boldsymbol{u}\|}$$

and the linearization model accuracy is characterised by

$$\Delta_{RB} = \sup_{\substack{\|u\|\neq 0\\ k\in\mathbb{N}_+}} \frac{\|(H_{RB}F_m(\boldsymbol{\Phi},\dot{\boldsymbol{\Phi}})|_{\bar{\boldsymbol{w}}_1(k)} - \overline{H_{RB}F_m})\boldsymbol{u}\|}{\|\boldsymbol{u}\|}.$$

Proof We apply the forms $N|_{\bar{\boldsymbol{u}}_1(k)} = H_{RB}F_m(\boldsymbol{\Phi},\dot{\boldsymbol{\Phi}})|_{\bar{\boldsymbol{w}}_1}H_{LAD}\boldsymbol{h}_{IRC}|_{\boldsymbol{u}_1(k)}$ and $M|_{\bar{\boldsymbol{u}}(k)} = \overline{H_{RB}F_m}H_{LAD}\bar{\boldsymbol{h}}_{IRC}$ within definition (4.39). From (4.42) this gives requirement

$$\sup_{\substack{\|u\|\neq 0\\ k\in\mathbb{N}_+}} \frac{\|(H_{RB}F_m(\boldsymbol{\Phi},\dot{\boldsymbol{\Phi}})|_{\bar{\boldsymbol{w}}_1(k)}H_{LAD}\boldsymbol{h}_{IRC}|_{\boldsymbol{u}_1(k)} - \overline{H_{RB}F_m}H_{LAD}\bar{\boldsymbol{h}}_{IRC})\boldsymbol{u}\|}{\|\boldsymbol{u}\|} < b_{\bar{M}//\bar{C}}^{-1}.$$

Taking, without loss of generality $\|H_{LAD}\| = 1$, the left hand side is bounded by

$$\sup_{\|u\|\neq 0} \frac{\|\bar{\boldsymbol{h}}_{IRC}\boldsymbol{u}\|}{\|\boldsymbol{u}\|} \sup_{\substack{\|\boldsymbol{u}\|\neq 0\\ k\in\mathbb{N}_+}} \frac{\|(H_{RB}F_m(\boldsymbol{\Phi},\dot{\boldsymbol{\Phi}})|_{\bar{\boldsymbol{w}}_1(k)} - \overline{H_{RB}F_m})\boldsymbol{u}\|}{\|\boldsymbol{u}\|}$$
$$+ \sup_{\substack{\|u\|\neq 0\\ k\in\mathbb{N}_+}} \frac{\|(\boldsymbol{h}_{IRC}|_{\boldsymbol{u}_1(k)} - \bar{\boldsymbol{h}}_{IRC})\boldsymbol{u}\|}{\|\boldsymbol{u}\|} \sup_{\substack{\|\boldsymbol{u}\|\neq 0\\ k\in\mathbb{N}_+}} \frac{\|H_{RB}F_m(\boldsymbol{\Phi},\dot{\boldsymbol{\Phi}})|_{\bar{\boldsymbol{w}}_1(k)}\|}{\|\boldsymbol{u}\|}$$

□

As in Theorem 3.4, this result bounds the effect of muscle fatigue which is embedded within the term Δ_{IRC}. It also bounds the accuracy of the linearized system that is used in the control procedure of Theorem 4.1. The feedback and/or ILC design can always

be modified to ensure condition (4.63) is satisfied, e.g. by sacrificing convergence speed, tracking accuracy of the first ILC attempt, and/or range of frequencies over which convergence occurs.

4.5 Conclusions

This chapter has introduced a feedforward signal into the feedback control scheme in order to improve the accuracy with which ES is able to assist joint angles in the human arm to track a specified reference trajectory. The framework 'learns' from previous attempts at the task, and thereby exploits the inherently repetitive nature of rehabilitation. General guidelines for designing the ILC operator have been given, together with conditions for convergence to zero tracking error.

This chapter has also extended the robustness analysis of the previous chapter to produce a powerful robust performance framework for combined feedback and ILC design. In particular, the design of each control component can be separated, with each utilizing the available robustness margins of the other to maximize overall performance.

The combined feedback and ILC framework is next employed in practice within a clinical rehabilitation programme with neurologically impaired participants.

References

1. D.A. Bristow, M. Tharayil, A.G. Alleyne, A survey of iterative learning control a learning-based method for high-performance tracking control. IEEE Control Syst. Mag. **26**(3), 96–114 (2006)
2. H.S. Ahn, Y. Chen, K.L. Moore, Iterative learning control: brief survey and categorization. IEEE Trans. Syst. Man Cybern. Part C: Appl. Rev. **37**(6), 1099–1121 (2007)
3. T. Seel, T. Schauer, J. Raisch, Iterative learning control for variable pass length systems, in *IFAC World Congress* (2011), pp. 4880–4885
4. H. Nahrstaedt, T. Schauer, S. Hesse, J. Raisch, Iterative learning control of a gait neuroprosthesis. Automatisierungs **56**(9), 494–501 (2008)
5. J. Bae, M. Tomizuka, A gait rehabilitation strategy inspired by an iterative learning algorithm. Mechatronics **22**(2), 213–221 (2012)
6. P.M. Aubin, M.S. Cowley, W.R. Ledoux, Gait simulation via a 6-DOF parallel robot with iterative learning control. IEEE Trans. Biomed. Eng. **55**, 1237–1240 (2008)
7. A.M. Hughes, C.T. Freeman, J.H. Burridge, P.H. Chappell, P. Lewin, E. Rogers, Feasibility of iterative learning control mediated by functional electrical stimulation for reaching after stroke. J. Neurorehabilitation Neural Repair **23**(6), 559–568 (2009)
8. C.T. Freeman, A.M. Hughes, J.H. Burridge, P.H. Chappell, P.L. Lewin, E. Rogers, A model of the upper extremity using FES for stroke rehabilitation. ASME J. Biomech. Eng. **131**(3), 031006-1–031006-10 (2009)
9. C.T. Freeman, A.M. Hughes, J.H. Burridge, P.H. Chappell, P.L. Lewin, E. Rogers, Iterative learning control of FES applied to the upper extremity for rehabilitation. Control Eng. Pract. **17**(3), 368–381 (2009)

10. C.T. Freeman, D. Tong, K. Meadmore, Z. Cai, E. Rogers, A.M. Hughes, J.H. Burridge, Phase-lead iterative learning control algorithms for functional electrical stimulation based stroke rehabilitation. Proc. Inst. Mech. Eng. Part I: J. Syst. Control Eng. **225**(6), 850–859 (2011)
11. K.L. Meadmore, A.-M. Hughes, C.T. Freeman, Z. Cai, D. Tong, J.H. Burridge, E. Rogers, Functional electrical stimulation mediated by iterative learning control and 3*d* robotics reduces motor impairment in chronic stroke. J. Neuroeng. Rehabil. **32**(9), 1–11 (2012)
12. K.L. Meadmore, T. Exell, E. Hallewell, A.-M. Hughes, C.T. Freeman, M. Kutlu, V. Benson, E. Rogers, J.H. Burridge, The application of precisely controlled functional electrical stimulation to the shoulder, elbow and wrist for upper limb stroke rehabilitation: a feasibility study. J. NeuroEng. Rehabil. **11**, 105 (2014)
13. P.J. Olver, Applied mathematics lecture notes. Technical report (2012)
14. J.M. Ortega, W.C. Rheinboldt, *Iterative Solution of Nonlinear Equations in Several Variables* (Academic Press, London, 1970)
15. N. Amann, D.H. Owens, E. Rogers, Iterative learning control using optimal feedback and feedforward actions. Int. J. Control **65**, 277–293 (1996)
16. S. Gunnarsson, M. Norrlof, On the design of ILC algorithms using optimization. Automatica **37**(12), 2011–2016 (2001)
17. J.H. Lee, K.S. Lee, W.C. Kim, Model-based iterative learning control with a quadratic criterion for time-varying linear systems. Automatica **36**, 641–657 (2000)
18. K.L. Barton, A.G. Alleyne, A norm optimal approach to time-varying ILC with application to a multi-axis robotic testbed. IEEE Trans. Control Syst. Technol. **19**(1), 166–180 (2011)
19. T. Lin, D.H. Owens, J.J. Hatonen, Newton method based iterative learning control for discrete non-linear systems. Int. J. Control **79**(10), 1263–1276 (2006)
20. C.T. Freeman, Constrained point-to-point iterative learning control with experimental verification. Control Eng. Pract. **20**(5), 489–498 (2012)
21. D.H. Owens, J.J. Hätönen, S. Daley, Robust monotone gradient-based discrete-time iterative learning control. Int. J. Robust Nonlinear Control **19**, 634–661 (2009)
22. N. Amann, D.H. Owens, E. Rogers, Iterative learning control for discrete-time systems with exponential rate of convergence. IEE Proc. Control Theory Appl. **143**(2), 217–224 (1996)
23. R. Bradley, The robust stability of iterative learning control. Ph.D. thesis, Electronics and Computer Science, University of Southampton (2010)
24. T.T. Georgiou, M.C. Smith, Robustness analysis of nonlinear feedback systems: an input-output approach. IEEE Trans. Autom. Control **42**(9), 1200–1221 (1997)

Chapter 5
Clinical Application: Multiple Sclerosis

Multiple Sclerosis (MS) is a chronic, degenerative disorder affecting the central nervous system. It leads to a wide range of symptoms including upper limb weakness which is experienced by a large percentage of people with MS (pwMS). Despite advances in pharmaceutical options to reduce the number and severity of relapses, rehabilitation continues to play an essential role in reducing motor disability [1], however few studies relate to rehabilitation of the upper limb in MS [2].

To address this, we employ the ES control framework developed in Chaps. 3 and 4 to assist pwMS in performing virtual reality (VR) training tasks. Stimulation is applied to the shoulder and elbow, and additional support is provided using the instrumented passive robotic support described in Sect. 3.2. A clinical feasibility study is conducted using the system with pwMS to establish the efficacy of the system for improving upper limb function for neurologically impaired participants. More detailed results of the study and in-depth analysis can be found in [3].

5.1 System Description and Set-Up

The system elements are shown schematically in Fig. 5.1. The passive robotic support described in Sects. 3.2 and 4.2 provides kinematic data to a real-time processor that interfaces with custom ES hardware, a VR task display, and a graphical user interface. The participant's screen (located on their hemiplegic side) shows the trajectory to be tracked and a representation of the participant's arm (which mirrors the participant's movements in real-time). The support and trajectory task are depicted in Fig. 5.2. The display provides the participant with immediate visual feedback and facilitates motivation for the tracking task. The second screen displays a custom graphical user interface which is used by the therapist to select the tasks and adjust the parameters used by the ES control system.

Since pwMS typically experience a weakness in arm extension, ES is applied to the anterior deltoid muscle and to the triceps to assist shoulder and elbow extension respectively. The combined support and stimulated arm system is represented

C. Freeman, *Control System Design for Electrical Stimulation in Upper Limb Rehabilitation*, DOI 10.1007/978-3-319-25706-8_5

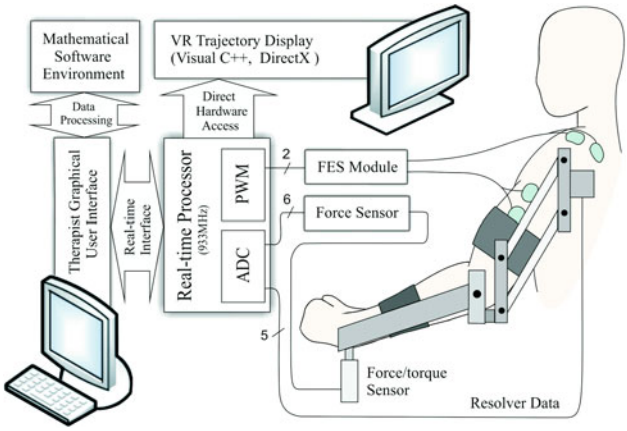

Fig. 5.1 Signal flow diagram showing system components: passive robot; real-time processor; ES hardware; therapist and participant displays

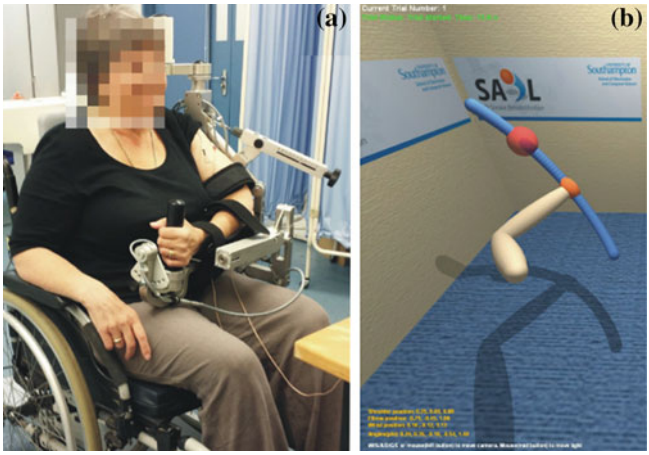

Fig. 5.2 **a** PwMS using mechanical support with ES applied to her left triceps and anterior deltoid muscles, **b** A monitor shows the trajectory task (*blue*) that the participant needs to follow with their arm (*white*) with a ball (*orange*) indicating they are on target for this reaching movement

using the anthropomorphic model of Sect. 2.2.5. Using this model, the ES control scheme comprises the combined input-output linearizing feedback controller and feedforward ILC scheme described in Sect. 4.2. Specifically NOILC update (4.32) was used with weights Q and R chosen to balance accuracy of task completion with the amount of ES applied to assist the participant's movement.

Following ethical approval (FoHS ETHICS-2013-5429) and written consent, five pwMS were recruited from local MS societies. Each attended one pilot, two assessment and eighteen intervention sessions with data collection performed by an

experienced physiotherapist. In the pilot session the electrodes were placed on the anterior deltoid and the triceps. The pulsewidth was set at a maximum value of 300 μs and the participant gradually increased the ES amplitude applied to each muscle until they reached a comfortable level that produced movement. The pulsewidth was then reduced to zero, and the stimulation amplitudes fixed for the remainder of each session to ensure comfort and safety. The procedure of Sect. 2.2.5 was used to identify the system model used throughout the intervention. During each of the 18 one-hour intervention sessions that followed, the workspace was identified, and the stimulation levels then set. The participant then practiced a minimum of six trajectories, each repeated six times, with a rest period of 2–10 s between each attempt. The reaching tasks comprised the nine reaching movements shown in Fig. 4.2, which were scaled to fit within the workspace to ensure a safe range of practice.

5.1.1 Outcome Measures

A primary outcome measure was the accuracy of unassisted task tracking over the treatment period. This was assessed by each participant tracking the same four trajectories at the beginning and end of every session, with no ES. A further primary outcome measure was the tracking performance during ES-assisted task training, and the corresponding change in amount of ES delivered over the treatment period.

Secondary outcome measures evaluated clinical changes to the upper limb and were measured in assessment sessions before treatment and within one week after the treatment period. The clinical outcome measures were: Action Research Arm Test (ARAT) [4–7]; Nine Hole Peg Test (9HPT) [7–9]; Manual Ability Measure (MAM-36) [10, 11]; and Fugl-Meyer Assessment (FMA) [7, 12–14]. Two independent physiotherapists performed the clinical assessments; the same physiotherapist performed both the pre and post assessment per participant.

The clinical outcome measures were analyzed using the Wilcoxon signed-rank test. Conforming to prior studies [15, 16], the performance of tracking with ES (assisted) and without ES (unassisted) was analyzed per participant for each of the 18 sessions by calculating best-fit linear regression slopes of performance for each task. Two-tailed t-tests were applied, and the level of significance was set at $p < 0.05$. The 95 % confidence intervals were also calculated to provide a measure of how precisely the true mean can be bounded given the limited sample size. Tracking performance for the anterior deltoid ($i = 2$) and triceps ($i = 5$) was normalized using

$$100 \times \left(1 - \frac{\|(\boldsymbol{e}_k)_i\|}{\|\hat{\boldsymbol{\Phi}}_i\|}\right), \qquad i \in \mathscr{P} = \{2, 5\}. \tag{5.1}$$

A value of 100 indicated perfect tracking and 0 corresponded to no movement.

5.2 Results

Participant characteristic data are given in Table 5.1. All participants were able to increase the number of reaching tasks practiced per session to between eight and eleven. All participants, except one, were able to receive less support from the passive robot during the reaching movements: the exception was caused by one participant's biceps tone increasing whenever the support was reduced, so her level of support was kept constant. No serious adverse events were reported during the intervention period.

5.2.1 Assisted Tracking Performance

Performance was calculated for the final attempt of every tracking task using (5.1). These performances were then averaged to calculate the overall tracking performance and the maximum amount of ES provided. Figure 5.3a, b show improved accuracy of tracking performance at both the shoulder and elbow and Fig. 5.3c, d show the percentage maximum ES required to improve participants' tracking reduced over the treatment period. Table 5.2 shows the p-value and mean slope of the tracking performance and percentage maximum ES, which was statistically significant for each muscle group: triceps (elbow) and anterior deltoid (shoulder). The mean tracking performance slopes (elbow 0.71, shoulder 1.31) correspond to an average improvement over 18 sessions of 12.8 and 23.6 % for the elbow and shoulder respectively. The mean percentage maximum ES slopes (elbow −2.6805, shoulder −2.7143) correspond to an average reduction over 18 sessions of 49.2 and 48.8 % for the elbow and shoulder respectively. This suggests that less ES was required to produce more accurate movement over the treatment period. This was confirmed when the slope of the tracking performance percentage was divided by the slope of the percentage maximum ES for each participant. Taking the mean over participants yields a statis-

Table 5.1 Socio-demographic characteristics of participants ($n = 5$)

Pt Id	MS1	MS2	MS3	MS4	MS5
Age (years)	60	40	61	51	61
Type of MS	SPMS	RRMS	PPMS	SPMS	SPMS
Years MS diagnosed	34	4	16	14	31
Female/Male	F	F	F	F	F
Side treated	L	R	L	L	R
Original dominant hand	R	R	R	R	R
Full time wheelchair user	Y	N	Y	Y	Y
Glasses	Y	N	Y	Y	Y

Pt Id–participant identification, SPMS–secondary progressive MS, RRMS–relapse-remitting MS, PPMS–primary progressive MS, F–female, M–male, L–left, R–right, Y–yes, N–no

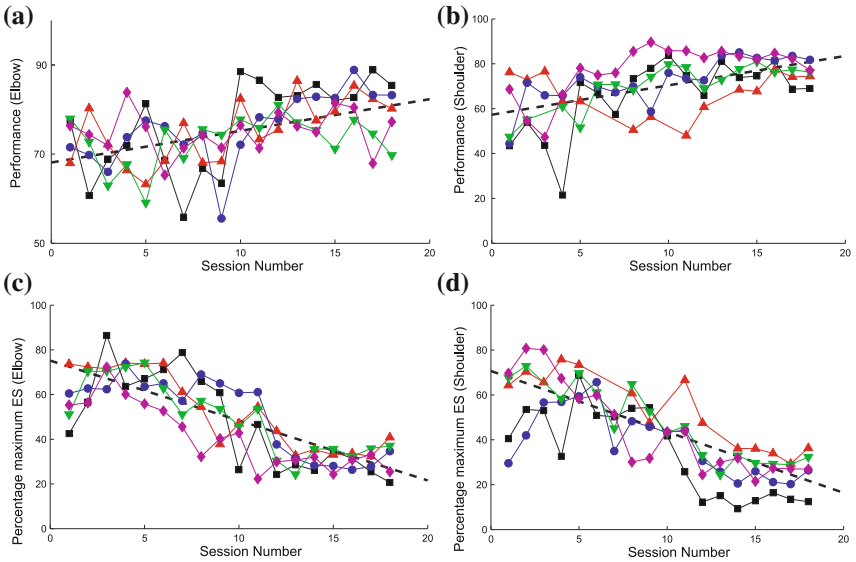

Fig. 5.3 Assisted task tracking accuracy and amount of ES, averaged over all tasks: **a** tracking accuracy at the elbow; **b** tracking accuracy at the shoulder; **c** amount of ES applied at the elbow; and **d** amount of ES applied at the shoulder. Mean of individual slopes is shown by a *dotted line*

Table 5.2 Tracking performance metrics at elbow and shoulder showing the mean slope and *p*-value of best fit linear regression lines collapsed across participants for assisted and unassisted tasks

Task	Elbow		Shoulder	
	Mean slope	*p*-value CI	Mean slope	*p*-value CI
Assisted				
Tracking perf. %	0.71	0.027 (0.13,1.28)	1.31	0.015 (0.42,2.20)
% maximum ES	−2.68	0.000 (−3.03,−2.33)	−2.71	0.000 (−3.38,−2.04)
Tracking perf. %/% max ES	0.12	0.000 (0.08,0.16)	0.19	0.021 (0.04,0.32)
Unassisted tracking perf. %				
Centre proximal	2.37	0.006 (1.10,3.62)	6.24	0.065 (−0.62,13.10)
Centre distal	1.91	0.011 (0.72,3.10)	6.31	0.051 (−0.08,12.69)
Off-centre middle %/% max ES	2.21	0.018 (0.61,3.81)	3.75	0.017 (1.09,6.40)
Far distal	2.33	0.006 (1.08,3.58)	3.33	0.004 (1.72,4.93)

Note Small slope values are due to different axis units. CI denotes 95 % confidence interval

tically significant slope (elbow mean slope = 0.12, $p < 0.001$, shoulder mean slope = 0.19, $p < 0.05$): see Table 5.2 under 'assisted'.

5.2.2 *Unassisted Tracking Performance*

Tracking performance was calculated for the four tasks, unassisted by ES, that were completed at the beginning and end of each session, and an average was taken for each task. Figures 5.4 and 5.5 show tracking performance at the elbow and shoulder respectively over the intervention. Statistically significant improved tracking accuracy for all four tracking tasks was identified across all participants at the elbow and for two tasks at the shoulder. Table 5.2 shows the p-value and mean slope of these unassisted tasks. The positive mean slopes of all the unassisted tasks correspond to performance increases of between 34.38 and 113.58 % over the intervention.

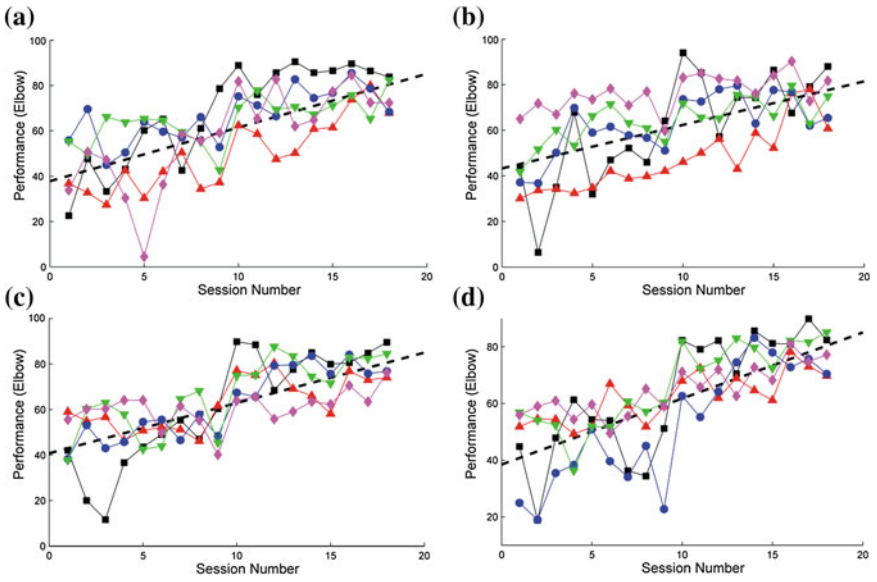

Fig. 5.4 Unassisted task tracking accuracy at the elbow. Each participant's performance is shown as a function of session for the four tracking tasks, before/after the intervention. The four tracking tasks are: **a** centre-proximal, **b** centre-distal, **c** off-centre-middle, and **d** far-distal

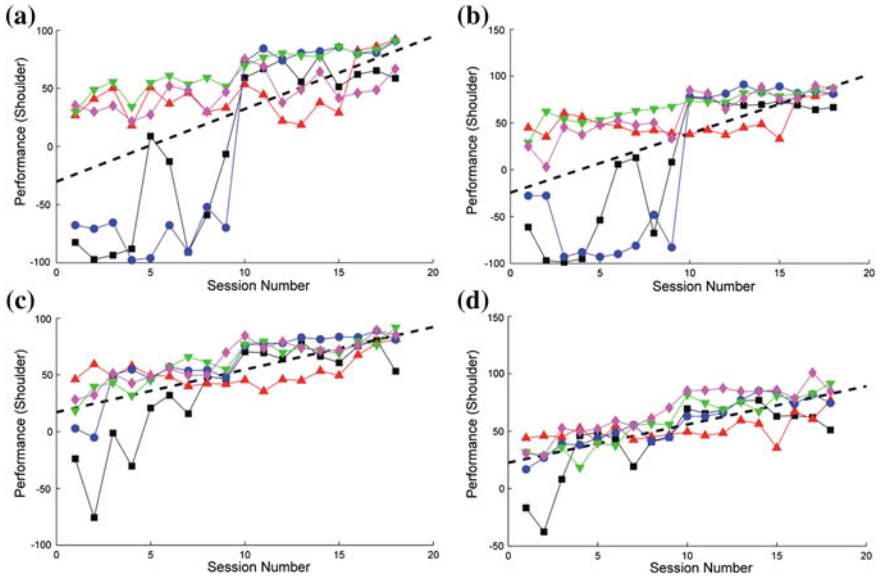

Fig. 5.5 Unassisted task tracking accuracy at the shoulder. Each participant's performance is shown as a function of session for the four tracking tasks, before/after the intervention. The four tracking tasks are: **a** centre-proximal, **b** centre-distal, **c** off-centre-middle, and **d** far-distal

5.2.3 Clinical Outcome Measures

All clinical outcome measures improved after the intervention period (Table 5.3). Improvements were seen at: impairment level, FMA increased by 6 (5.5) points from 44.8 (5.8) to 50.8 (8.2) out of a maximum score of 66; perceived ability, MAM-36 measure [11] increased by 3.6 (8.1) from 46.8 (10) to 50.4 (8); and actual ability in arm function, ARAT increased by 0.6 (3.7) points from 45.6 (10.5) to 50.8 (8.2) out of a maximum score of 57. The 9HPT time decreased from 145.3 (96) to 116.3 (88). Only the proximal arm section of the FMA, where the intervention was aimed, identified statistically significant improvement ($z = -2.06$, $p = 0.039$) with an improvement of 5.6 (3.9) points from 22.4 (4.1) to 28 (5.4) out of a possible 36 points. The distal arm section of the FMA was not trained and did not significantly improve, suggesting that specificity in training is required.

5.3 Discussion

The main aim of this study was to determine the feasibility and effectiveness of using the training system for pwMS; this is the first time passive robotic arm support has been combined with ES to improve movement quality for this user group, and the first

Table 5.3 Clinical outcome results showing baseline and post-intervention scores for five PwMS

Pt ID[1]		MS1	MS2	MS3	MS4	MS5	Mean (SD)	p-value	% change[2]
MAM-36 %[3]	B'line	40	56	59	37	42	46.8 (9.99)	0.345	3.6
	Post	57	57	54	39	45	50.4 (8.05)		
ARAT (57)[4]	B'line	56	57	33	42	40	45.6 (10.50)	1.0	1.05
	Post	53	57	33	41	47	46.2 (9.55)		
FMA (66)[4]	B'line	54	46	44	41	39	44.8 (5.81)	0.078	9.09
	Post	64	50	43	45	52	50.8 (8.23)		
FMA prox' arm (36)[4,5]	B'line	30	23	20	18	21	22.4 (4.62)	0.039	15.56
	Post	35	28	21	23	33	28.0 (6.08)		
FMA distal arm (30)[4,6]	B'line	24	23	24	23	18	22.4 (2.5)	0.891	1.33
	Post	29	22	22	22	19	22.8 (3.7)		
9HPT (300 secs)[7]	B'line	64	220	237	utc[8]	70	145.3 (96.39)	0.465	8.17
	Post	229	143	43	utc[8]	78	116.3 (87.91)		

[1]participant identification [2]change in score divided by maximum possible score
[3]motor ability measure with 36 items converted to percentage using Rasch analysis tables [11]
[4]maximum score in brackets [5]proximal arm section of FMA (shoulder-elbow-forearm)
[6]distal arm section of FMA (wrist-hand) [7]9 hole peg test time in seconds [8]unable to complete

use of advanced model-based controllers to promote accuracy and voluntary effort. The participants tolerated the intervention with no adverse effects and attended all 18 treatment sessions over a 10 week period. An improvement in arm awareness, better arm control and daily usage of their impaired arm was reported. Three important findings were identified following the intervention: improved tracking performance during the unassisted task; reduced ES required during the assisted tasks and an improvement in the proximal arm section of the FMA. Furthermore there were clear trends for clinical improvement in most measures by most patients.

The implication of improved tracking performance during assisted tasks over the treatment period, achieved with less ES supplied by the controller, suggests that the participants' voluntary effort (muscle power and arm control) increased. Similarly, as participants progressed through the treatment sessions they were able to make more accurate reaching movements with no ES applied. All participants improved in the impairment domain of the International Classification of Functioning Disability and Health (ICF), measured by the proximal arm section of the FMA. In particular, statistical significance was identified at the shoulder and elbow active movement control where the intervention was aimed. This is a new finding that indicates that movement quality improved following training. As with all statistical tests using small sample sizes, these conclusions must be treated with caution.

5.4 Conclusions

The results demonstrate the feasibility of the ES and passive support training system with pwMS. In particular, they show the identification and control design procedures of Chaps. 3 and 4 can be applied to assist task tracking in a clinical setting. The efficacy of task performance has translated into tangible outcome measures which suggest there is treatment potential for this novel system to aid recovery. These results are comparable to previous work undertaken on persons with stroke [15, 16] using the same control framework. Other robotic studies on pwMS [17, 18] have identified improvements on arm capacity tests but this is the first study to show improvements in movement quality.

The results also show that training of the distal movements incorporating the wrist and hand is important in future system development to enable all sections of the FMA to be addressed. Extensions to the control framework to enable this are undertaken in the next chapter.

References

1. F. Khan, L. Turner-Stokes, L. Ng, T. Kilpatrick, Multidisciplinary rehabilitation for adults with multiple sclerosis. Cochrane Database Syst. Rev. **18**(2), CD006036 (2007)
2. A.I. Spooren, A.A. Timmermans, H.A. Seelen, Motor training programs of arm and hand in patients with MS according to different levels of the ICF: a systematic review. BMC Neurol. **12**, 49 (2012)
3. P. Sampson, C.T. Freeman, S. Coote, S. Demain, P. Feys, K.L. Meadmore, A.M. Hughes, Using functional electrical stimulation mediated by iterative learning control and robotics to improve arm movement for people with multiple sclerosis. IEEE Trans. Neural Syst. Rehabil. Eng. (2015)
4. I. Lamers, A.A. Timmermans, L. Kerkhofs, D. Severijns, B. Van Wijmeersch, P. Feys, Self-reported use of the upper limbs related to clinical tests in persons with multiple sclerosis. Disabil. Rehabil. **35**, 2016–2020 (2013)
5. N. Yozbatiran, L. Der-Yeghiaian, S.C. Cramer, A standardized approach to performing the action research arm test. Neurorehabil. Neural Repair **22**, 78–90 (2008)
6. R.C. Lyle, A performance test for assessment of upper limb function in physical rehabilitation treatment and research. Int. J. Rehabil. Res. **4**, 483–492 (1981)
7. I. Lamers, L. Kerkhofs, J. Raats, D. Kos, B. Van Wijmeersch, P. Feys, Perceived and actual arm performance in multiple sclerosis: relationship with clinical tests according to hand dominance. Mult. Scler. **19**, 1341–1348 (2013)
8. V. Mathiowetz, K. Weber, N. Kashman, G. Volland, Adult norms for the nine hole peg test of finger dexterity. Occup. Ther. J. Res. **5**, 24–38 (1985)
9. D.E. Goodkin, D. Hertsgaard, J. Seminary, Upper extremity function in multiple sclerosis: improving assessment sensitivity with box-and-block and nine-hole peg tests. Arch. Phys. Med. Rehabil. **69**, 850–854 (1988)
10. B. Kopp, A. Kunkel, H. Flor, T. Platz, U. Rose, K.H. Mauritz, K. Gresser, K.L. Mcculloch, E. Taub, The arm motor ability test: reliability, validity, and sensitivity to change of an instrument for assessing disabilities in activities of daily living. Arch. Phys. Med. Rehabil. **78**, 615–620 (1997)

11. C.C. Chen, R.K. Bode, Psychometric validation of the manual ability measure-36 (MAM-36) in patients with neurologic and musculoskeletal disorders. Arch. Phys. Med. Rehabil. **91**, 414–420 (2010)
12. A.R. Fugl-Meyer, L. Jaasko, I. Leyman, S. Olsson, S. Steglind, The post-stroke hemiplegic patient. 1. a method for evaluation of physical performance. Scand. J. Rehabil. Med. **7**, 13–31 (1975)
13. P.W. Duncan, M. Propst, S.G. Nelson, Reliability of the fugl-meyer assessment of sensorimotor recovery following cerebrovascular accident. Phys. Ther. **63**, 1606–1610 (1983)
14. D.J. Gladstone, C.J. Danells, S.E. Black, The fugl-meyer assessment of motor recovery after stroke: a critical review of its measurement properties. Neurorehabil. Neural. Repair **16**, 232–240 (2002)
15. A.M. Hughes, C.T. Freeman, J.H. Burridge, P.H. Chappell, P. Lewin, E. Rogers, Feasibility of iterative learning control mediated by functional electrical stimulation for reaching after stroke. J. Neurorehabil. Neural Repair **23**(6), 559–568 (2009)
16. K.L. Meadmore, A.-M. Hughes, C.T. Freeman, Z. Cai, D. Tong, J.H. Burridge, E. Rogers, Functional electrical stimulation mediated by iterative learning control and 3*d* robotics reduces motor impairment in chronic stroke. J. Neuroeng. Rehabil. **32**(9), 1–11 (2012)
17. D. Gijbels, I. Lamers, L. Kerkhofs, G. Alders, E. Knippenberg, P. Feys, The armeo spring as training tool to improve upper limb functionality in multiple sclerosis: a pilot study. J. Neuroeng. Rehabil. **8**, 5–5 (2011)
18. I. Carpinella, D. Cattaneo, S. Abuarqub, M. Ferrarin, Robot-based rehabilitation of the upper limbs in multiple sclerosis: feasibility and preliminary results. J. Rehabil. Med. (Stiftelsen Rehabiliteringsinformation) **41**, 966–970 (2009)

Chapter 6
Constrained ILC for Human Motor Control

In Chap. 4 we considered the system shown in Fig. 6.1, and addressed the need for joint angles $\boldsymbol{\Phi}_{\mathscr{D}} = G_{\mathscr{D}}(\hat{\boldsymbol{\Phi}} + \boldsymbol{\nu})$ to track reference trajectory $\hat{\boldsymbol{\Phi}}_{\mathscr{D}}$, where operator $G_{\mathscr{D}}$ is defined by (4.1). This objective assumes that a trajectory $\hat{\boldsymbol{\Phi}}_{\mathscr{D}}(t),\ t \in [0, T]$ is available. In the rehabilitation domain this is appropriate if the task is defined and explicitly presented to the patient as it was in Chap. 5. However, this is not possible when training more natural, everyday activities such as eating, washing or manipulating objects. To address this, the problem definition is now extended to encompass fully functional tasks.

6.1 Extended Task Representation

To expand the task definition to capture the needs of human motor control, we define $0 = t_0 \leq t_1 \leq \cdots \leq T_S = T$ distinct points in $[0, T]$ which are deemed important to the task completion. These break the task down into S intervals in which one or more joints may be required to perform a synchronized movement. For example, time interval $[t_{j-1}, t_j]$ may correspond to the hand palm pushing a drawer along its runners, or the fingers holding a cup during a pouring movement. If $t_{j-1} = t_j$ is

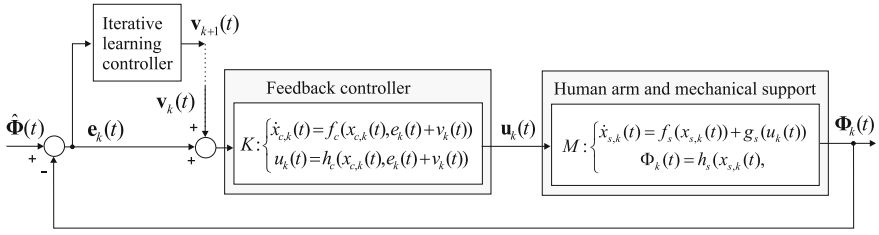

Fig. 6.1 Combined feedback and ILC control structure

C. Freeman, *Control System Design for Electrical Stimulation in Upper Limb Rehabilitation*, DOI 10.1007/978-3-319-25706-8_6

specified then the interval is an isolated time point, and may for example represent the time where the index finger makes contact with a light switch.

Given joint angle signal $\boldsymbol{\Phi}_{\mathscr{P}}$ defined over $[0, T]$, we extract the single or linear combination of joints involved in any coordinated action by using the projection

$$P : \mathscr{L}_2^{n_p}[0, T] \to \mathscr{L}_2^{p_1}[0, t_1] \times \cdots \times \mathscr{L}_2^{p_S}[t_{S-1}, t_S] : \boldsymbol{\Phi}_{\mathscr{P}} \mapsto \begin{bmatrix} (P\boldsymbol{\Phi}_{\mathscr{P}})_1 \\ \vdots \\ (P\boldsymbol{\Phi}_{\mathscr{P}})_S \end{bmatrix} \tag{6.1}$$

with each component, $(P\boldsymbol{\Phi}_{\mathscr{P}})_j : \mathscr{L}_2^{n_p}[0, T] \to \mathscr{L}_2^{p_j}[t_{j-1}, t_j]$, defined by

$$((P\boldsymbol{\Phi}_{\mathscr{P}})_j)(t) = P_j \boldsymbol{\Phi}_{\mathscr{P}}(t), \qquad t \in [t_{j-1}, t_j], \quad j = 1, 2, \ldots, S, \tag{6.2}$$

where P_j is a $p_j \times n_p$ matrix of full row rank specifying the joint angles involved in the gesture or movement stipulated over time interval $[t_{j-1}, t_j]$.

For ease of notation, the projected output $P\boldsymbol{\Phi}_{\mathscr{P}}$ is termed the "extended output" and denoted by $\boldsymbol{\Phi}^e_{\mathscr{P}} \in \mathscr{L}_2^{p_1}[0, t_1] \times \cdots \times \mathscr{L}_2^{p_S}[t_{S-1}, t_S]$. We can also incorporate the projection into the system operator to yield the extended system operator $G^e_{\mathscr{P}} : \mathscr{L}_2^{p}[0, T] \to \mathscr{L}_2^{p_1}[0, t_1] \times \cdots \times \mathscr{L}_2^{p_S}[t_{S-1}, t_S]$ defined by

$$\boldsymbol{\Phi}^e_{\mathscr{P}} = G^e_{\mathscr{P}}(\hat{\boldsymbol{\Phi}} + \boldsymbol{v}) \ : \ G^e_{\mathscr{P}}(\hat{\boldsymbol{\Phi}} + \boldsymbol{v}) = (PG_{\mathscr{P}})(\hat{\boldsymbol{\Phi}} + \boldsymbol{v}). \tag{6.3}$$

Using this extended task representation allows us to replace the ILC tracking problem (4.3) by the more general form

$$\boldsymbol{v}_\infty := \min_{\boldsymbol{v}} J(\boldsymbol{v}), \qquad J(\boldsymbol{v}) = \left\| \hat{\boldsymbol{\Phi}}^e_{\mathscr{P}} - G^e_{\mathscr{P}}(\hat{\boldsymbol{\Phi}} + \boldsymbol{v}) \right\|^2, \tag{6.4}$$

where the extended reference trajectory and extended error are respectively

$$\hat{\boldsymbol{\Phi}}^e_{\mathscr{P}} = \begin{bmatrix} \hat{\boldsymbol{\Phi}}^{p_1}_{\mathscr{P}} \\ \vdots \\ \hat{\boldsymbol{\Phi}}^{p_S}_{\mathscr{P}} \end{bmatrix}, \quad \boldsymbol{e}^e_{\mathscr{P}} = \begin{bmatrix} \hat{\boldsymbol{\Phi}}^{p_1}_{\mathscr{P}} - (PG_{\mathscr{P}})_1(\hat{\boldsymbol{\Phi}} + \boldsymbol{v}) \\ \vdots \\ \hat{\boldsymbol{\Phi}}^{p_S}_{\mathscr{P}} - (PG_{\mathscr{P}})_S(\hat{\boldsymbol{\Phi}} + \boldsymbol{v}) \end{bmatrix} = \hat{\boldsymbol{\Phi}}^e_{\mathscr{P}} - G^e_{\mathscr{P}}(\hat{\boldsymbol{\Phi}} + \boldsymbol{v}). \tag{6.5}$$

Here $\hat{\boldsymbol{\Phi}}^e_{\mathscr{P}}$ contains the reference trajectories/points that must be followed at time points $t_{j-1} = t_j$ or over intervals $[t_{j-1}, t_j]$. Note that the extended reference can be represented as the projection of a "virtual reference", $\hat{\boldsymbol{\Phi}}_{\mathscr{P}}$, denoted by $\hat{\boldsymbol{\Phi}}^e_{\mathscr{P}} = P\hat{\boldsymbol{\Phi}}_{\mathscr{P}}$, however $\hat{\boldsymbol{\Phi}}_{\mathscr{P}}$ is not required in the control strategy. If the designer chooses $S = 1$, $t_0 = 0$, $t_1 = T$, and $P_1 = I$ then (6.4) collapses to the standard form (4.3).

6.2 Reduced Stimulation and Joint Subspaces

To reduce the number of degrees of freedom in problem (6.4) we can mimic the natural strategy of human motor control which involves a single neural command signal controlling multiple muscles. Each group of muscles working together is called a synergy, and the same muscle can potentially be employed within multiple synergies. To do this we introduce a set of $q \leq m$ neural signals, denoted $\boldsymbol{x} \in \mathscr{L}_2^q[0,T]$. The mapping between $\boldsymbol{x}$ and the m muscle stimulation signals $\boldsymbol{u} \in \mathscr{L}_2^m[0,T]$, can be represented at time t by $\boldsymbol{u}(t) = \bar{X}\boldsymbol{x}(t)$. Here $\bar{X}$ is a $m \times q$ matrix with full column rank, with the jth column defining which muscles make up the jth synergy. The map between neural and muscle stimulation signals is therefore defined by $\boldsymbol{u} = X\boldsymbol{x}$, with

$$X : \mathscr{L}_2^q[0,T] \to \mathscr{X}[0,T] : \boldsymbol{x} \mapsto \boldsymbol{u},\ \boldsymbol{u}(t) = \bar{X}\boldsymbol{x}(t). \tag{6.6}$$

Here $\mathscr{X}[0,T]$ is that subset of stimulation space $\mathscr{L}_2^m[0,T]$ which is achievable given the specified set of q synergistic muscle combinations, and is defined by

$$\mathscr{X}[0,T] := \left\{\boldsymbol{u} = X\boldsymbol{x},\ \boldsymbol{x} \in \mathscr{L}_2^q[0,T]\right\} \subset \mathscr{L}_2^m[0,T]. \tag{6.7}$$

The subspace $\mathscr{X}[0,T]$ is convex: to see this let $\tilde{\boldsymbol{x}}, \tilde{\boldsymbol{y}} \in \mathscr{X}$, then $\tilde{\boldsymbol{x}}(t) = \bar{X}\boldsymbol{x}(t)$, $\tilde{\boldsymbol{y}}(t) = \bar{X}\boldsymbol{y}(t)$ then $\tilde{\boldsymbol{x}}(t) + a(\tilde{\boldsymbol{y}}(t) - \tilde{\boldsymbol{x}}(t)) = X(\boldsymbol{x}(t) + a(\boldsymbol{y}(t) - \boldsymbol{x}(t)))$, $a = [0,1]$. Since $\boldsymbol{x} + a(\boldsymbol{y} - \boldsymbol{x}) \in \mathscr{L}_2^q[0,T]$ it follows from (6.7) that $\tilde{\boldsymbol{x}} + a(\tilde{\boldsymbol{y}} - \tilde{\boldsymbol{x}}) \in \mathscr{X}[0,T]$.

Operator X restricts the stimulation signal $\boldsymbol{u}$ to belong to a subspace $\mathscr{X}[0,T]$ of $\mathscr{L}_2^m[0,T]$. However, we can also reduce the degree of freedom of control problem (6.4) by restricting the joint demand signal, $\boldsymbol{v}$, generated by ILC to belong to a suitable subspace of $\mathscr{L}_2^p[0,T]$. To do this we introduce a set of q signals which represent synergies in joint space, and define the mapping between $\mathscr{L}_2^q[0,T]$ and the achievable subset of joint space by

$$W : \mathscr{L}_2^q[0,T] \to \mathscr{W}[0,T] : \boldsymbol{r} \mapsto \boldsymbol{v},\ \boldsymbol{v}(t) = \bar{W}\boldsymbol{r}(t). \tag{6.8}$$

where $p \times q$ matrix W has full column rank. The corresponding joint subspace is

$$\mathscr{W}[0,T] := \left\{\boldsymbol{v} = W\boldsymbol{r},\ \boldsymbol{r} \in \mathscr{L}_2^q[0,T]\right\} \subset \mathscr{L}_2^p[0,T]. \tag{6.9}$$

Embedding these subspaces into control problem (6.4) gives rise to:

Definition 6.1 Consider the system of Fig. 6.1 with control objective (6.4). If the stimulation signal is restricted to subspace $\mathscr{X}[0,T]$, ILC problem (6.4) is exchanged for

$$\boldsymbol{v}_\infty := \min_{\boldsymbol{v}} J(\boldsymbol{v}), \qquad J(\boldsymbol{v}) = \Big\| \overbrace{\hat{\boldsymbol{\Phi}}^e_{\mathscr{D}} - G^e_{\mathscr{D}}(\hat{\boldsymbol{\Phi}} + \boldsymbol{v})}^{\boldsymbol{e}^e_{\mathscr{D}}} \Big\|^2, \quad \boldsymbol{u}_k \in \mathscr{X}[0,T]\ \forall\ k \tag{6.10}$$

which simplifies to (6.4) if we impose the feedback controller structure

$$K : \mathscr{L}^p[0,T] \mapsto \mathscr{X}[0,T] \ : K = XK_X, \ K_X : \mathscr{L}^p[0,T] \to \mathscr{L}^q[0,T]. \tag{6.11}$$

If instead the joint space demand signal is restricted to subspace $\mathscr{W}[0,T]$, ILC problem (6.4) is exchanged for

$$\boldsymbol{v}_\infty := \min_{\boldsymbol{v}} J(\boldsymbol{v}), \qquad J(\boldsymbol{v}) = \Big\| \underbrace{\hat{\boldsymbol{\Phi}}^e_{\mathscr{P}} - G^e_{\mathscr{P}}(\hat{\boldsymbol{\Phi}} + \boldsymbol{v})}_{\boldsymbol{e}^e_{\mathscr{P}}} \Big\|^2, \quad \boldsymbol{v}_k \in \mathscr{W}[0,T] \ \forall \ k. \tag{6.12}$$

The most general form of ILC problem we need to solve is therefore (6.12), which reduces to problem (6.4) if $W = I$, in which case $\mathscr{W} = \mathscr{L}^p_2[0,T]$.

6.3 Extended ILC Framework

To address the problem (6.12) we extend Theorem 4.1 as follows:

Theorem 6.1 *Consider the ILC update sequence*

$$\boldsymbol{v}_{k+1} = \boldsymbol{v}_k + WL_k(\boldsymbol{e}_k)^e_{\mathscr{P}}, \qquad k = 0, 1, \ldots, \quad \boldsymbol{v}_0 \in \mathscr{W}[0,T]. \tag{6.13}$$

If learning operator $L_k : \mathscr{L}^{p_1}_2[0,t_1] \times \cdots \times \mathscr{L}^{p_S}_2[t_{S-1},t_S] \to \mathscr{L}^p_2[0,T]$ *satisfies*

$$\left\| I - \bar{G}^e_{\mathscr{P}}|_{\hat{\boldsymbol{\Phi}}+\boldsymbol{v}_\infty} WL_k \right\| < 1 \quad \forall \ k \tag{6.14}$$

where the operator norm is induced from the inner product $\langle \cdot, \cdot \rangle$*, then*

$$\lim_{k\to\infty} (\boldsymbol{e}_k)^e_{\mathscr{P}} = \boldsymbol{0} \tag{6.15}$$

and, for $\boldsymbol{v}_0$ *chosen sufficiently close to* $\boldsymbol{v}_\infty$*, the ILC update converges to*

$$\lim_{k\to\infty} (\hat{\boldsymbol{\Phi}} + \boldsymbol{v}_k) = WL_\infty (\bar{G}^e_{\mathscr{P}}|_{\hat{\boldsymbol{\Phi}}+\boldsymbol{v}_\infty} WL_\infty)^{-1} \hat{\boldsymbol{\Phi}}^e_{\mathscr{P}}, \quad \textit{with} \quad \boldsymbol{v}_k \in \mathscr{W}[0,T] \ \forall \ k. \tag{6.16}$$

Alternatively, if the learning operator L_k satisfies

$$\|I - L_k \bar{G}^e_{\mathscr{P}}|_{\boldsymbol{v}_\infty} W\| < 1 \quad \forall\, k \tag{6.17}$$

then, for $\boldsymbol{v}_0$ chosen sufficiently close to $\boldsymbol{v}_\infty$, the ILC update converges to

$$\lim_{k\to\infty} (\hat{\boldsymbol{\Phi}} + \boldsymbol{v}_k) = W(L_\infty \bar{G}^e_{\mathscr{P}}|_{\hat{\boldsymbol{\Phi}}+\boldsymbol{v}_\infty} W)^{-1} L_\infty \hat{\boldsymbol{\Phi}}^e_{\mathscr{P}} \quad \textit{with} \quad \boldsymbol{v}_k \in \mathscr{W}[0,T]\ \forall\, k. \tag{6.18}$$

Proof Update (6.13) is equivalent to applying $\boldsymbol{v}_k = W\boldsymbol{r}_k$ to system (6.3) where

$$\boldsymbol{r}_{k+1} = \boldsymbol{r}_k + L_k(\boldsymbol{e}_k)^e_{\mathscr{P}}, \qquad k = 0, 1, \ldots, \quad \boldsymbol{r}_0 \in \mathscr{L}^q_2[0,T] \tag{6.19}$$

and hence $\boldsymbol{v}_k \in \mathscr{W}[0,T]\ \forall\, k$. The error dynamics locally satisfy

$$(\boldsymbol{e}_{k+1})^e_{\mathscr{P}} = (\boldsymbol{e}_k)^e_{\mathscr{P}} - P\bar{G}_{\mathscr{P}}|_{\hat{\boldsymbol{\Phi}}+\boldsymbol{v}_k} W L_k (\boldsymbol{e}_k)^e_{\mathscr{P}} = (I - P\bar{G}_{\mathscr{P}}|_{\hat{\boldsymbol{\Phi}}+\boldsymbol{v}_k} W L_k)(\boldsymbol{e}_k)^e_{\mathscr{P}}\ \forall\, k$$

so if (6.14) holds, the extended error converges monotonically to zero since

$$\|(\boldsymbol{e}_{k+1})^e_{\mathscr{P}}\| \le \|I - P\bar{G}_{\mathscr{P}}|_{\hat{\boldsymbol{\Phi}}+\boldsymbol{v}_k} W L_k\| \|(\boldsymbol{e}_k)^e_{\mathscr{P}}\| < \|(\boldsymbol{e}_k)^e_{\mathscr{P}}\|\ \forall\, k. \tag{6.20}$$

For $\boldsymbol{v}_0$ sufficiently close to $\boldsymbol{v}_\infty$, then $\bar{G}_{\mathscr{P}}|_{\hat{\boldsymbol{\Phi}}+\boldsymbol{v}_k} = \bar{G}_{\mathscr{P}}|_{\hat{\boldsymbol{\Phi}}+\boldsymbol{v}_\infty}$ and $L_k = L_\infty\ \forall k$, and

$$\begin{aligned}
\boldsymbol{v}_{k+1} &= \boldsymbol{v}_0 + WL_\infty \sum_{i=0}^{k} (\boldsymbol{e}_i)^e_{\mathscr{P}} = \boldsymbol{v}_0 + WL_\infty \sum_{i=0}^{k} \left(I - P\bar{G}_{\mathscr{P}}|_{\hat{\boldsymbol{\Phi}}+\boldsymbol{v}_\infty} WL_\infty\right)^i \\
&\quad \times \left(\hat{\boldsymbol{\Phi}}^e_{\mathscr{P}} - PG_{\mathscr{P}}|_{\hat{\boldsymbol{\Phi}}+\boldsymbol{v}_\infty}(\hat{\boldsymbol{\Phi}} + \boldsymbol{v}_0)\right) \\
&= WL_\infty \sum_{i=0}^{k} \left(I - P\bar{G}_{\mathscr{P}}|_{\hat{\boldsymbol{\Phi}}+\boldsymbol{v}_\infty} WL_\infty\right)^i \hat{\boldsymbol{\Phi}}^e_{\mathscr{P}} - \hat{\boldsymbol{\Phi}}
\end{aligned}$$

so that if (6.14) holds

$$\lim_{k\to\infty} \boldsymbol{v}_k = WL_\infty \left(P\bar{G}_{\mathscr{P}}|_{\hat{\boldsymbol{\Phi}}+\boldsymbol{v}_\infty} WL_\infty\right)^{-1} \hat{\boldsymbol{\Phi}}^e_{\mathscr{P}} - \hat{\boldsymbol{\Phi}}. \tag{6.21}$$

In addition, the input signals locally satisfy

$$\begin{aligned}\boldsymbol{r}_{k+1} &= \boldsymbol{r}_k + L_\infty\big(\hat{\boldsymbol{\Phi}}^e_{\mathscr{P}} - P\bar{G}_{\mathscr{P}}|_{\hat{\boldsymbol{\Phi}}+\boldsymbol{v}_\infty}(\hat{\boldsymbol{\Phi}} + W\boldsymbol{r}_k)\big)\\ &= \big(I - L_\infty P\bar{G}_{\mathscr{P}}|_{\hat{\boldsymbol{\Phi}}+\boldsymbol{v}_\infty} W\big)\boldsymbol{r}_k + L_\infty\big(\hat{\boldsymbol{\Phi}}^e_{\mathscr{P}} - P\bar{G}_{\mathscr{P}}|_{\hat{\boldsymbol{\Phi}}+\boldsymbol{v}_\infty}\hat{\boldsymbol{\Phi}}\big)\\ &= \big(I - L_\infty P\bar{G}_{\mathscr{P}}|_{\hat{\boldsymbol{\Phi}}+\boldsymbol{v}_\infty} W\big)^{k+1}\boldsymbol{r}_0\\ &\quad + \sum_{i=0}^{k}\big(I - L_\infty P\bar{G}_{\mathscr{P}}|_{\hat{\boldsymbol{\Phi}}+\boldsymbol{v}_\infty} W\big)^i L_\infty\big(\hat{\boldsymbol{\Phi}}^e_{\mathscr{P}} - P\bar{G}_{\mathscr{P}}|_{\hat{\boldsymbol{\Phi}}+\boldsymbol{v}_\infty}\hat{\boldsymbol{\Phi}}\big)\end{aligned}$$

so that, if (6.17) is satisfied,

$$\begin{aligned}\lim_{k\to\infty}\boldsymbol{v}_k &= W\big(L_\infty P\bar{G}_{\mathscr{P}}|_{\hat{\boldsymbol{\Phi}}+\boldsymbol{v}_\infty} W\big)^{-1} L_\infty P\big(\hat{\boldsymbol{\Phi}}^e_{\mathscr{P}} - \bar{G}_{\mathscr{P}}|_{\hat{\boldsymbol{\Phi}}+\boldsymbol{v}_\infty}\hat{\boldsymbol{\Phi}}\big)\\ &= W\big(L_\infty P\bar{G}_{\mathscr{P}}|_{\hat{\boldsymbol{\Phi}}+\boldsymbol{v}_\infty} W\big)^{-1} L_\infty\hat{\boldsymbol{\Phi}}^e_{\mathscr{P}} - \hat{\boldsymbol{\Phi}}.\end{aligned} \tag{6.22}$$

□

Within Theorem 6.1, the linearized extended plant operator is defined by:

Lemma 6.1 *Around operating point $\tilde{\boldsymbol{v}}$ the dynamics $\boldsymbol{\Phi}^e_{\mathscr{P}} = G^e_{\mathscr{P}}\boldsymbol{v}$ are captured by the map $\bar{G}^e_{\mathscr{P}}|_{\tilde{\boldsymbol{v}}} : \mathscr{L}_2^p[0,T] \to \mathscr{L}_2^{p_1}[0,t_1]\times\cdots\times\mathscr{L}_2^{p_S}[t_{S-1},t_S]$ defined by*

$$\bar{G}^e_{\mathscr{P}}|_{\tilde{\boldsymbol{v}}}\boldsymbol{v} = \begin{bmatrix}(P\bar{G}_{\mathscr{P}}|_{\tilde{\boldsymbol{v}}})_1\boldsymbol{v}\\ \vdots\\ (P\bar{G}_{\mathscr{P}}|_{\tilde{\boldsymbol{v}}})_S\boldsymbol{v}\end{bmatrix} \tag{6.23}$$

where

$$((P\bar{G}_{\mathscr{P}}|_{\tilde{\boldsymbol{v}}})_j\boldsymbol{v})(t) = P_j\int_0^t C(t)\Gamma(t,\tau)B(\tau)\boldsymbol{v}(\tau)\mathrm{d}\tau,\quad t\in[t_{j-1},t_j],\ j=1,\ldots,S \tag{6.24}$$

in which $A(t)$, $B(t)$, $C(t)$ and $\Gamma(t,\tau)$ are defined in Lemma 4.2.

Theorem 6.2 *Within (6.13), let the ILC operator be given by*

$$L_k = (\bar{G}^e_{\mathscr{P}}|_{\hat{\boldsymbol{\Phi}}+\boldsymbol{v}_k} W)^*\big(I + \bar{G}^e_{\mathscr{P}}|_{\hat{\boldsymbol{\Phi}}+\boldsymbol{v}_k} W(\bar{G}^e_{\mathscr{P}}|_{\hat{\boldsymbol{\Phi}}+\boldsymbol{v}_k} W)^*\big)^{-1}. \tag{6.25}$$

Setting $\boldsymbol{v}_{k+1} - \boldsymbol{v}_k = W(\boldsymbol{r}_{k+1} - \boldsymbol{r}_k) = W\Delta\boldsymbol{r}_k$, this is equivalent to solving the underlying subspace problem

$$\Delta\boldsymbol{r}_k := \min_{\Delta\boldsymbol{r}}\Big\{\|\Delta\boldsymbol{r}\|^2_{[R]} + \|(\boldsymbol{e}_k)^e_{\mathscr{P}} - \bar{G}^e_{\mathscr{P}}|_{\hat{\boldsymbol{\Phi}}+\boldsymbol{v}_k} W\Delta\boldsymbol{r}\|^2_Q\Big\},\qquad \boldsymbol{r}_0 = \boldsymbol{0}. \tag{6.26}$$

where $[R] = W^\top RW$, with symmetric positive-definite weights Q and R.

If $\hat{\boldsymbol{\Phi}}^e_{\mathscr{P}} \in im(G^e_{\mathscr{P}}W)$ *then ILC operator (6.25) satisfies (6.14) and generates an input sequence satisfying*

$$\lim_{k\to\infty} \boldsymbol{v}_k = \boldsymbol{v}_\infty, \quad \boldsymbol{v}_\infty := \min_{\boldsymbol{v}} \|\boldsymbol{v}\|^2_R \;\; s.\,t. \;\; \boldsymbol{e}^e_{\mathscr{P}} = \hat{\boldsymbol{\Phi}}^e_{\mathscr{P}} - G^e_{\mathscr{P}}(\hat{\boldsymbol{\Phi}} + \boldsymbol{v}) = \boldsymbol{0}. \tag{6.27}$$

If $\hat{\boldsymbol{\Phi}}^e_{\mathscr{P}} \notin im(G^e_{\mathscr{P}}W)$ *then ILC operator (6.25) satisfies (6.17) and generates an input sequence satisfying*

$$\lim_{k\to\infty} \boldsymbol{v}_k = \boldsymbol{v}_\infty, \quad \boldsymbol{v}_\infty := \min_{\boldsymbol{v}} \left\|\boldsymbol{e}^e_{\mathscr{P}}\right\|^2. \tag{6.28}$$

Proof If $\hat{\boldsymbol{\Phi}}^e_{\mathscr{P}} \in \text{im}(G^e_{\mathscr{P}}W)$ for all possible $\hat{\boldsymbol{\Phi}}^e_{\mathscr{P}}$, it follows that $\ker((\bar{G}^e_{\mathscr{P}}|_{\hat{\boldsymbol{\Phi}}+\boldsymbol{v}_k}W)^*) = \{\boldsymbol{0}\}\ \forall\ k$. If $\ker((\bar{G}^e_{\mathscr{P}}|_{\hat{\boldsymbol{\Phi}}+\boldsymbol{v}_k}W)^*) = \{\boldsymbol{0}\}$ the solution to (6.26) is $\Delta\boldsymbol{r}_k = L_k(\boldsymbol{e}_k)^e_{\mathscr{P}}$ with L_k given by (6.25) which satisfies (6.14) with limiting solution

$$\boldsymbol{v}_\infty = W\boldsymbol{r}_\infty = W(\bar{G}^e_{\mathscr{P}}|_{\hat{\boldsymbol{\Phi}}+\boldsymbol{v}_k}W)^*\left(\bar{G}^e_{\mathscr{P}}|_{\hat{\boldsymbol{\Phi}}+\boldsymbol{v}_k}W(\bar{G}^e_{\mathscr{P}}|_{\hat{\boldsymbol{\Phi}}+\boldsymbol{v}_k}W)^*\right)^{-1}\hat{\boldsymbol{\Phi}}^e_{\mathscr{P}} \tag{6.29}$$

corresponding to

$$(\boldsymbol{e}_\infty)^e_{\mathscr{P}} = \left(I - \bar{G}^e_{\mathscr{P}}|_{\hat{\boldsymbol{\Phi}}+\boldsymbol{v}_k}W(\bar{G}^e_{\mathscr{P}}|_{\hat{\boldsymbol{\Phi}}+\boldsymbol{v}_k}W)^*\left(\bar{G}^e|_{\hat{\boldsymbol{\Phi}}+\boldsymbol{v}_k}W(\bar{G}^e_{\mathscr{P}}|_{\hat{\boldsymbol{\Phi}}+\boldsymbol{v}_k}W)^*\right)^{-1}\right)\hat{\boldsymbol{\Phi}}^e_{\mathscr{P}} = \boldsymbol{0}.$$

The Lagrangian associated with minimum energy problem (6.27) is just, with Lagrange multiplier $\boldsymbol{\lambda} \in \mathscr{L}_2^{p_1}[0, t_1] \times \cdots \times \mathscr{L}_2^{p_S}[t_{S-1}, t_S]$,

$$\mathscr{L}(\boldsymbol{r}, \boldsymbol{\lambda}) = \|\boldsymbol{v}\|^2_R + 2 < \boldsymbol{\lambda}, \hat{\boldsymbol{\Phi}}^e_{\mathscr{P}} - \bar{G}^e|_{\hat{\boldsymbol{\Phi}}+\boldsymbol{v}_k}\boldsymbol{v} > = \|\boldsymbol{r}\|^2_{[R]} + 2 < \boldsymbol{\lambda}, \hat{\boldsymbol{\Phi}}^e_{\mathscr{P}} - \bar{G}^e|_{\hat{\boldsymbol{\Phi}}+\boldsymbol{v}_k}W\boldsymbol{r} >$$

which has a stationary point when $\boldsymbol{r}_\infty = (\bar{G}^e_{\mathscr{P}}|_{\hat{\boldsymbol{\Phi}}+\boldsymbol{v}_k}W)^*\boldsymbol{\lambda}$ and $\hat{\boldsymbol{\Phi}}^e_{\mathscr{P}} = \bar{G}^e_{\mathscr{P}}|_{\hat{\boldsymbol{\Phi}}+\boldsymbol{v}_k}W\boldsymbol{r}_\infty$. The stationary point solution $\boldsymbol{\lambda} = \left(\bar{G}^e_{\mathscr{P}}|_{\hat{\boldsymbol{\Phi}}+\boldsymbol{v}_k}W(\bar{G}^e_{\mathscr{P}}|_{\hat{\boldsymbol{\Phi}}+\boldsymbol{v}_k}W)^*\right)^{-1}\hat{\boldsymbol{\Phi}}^e_{\mathscr{P}}$ is unique as is the defined input solution $\boldsymbol{r}_\infty = (\bar{G}^e_{\mathscr{P}}|_{\hat{\boldsymbol{\Phi}}+\boldsymbol{v}_k}W)^*\left(\bar{G}^e_{\mathscr{P}}|_{\hat{\boldsymbol{\Phi}}+\boldsymbol{v}_k}W(\bar{G}^e_{\mathscr{P}}|_{\hat{\boldsymbol{\Phi}}+\boldsymbol{v}_k}W)^*\right)^{-1}\hat{\boldsymbol{\Phi}}^e_{\mathscr{P}}$. This matches (6.29). If $\ker((\bar{G}^e|_{\hat{\boldsymbol{\Phi}}+\boldsymbol{v}_k}W)^*) \neq \{\boldsymbol{0}\}$ the solution to (6.26) is $\Delta\boldsymbol{r}_k = L_k(\boldsymbol{e}_k)^e_{\mathscr{P}}$ with

$$L_k = \left(I + (\bar{G}^e_{\mathscr{P}}|_{\hat{\boldsymbol{\Phi}}+\boldsymbol{v}_k}W)^*\bar{G}^e_{\mathscr{P}}|_{\hat{\boldsymbol{\Phi}}+\boldsymbol{v}_k}W\right)^{-1}(\bar{G}^e_{\mathscr{P}}|_{\hat{\boldsymbol{\Phi}}+\boldsymbol{v}_k}W)^* \tag{6.30}$$

which satisfies (6.17) with limiting solution, from (6.18),

$$\boldsymbol{v}_\infty = W\boldsymbol{r}_\infty = W\left((\bar{G}^e_{\mathscr{P}}|_{\hat{\boldsymbol{\Phi}}+\boldsymbol{v}_k}W)^*\bar{G}^e_{\mathscr{P}}|_{\hat{\boldsymbol{\Phi}}+\boldsymbol{v}_k}W\right)^{-1}(\bar{G}^e_{\mathscr{P}}|_{\hat{\boldsymbol{\Phi}}+\boldsymbol{v}_k}W)^*\hat{\boldsymbol{\Phi}}^e_{\mathscr{P}} \tag{6.31}$$

with corresponding

$$(\boldsymbol{\Phi}_\infty)^e_{\mathscr{P}} = \bar{G}^e_{\mathscr{P}}|_{\hat{\boldsymbol{\Phi}}+\boldsymbol{v}_k} W\big((\bar{G}^e_{\mathscr{P}}|_{\hat{\boldsymbol{\Phi}}+\boldsymbol{v}_k} W)^* \bar{G}^e_{\mathscr{P}}|_{\hat{\boldsymbol{\Phi}}+\boldsymbol{v}_k} W\big)^{-1} (\bar{G}^e_{\mathscr{P}}|_{\hat{\boldsymbol{\Phi}}+\boldsymbol{v}_k} W)^* \hat{\boldsymbol{\Phi}}^e_{\mathscr{P}} \quad (6.32)$$

which is the minimizing solution of (6.28). □

Lemma 6.2 *Choosing $R = rI$, $Q = qI$, $q/r \to \infty$, the ILC update (6.25) realizes minimizing solutions (6.29) and (6.31) respectively in a single ILC iteration. In both cases the required term $WL_k(\boldsymbol{e}_k)^e_{\mathscr{P}}$ in (4.4) can be computed efficiently as the outcome, $\Delta\boldsymbol{v}^J$, of J iterations of the computation*

$$\begin{aligned} \dot{\boldsymbol{z}}(t) &= -A^\top(t)\boldsymbol{z}(t) - C^\top(t)Q(t)P_i^\top P_i\big((\boldsymbol{e}_k)_{\mathscr{P}}(t) - \bar{G}_{\mathscr{P}}|_{\hat{\boldsymbol{\Phi}}+\boldsymbol{v}_k}\Delta\boldsymbol{v}_k^j(t)\big), \\ \boldsymbol{z}(T) &= \boldsymbol{0}, \quad t \in (t_{i-1}, t_i), \quad i = 1, \ldots, S \qquad (6.33) \\ \Delta\boldsymbol{v}_k^{j+1}(t) &= \Delta\boldsymbol{v}_k^j(t) + \alpha\bar{W}\bar{W}^\top R^{-1}(t)B^\top(t)\boldsymbol{z}(t) \qquad (6.34) \end{aligned}$$

where J and $\alpha > 0$ are sufficiently large and small values respectively.

Proof As $q/r \to \infty$, update (6.25) and (6.30) respectively converge to

$$\begin{aligned} L_k &= (\bar{G}^e_{\mathscr{P}}|_{\hat{\boldsymbol{\Phi}}+\boldsymbol{v}_k} W)^*\big(\bar{G}^e_{\mathscr{P}}|_{\hat{\boldsymbol{\Phi}}+\boldsymbol{v}_k} W(\bar{G}^e_{\mathscr{P}}|_{\hat{\boldsymbol{\Phi}}+\boldsymbol{v}_k} W)^*\big)^{-1}, \quad \text{and} \\ L_k &= \big((\bar{G}^e_{\mathscr{P}}|_{\hat{\boldsymbol{\Phi}}+\boldsymbol{v}_k} W)^* \bar{G}^e_{\mathscr{P}}|_{\hat{\boldsymbol{\Phi}}+\boldsymbol{v}_k} W\big)^{-1}(\bar{G}^e_{\mathscr{P}}|_{\hat{\boldsymbol{\Phi}}+\boldsymbol{v}_k} W)^* \end{aligned}$$

which it is shown in [1] correspond to solutions of the minimum energy problem

$$\min_{\Delta\boldsymbol{r}_k} \big\|(\boldsymbol{e}_k)^e_{\mathscr{P}} - P\bar{G}^e_{\mathscr{P}}|_{\hat{\boldsymbol{\Phi}}+\boldsymbol{v}_k} W\Delta\boldsymbol{r}_k\big\|^2, \qquad \boldsymbol{r}_0 = \boldsymbol{0} \qquad (6.35)$$

using gradient based ILC [2]. This equates to $j = 1, 2, \ldots, J$ iterations of update

$$\begin{aligned} \Delta\boldsymbol{r}_k^{j+1} &= \Delta\boldsymbol{r}_k^j + \alpha(P\bar{G}^e|_{\hat{\boldsymbol{\Phi}}+\boldsymbol{v}_k} W)^*\big((\boldsymbol{e}_k)^e_{\mathscr{P}} - P\bar{G}^e_{\mathscr{P}}|_{\hat{\boldsymbol{\Phi}}+\boldsymbol{v}_k} W\Delta\boldsymbol{r}_k^j\big) \\ \Rightarrow \Delta\boldsymbol{v}_k^{j+1} &= \Delta\boldsymbol{v}_k^j + \alpha W(P\bar{G}^e_{\mathscr{P}}|_{\hat{\boldsymbol{\Phi}}+\boldsymbol{v}_k} W)^*\big((\boldsymbol{e}_k)^e_{\mathscr{P}} - P\bar{G}^e_{\mathscr{P}}|_{\hat{\boldsymbol{\Phi}}+\boldsymbol{v}_k}\Delta\boldsymbol{v}_k^j\big). \qquad (6.36) \end{aligned}$$

Operator $(P\bar{G}^e_{\mathscr{P}}|_{\hat{\boldsymbol{\Phi}}+\boldsymbol{v}_k} W)^* = W^*(\bar{G}^e_{\mathscr{P}}|_{\hat{\boldsymbol{\Phi}}+\boldsymbol{v}_k})^* P^*$ is defined by a relation of the form $\boldsymbol{w} = (P\bar{G}^e_{\mathscr{P}}|_{\hat{\boldsymbol{\Phi}}+\boldsymbol{v}_k} W)^*(\boldsymbol{v}_1, \ldots, \boldsymbol{v}_S)$ as the continuous solution of the costate equation

$$\begin{aligned} &\dot{\boldsymbol{p}}(t) = -A^\top(t)\boldsymbol{p}(t) - C^\top(t)Q(t)P_j^\top\boldsymbol{v}_j(t) \quad : \quad t \in [t_{j-1}, t_j), \quad \boldsymbol{p}(T) = 0 \\ &\boldsymbol{w}(t) = \bar{W}^\top R^{-1}(t)B^\top(t)\boldsymbol{p}(t). \qquad (6.37) \end{aligned}$$

Finally, $((\boldsymbol{e}_k)^e_{\mathscr{P}}(t))_i = P_i(\boldsymbol{e}_k)_{\mathscr{P}}(t)$, $t \in [t_{i-1}, t_i]$, so that $\big((\boldsymbol{e}_k)^e_{\mathscr{P}}(t) - \bar{G}^e_{\mathscr{P}}|_{\hat{\boldsymbol{\Phi}}+\boldsymbol{v}_k} \Delta \boldsymbol{v}^j_k(t)\big)_i = P_i\big((\boldsymbol{e}_k)_{\mathscr{P}}(t) - \bar{G}_{\mathscr{P}}|_{\hat{\boldsymbol{\Phi}}+\boldsymbol{v}_k} \Delta \boldsymbol{v}^j_k(t)\big)$, $t \in [t_{i-1}, t_i]$. □

Theorem 6.2 and Lemma 6.2 define specific ILC updates which satisfy Theorem 6.1. In turn, Theorem 6.1 provides solutions to the most general form of extended tracking problem, with optimal restricted stimulation and joint subspaces. We hence have the tools needed to assist patients in tracking fully functional tasks.

Within subspace definition (6.8), W is not unique in defining a subspace. For example, $\bar{W}$ can be replaced by any matrix of the form $\bar{W}\bar{W}_R$, where $\bar{W}_R \in \mathbb{R}^{q\times q}$ is full rank, and it will yield the same subspace W_R. In Theorem 6.2 the convergence behavior of NOILC depends on the operator, $\bar{G}^e_{\mathscr{P}} W$, and hence depends on the arbitrary matrix W_R. The next theorem shows how the convergence behavior can be made independent of W_R, thereby retaining control over convergence properties.

Theorem 6.3 *Using the subspace operator WW_R, application of NOILC update (6.26) generates an input sequence $\{\boldsymbol{v}_k\}_{k=0,1,\ldots,\infty}$ that is independent of W_R provided that the input subspace weight takes the form $[R] = (WW_R)^* R WW_R$.*

Proof W_R can be interpreted as a similarity transform on the subspace, changing the underlying basis while preserving the subspace. In particular let $\tilde{W} = WW_R$, then if $\ker((\bar{G}^e_{\mathscr{P}}|_{\hat{\boldsymbol{\Phi}}+\boldsymbol{v}_k} W)^*) = \{\boldsymbol{0}\}$ it follows that $(\hat{\boldsymbol{\Phi}}_{k+1})^e_{\mathscr{P}} = (\hat{\boldsymbol{\Phi}}_k)^e_{\mathscr{P}} + \bar{G}^e_{\mathscr{P}}|_{\hat{\boldsymbol{\Phi}}+\boldsymbol{v}_k} \bar{W}(\bar{G}^e_{\mathscr{P}}|_{\hat{\boldsymbol{\Phi}}+\boldsymbol{v}_k} \tilde{W})^*(\bar{G}^e_{\mathscr{P}}|_{\hat{\boldsymbol{\Phi}}+\boldsymbol{v}_k} \tilde{W}(\bar{G}^e_{\mathscr{P}}|_{\hat{\boldsymbol{\Phi}}+\boldsymbol{v}_k} \tilde{W})^*)^{-1}(\boldsymbol{e}_k)^e_{\mathscr{P}}$ with

$$\begin{aligned}\bar{G}^e_{\mathscr{P}}|_{\hat{\boldsymbol{\Phi}}+\boldsymbol{v}_k} \tilde{W}(\bar{G}^e_{\mathscr{P}}|_{\hat{\boldsymbol{\Phi}}+\boldsymbol{v}_k} \bar{W})^* &= \bar{G}^e_{\mathscr{P}}|_{\hat{\boldsymbol{\Phi}}+\boldsymbol{v}_k} \tilde{W}(\tilde{W}^*\tilde{W})^{-1}\tilde{W}^*(\bar{G}^e_{\mathscr{P}}|_{\hat{\boldsymbol{\Phi}}+\boldsymbol{v}_k})^* \\ &= \bar{G}^e_{\mathscr{P}}|_{\hat{\boldsymbol{\Phi}}+\boldsymbol{v}_k} \tilde{W}\tilde{W}^\dagger(\bar{G}^e_{\mathscr{P}}|_{\hat{\boldsymbol{\Phi}}+\boldsymbol{v}_k})^* \\ &= \bar{G}^e_{\mathscr{P}}|_{\hat{\boldsymbol{\Phi}}+\boldsymbol{v}_k}(\bar{G}^e_{\mathscr{P}}|_{\hat{\boldsymbol{\Phi}}+\boldsymbol{v}_k})^*.\end{aligned}$$

Hence each $(\hat{\boldsymbol{\Phi}}_{k+1})^e_{\mathscr{P}}$ is independent of W_R. A similar result occurs in the case that $\ker((\bar{G}^e_{\mathscr{P}}|_{\hat{\boldsymbol{\Phi}}+\boldsymbol{v}_k} W)^*) \neq \{\boldsymbol{0}\}$. Finally note that, since the subspace is invariant of W_R,

$$\ker((\bar{G}^e_{\mathscr{P}}|_{\hat{\boldsymbol{\Phi}}+\boldsymbol{v}_k} W)^*) = \{\boldsymbol{0}\} \Leftrightarrow \ker((\bar{G}^e_{\mathscr{P}}|_{\hat{\boldsymbol{\Phi}}+\boldsymbol{v}_k} WW_R)^*) = \{\boldsymbol{0}\} \tag{6.38}$$

so that if either of (6.38) holds then convergence to zero error is guaranteed. □

If a stimulation subspace is employed, we use feedback controller structure (6.11) and set $W = I$ within Theorem 6.1. If X is replaced by XX_R where X_R is a similarity transform, then its effect can be directly removed by setting K_X equal to $X_R^{-1}K_X$. This means that the control action is also invariant to the arbitrary choice of X_R.

We finally note:

- Appropriate selection of weight R in the NOILC update of Theorem 6.2 can be used to not only minimize the ILC control action, but other control signals. For example, choosing $R = H^*H$, where $H = (I + MK)^{-1}K$ yields the minimum stimulation solution to the problem, with (6.27) becoming

$$\lim_{k\to\infty} \boldsymbol{v}_k = \boldsymbol{v}_\infty, \quad \boldsymbol{v}_\infty := \min_{\boldsymbol{v}} \|\boldsymbol{u}\|^2 \quad \text{s. t.} \quad \boldsymbol{e}^e_{\mathscr{P}} = \boldsymbol{0}. \tag{6.39}$$

- The solution (6.26) can also be implemented in the form of a combined state feedback plus feedforward update, by extending the approach of [3]. These can be chosen to replace the form of L_k given by (6.25).
- A variety of extensions to the constrained NOILC problem have recently been proposed, including the case where the control effort minimization $\boldsymbol{v}_\infty := \min_{\boldsymbol{v}} \|\boldsymbol{v}\|^2$ in (6.27) is replaced by a more general 'auxiliary function', to give

$$\boldsymbol{v}_\infty := \min_{\boldsymbol{v}} J(\boldsymbol{z}, \boldsymbol{v}) \quad \text{s. t.} \quad \hat{\boldsymbol{\Phi}}^e_{\mathscr{P}} = G^e_{\mathscr{P}}(\boldsymbol{v} + \hat{\boldsymbol{\Phi}}), \quad J(\boldsymbol{z}, \boldsymbol{v}) = \|\boldsymbol{z}\|^2 + \|\boldsymbol{v}\|^2 \tag{6.40}$$

  where $\boldsymbol{z} = H\boldsymbol{v}$ is a signal that is considered important in the problem, e.g. acceleration or jerk. For more details see [4, 5].
- Constraints involving signals other than the joint angles (e.g. joint velocity or acceleration) are easily absorbed within the framework by incorporating dynamics into the plant definition, e.g. by defining an augmented system operator as follows:

Lemma 6.3 *Suppose P operator definition (6.2) is exchanged for the augmented counterpart*

$$((P\boldsymbol{\Phi}_{\mathscr{P}})_j)(t) = P_j \begin{bmatrix} \boldsymbol{\Phi}_{\mathscr{P}}(t) \\ \dot{\boldsymbol{\Phi}}_{\mathscr{P}}(t) \end{bmatrix}, \qquad t \in [t_{j-1}, t_j], \quad 1 \le j \le S. \tag{6.41}$$

The corresponding $P\bar{G}|_{\tilde{\boldsymbol{v}}} = \bar{G}^e|_{\tilde{\boldsymbol{v}}}$ definition of (6.24) is simply replaced by

$$((P\bar{G}|_{\tilde{\boldsymbol{v}}})_j\boldsymbol{v})(t) = P_j \int_0^t \begin{bmatrix} C(t) \\ C(t)A(\tau) \end{bmatrix} \Gamma(t,\tau)B(\tau)\boldsymbol{v}(\tau)\mathrm{d}\tau + \begin{bmatrix} \boldsymbol{0} \\ C(t)B(t) \end{bmatrix}, \quad t \in [t_{j-1}, t_j], \ 1 \le j \le S. \tag{6.42}$$

- Inequality constraints involving any of the signals appearing in Fig. 6.1 can also be imposed by applying a projection to the NOILC operator L_k given by (6.25). See [6] for full details.

6.4 Robust Performance

Building on our previous robustness results in Chap. 4, we now consider the set-up shown in Fig. 6.2. Here the ILC update of (4.4) has been replaced by its extended counterpart (6.13). This includes projection P and joint subspace W operators defined by (6.1) and (6.8) respectively. The aim of this section is to establish robust performance conditions for this extended system. To do this, we can apply the general robust performance condition of Theorem 4.5 directly to this system. However to generate more specific design-orientated stability conditions we must calculate new bounds between the external and internal signals to replace the previous result of Theorem 4.6. This is undertaken in the following theorem.

Theorem 6.4 *Let plant model M and controller K be linear, and ILC operator L be designed to satisfy either (6.14) or (6.17) of Theorem 6.1. Then*

$$b_{\bar{M}//\bar{C}} = b_{M//K} + \frac{\left\| \begin{pmatrix} I \\ M \end{pmatrix} K(I+MK)^{-1} W \right\| \|L\| \left\| P(I+MK)^{-1}(-M, I) \right\|}{1-\gamma} \tag{6.43}$$

where $b_{M//K}$ is defined by (4.45) and $\gamma = \|I - \bar{G}^e_{\mathscr{P}} WL\|$ or $\|I - L\bar{G}^e_{\mathscr{P}} W\|$ depending on whether it is condition (6.14) or (6.17) that is satisfied.

Proof For the case of Fig. 4.8, we have from (4.49) the expression

$$\begin{aligned} \boldsymbol{u}(k+1) = {} & (I+KM)^{-1}(I,K)\boldsymbol{w}_0(k+1) + K(I+MK)^{-1}\hat{\boldsymbol{\Phi}} + K(I+MK)^{-1} \\ & \times \left(\sum_{i=0}^{k} (I-LG)^i L\hat{\boldsymbol{\Phi}} + \sum_{i=0}^{k-1} (I-LG)^i L(I+MK)^{-1}(-M, I)\boldsymbol{w}_0(k-i) \right). \end{aligned}$$

where $G := (I+MK)^{-1}MK = \bar{G}_{\mathscr{P}} = G_{\mathscr{P}}$ as M and K are linear. Comparing update (6.13) with (4.4) we see that $L \Rightarrow WLP$, and hence it follows that

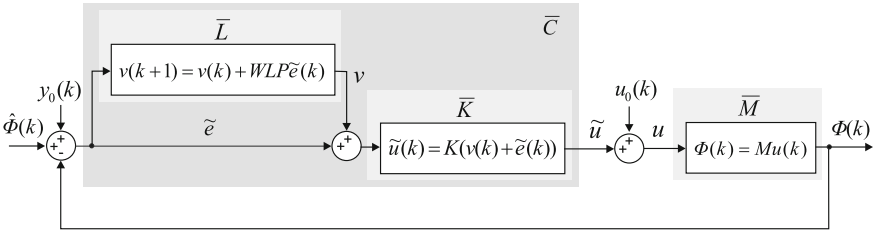

Fig. 6.2 ILC and feedback control scheme in lifted form

$$\boldsymbol{u}(k+1) = (I+KM)^{-1}(I,K)\boldsymbol{w}_0(k+1) + K(I+MK)^{-1}\hat{\boldsymbol{\Phi}} + K(I+MK)^{-1} \times \Bigg(\sum_{i=0}^{k} (I - WLPG)^i WLP\hat{\boldsymbol{\Phi}} + \sum_{i=0}^{k-1} (I - WLPG)^i WLP(I+MK)^{-1}(-M,I)\boldsymbol{w}_0(k-i) \Bigg).$$

We next employ the identity:

$$WL\sum_{i=0}^{k}\left(I - PGWL\right)^i = \sum_{i=0}^{k}\left(I - WLPG\right)^i WL \quad \forall\, k$$

to obtain

$$\boldsymbol{u}(k+1) = (I+KM)^{-1}(I,K)\boldsymbol{w}_0(k+1) + K(I+MK)^{-1}\hat{\boldsymbol{\Phi}} + K(I+MK)^{-1}WL \times \Bigg(\sum_{i=0}^{k} (I - PGWL)^i P\hat{\boldsymbol{\Phi}} + \sum_{i=0}^{k-1} (I - PGWL)^i P(I+MK)^{-1}(-M,I)\boldsymbol{w}_0(k-i) \Bigg) \tag{6.44}$$

which if condition (6.14) holds, ultimately produces the bound

$$\|\Pi_{\bar{M}//\bar{C}}\|_{\begin{pmatrix}\mathbf{0}\\ \hat{\boldsymbol{\Phi}}\end{pmatrix}} \leq b_{M//K} + \frac{\left\|\begin{pmatrix} I \\ M \end{pmatrix} K(I+MK)^{-1}WL\right\| \left\|P(I+MK)^{-1}(-M,I)\right\|}{1 - \|I - PGWL\|}. \tag{6.45}$$

Next use the identity:

$$L\sum_{i=0}^{k}\left(I - PGWL\right)^i = \sum_{i=0}^{k}\left(I - LPGW\right)^i L \quad \forall\, k \tag{6.46}$$

and substitute it into (6.44) to obtain

$$\boldsymbol{u}(k+1) = (I+KM)^{-1}(I,K)\boldsymbol{w}_0(k+1) + K(I+MK)^{-1}\hat{\boldsymbol{\Phi}} + K(I+MK)^{-1}W \times \Bigg(\sum_{i=0}^{k} (I - LPGW)^i LP\hat{\boldsymbol{\Phi}} + \sum_{i=0}^{k-1} (I - LPGW)^i LP(I+MK)^{-1}(-M,I)\boldsymbol{w}_0(k-i) \Bigg)$$

which, if condition (6.17) holds, ultimately produces the bound

$$\|\Pi_{\bar{M}//\bar{C}}\|_{\begin{pmatrix}\mathbf{0}\\ \dot{\boldsymbol{\phi}}\end{pmatrix}} \leq b_{M//K} + \frac{\left\|\begin{pmatrix}I\\ M\end{pmatrix}K(I+MK)^{-1}W\right\|\|LP(I+MK)^{-1}(-M,I)\|}{1-\|I-LPGW\|}. \tag{6.47}$$

Hence (6.43) is an upper bound for both (6.45) and (6.47) cases. □

Therefore the definition of $b_{\bar{M}//\bar{C}}$ given by Theorem 6.4 replaces that of (4.44), allowing us to directly apply Theorems 4.5, 4.7 and Proposition 4.1 to the system of Fig. 6.2. These supply precise conditions for robust performance. Assuming a model and feedback controller have been designed, they also motivate the following design procedure:

Procedure 4 (Design guidelines for robust stability)
Define task: Represent functional tasks as a minimum set of position and/or velocity and/or acceleration requirements involving subsets of joints, over subsets of intervals. Almost all functional tasks can be represented in this way. Use these parameters to define P via (6.1) and Lemma 6.3.
Define subspace: If necessary to improve realism or reduce identification time (as will be discussed in Chap. 8), introduce subspaces $\mathscr{W}$ and/or $\mathscr{X}$ by defining the matrices $\bar{W}$ and $\bar{X}$ respectively. In the latter case K is designed to satisfy (6.11) and we set $W = I$.
ILC design: Compute an ILC operator L to satisfy Theorem 6.1. Suitable examples are provided by the NOILC operators of Lemma 6.1.
Gain bound computation: Use Theorem 6.4 to compute the gain bound $b_{\bar{M}//\bar{C}}$, trying to produce the smallest value that can achieve the desired performance. Note that the ILC component (right hand term of (6.43)) can be made arbitrarily small if convergence speed is not an issue (i.e. through choice of L with a small norm).
Establish robust uncertainty: Use $b_{\bar{M}//\bar{C}}$ to compute robustness bounds for realistic uncertainty using Theorem 4.7 and Proposition 4.1. These define a 'ball' of stabilized plants in the uncertainty space of radius $b^{-1}_{\bar{M}//\bar{C}}$.
Experimental evaluation: Implement the controller, measure and quantify performance. If necessary, redefine the task (to reduce $\|P\|$), slow learning (to reduce $\|L\|$) or de-tune feedback tracking performance (to reduce $b_{M//K}$) in order to increase the radius of the stabilized ball of plants. Alternatively, re-identify the plant model M to reduce the mismatch, $\delta(M,N)$, between it and the true stimulated arm system N.
Refine control system: If performance deteriorates, update the task definition, subspace(s), model, and control operator design between experiments to maximize robust performance. In practice, the process of switching the controller to a more robust design that provides stability at the expense of tracking performance can be automated.

6.5 Human Motor Control

Task description (6.4) embeds natural motion into the control action, and removes the need for a predefined reference trajectory. In this section we show how functional tasks relevant to rehabilitation can be expressed as the required set of gestures or coordinated joint movements occurring at distinct time-points or over sub-intervals. We start by placing this problem in the wider context of human motor control.

6.5.1 Computational Models of Upper Limb Motion

Human motor control is a well-established field of research, and many studies have been reported characterizing motion during upper limb reaching tasks. The majority extract relationships between key variables (e.g. timing and amplitude of kinematic, kinetic or electromyographic data) in order to examine the effect of task conditions and/or participant groups on task execution. These include effect of age [7], task conditions [8], and compensatory strategies post stroke [9]. For example [10–12] find significant inter-patient differences in the performance of reaching tasks following stroke compared with unimpaired participants. Human sensorimotor control has also been expressed computationally in order to more fully capture the underlying dynamics of movement [13, 14]. Approaches can be divided into those that attempt to simulate the internal feedback/feedforward mechanisms present in the central nervous system, and those that try only to model the resulting kinematic motion at the task level. The latter have traditionally posed reaching tasks as optimization problems, involving, for example, the minimization of jerk [15], torque change [16], variance [17], interaction torques or combinations of these [18]. However the focus has so far overwhelmingly been on planar point to point tasks. The case of functional tasks necessary to complete activities of daily living has not yet been addressed.

To show how general classes of functional tasks fit within the extended task description (6.4) we next describe a series of experiments in which functional movements are recorded from unimpaired subjects. Using their identified arm models, task parameters within the projection P are then fitted in simulation so that the solution to (6.4) corresponds with their recorded arm movements as closely as possible. More details of the experimental results reported in this section can be found in [19].

6.5.2 Unimpaired Motion Data Collection

Following ethical approval, twelve unimpaired volunteers were recruited to the study. Inclusion criteria were that the participants had to be: (i) aged 30–80 years old; (ii) able to comply with study protocol; (iii) able to communicate effectively and (iv) able to provide written informed consent. Exclusion criteria were: (i) the requirement

of an interpreter; (ii) uncorrected visual impairment (iii) a skin disease or allergy to sticky tape; (iv) severe pain in the arm, shoulder or hand; and, for the control participants, (v) a neurological condition that affects movement in the arm.

The unimpaired participants (six male and six female) were aged between 49 and 77 (M = 64, SD = 10). All unimpaired participants, except for one, were right handed. The side tested for each participant was randomized; six participants completed the tasks using their right hand and six using their left hand. Five participants were tested using their dominant hand. The testing side for unimpaired participants was randomized so as to be more representative of the stroke population, which are almost equally distributed between left and right sided incidence [20].

All participants attended one testing session lasting 2-3 hours in which the kinematic movements of the upper limb and hand during three functional reaching tasks were recorded. The tasks were closing a drawer, turning off a light switch and picking up a can to drink from. Position data were recorded using a Vicon MX T-Series motion capture system (Vicon, Oxford, UK) using 12 cameras (6 x T40 and 6 x T160) sampling at 100 Hz. Reflective anatomical markers were positioned on key landmarks of the torso, shoulder complex, upper limb, wrist and hand, as shown in Fig. 6.3. Marker clusters were attached to the sternum and acromion on the side that was being tested, with additional markers placed on the radial and ulnar styloids and the second and fifth carpometacarpal (CMC) and metacarpophalangeal (MCP) joints of the hand. A marker wand was used to locate specific anatomical landmarks with respect to the relevant marker cluster, see [21]. These additional bony landmarks consisted of: sternal notch, xyphoid process, C7 vertebrae, T8 vertebrae, sternoclavicular joint, acromioclavicular joint, scapula acromion angle, scapula medial spine scapula, scapula inferior angle and medial and lateral epicondyles of the elbow. The elbow joint centre was estimated as the midpoint between the medial and lateral epicondyles. The glenohumeral joint centre was defined according to the regres-

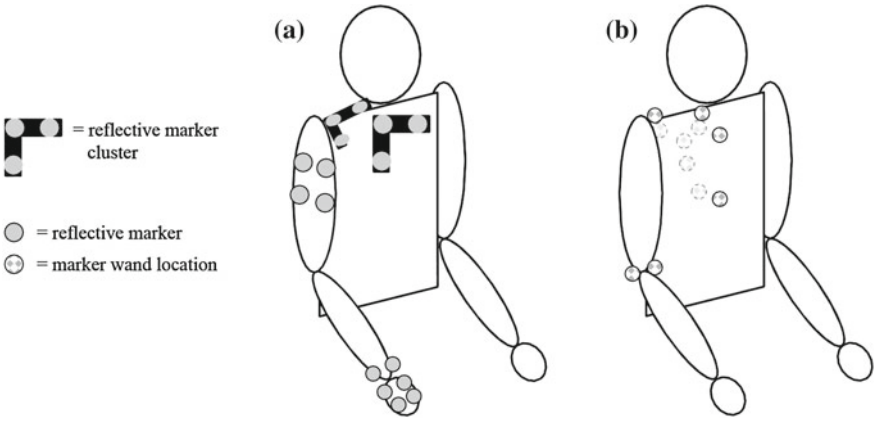

Fig. 6.3 **a** Positioning of Vicon marker clusters used during trials and **b** additional marker wand locations used for calibration

sion method of [22]. Additional markers were positioned on the task objects to aid movement identification. Four markers were positioned in a square on the front edge of the drawer and light switch. Markers were located so that they did not inhibit participants' movements during tasks.

Participants were seated at a table that was adjusted so that the underside was 10 cm above their knee. For each task, the participant was asked to start with their hand (palm down) on their knee. On a 'start' command, the participant completed the task and then placed their hand back on their knee. Tasks were performed at both self-selected and maximal speeds. Five successful trials were collected for each task and each speed; trials were repeated if any of the reflective markers were occluded for more than 25 epochs during the trial. Participants were given a 15–30 s break between each trial. All participants completed the drawer closing task first. Maximum reach for each participant was measured from the anterior edge of the acromion to the end of the index finger.

Drawer Closing Task

A custom made cabinet that had a drawer with a large, round, central knob was placed on the table in front of the participant so that the drawer knob was directly in line with the participant's shoulder for the side being tested. The cabinet was placed at a distance corresponding to 100 % of the participant's maximum reach, with the drawer knob directly in line with the participant's shoulder for the side being tested. When opened, the drawer knob was at a distance of 75 % of the participant's maximum reach. Participants were asked to move their hand from their knee to push the drawer closed using the knob and to return their hand back to their knee.

Light Switch Task

A standard light switch is mounted on the opposite side of the cabinet. The cabinet was positioned so that the light switch was in line with the participant's shoulder, at 75 % of their maximum reach. Participants were asked to move their hand from their knee to turn off the light switch and to return their hand back to their knee. Participants were always required to push in the top of the light switch, which required more arm control and stability than pressing the bottom of the switch.

6.5.3 Data Analysis

Vicon Nexus (Version 1.8) software reconstructed 3D position data for all the markers. Marker position data were filtered using a 4th order low-pass Butterworth filter, with a cut-off frequency of 10 Hz. Anatomical landmarks, recreated from their known positions with respect to the marker clusters, were used to define local coordinate systems for the thorax, scapular, humorous and ulna following ISB guidelines [23]. The hand was defined with an origin at the midpoint between the second and fifth CMC markers, the Y axis was defined as being parallel with the line formed by the

mid-point of the CMC markers to the mid-point of the MCP markers pointing dorsally, the Z axis parallel to the line from the second CMC marker to the fifth CMC marker pointing laterally (with the hand supinated), with the X axis orthogonal to the Y and Z axes. Positional data were averaged at each time point across the five repetitions, for each participant, task, and speed. Key timings were then extracted, comprising the start and end of the movement, defined by the initial hand movement from the participant's knee and the hand returning to the knee, respectively. For the light task an additional timing was when the light switch was pressed. For the drawer task two additional timings were the start and end of the drawer movement.

6.6 Computational Model Development

The electrically stimulated human arm model of Sect. 2.2.5 has been extended to include forearm rotation, wrist flexion/extension and abduction/adduction through inclusion of joints ϕ_i, $i = 6, 7, 8$. The model parameters are shown in Fig. 6.4, where l_i and a_i denote link and centre of mass lengths respectively for $i \in \{u, f, w\}$, and m_i, I_i are mass and inertias respectively. The general form $\boldsymbol{F}\left(\boldsymbol{\Phi}(t), \dot{\boldsymbol{\Phi}}(t)\right)$ given by (2.14) is assumed. The resulting model retains the structure of (2.6) with $\boldsymbol{\Phi} = [\phi_1, \ldots, \phi_8]^\top$, and has state-space implementation (2.7). Note that $\boldsymbol{u}(t)$ specifies the innervation input, which could be through either voluntary action or application of electrical stimulation.

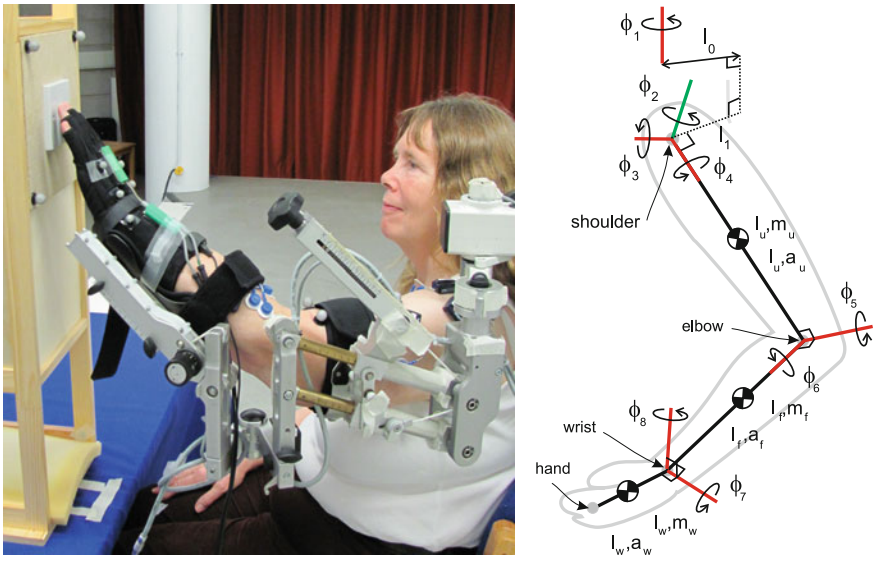

Fig. 6.4 Unimpaired participant performing task, and corresponding 8 dof upper limb model

The minimum input energy model of human movement proposed by [13, 14] can be expressed using the extended task description of (6.4) and, in particular, exactly corresponds to the NOILC solution (6.27). Adopting this form means we only need to define parameters in projection P. The problem of coming to rest at the light switch at time $t = T$ is expressed by the following definitions of P and $P\bar{G}_{\mathscr{P}}$:

Lemma 6.4 *Let operator P be defined by*

$$(P\boldsymbol{\Phi}_{\mathscr{P}})(t) = P_1\left(\begin{bmatrix}\boldsymbol{\Phi}_{\mathscr{P}}(t)\\ \dot{\boldsymbol{\Phi}}_{\mathscr{P}}(t)\end{bmatrix}\right) = \begin{bmatrix}\boldsymbol{k}(\boldsymbol{\Phi}_{\mathscr{P}}(t))\\ \boldsymbol{J}\left(\boldsymbol{\Phi}_{\mathscr{P}}(t)\right)\dot{\boldsymbol{\Phi}}_{\mathscr{P}}(t)\end{bmatrix}, \qquad t = t_1 = T. \tag{6.48}$$

with corresponding linearized extended plant operator, (6.24), given by

$$(P\bar{G}_{\mathscr{P}}|_{\tilde{\boldsymbol{\nu}}}\boldsymbol{\nu})(t) = \int_0^t J(\tilde{\boldsymbol{\Phi}}(t))C(t)\begin{bmatrix}I\\ A(t)\end{bmatrix}\Gamma(t,\tau)B(\tau)\boldsymbol{\nu}(\tau)\mathrm{d}\tau, \quad t = t_1 = T. \tag{6.49}$$

In (6.48), projection P extracts the Cartesian hand position $\boldsymbol{k}(\boldsymbol{\Phi}_{\mathscr{P}})(t)$ and velocity $\frac{\mathrm{d}}{\mathrm{d}t}\boldsymbol{k}(\boldsymbol{\Phi}_{\mathscr{P}})(t) = \boldsymbol{J}\left(\boldsymbol{\Phi}_{\mathscr{P}}(t)\right)\dot{\boldsymbol{\Phi}}_{\mathscr{P}}(t)$, which hence makes P a nonlinear function of $\boldsymbol{\Phi}_{\mathscr{P}}$. This means that $\bar{G}^e_{\mathscr{P}}|_{\tilde{\boldsymbol{\nu}}} = P\bar{G}_{\mathscr{P}}|_{\tilde{\boldsymbol{\nu}}}$ is defined as in (6.49), where $\tilde{\boldsymbol{\Phi}} = \int_0^t C(t)\Gamma(t,\tau)B(\tau)\boldsymbol{\nu}(\tau)\mathrm{d}\tau$ is the joint operating point. Form (6.49) then replaces (6.24) for application in the ILC updates of Theorems 6.1 and 6.2. The drawer closing task is similarly defined, and includes an additional time-point so that $M = 2$. Tracking is defined on interval $[t_1, t_2]$ to stipulate the drawer moving along its runners.

Having defined the task, the next step is to solve (6.4). This is done in simulation in order to efficiently predict the movement generated by the control system if it were used to assist motion. Results will then be compared with the experimental motion actually produced by the unimpaired participant. Accordingly, we apply $\boldsymbol{\nu}_k$ to model $\bar{G}^e_{\mathscr{P}}$ to generate $(\boldsymbol{e}_k)^e_{\mathscr{P}} = \hat{\boldsymbol{\Phi}}^e_{\mathscr{P}} - \bar{G}^e_{\mathscr{P}}\boldsymbol{\nu}_k$. The next input is then calculated using NOILC update (6.34), which is repeated until convergence occurs.

6.7 Results

For each participant dynamic model (2.7) was identified using the simple decoupled form $F_i(\phi_i(t), \dot{\phi}_i(t)) = b_i\dot{\phi}_i(t) + k_i(\phi_i(t) - \tilde{\theta}_i)$ where b_i, k_i and set-point $\tilde{\phi}_i$ are scalars for the joint angles $i \in \{1, \ldots, 8\}$ employed in the model. Reference positions $\hat{\boldsymbol{\Phi}}(t_i)$, $i \in \{0, 1\}$ and $i \in \{0, 1, 2\}$ for the light switch and drawer tasks respectively were defined by the placement of the participant and manipulated objects. In particular, $\hat{\boldsymbol{\Phi}}(0) = \hat{\boldsymbol{\Phi}}_0$ was taken by averaging the initial arm position over the five repetitions of each task. For the light switch task, t_1 was the average time taken to press the

Table 6.1 Light switch pressing task fitting error norms

		Maximal speed				Self-selected speed			
		Reach only	Reach	Return	Reach & ret.	Reach only	Reach	Return	Reach & ret.
$\|\boldsymbol{\Phi} - \hat{\boldsymbol{\Phi}}\|$	P1	2.035	2.363	2.440	3.436	4.169	5.563	4.110	7.049
	P2	3.793	4.409	3.431	5.674	5.711	5.909	4.110	7.542
	P3	4.762	5.674	4.483	7.275	5.411	8.515	6.272	10.759
	P4	3.914	4.645	2.337	5.252	5.783	6.156	2.825	6.924
	P5	3.523	4.348	4.267	6.367	6.174	7.437	4.458	8.732
	P6	3.190	3.973	3.474	5.678	2.702	4.409	3.458	5.770
	P7	2.927	3.206	3.066	4.597	4.720	4.902	5.740	7.640
	P8	2.961	3.555	3.580	5.257	4.507	5.579	7.748	9.667
	P9	3.770	4.943	5.706	7.620	10.501	11.404	10.099	15.715
	P10	2.027	2.236	2.717	3.528	2.396	3.635	5.697	6.741
	P11	1.863	2.034	3.057	3.809	4.785	5.573	4.578	7.225
	P12	1.444	2.921	2.979	4.200	2.180	2.752	3.386	4.589
$\|\hat{\boldsymbol{\Phi}} - \boldsymbol{\Phi}\|/\|\hat{\boldsymbol{\Phi}} - \boldsymbol{\Phi}_0\| \times 100$	P1	80.443	76.167	77.880	76.557	70.808	58.704	71.682	64.067
	P2	74.847	69.629	70.820	69.164	65.422	63.980	71.761	64.901
	P3	66.837	59.148	66.722	61.833	69.532	48.041	67.538	56.506
	P4	74.538	68.472	86.136	74.953	62.525	59.650	81.948	66.563
	P5	70.221	61.606	73.449	66.826	63.403	54.481	74.016	62.243
	P6	69.278	60.013	60.456	57.007	76.493	57.219	66.276	59.866
	P7	75.090	72.054	80.686	76.054	66.414	64.847	67.957	66.260
	P8	78.587	72.880	77.303	73.689	82.256	76.372	67.470	70.961
	P9	73.831	63.517	60.228	60.975	59.113	54.992	57.535	54.736
	P10	78.050	75.057	68.387	71.068	85.413	74.253	59.983	65.830
	P11	83.692	81.552	69.366	73.323	71.778	65.978	68.483	66.824
	P12	85.286	70.227	67.530	68.537	84.091	79.915	76.047	76.759
Mean (s.d)		75.892 (5.620)	69.194 (6.969)	71.580 (7.857)	69.166 (6.407)	71.437 (8.839)	63.203 (9.667)	69.225 (6.624)	64.626 (5.974)

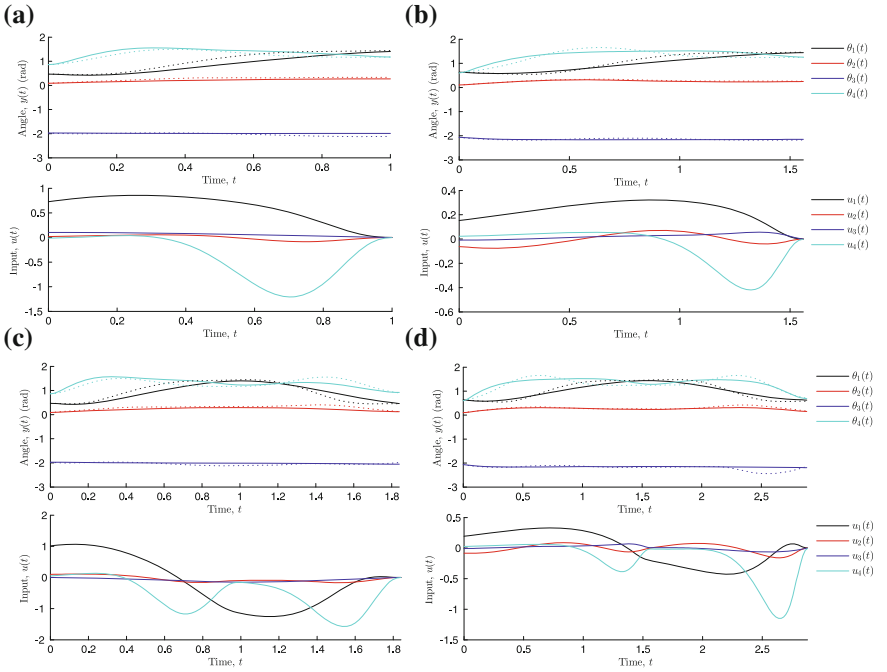

Fig. 6.5 Simulated and experimental joint angles for light switch task **a** maximal speed reach component, **b** self-selected speed reach component, **c** maximal speed reach and return components, **d** self-selected speed reach and return components

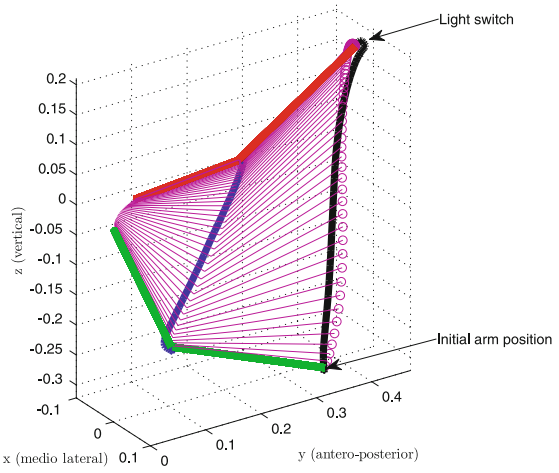

Fig. 6.6 Simulated and experimental paths in Cartesian space for maximal speed reach component of the light switching task

Table 6.2 Drawer closing task fitting error norms

		Maximal speed				Self-selected speed			
		Reach only	Reach	Return	Reach & ret.	Reach only	Reach	Return	Reach & ret.
$\|\boldsymbol{\Phi} - \hat{\boldsymbol{\Phi}}\|$	P1	1.328	2.082	2.273	3.139	2.552	2.969	2.954	4.429
	P2	2.531	3.147	2.367	3.986	3.421	2.187	2.350	3.247
	P3	1.508	1.982	1.672	2.621	5.129	7.294	6.760	9.930
	P4	1.636	2.043	1.511	2.561	4.049	4.937	3.371	6.038
	P5	3.156	3.118	2.835	4.232	3.803	4.614	2.832	5.492
	P6	1.738	2.070	1.753	2.827	3.976	3.851	2.883	5.098
	P7	1.368	2.371	2.261	3.457	4.631	5.386	3.211	6.478
	P8	1.785	2.500	2.291	3.405	3.226	6.617	7.294	9.849
	P9	2.203	2.741	2.815	3.978	5.117	8.186	6.673	10.592
	P10	1.358	1.643	2.208	2.899	3.032	2.412	3.380	4.150
	P11	2.877	3.849	2.721	4.847	4.595	5.832	2.335	6.427
	P12	0.987	1.733	1.460	2.367	1.684	2.098	2.985	3.690
$\|\hat{\boldsymbol{\Phi}} - \boldsymbol{\Phi}\|/\|\hat{\boldsymbol{\Phi}} - \boldsymbol{\Phi}_0\| \times 100$	P1	87.322	76.145	66.027	71.049	85.700	82.214	75.330	77.926
	P2	81.354	75.111	73.165	73.581	78.526	88.795	77.579	84.258
	P3	83.094	75.560	76.768	75.327	65.728	48.316	50.554	49.103
	P4	92.415	88.785	90.010	88.776	79.660	73.670	79.437	75.413
	P5	79.702	80.032	77.310	78.616	75.571	68.872	75.934	70.562
	P6	75.197	69.108	67.084	65.969	68.313	69.527	65.514	65.888
	P7	89.082	75.945	72.624	72.322	67.740	61.342	75.350	65.860
	P8	90.332	83.656	78.108	81.202	91.522	75.256	66.771	71.364
	P9	79.869	73.252	65.172	69.101	75.836	57.150	56.837	57.006
	P10	85.693	81.237	61.533	70.634	80.340	85.782	65.888	77.425
	P11	75.930	65.432	63.304	63.460	71.154	61.506	77.360	64.228
	P12	87.548	78.147	69.372	74.342	86.234	82.848	58.833	73.976
Mean (s.d)		83.961 (5.634)	76.868 (6.245)	71.706 (8.044)	73.698 (6.841)	77.194 (8.078)	71.273 (12.512)	68.782 (9.528)	69.417 (9.711)

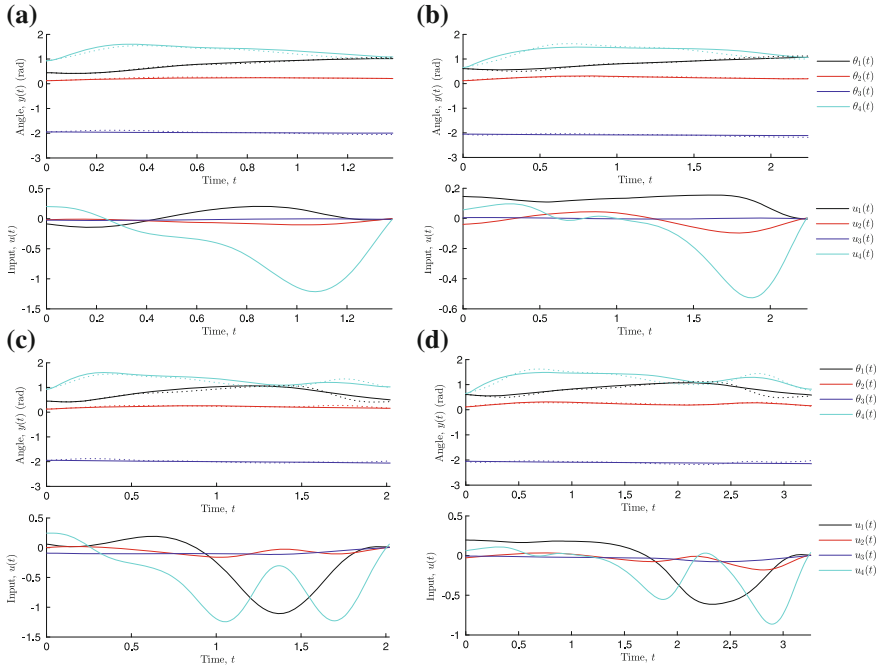

Fig. 6.7 Simulated and experimental joint angles for drawer closing task **a** maximal speed reach component, **b** self-selected speed reach component, **c** maximal speed reach and return components, **d** self-selected speed reach and return components

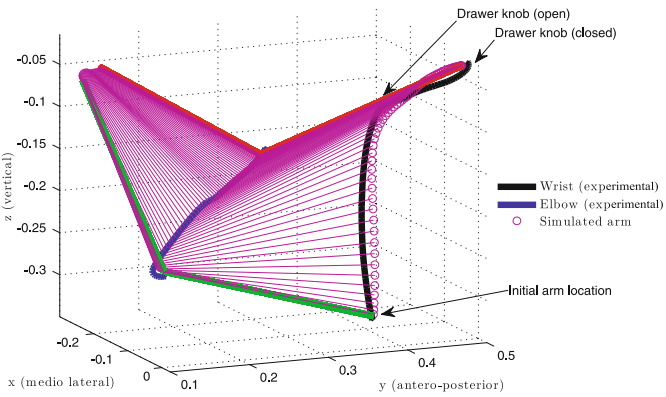

Fig. 6.8 Simulated and experimental paths in Cartesian space for maximal speed reach component of the drawer closing task

switch, and for the drawer task, t_2 was the average time taken to first make contact with the drawer knob and t_3 the average time to fully close the drawer.

To solve (6.4), update (6.34) was iterated in simulation until $\|(\boldsymbol{e}_k)^e\| < 0.001$ was achieved, and the corresponding 'virtual reference' $\hat{\boldsymbol{\Phi}} = G\boldsymbol{v}_k$ computed. Results expressing the difference in experimental and simulated joint angles appear in Table 6.1 for the self-selected speed where the normalized error, expressed as a percentage, is $100 \times \|\hat{\boldsymbol{\Phi}} - \boldsymbol{\Phi}\|/\|\hat{\boldsymbol{\Phi}} - \boldsymbol{\Phi}_0\|$. For the reach component of the light switch task at self-selected speed, the mean fitting across the 12 participants is 71.437 % confirming high accuracy. The procedure has been repeated for the maximal speed light switch task, with fitting results shown in Table 6.1. The fitting is now 75.892 %. Figure 6.5a and b show the signals $\boldsymbol{\Phi}$ and $\hat{\boldsymbol{\Phi}}$ (solid and dotted lines respectively) at both speeds for a single participant (P1). Figure 6.6 shows the corresponding paths in Cartesian space for the reach component of the maximal speed light switch task.

Fitting results for the full reach and return light switch task are shown in Table 6.1 at both speeds, with values also given for the reach and return sub-components of the task. This incorporates the arm returning to the start position after completing the switch task, and hence an additional time point is required in the definition of P. The mean fitting for the reach and return light switch task across the 12 participants is now 69.166 % and 64.626 % for maximal and self-selected speeds respectively. Figure 6.5c and d shows the signals $\boldsymbol{\Phi}$ and $\hat{\boldsymbol{\Phi}}$ (solid and dotted lines respectively) at both speeds for participant P1.

Fitting results for the drawer closing task are shown in Table 6.2 and confirm a mean accuracy of 77.194 and 83.961 % for the self-selected and maximal speeds respectively. Figure 6.7a and b show experimental and simulated joint angles at both speeds for participant P1. Figure 6.8 shows the corresponding paths in Cartesian space for the reach component of the maximal speed drawer closing task.

Mean fitting results for the reach and return drawer closing task are shown in Table 6.2 and confirm a total accuracy of 69.417 and 73.698 % for the self-selected and maximal speeds respectively. This incorporates the arm returning to the start position after closing the drawer, and hence the definition of P is augmented to employ an additional time-point. Figure 6.7c and d shows the signals $\boldsymbol{\Phi}$ and $\hat{\boldsymbol{\Phi}}$ (solid and dotted lines respectively) at both speeds for participant P1.

6.8 Conclusions

The tracking control problem has been extended to encompass fully functional motion, and illustrated by comparing model outputs with experimental data collected from unimpaired subjects performing common activities of daily living. This model description accurately represents natural movements, and means that a reference trajectory defined over $t \in [0, T]$ is no longer required. A framework to design ILC control algorithms has been proposed to enforce tracking of these extended tasks. In the next chapter the control scheme is used within a clinical trial to examine whether its ability to assist functional tasks leads to improved outcome measures.

References

1. C.T. Freeman, Constrained point-to-point iterative learning control with experimental verification. Control Eng. Pract. **20**(5), 489–498 (2012)
2. D.H. Owens, J.J. Hätönen, S. Daley, Robust monotone gradient-based discrete-time iterative learning control. Int. J. Robust Nonlinear Control **19**, 634–661 (2009)
3. D.H. Owens, C.T. Freeman, T. Van Dinh, Norm-optimal iterative learning control with intermediate point weighting: theory, algorithms, and experimental evaluation. IEEE Trans. Control Syst. Technol. **21**(3), 999–1007 (2012)
4. D.H. Owens, C.T. Freeman, B. Chu, An inverse model approach to multivariable norm optimal iterative learning control with auxiliary optimization. Int. J. Control **87**(8), 1646–1671 (2014)
5. D.H. Owens, C.T. Freeman, B. Chu, Multivariable norm optimal iterative learning control with auxiliary optimization. Int. J. Control **86**(6), 1026–1045 (2013)
6. B. Chu, C.T. Freeman, D.H. Owens, A novel design framework for point-to-point ilc using successive projection. EEE Trans. Control Syst. Technol. **23**(3),1156–1163 (2015)
7. S. Zoia, E. Pezzetta, L. Blason, A. Scabar, M. Carrozzi, M. Bulgheroni, U. Castiello, A comparison of the reach-to-grasp movement between children and adults: a kinematic study. Dev. Neuropsychol. **30**(2), 719–738 (2006)
8. A. Viau, A.G. Feldman, B.J. McFadyen, M.F. Levin, Reaching in reality and virtual reality: a comparison of movement kinematics in healthy subjects and in adults with hemiparesis. J. Neuroeng. Rehabil. **1**(11), 1–7 (2004)
9. C. Wu, C.A. Trombly, K. Lin, L. Tickle-Degnen, A kinematic study of contextual effects on reaching performance in persons with and without stroke: influences of object availability. Arch. Phys. Med. Rehabil. **81**(1), 95–101 (2000)
10. S.B. Thies, P.A. Tresadern, L.P. Kenney, J. Smith, D. Howard, J.Y. Goulermas, C. Smith, J. Rigby, Movement variability in stroke patients and controls performing two upper limb functional tasks: a new assessment methodology. J. Neuroeng. Rehabil. **6**, 2 (2009)
11. M.C. Cirstea, M.F. Levin, Compensatory strategies for reaching in stroke. Brain **123**(5), 940–953 (2000)
12. W. Tippett, L. Alexander, M. Rizkalla, L. Sergio, S. Black, True functional ability of chronic stroke patients. J. Neuroeng. Rehabil. **10**, 1–13 (2013)
13. D.M. Wolpert, Z. Ghahramani, J.R. Flanagan, Perspectives and problems in motor learning. TRENDS Cogn. Sci. **5**(11), 487–494 (2001)
14. V.S. Huang, J.W. Krakauer, Robotic neurorehabilitation: a computational motor learning perspective. J. Neuroeng. Rehabil. **6**, 5 (2009)
15. T. Flash, N. Hogan, The coordination of arm movements: an experimentally confirmed mathematical model. J. Neurosci. **5**, 1688–1703 (1985)
16. Y. Uno, M. Kawato, R. Suzuki, Formation and control of optimal trajectory in human multijoint arm movement. Minimum torque-change model. Biol. Cybern. **61**(2), 89–101 (1989)
17. C.M. Harris, D.M. Wolpert, Signal-dependent noise determines motor planning. Nature **20**(394(6695), 780–784 (1998)
18. K. Ohta, M.M. Svinin, Z. Luo, S. Hosoe, Rl Laboissiere, Optimal trajectory formation of constrained human arm reaching movements. Biol. Cybern. **91**(1), 23–36 (2004)
19. C.T. Freeman, T. Exell, K.L. Meadmore, E. Hallewell, A.-M. Hughes, Computational models of upper limb motion during functional reaching tasks for application in FES based stroke rehabilitation. Biomed. Eng. J. **60**(3), 179–191 (2015)
20. V.S. Hedna, A.N. Bodhit, S. Ansari, A.D. Falchook, L. Stead, K.M. Heilman, M.F. Waters, Hemispheric dfferences in ischemic stroke: is left-hemisphere stroke more common? J. Clin. Neurol. **9**(2), 97–102 (2013)
21. M. Warner, P. Chappell, M. Stokes, Measuring scapular kinematics during arm lowering using the acromion marker cluster. Hum. Mov. Sci. **31**(2), 386–396 (2012)

22. C. Meskers, F. van der Helm, L. Rozendaal, P. Rozing, In vivo estimation of the glenohumeral joint rotation center from scapular bony landmarks by linear regression. J. Biomech. **31**(1), 93–96 (1998)
23. G. Wu, F. van der Helm, H. Veeger, M. Makhsous, P. Van Roy, C. Anglin, J. Nagels, A. Karduna, K. McQuade, X. Wang, F. Werner, B. Buchholz, Isb recommendation on definitions of joint coordinate systems of various joints for the reporting of human joint motion - part ii: shoulder, elbow, wrist and hand. J. Biomech. **38**(5), 981–992 (2005)

Chapter 7
Clinical Application: Goal-Orientated Stroke Rehabilitation

The control framework of Chap. 6 enables functional tasks to be assisted in a natural manner by exploiting underlying human motor control principles. To confirm its utility for rehabilitation, these are now used to assist tasks involving real objects, with ES applied to the wrist and finger extensors, as well as to muscles in the arm and shoulder. As highlighted in Chap. 5, there is strong evidence that functional improvement following training is mostly restricted to the actually trained functions and activities [1]. By supporting functional, whole arm tasks including wrist extension and opening of the hand, we therefore address limitations in the previous system. In addition, we incorporate non-invasive, markerless sensing technology. More detailed results of the study and in-depth analysis can be found in [2].

7.1 System Description and Set-Up

The underlying kinematics are shown in Fig. 7.1 and include the wrist action considered in Chap. 6. The rehabilitation system is shown in Fig. 7.2 and facilitates recovery of upper limb motor control and function through goal-oriented, functional tasks assisted by ES. The stroke participant sits at the workstation and ES electrodes are positioned on the anterior deltoid, triceps and wrist and finger extensors of their impaired arm. If required, mechanical support is provided by the SaeboMAS unweighting device described in Sect. 2.1.3 that facilitates movement by supporting the arm against gravity. A Microsoft Kinect (Microsoft, Washington, USA) is used to provide shoulder, elbow and wrist joint positions, and has an accuracy of approximately 10 mm [3, 4]. It is combined with an electro-goniometer (Model SG75, Biometrics Ltd, Newport, UK) placed over the wrist joint to measure flexion/extension and abduction/adduction. Using these data, the joint angles shown in Fig. 7.1 are computed and used by the ES control scheme. A custom made graph-

C. Freeman, *Control System Design for Electrical Stimulation in Upper Limb Rehabilitation*, DOI 10.1007/978-3-319-25706-8_7

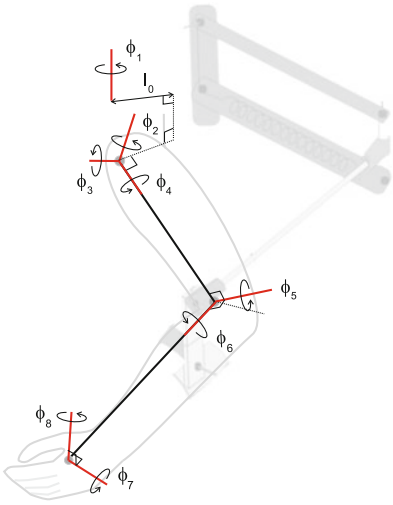

Fig. 7.1 Human arm kinematic relationships

ical user interface is used to select appropriate tasks and monitor training. For safety purposes an over-ride 'stop' button terminated trials with immediate effect.

The rehabilitation system incorporates five main functional tasks that span a 3-dimensional workspace and offers a range of reaching and grasping challenge. They comprise closing a drawer, pressing a light switch (located at 90° or 115° of shoulder elevation), stabilizing an object, pressing a button (placed at one of four different locations in the workspace) and lifting to reposition an object. Objects can be placed at different locations on the table corresponding to percentages of arm reach (60, 75, 80, 95 %), and either directly in line with the shoulder or 45° to either side (see Fig. 7.2). The table was at a distance of 45 % of arm length away from the gleno-humeral joint and 35 cm below the arm when held 90° horizontal to the shoulder. These values were used to define the extended task tracking problem (6.4) of Chap. 6 which is then solved by following control design Procedure 4. Since only the reaching component was used, the button pressing and drawer closing tasks were defined as in Sect. 6.6 with parameter T modified for each participant. Repositioning of objects involved specifying a further point to correspond to the original and final object positions.

A convenience sample of five chronic stroke participants was recruited with characteristics displayed in Table 7.1. All participants had suffered strokes between 22 months and 7 years prior to recruitment to the study; four had left hemiplegia and one right hemiplegia. None had visual neglect or visual field deficits. A pre and post study design was adopted in which participants' upper limb motor activity and impairment were assessed before and after 18 intervention sessions. Feedback regarding the system was also obtained via a semi-structured interview. The assessments and interviews were conducted according to standard protocol, by assessors who were independent of the study. Data collection was carried out by a team of experienced researchers.

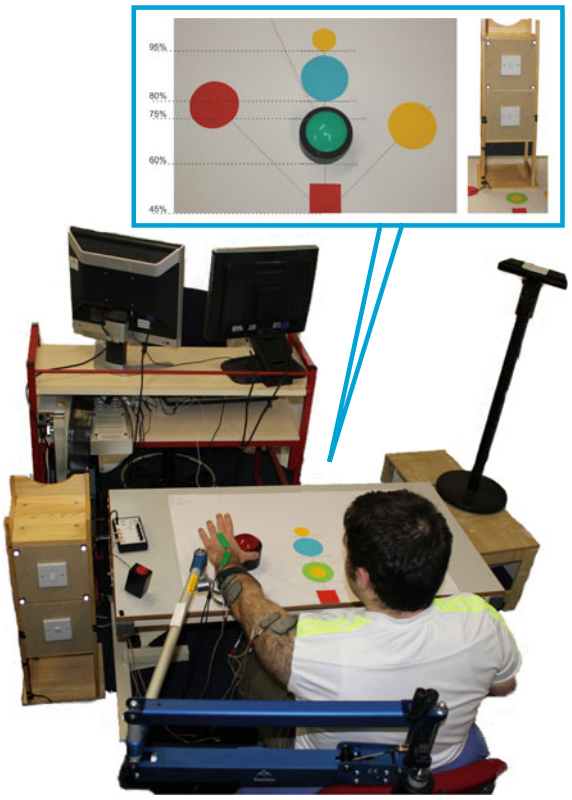

Fig. 7.2 Rehabilitation system incorporating SaeboMAS, Microsoft Kinect, task display, operator monitor and real-time control hardware. The bubble displays the task template customized to each participants arm length. *Green* = button located at 60 % of arm length; *Blue* = button located at 80 % of arm length; *Red* = button located at 75 % of arm length, 45° to the impaired side; *Yellow* = button located at 75 % of arm length, 45° across body; small *yellow circles* = location that object was grasped from and repositioned to (60 and 95 % of arm length). The cabinet housed the light switch tasks (located at 75 and 80 % of reach for the high and low light switch tasks respectively); the draw task (located at 80 % of reach) was on the reverse side of the cabinet

At the beginning of each session, participants were positioned at the workstation and their hemiplegic arm strapped into the arm support which was adjusted to allow the participant's hand to rest easily on the table top. ES electrodes were place over the anterior deltoid, triceps and wrist/finger extensors. To identify ES amplitudes for each muscle, the pulsewidth was set at a maximum value and the therapist gradually increased the ES amplitude applied to each muscle until they reached the maximum comfortable level. The pulsewidth was then reduced to zero. Following this the biomechanical model was identified using the procedure of Chap. 2.

During the intervention, the therapist selected a range of tasks that spanned the workspace. Participants repeated each task 6-12 times, starting each with their hand resting on the red square shown in Fig. 7.2. Participants were instructed to contribute maximum voluntary effort.

Table 7.1 Socio-demographic characteristics of participants ($n = 5$)

Pt Id	P1	P2	P3	P4	P5
Age (years)	53	42	49	46	48
Type of stroke	I	I	I	I	H
Time since stroke (months)	22	84	52	48	84
Female/Male	M	M	M	F	M
Side of stroke	R	R	R	R	L
Original dominant hand	R	R	R	R	L

Pt Id–participant identification, I–infarct, H–haemorrhage, F–female, M–male, L–left, R– right

7.1.1 Outcome Measures

Clinical assessments: As in Chap. 5, the FMA and ARAT were used to assess upper limb motor impairment and motor activity respectively. Their assessment was completed one to six days before and after the 18 intervention sessions.

ES-unassisted performance: Participants completed five unassisted tasks (i.e. without ES): the four button pushing tasks (located at 60 % or 80 % of reach in-line with the shoulder, or at 75 % of reach, 45° to the left or right of the shoulder), and the high light switch task (located at 75 % of reach and 115° of elevation) at the beginning and end of each session. The unassisted tasks consisted of one trial only. The time it took to complete a task (or until maximum effort was achieved), joint angles and task success (i.e. whether the task was successfully performed) were recorded for each trial. ES-unassisted data obtained at the beginning of each training session were used to map changes in these performance measures over time.

ES-assisted performance: The tracking error for each muscle group was calculated across the six repetitions of each assisted task to quantify the change in task performance elicited by ILC. The error was calculated over the full task duration using the virtual reference $\hat{\boldsymbol{\Phi}}(t) = (G_{\mathscr{P}} \boldsymbol{v}_\infty)(t),\ t \in [0, T]$.

Level of Arm support used during ES-assisted tasks: To maximize voluntary effort, the level of arm support was reduced following consistently successful performance, and was monitored and recorded for each task completed. Note that the level of arm support remained constant for the ES-unassisted tasks.

As in Chap. 5 and our previous clinical trials [5, 6], a one-tailed, paired t-test, with a significance level of $p < 0.05$, was used to compare pre- and post-intervention FMA and ARAT outcome measures. Changes in the ES-unassisted and ES-assisted performance, and level of arm support required across the 18 sessions were analyzed by calculating best-fit linear regression slopes of performance against session number collapsed across all participants. Significance was associated with a value of $p < 0.05$.

7.2 Results

All five participants complied with the study protocol and there was no withdrawal. Participants reported no intervention adverse effects.

7.2.1 Assisted Tracking Performance

ES improved performance compared to when no ES was provided (see Fig. 7.3). Furthermore, ILC successfully controlled the amount of ES applied independently to each muscle, facilitating movement patterns more similar to the reference trajectories over a series of trials. This is illustrated in Fig. 7.3, in which the participant completes the task more quickly in trial 6 compared to trial 1 and their movement more closely resembles the ideal reference movement (as defined by the virtual reference).

The amount of support delivered by the un-weighting arm mechanism was reduced over the 18 sessions for all participants for the case of ES-assisted button tasks, the drawer task and the low light switch task, but not the high light switch task (see Table 7.2 and Fig. 7.4). The results demonstrate that the amount of mechanical

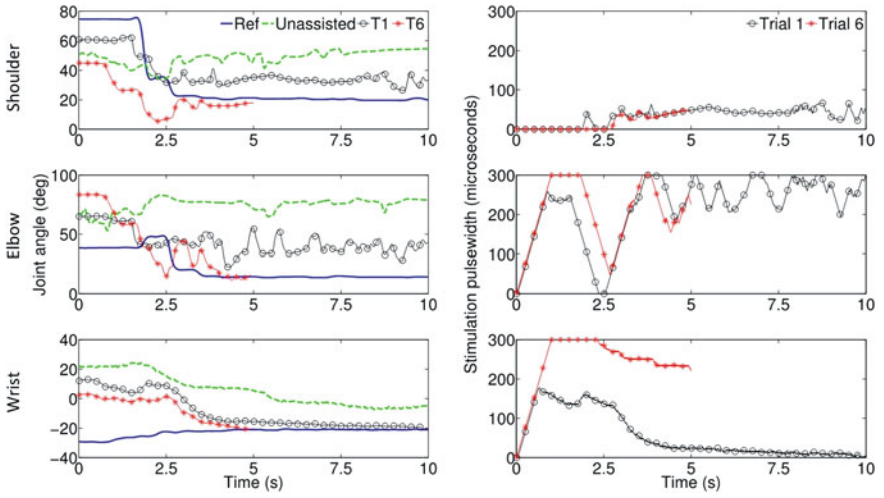

Fig. 7.3 Tracking detail. The *left panel* shows the reference movement (*blue line*) and a participant's movement when unassisted (*dashed green line*), assisted for trial 1 (*black line with circles*) and trial 6 (*red line with asterisks*) of a set of button pressing tasks at 80 % of reach for the shoulder (*top panel*), elbow (*middle panel*) and wrist (*bottom panel*). Note that the movement produced in trial 6 is shorter than trial 1 (i.e. participant completes the task more quickly) and more closely resembles the ideal reference movement. Note also that the reference movement is completed when the movement plateaus but the end position is held until 20 s elapses. The right panel shows the stimulation applied on trial 1 (*black line with circles*) and trial 6 (*red line with asterisks*)

Table 7.2 Best-fitting regression slopes and p-values for arm support levels in ES-assisted tasks

Task	Mean slope	p-value	t-value
Button	−0.226	0.00	−11.62
Drawer	−0.202	0.00	−7.95
Low light switch	−0.173	0.00	−6.86
High light switch	0.019	0.66	0.44

Note The small slope values are due to the different units in the axes

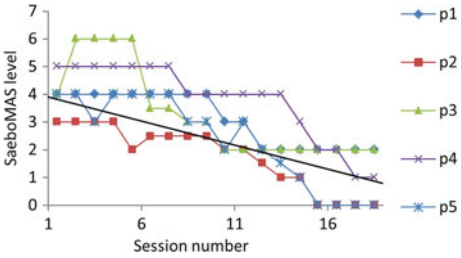

Fig. 7.4 Arm support levels for the button pressing tasks for each participant across the 18 training sessions. The *black solid line* = the line of best fit across all participants

assistance in the button tasks was decreased by at least 2 support levels for each participant, with two participants no longer requiring any support whatsoever to complete the tasks. Note that each level corresponds to an un-weighting action of approximately 0.5 Kg.

7.2.2 Unassisted Tracking Performance

Table 7.3 shows that significant reductions were found in the time taken to perform both the button press at 80 % of reach and button press at 75 % of reach, 45° to the impaired side. In addition, the end positions of the hand away from the participant in terms of distance in the direction of the button were found to increase over the 18 sessions (significantly so for the far button). Taken together, these results indicate that participants became more successful at reaching these buttons and did so in a shorter time over the course of the 18 sessions (see Table 7.3).

None of the participants were able to complete the high light switch task unassisted by ES. However, the time taken on this task and the maximum elevation at the shoulder achieved by participants were both found to significantly increase over the 18 sessions ($ts > 3.51$, $ps < 0.001$, see Fig. 7.5). This demonstrates that, as the intervention progressed, participants spent more time trying to achieve this task, and got closer to completing it (i.e., they could lift their arm higher and nearer to the target and could maintain this position for longer).

Table 7.3 Regression slopes and p-values for ES-unassisted tasks

Task	End hand position		Time taken		Maximum Extension	
	Mean slope	p-value t-value	Mean slope	p-value t-value	Mean slope	p-value t-value
Button at 80 %	25.62	0.01	−0.38	−2.44		
		2.61		0.02		
Button on impaired side	12.08	1.47	−0.29	0.03		
		0.15		−2.17		
High light switch			0.55	0.00	−0.08	0.001
				5.37		−3.51

Note The small slope values are due to the different units in the axes

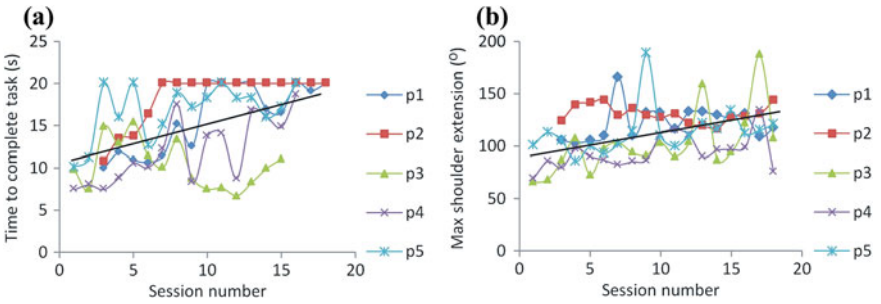

Fig. 7.5 High light switch task **a** time taken and **b** maximum extension for each participant across the 18 training sessions. The *black solid line* = the line of best fit across all participants. For maximum extension 0° corresponds to the arm by side of the body, 90° corresponds to the arm held horizontal to the body; 180° corresponds to pointing upwards

7.2.3 Clinical Outcome Measures

The scores from the two clinical outcome measures are shown in Table 7.4. Improvements were seen in scores; in four participants for the FMA and for all participants for the ARAT. This improvement was statistically significant for both FMA ($t(4) = 2.44$, $p = 0.036$) and ARAT ($t(4) = 4.49$, $p = 0.005$).

Table 7.4 Clinical outcome assessment baseline and post-intervention scores

Pt ID[1]		MS1	MS2	MS3	MS4	MS5	Mean (SD)	p-value	% change[2]
ARAT (57)[3]	Baseline	0	3	4	3	3	2.6(1.52)	0.036	7.719
	Post	7	7	5	8	8	7(1.22)		
FMA (66)[3]	Baseline	15	19	17	21	22	18.8 (2.86)	0.005	6.667
	Post	24	24	21	27	20	23.2 (2.77)		

[1]participant identification [2]change in score divided by maximum possible score
[3]maximum score in brackets

7.3 Discussion

Results demonstrate that the control scheme of Chap. 6 is able to independently and precisely control stimulation applied to the shoulder, elbow and wrist and finger extensors of chronic stroke participants to facilitate coordinated reach to grasp tasks. Statistically significant improvement was measured in four different outcome measures following completion of the intervention: an increase in both FMA and ARAT clinical assessment scores, an improvement in ES-unassisted performance, and a reduction in the arm support levels. This translated into a clinically relevant change in the clinical assessment measures (defined as 10 % of the value of the scale) for only one participant. In addition to measured quantitative outcomes, participant feedback provided positive qualitative responses. These results are reported in [2].

An important finding from this study is that both the primary outcome measures, FMA and ARAT scores, showed statistically significant improvements from pre to post intervention. Thus, following the intervention participants showed reductions in motor impairment and were able to perform more functional motor activities. The same intervention period of one hour was used to facilitate comparison with previous work using ILC mediated ES which showed statistically significant improvements only in the FMA assessment and not the ARAT (see Chap. 5 as well as the additional studies [5, 6]). This has been attributed to the fact that in these studies wrist and hand extensors were not specifically trained, with only the triceps and/or anterior deltoid being stimulated. Indeed, upper limb treatments and therapies are suggested to be location specific [7]. Training of the shoulder and elbow will only improve motor impairment in the shoulder and elbow [5, 6, 8], just as training of the wrist and finger extensors shows improvements in hand function [9]. As such, to achieve functional changes the whole upper limb should be considered in training. This study set out to address this by incorporating ILC mediated wrist and finger stimulation, and the results are very promising to the recovery of whole arm functional movements.

Nevertheless, despite observing an improvement and participants reporting greater ability to perform everyday tasks at home, such as lifting, stabilizing and pressing light switches, it was still evident that fine finger movement is required to translate the benefits observed to activities of daily living.

7.4 Conclusions

The next chapter will address the problem of achieving precise control of hand and wrist movement that has been highlighted as a critical limitation to achieving more significant clinical outcome measures. Electrode arrays show potential in providing the required muscle selectivity, but the feasibility of incorporating them into a clinical system is a challenging problem due to the difficulty in obtaining an underlying model relating stimulation and resulting movement. Our objective is therefore to integrate model-based electrode array controllers into the existing design framework in order

to assist fine wrist and finger movements. This will allow us to subsequently extend the rehabilitation system demonstrated in this chapter so that it can provide more effective therapy.

References

1. J.M. Veerbeek, E. van Wegen, R. van Peppen, P.J. van der Wees, E. Hendriks, M. Rietberg, G. Kwakkel, What is the evidence for physical therapy poststroke? a systematic review and meta-analysis. PLoS One **9**(2), e87987 (2014). February
2. K.L. Meadmore, T. Exell, E. Hallewell, A.-M. Hughes, C.T. Freeman, M. Kutlu, V. Benson, E. Rogers, J.H. Burridge, The application of precisely controlled functional electrical stimulation to the shoulder, elbow and wrist for upper limb stroke rehabilitation: A feasibility study. J. Neuroeng. Rehabil. **11**, 105 (2014)
3. R.A. Clark, Y.-H. Pua, K. Fortin, C. Ritchie, K.E. Webster, L. Denehy, A.L. Bryant, Validity of the microsoft kinect for assessment of postural control. Gait Posture **36**(3), 372–377 (2012)
4. T. Dutta, Evaluation of the kinect sensor for 3-d kinematic measurement in the workplace. Appl. ergon. **43**(4), 645–649 (2012)
5. A.M. Hughes, C.T. Freeman, J.H. Burridge, P.H. Chappell, P. Lewin, E. Rogers, Feasibility of iterative learning control mediated by functional electrical stimulation for reaching after stroke. J. Neurorehabil. Neural Repair **23**(6), 559–568 (2009)
6. K.L. Meadmore, A.-M. Hughes, C.T. Freeman, Z. Cai, D. Tong, J.H. Burridge, E. Rogers, Functional electrical stimulation mediated by iterative learning control and 3*d* robotics reduces motor impairment in chronic stroke. J. Neuroeng. Rehabil. **32**(9), 1–11 (2012)
7. M.J. Johnson, Recent trends in robot-assisted therapy environments to improve real-life functional performance after stroke. J. Neuroeng. Rehabil. **3**, 29 (2006)
8. P. Sampson, C.T. Freeman, S. Coote, S. Demain, P. Feys, K.L. Meadmore, A.M. Hughes, Using functional electrical stimulation mediated by iterative learning control and robotics to improve arm movement for people with multiple sclerosis. IEEE Trans. Neural Syst. Rehabil. Eng. (2015)
9. G. Mann, P.N. Taylor, R. Lane, Accelerometer-triggered electrical stimulation for reach and grasp in chronic stroke patients: a pilot study. Neurorehabil. Neural Repair **25**, 774–781 (2011)

Chapter 8
Electrode Array Control Design

The recent emergence of transcutaneous electrode arrays has potential to improve selectivity, automate placement, and reduce fatigue and discomfort compared with single pad electrodes [1, 2]. The freedom they embed to adjust the size and shape of the electrode means they can isolate smaller muscle groups, and thereby enable the user to perform a variety of functional tasks including walking [3, 4], and hand/wrist motion [2, 5]. However, existing control strategies are open-loop and use time-consuming electrode element selection procedures, limiting accuracy and usability.

In this chapter the model developed in Chap. 2 is extended to represent electrode arrays. The control procedures of Chaps. 3, 4 and 6 are then applied using locally linear models which embed a restricted stimulation subspace. Clinically feasible model identification procedures are proposed for this form to replace the identification method of Chap. 2 which is unsuitable for arrays due to the impracticality of manipulating each joint of the hand and wrist while measuring applied force. Finally, the robustness properties established in Chaps. 3, 4 and 6 are extended to provide transparent robust performance margins for the electrode array scheme.

8.1 Modeling of a Single Array

For simplicity we consider control of a single electrode array in this chapter, but will integrate this into a general framework encompassing an arbitrary number of arrays and single pad electrodes in Chap. 9. We have assumed each channel, u_i, of ES signal $\boldsymbol{u} \in \mathscr{L}_2^m[0, T]$ represents the electrical stimulation applied to the ith muscle. Since each array element does not necessarily correspond to a single muscle, we now introduce signal $\boldsymbol{z} \in \mathscr{L}_2^n[0, T]$ containing the stimulation applied to each of the n elements of the array over $t \in [0, T]$. The stimulation provided to the ith muscle

C. Freeman, *Control System Design for Electrical Stimulation in Upper Limb Rehabilitation*, DOI 10.1007/978-3-319-25706-8_8

is assumed to be a linear combination of those array elements within spatial range, and hence can be modeled using the relationship

$$u_i(t) = \sum_{j=1}^{n} a_{i,j} z_j(t), \quad i = 1, \ldots, m, \quad t \in [0, T]. \tag{8.1}$$

From Chap. 3, the resulting system is hence expressed in operator form as

$$M : \boldsymbol{\Phi} = H_{RB} F_m(\boldsymbol{\Phi}, \dot{\boldsymbol{\Phi}}) H_{LAD} h_{IRC}(Az), \quad A : z \mapsto \boldsymbol{u} : \boldsymbol{u}(t) = \begin{bmatrix} a_{1,1} & \cdots & a_{1,n} \\ \vdots & \ddots & \vdots \\ a_{m,1} & \cdots & a_{m,n} \end{bmatrix} z(t) \tag{8.2}$$

with elements defined by (3.39)–(3.42). This reduces to (3.38) when $n = m$ and $A = I$ (i.e. each ES channel is associated with a single muscle).

It is possible to identify parameters in (8.2) by extending the approach developed in Chap. 2. However, in the case of the wrist and hand there are at least 41 musculo-tendon units actuating16 joints with 23 degrees of freedom [6]. This makes measurement of all joint angles and application and sensing of force/moments about each axis highly challenging. In addition, since the muscles are small and closely packed, the model system is sensitive to small changes in array position as well as to physiological changes such as fatigue and spasticity, and environmental conditions such as temperature and humidity. This makes the previous approach impractical, and therefore it will be exchanged for the identification of local linear models (as incorporated as an option within the design procedures of Chaps. 3, 4 and 6).

8.2 General Array Control Framework

Application of control design Procedure 4 of Sect. 6.4 to the array control problem first requires designing feedback controller K to stabilise the linearised model description $M|_{z_k}$. The impractically of obtaining a global non-linear model means that we must identify $M|_{z_k}$ around each operating point z_k. The structure of $M : z \mapsto \boldsymbol{\Phi}$ is given by (8.2) and has n inputs and p outputs, making it potentially high dimension. To recover a tractable identification problem we therefore embed a restricted plant stimulation space with dimension $q < n$. From Definition 6.1, this necessitates feedback structure (6.11), and hence the control scheme takes the form shown in Fig. 8.1, where operator X is given by (6.6) with full rank $\bar{X} \in \mathbb{R}^{n \times q}$. We can expand the previous design procedure as follows:

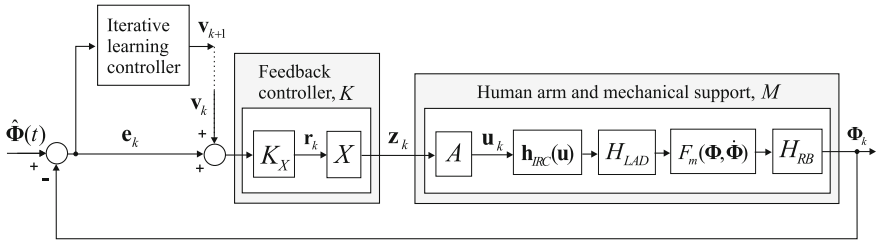

Fig. 8.1 Feedback and ILC control scheme specified to electrode array structure

Procedure 5 (Design for Robust stability: specification to electrode array)

Define task: Choose P via (6.1) and Lemma 6.3 to capture the required functional task (or for simplicity choose $P = I$ to track reference $\hat{\mathbf{\Phi}}$ over $t \in [0, T]$).
Define stimulation subspace, X: This will be addressed in Sect. 8.3.
Model identification: Apply input sequence $z_k = X\boldsymbol{r}_k$ to the ES electrode array, and use resulting input-output data set $\{z_k, \mathbf{\Phi}_k\}$ to identify a linear approximation to the dynamics $M|_{z_k}$ about $z_k = X\boldsymbol{r}_k$. Here

$$M|_{z(k)} : \mathscr{L}_2^n[0, T] \to \mathscr{L}_2^p[0, T] : z \mapsto \mathbf{\Phi}$$
$$: \mathbf{\Phi} = \left(H_{RB}|_{\boldsymbol{w}} F_m(\mathbf{\Phi}, \dot{\mathbf{\Phi}}) H_{LAD} \boldsymbol{h}_{IRC}(Az)\right)|_{z_k} z \quad (8.3)$$

Feedback controller design: Design $K_X : \mathscr{L}_2^p[0, T] \to \mathscr{L}_2^q[0, T]$ to stabilize $M|_{z(k)}X$. This is equivalent to designing K to stabilize $M|_{z(k)}$ given structure (6.11).
ILC design: Design L to satisfy condition (6.14) or (6.17) of Theorem 6.1 for the resulting closed-loop system

$$G|_{\hat{\mathbf{\Phi}}+\boldsymbol{v}_k} : \mathscr{L}_2^p[0, T] \to \mathscr{L}_2^p[0, T] : \boldsymbol{v} \mapsto \mathbf{\Phi} : \mathbf{\Phi} = (I + M|_{z(k)}K)^{-1} M|_{z(k)} K\boldsymbol{v}. \quad (8.4)$$

The first condition guarantees nominal convergence to zero error, but requires $q \geq p$. In both cases, implement ILC update using (6.26).
Examine robustness: Calculate $b_{\bar{M}//\bar{C}}$ for above K and L forms using Theorem 6.4. Use in Theorem 4.7 and Proposition 4.1 to inspect allowable model mismatch and its effect on robust performance.

We next present examples of explicit forms of K_X and L for application in the above procedure. These assume that the form of linearized system (8.3) is stipulated by the designer as a static $p \times n$ mapping, i.e. with form

$$F : \mathscr{L}^n[0,T] \to \mathscr{L}^p[0,T] : \boldsymbol{z} \mapsto \boldsymbol{\Phi} : \boldsymbol{\Phi}(t) = \bar{F}\boldsymbol{z}(t), \quad \bar{F} \in \mathbb{R}^{p\times n}, \tag{8.5}$$

followed by SISO linear dynamics. In practice this assumption is supported by similar muscle and rigid body dynamics in the wrist and hand, together with the presence of spasticity, inherent stiffness, and the low bandwidth of required movements.

Proposition 8.1 *Let linearized dynamics (8.3) have form $M|_z = \bar{H}(s)F$ where F is given by (8.5) and $\bar{H}(s)$ is a SISO system. The feedback control action $K_X : \boldsymbol{e} \mapsto \boldsymbol{r} : \boldsymbol{r} = \bar{K}(s)(FX)^\dagger \boldsymbol{e}$, where $\bar{K}(s)$ is a SISO system, applied to system $\boldsymbol{\Phi} = M|_z X\boldsymbol{r}$ realizes stimulation input*

$$\boldsymbol{r} = N_w(s)\boldsymbol{r}^\star \tag{8.6}$$

where $\boldsymbol{r}^\star$ is the unique minimizer of a weighted norm of the tracking error, $\boldsymbol{e} = \hat{\boldsymbol{\Phi}} - \boldsymbol{\Phi}$, and the SISO system

$$N_w(s) := (I + \bar{K}(s)\bar{H}(s))^{-1}\bar{K}(s)\bar{H}(s). \tag{8.7}$$

The resulting closed-loop system dynamics are

$$\boldsymbol{\Phi} = N_w(s)(FX)^\perp \hat{\boldsymbol{\Phi}} \tag{8.8}$$

where the orthogonal projection onto the range of FX is $FX(FX)^\dagger = (FX)^\perp$,

$$(FX)^\perp : \mathscr{L}^p[0,T] \to \mathscr{L}^p[0,T] : \hat{\boldsymbol{\Phi}} \mapsto \boldsymbol{x} : \boldsymbol{x}(t) = \bar{F}\bar{X}(\bar{F}\bar{X})^\dagger \hat{\boldsymbol{\Phi}}(t). \tag{8.9}$$

Proof Consider the weighted tracking error $\boldsymbol{r}^\star = \min_{\boldsymbol{r}} \|\hat{\boldsymbol{\Phi}} - \boldsymbol{\Phi}\|_Q^2$ where weight $Q = (\bar{H}(s)^{-1})^* \bar{H}(s)^{-1}$ with $(\cdot)^*$ the adjoint operator. This has solution

$$\boldsymbol{r}^\star = \min_{\boldsymbol{r}} \|\hat{\boldsymbol{\Phi}} - \boldsymbol{\Phi}\|_Q^2 = \min_{\boldsymbol{r}} \|\hat{\boldsymbol{\Phi}} - \bar{H}FX\boldsymbol{r}\|_Q^2 = \min_{\boldsymbol{r}} \|\bar{H}^{-1}\hat{\boldsymbol{\Phi}} - FX\boldsymbol{r}\|^2 = (FX)^\dagger \bar{H}^{-1}\hat{\boldsymbol{\Phi}}.$$

The proposed control action $K_X = \bar{K}(s)(FX)^\dagger$ realizes (when $q \le p$)

$$\begin{aligned} \boldsymbol{r} = \bar{K}(FX)^\dagger(\hat{\boldsymbol{\Phi}} - \bar{H}FX\boldsymbol{r}) &\Rightarrow (I + \bar{K}(FX)^\dagger \bar{H}FX)\boldsymbol{r} = \bar{K}(FX)^\dagger \hat{\boldsymbol{\Phi}} \\ \Rightarrow (I + \bar{K}\bar{H})\boldsymbol{r} &= \bar{K}(FX)^\dagger \hat{\boldsymbol{\Phi}} \\ \Rightarrow \boldsymbol{r} = (I + \bar{K}\bar{H})^{-1}\bar{K}(FX)^\dagger \bar{H}\bar{H}^{-1}\hat{\boldsymbol{\Phi}} &\Rightarrow \boldsymbol{r} = N_w\boldsymbol{r}^\star \end{aligned} \tag{8.10}$$

The corresponding closed-loop dynamics are

$$\boldsymbol{\Phi} = \bar{H}FX\boldsymbol{r} = \bar{H}FX(I + \bar{K}\bar{H})^{-1}\bar{K}(FX)^{\dagger}\bar{H}\bar{H}^{-1}\hat{\boldsymbol{\Phi}} = N_w(s)FX(FX)^{\dagger}\hat{\boldsymbol{\Phi}}.$$

□

The feedback control action $K_X = \bar{K}(s)(FX)^{\dagger}$ of Proposition 8.1 therefore ensures that $\boldsymbol{\Phi}$ tracks the demand input $\hat{\boldsymbol{\Phi}}$ (or $\hat{\boldsymbol{\Phi}} + \boldsymbol{v}_k$ if ILC is also applied) as closely as possible, subject to dynamics N_w specified by the designer. It requires only that SISO feedback controller $\bar{K}(s)$ be selected to stabilize dynamics (8.7), but has the property of stabilizing all p joints. By enforcing dynamics $G|_{\hat{\boldsymbol{\Phi}}+\boldsymbol{v}_k} = N_w(s)(FX)^{\perp}$, it also facilitates the following simplified ILC update:

Proposition 8.2 *The system of Fig. 8.1 with $M = \bar{H}(s)F$, the feedback action of Proposition 8.1, and ILC update*

$$\boldsymbol{v}_{k+1} = \boldsymbol{v}_k + LP\boldsymbol{e}_k, \quad L = l(PN_w(FX)^{\perp})^{\dagger}, \quad l \in (0, 1] \tag{8.11}$$

satisfies (6.17) and enforces convergence to the minimum extended error norm, i.e.

$$\lim_{k\to\infty} \boldsymbol{v}_k = \boldsymbol{v}^{\star}, \quad \boldsymbol{v}^{\star} = \min_{\boldsymbol{v}} \|\hat{\boldsymbol{\Phi}}^{e} - \boldsymbol{\Phi}^{e}\|^2. \tag{8.12}$$

Furthermore, if $\bar{K}(s)$ is tuned so that $N_w(s)$ approximates a pure delay of λ seconds then (8.11) corresponds to the phaselead update

$$\boldsymbol{v}_{k+1}(t) = \boldsymbol{v}_k(t) + l(P_j(\bar{F}\bar{X})^{\perp})^{\dagger}\boldsymbol{e}_k^{e}(t + \lambda), \qquad t \in [t_{j-1}, t_j],\ j = 1, \ldots S. \tag{8.13}$$

Proof We set $W = I$ in Theorem 6.1 and assume $q \le p$. Since Proposition 8.1 yields closed-loop dynamics $G|_{\hat{\boldsymbol{\Phi}}+\boldsymbol{v}_k} = N_w(s)(FX)^{\perp}$, we then substitute $L = l(PN_w(FX)^{\perp})^{\dagger}$ and $G = N_w(s)(FX)^{\perp}$ into $I - LPG$ to give $I - l(P(FX)^{\perp})^{\dagger}P(FX)^{\perp} = I(1 - l)$ which satisfies (6.17). The corresponding limiting error solution (6.22), $\left(I - PG(LPG)^{-1}L\right)\hat{\boldsymbol{\Phi}}^{e}$, is given by $(I - (P(FX)^{\perp})^{\perp})\hat{\boldsymbol{\Phi}}^{e}$ which is the orthogonal projection onto the kernel of $\hat{\boldsymbol{\Phi}}^{e}$. This is the minimum achievable error and hence solves (8.12). If $N_w(s) = e^{-s\lambda}$ then $L = l(e^{-s\lambda}P(FX)^{\perp})^{\dagger} = le^{s\lambda}(P(FX)^{\perp})^{\dagger}$ with time-based implementation (8.13). □

Note that update (8.13) takes the 'phase-lead ILC' form, which has received significant research attention due to its simple structure (with only two parameters, l, λ) that enables heuristic tuning [7–9].

We next examine how stimulation subspace X can be chosen to balance tracking accuracy with practicality of identification.

8.3 Subspace Identification

The identification of subspace $\mathscr{X}$ is addressed in this section, with subsequent identification of the q input, p output system $M|_{\bar{\boldsymbol{u}}(k)}X$ following in Sect. 8.4. The purpose of $\mathscr{X}$ is to reduce the dimension of the latter problem so that it can feasibly be performed within the limited time available in practice. The use of $\mathscr{X}$ is motivated by the observation that only a subset of muscles are required for a given posture, and the underlying muscle locations can be assumed to not change. It is hence possible to select an input subspace that covers those muscles needed to perform a required set of tasks, together with the possible variation in array placement. In practice a suitable input subspace can be constructed using:

- previous experimental input and output data, and/or
- structural information based on prior system knowledge.

From the comments made following Theorem 6.3, any basis can be used to define the stimulation subspace without affecting subsequent performance (i.e. X may be exchanged for XX_R with any full rank X_R).

8.3.1 Selection Using Experimental Data

Assume that previous experiments (with any choice of input subspace) have yielded input and output signal pairs $\{z, \boldsymbol{\Phi}\}$ for plant M given by (8.2) (where z is the stimulation applied to the n elements of the array). From these select those with outputs close to the required movement(s), and denote as $\{z^i, \boldsymbol{\Phi}^i\}$, $i = 1, \ldots, c$. These can be used to produce a basis for the input set by directly inserting in X as

$$\bar{X}(t) = [z^1(t), z^2(t), \ldots, z^c(t)] \in \mathbb{R}^{n \times c} \tag{8.14}$$

and setting $q = c$. If X is time-invariant, then a finite set of $\{z^i(t_j)\}_{i,j}$ can instead be employed. In the case of linear M, any reference in the set spanned by a linear combination of $\boldsymbol{\Phi}^i$ (corresponding to the range of MX, $\mathrm{im}(MX)$), will be tracked with zero error using the ILC algorithms of Theorem 6.1. If $\hat{\boldsymbol{\Phi}}$ does not belong to this set, then the subsequent error is the orthogonal projection of $\hat{\boldsymbol{\Phi}}$ onto $\ker((MX)^*)$, as shown in Fig. 8.2. If $c \ll n$, the dimension of MX is far smaller than that of M. The direct use of previous inputs is not ideal as q cannot be independently prescribed (since $q = c$). Inputs may also be linearly dependent, and thereby provide no new information. This is now addressed.

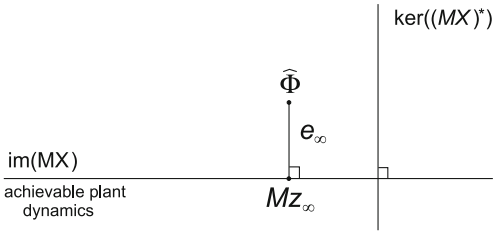

Fig. 8.2 Output space showing error as an orthogonal projection onto achievable plant dynamics

8.3.1.1 Previous Input Data

Let subspace dimension q be prescribed and data sets $\{\boldsymbol{z}^i, \boldsymbol{\Phi}^i\}$, $i = 1, \ldots, c$ available. The next proposition provides optimizations to yield $X : \mathscr{L}_2^q[0, T] \to \mathscr{L}_2^n[0, T]$:

Proposition 8.3 *The distance between each $\boldsymbol{z}^i \in \mathscr{L}_2^n[0, T]$ and the closest element in the image of X is minimized by solving*

$$\min_{(X,H)} J(X, H), \quad J(X, H) = \|Z - XH\|_{HS}^2 \tag{8.15}$$

where $\|\cdot\|_{HS}$ is the Hilbert-Schmidt norm and operators

$$\begin{aligned} H : \mathbb{R}^c &\to \mathscr{L}_2^q[0, T] : \boldsymbol{a} \mapsto \boldsymbol{b} : \boldsymbol{b}_i = \sum_{i=1}^{c} H_i \boldsymbol{a}_i, \\ Z : \mathbb{R}^c &\to \mathscr{L}_2^n[0, T] : \boldsymbol{a} \mapsto \boldsymbol{b} : \boldsymbol{b}_i = \sum_{i=1}^{c} \boldsymbol{z}^i \boldsymbol{a}_i. \end{aligned} \tag{8.16}$$

Using the Frobenius norm $\|\cdot\|_F$, this can also be expressed as

$$\min_{(X,H)} J(X, H), \quad J(X, H) = \int_0^t \left\| Z(t) - \bar{X}(t) H(t) \right\|_F^2 dt. \tag{8.17}$$

Proof The total distance between each $\boldsymbol{z}^i \in \mathscr{L}_2^n[0, T]$ and the closest element in the image of

$$X : \mathscr{L}_2^q[0, T] \to \mathscr{L}_2^n[0, T] : \boldsymbol{r} \mapsto \boldsymbol{z} : \boldsymbol{z}(t) = \bar{X}(t)\boldsymbol{r}(t). \tag{8.18}$$

is minimized by solving

$$\min_{(X,H)} J(X, H), \quad J(X, H) = \sum_{i=1}^{c} \|\boldsymbol{z}_i - XH_i\|^2 \tag{8.19}$$

$$= \sum_{i=1}^{c} \int_0^t \|\boldsymbol{z}_i(t) - \bar{X}(t) H_i(t)\|^2 dt \tag{8.20}$$

where $H_i \in \mathscr{L}_2^q[0, T]$. This is simplified by using

$$\left\| z^i - XH_i \right\|^2 = \left\| Zq^i - XHq^i \right\|^2, \quad q^i \in \mathbb{R}^c := q_i^i = 1,\ q_j^i = 0,\ j \neq i,\ j, i\ \in \{1, \ldots, c\}$$

since $\{q^i \in \mathbb{R}^c : i = \in \{1, \ldots, c\}\}$ is an orthogonal basis of $\mathbb{R}^c$, it follows that

$$J(X, H) = \sum_{i=1}^{c} \|z_i - XH_i\|^2 = \sum_{i=1}^{c} \left\| (Z - XH)q^i \right\|^2 = \|Z - XH\|_{HS}^2 . \tag{8.21}$$

Note, from (8.20), that this can also be expressed as

$$\begin{aligned} J(X, H) &= \sum_{i=1}^{c} \int_0^t \|z^i(t) - \bar{X}(t)H_i(t)\|^2 dt = \int_0^t \left\| Z(t) - \bar{X}(t)H(t) \right\|_{HS}^2 dt \\ &= \int_0^t \left\| Z(t) - \bar{X}(t)H(t) \right\|_F^2 dt. \end{aligned} \tag{8.22}$$

□

Solutions of factorization procedures (8.15) and (8.17) are generally non-unique, and there exist many solution methods through incorporation of different constraints (e.g. principal component analysis, singular value decomposition, nonnegative operator factorization [10]). Optimization (8.19) has the interpretation of calculating a 'line of best fit' between $\{z^i\}$ in the input space, as shown in Fig. 8.3.This procedure ensures that inputs close to those previously encountered are achievable, and hence minimizes corresponding tracking error. As the prescribed parameter q is increased, the image of X enlarges to ultimately satisfy $z^i \in \text{im}(X)\ \forall i$, $\Phi^i \in \text{im}(MX)\ \forall i$.

8.3.1.2 Previous Output Data

A more direct procedure is to select a subspace which minimizes the distance between each element of the set $\{\Phi^i\}$ and the closest achievable joint trajectory. Having identified a linear M, we select q and compute X using:

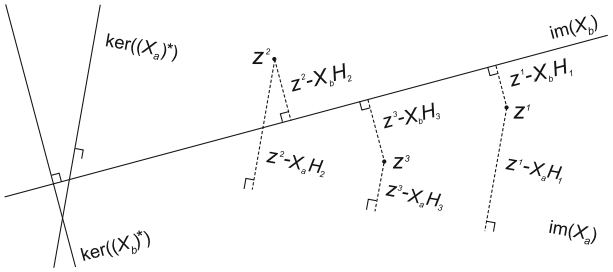

Fig. 8.3 Input space projections of $\{z^i\}$ onto range of subspaces X_a, X_b. Note the latter corresponds to a reduced total projection length

Proposition 8.4 *The distance between each* $\boldsymbol{\Phi}^i \in \mathscr{L}_2^p[0,T]$ *and the closest element in the image of MX is minimized by solving*

$$\min_{(X,H)} J(X,H), \quad J(X,H) = \|Z - XH\|^2_{HS,[M^*M]} \tag{8.23}$$

where H and Z are defined in (8.16).

Proof In this case (8.19) is replaced by

$$\begin{aligned}\min_{(X,H)} J(X,H), \quad J(X,H) &= \sum_{i=1}^{c} \left\| \boldsymbol{\Phi}^i - MXH_i \right\|^2 = \sum_{i=1}^{c} \left\| Mz^i - MXH_i \right\|^2 \\ &= \sum_{i=1}^{c} \left\| z^i - XH_i \right\|^2_{[M^*M]} = \sum_{i=1}^{c} \left\| (Z - XH)\boldsymbol{q}^i \right\|^2_{[M^*M]} \\ &= \|Z - XH\|^2_{HS,[M^*M]} \,.\end{aligned} \tag{8.24}$$

□

Problem (8.23) can be solved using a suitably weighted operator factorization procedure. This has the interpretation of calculating a 'line of best fit' to the points $\{\boldsymbol{\Phi}^i\}$ in the joint output space, as shown in Fig. 8.4. For any $\hat{\boldsymbol{\Phi}}$ lying near an element in the set $\{\boldsymbol{\Phi}^i\}$, the resulting error is then small since it is also the orthogonal projection onto this line which corresponds to the achievable plant dynamics. The disadvantage of this approach is that M is assumed to be a known linear operator.

Procedure 6 (Computational Procedure)

If z^i is sampled with period T_s, then (8.15) and (8.23) can be replaced by equivalent matrix computations by taking

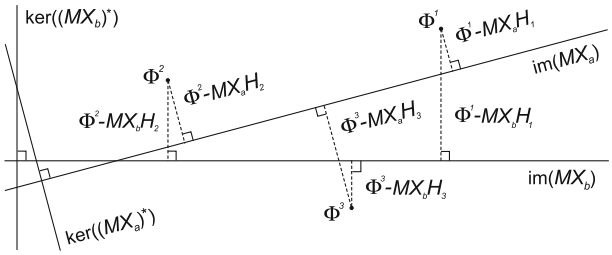

Fig. 8.4 Output space projections of $\{\boldsymbol{\Phi}^i\}$ onto range of MX_a, MX_b, where X_a, X_b are subspaces. Note the former corresponds to a reduced total projection length

$$Z = \left[z^1, z^2, \ldots z^c \right] \in \mathbb{R}^{nN \times c}, \quad z^i = \begin{bmatrix} z^i(0) \\ z^i(T_s) \\ \vdots \\ z^i(T) \end{bmatrix} \in \mathbb{R}^{nN}, \tag{8.25}$$

with corresponding $H \in \mathbb{R}^{qN \times c}$ and $X \in \mathbb{R}^{nN \times qN}$, where $N = 1 + T/T_s$. Alternatively, we can instead use $H \in \mathbb{R}^{q \times c}$ and $X \in \mathbb{R}^{nN \times q}$ to produce a solution X with embeds the required structure $[\bar{X}(0), \bar{X}(T_s), \ldots \bar{X}(T)]^\top$, which is then interpolated to produce $\bar{X}(t),\ t \in [0, T]$. Optimizations (8.15) and (8.23) can also be performed for time-invariant subspaces, that is

$$X : \mathscr{L}_2^q[0, T] \to \mathscr{X}[0, T] \subset \mathscr{L}_2^n[0, T] : \boldsymbol{r} \mapsto z : z(t) = \bar{X}\boldsymbol{r}(t). \tag{8.26}$$

If the above matrix computation is used, then (8.25) is replaced by

$$Z = \left[z^1, z^2, \ldots z^c \right] \in \mathbb{R}^{n \times cN}, \quad z^i = \left[z^i(0), z^i(T_s), \ \ldots \ z^i(T) \right] \in \mathbb{R}^{n \times N}, \tag{8.27}$$

with $H \in \mathbb{R}^{q \times cN}$ and $\bar{X} \in \mathbb{R}^{n \times q}$, and M expressed in discrete 'lifted' form.

If an extended task description is used, then sampling should be conducted in the intervals $[t_{j-1}, t_j], j = 1, \ldots S$ that appear in extended task operator definition (6.1).

8.3.2 Selection Using Structural Knowledge

The limited experimental data available may be replaced or enriched by musculoskeletal physiology and/or array geometry data in the construction of a subspace. Note that the proximity and complexity of musculo-tendon structures in areas such as the forearm means it is inadvisable to rely solely on assumed anatomical relationships.

8.3.2.1 Muscle Locations

Knowledge of the underlying musculoskeletal physiology can be directly embedded by selecting q muscles that provide the required movements, and specifying a stimulation pattern, z^i, for each one. If the subspace is time-varying, $z^i \in \mathscr{L}_2^q[0, T]$ generate $\bar{X}(t)$ via (8.14). If the subspace is time-invariant, then each $z^i \in \mathbb{R}^q$ is the

steady-state stimulation level needed to activate the ith muscle, and $\bar{X}$ is given by

$$\bar{X} = \left[z^1, z^2, \ldots, z^q\right] \in \mathbb{R}^{n\times q} \tag{8.28}$$

which then generates the subspace operator X via (8.26).

8.3.2.2 Muscle Synergies

As previously described, synergies comprise groups of muscles that are recruited in blocks, maintaining constant amplitude relationships. These are often assumed time-invariant, with many studies focusing on identification and analysis using EMG [11]. Suppose a total of d muscles are required to perform the task set, and the spatial location of each is specified using the notation of Sect. 8.3.2.1. We then express a synergistic combination of muscles using the vector $P_i \in \mathbb{R}^d$ which contains the relative amplitude of each of the d muscles. If q synergies are identified, the resultant subspace of possible stimulation inputs are defined by using

$$\bar{X} = \left[z^1, z^2, \ldots, z^d\right]\left[P_1, P_2, \ldots, P_q\right] \in \mathbb{R}^{n\times q}, \tag{8.29}$$

$$\bar{X}(t) = \left[z^1(t), z^2(t), \ldots, z^d(t)\right]\left[P_1, P_2, \ldots, P_q\right] \in \mathbb{R}^{n\times q} \tag{8.30}$$

within the operator definitions (8.26) and (8.18) for time-invariant and time-varying cases respectively. If synergies are not known, they can be constructed from known literature or the approaches of Sects. 8.3.1.1 and 8.3.1.2 can be interpreted as an alternative method for their identification.

8.3.2.3 Array Positional Variation

The model is highly dependent on small changes in where the electrode array is placed on the patient. Hence it is necessary to expand any input set $\{z^i\}$, such as those used in Sects. 8.3.1.1, 8.3.2.1, and 8.3.2.2, based on all possible transformations that capture this variation in array placement. Consider an n element array with h horizontal and v vertical elements. Let element (i, j) be indexed at position $(i-1)h + j$ within vector $z(t) \in \mathbb{R}^n$. Then the transformation matrices

$$T_v = \begin{bmatrix} 0 & I_{h(v-1)} \\ I_h & 0 \end{bmatrix} \in \mathbb{R}^{n\times n}, \quad T_h = \begin{bmatrix} 0 & 1 \\ I_{hv-1} & 0 \end{bmatrix} \in \mathbb{R}^{n\times n} \tag{8.31}$$

respectively denote vertical and horizontal shifts in array position by the height or width of a single array element. Hence $\text{diag}\{T_v, \ldots, T_v\}z(t)$ transforms $z(t)$ to account for repositioning. Similarly, clockwise rotation of the array by angle θ results in the input transformation: map the input row index i to the array position vector $p(i)$, and thence to the new array position $p'(i)$ using rotation matrix $R(\theta)$,

$$\underbrace{\begin{bmatrix} p_1'(i) \\ p_2'(i) \end{bmatrix}}_{p'(i)} = \underbrace{\begin{bmatrix} \cos(\theta) & \sin(\theta) \\ -\sin(\theta) & \cos(\theta) \end{bmatrix}}_{R(\theta)} \underbrace{\begin{bmatrix} i-1-\lfloor (i-1)/h \rfloor h \\ \lfloor (i-1)/h \rfloor \end{bmatrix}}_{p(i)}. \tag{8.32}$$

Mapping back to the new input index yields the transformation

$$T_\theta \ : \ (i,j) = \begin{cases} 1 & \text{if} \quad j = p_1'(i) + p_2'(i)h \\ 0 & \text{otherwise.} \end{cases} \tag{8.33}$$

If the new index $(p_1'(i) + p_2'(i)h)$ is not an integer, $p_1'(i)$ and $p_2'(i)$ must instead be used to weight their four surrounding integer indices. Each of these is then used in (8.33) and the results summed in relation to their associated weights. This extrapolation technique can also be used to form non-integer transformations (8.31). Transformations T_v, T_h, T_θ do not define a subspace themselves, but are used in the general procedure given next.

8.3.3 General Stimulation Subspace Identification Procedure

The following procedure combines the placement variation of Sect. 8.3.2.3 with the procedures of Sects. 8.3.1.1, 8.3.1.2, 8.3.2.1, and 8.3.2.2, including each of the former as a special case. It enables all available system knowledge to be fused in a flexible, transparent manner. It is assumed that the array element indexing of Sect. 8.3.2.3 is used.

Procedure 7 (Stimulation subspace $\mathscr{X}$ construction procedure)

(a) Assemble input data set $\{z^i\}$ encompassing possible solutions to the tracking task(s). These time-varying or time-invariant data may include previous experimental inputs or solutions based on an assumed model(s).
(b) Use physiological knowledge (perhaps augmented by tests performed with a single electrode moved over the patient's arm) to assemble a set of input data $\{z^i\}$ which specifies electrode elements that correspond to known muscle positions. Use (8.29) or (8.30) to embed known synergies.
(c) Combine the two data sets of steps (a) and (b) to form the set $\{z^i\}_{i=1,\ldots,c}$, and decide on weights to reflect relevance/reliability of each element.
(d) Decide on a set of transformations and rotations that describe the range of possible array placement variations. Suppose the possible range of vertical and horizontal positional variation be represented by n_v, n_h levels respectively. Similarly select n_θ levels to span the expected rotation variation. Applying every possible transformation and rotation to the set $\{z^i\}$ expands it from c to $c \times n_v \times n_h \times n_\theta$ elements.

(e) Decide on the required dimension, q, of the input subspace based on the available identification time.
(f) Apply Procedure 6 to solve (8.15) or (8.23) using the weighting of step (c) to generate a subspace which approximates the required search space given the dimensional constraint q.
(g) Generate X using (8.18) or (8.26) for time-invariant and time-varying cases respectively.

Remark 8.1 A restricted stimulation subspace may also be used to prevent stimulation areas comprising single array elements, which may cause discomfort and muscle fatigue to the patient. This is achieved by ensuring that each input comprises a set of two or more adjacent array elements. Adopting the same array indexing as previously, introduce the notation

$$\tilde{I}_{a,b} = \begin{bmatrix} I_b & 0 & \cdots & \cdots & 0 \\ I_b & I_b & \cdots & \cdots & 0 \\ 0 & I_b & \ddots & \ddots & 0 \\ \vdots & \vdots & \ddots & \ddots & \vdots \\ 0 & 0 & \cdots & \ddots & I_b \\ 0 & 0 & \cdots & \cdots & I_b \end{bmatrix} \in \mathbb{R}^{ab\times(a-1)b}. \tag{8.34}$$

Every possible arrangement of two horizontally adjacent elements is realized using

$$\bar{X} = \operatorname{diag}\{\overbrace{\tilde{I}_{h,1},\ \tilde{I}_{h,1},\ \cdots,\ \tilde{I}_{h,1}}^{v}\} \in \mathbb{R}^{n\times(h-1)v} \tag{8.35}$$

so that the time-invariant input subspace dimension is $q = (h-1)v$. Similarly, arrangement of two vertical elements corresponds to the time-invariant input subspace

$$\bar{X} = \tilde{I}_{v,h} \in \mathbb{R}^{n\times h(v-1)} \tag{8.36}$$

with the input subspace dimension reducing to $q = h(v-1)$. In the case of two by two adjacent elements the time-invariant input subspace is

$$\bar{X} = \begin{bmatrix} \tilde{I}_{h,1} & 0 & \cdots & \cdots & 0 \\ \tilde{I}_{h,1} & \tilde{I}_{h,1} & \cdots & \cdots & 0 \\ 0 & \tilde{I}_{h,1} & \ddots & \ddots & 0 \\ \vdots & \vdots & \ddots & \ddots & \vdots \\ 0 & 0 & \cdots & \ddots & \tilde{I}_{h,1} \\ 0 & 0 & \cdots & \cdots & \tilde{I}_{h,1} \end{bmatrix} \in \mathbb{R}^{n\times(h-1)(v-1)} \tag{8.37}$$

so that the dimension further reduces to $q = (h-1)(v-1)$.

8.4 Model Identification

Having established a suitable X, the problem of identifying linearized system $M|_{\boldsymbol{x}}X$ in Step 2 of Procedure 5 can be stated as follows:

$$M|_{z_k}X = \underset{\Lambda:\mathscr{L}_2^q[0,T]\to\mathscr{L}_2^p[0,T]}{\arg\min}\ J(\Lambda), \quad J(\Lambda) = \|\Delta\boldsymbol{\Phi} - \Lambda\Delta\boldsymbol{r}\|^2 \tag{8.38}$$

where $X : \mathscr{L}_2^q[0,T] \to \mathscr{L}_2^p[0,T]$ takes form (8.18) or (8.26). Here $\{\Delta\boldsymbol{r}, \Delta\boldsymbol{\Phi}\} \in \mathscr{L}_2^q[0,T] \times \mathscr{L}_2^p[0,T]$ are an experimental signal pair chosen to sufficiently excite the system dynamics about $\boldsymbol{r}_k$. Note that $\Delta\boldsymbol{r}$ and $\Delta\boldsymbol{\Phi}$ are taken relative to the operating point, hence $\boldsymbol{r} = \boldsymbol{r}_k + \Delta\boldsymbol{r}$, $\boldsymbol{\Phi} = \boldsymbol{\Phi}_k + \Delta\boldsymbol{\Phi}$ are the local experimental input and output signals. Many methods are available to solve (8.38), each of which benefit from the reduced input subspace $\mathscr{X}$ constructed in Sect. 8.3.3. The selected method must be fast, sufficiently exciting, and avoid injecting large or rapidly varying signals which may be uncomfortable for the patient.

Simplification is immediately possible by using tests in which only one channel of $\boldsymbol{r}$ is varied at a time. This requires q tests each, where in the ith test a signal $\boldsymbol{r}^i \in \mathscr{L}_2^q[0,T]$ is applied, whose ith input channel is $\boldsymbol{r}_i^i = \boldsymbol{r}_{k,i} + \Delta\boldsymbol{r}_i^i$, while the remaining input components are fixed at $\boldsymbol{r}_{k,j}$, $j \neq i$. To guarantee sufficient excitation of dynamics, a maximum range of stimulation, $z_{i,width}$, is specified for the ith test to affect a compromise between accuracy and proximity to the operating point, which is then translated to the signal $\boldsymbol{r}$ using $\boldsymbol{r}_{i,width} = \|\bar{X}_i\|_\infty^{-1} z_{i,width}$. The zero entries in $\Delta\boldsymbol{r}^i$ mean that (8.38) is replaced by the q lower order subproblems

$$(M|_{z_k}X)_i : \boldsymbol{r}_i \to \boldsymbol{\Phi} := \underset{\Lambda_i:\mathscr{L}_2[0,T]\to\mathscr{L}_2^p[0,T]}{\arg\min}\ J(\Lambda_i), \quad J(\Lambda_i^i) = \left\|\Delta\boldsymbol{\Phi}^i - \Lambda_i\Delta\boldsymbol{r}_i^i\right\|^2 \tag{8.39}$$

with $\Delta\boldsymbol{\Phi}^i \in \mathscr{L}_2^p[0,T]$ the output of test i relative to the operating point.

Further simplification occurs if $M|_{z_k}X$ has the form $H(s)FX$ assumed in Propositions 8.1 and 8.2, where F has structure (8.5) and $H(s)$ is a SISO transfer-function.

Procedure 8 (Simplified identification procedure)

Perform q tests, where in the ith test $\boldsymbol{r}^i$ is applied to stimulate channel i to give $\boldsymbol{\Phi}^i$. Collect data set $\{\Delta\boldsymbol{\Phi}^i, \Delta\boldsymbol{r}^i\}$, and perform the following computations:

(a) $H(s)$: For any i, j, fit SISO transfer-function to the pair $\{\Delta\boldsymbol{\Phi}_j^i, \Delta\boldsymbol{r}_i^i\}$.

(b) FX: Compute $\Delta\boldsymbol{\xi}_i^i = H(s)\Delta\boldsymbol{r}_i^i$ and substitute in (8.39) to give

$$(FX)_i := \underset{\Lambda_i:\mathscr{L}_2[0,T]\to\mathscr{L}_2^p[0,T]}{\arg\min}\ J(\Lambda_i), \quad J(\Lambda_i) = \left\|\Delta\boldsymbol{\Phi}^i - \Lambda_i\Delta\boldsymbol{\xi}_i^i\right\|^2$$
$$= \int_0^T \|\Delta\boldsymbol{\Phi}^i(t) - \Lambda_i(t)\Delta\boldsymbol{\xi}_i^i(t)\|^2 dt.$$

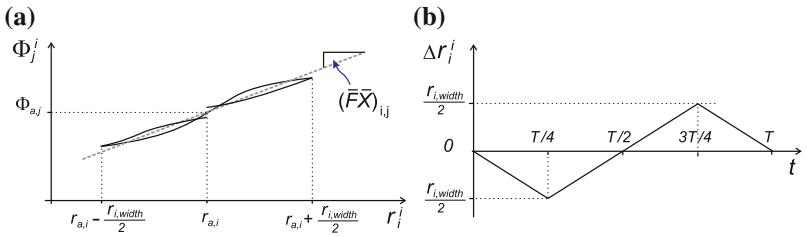

Fig. 8.5 Signals on ith test: **a** jth output against ith input $\boldsymbol{r}_i^i$ (where $\boldsymbol{r}_j^i, j \neq i$ are fixed), and **b** $\Delta\boldsymbol{r}_i^i$, where $\boldsymbol{r}_i^i = \boldsymbol{r}_{a,i} + \Delta\boldsymbol{r}_i^i$

For time-varying X, FX is defined by $\boldsymbol{y} = FX\boldsymbol{r}, \boldsymbol{y}(t) = (\bar{F}\bar{X})(t)\boldsymbol{r}(t)$, where the columns and individual elements of $(\bar{F}\bar{X})(t)$ are respectively

$$(\bar{F}\bar{X})_i(t) = (\boldsymbol{\xi}_i^i(t))^{-1}\Delta\boldsymbol{\Phi}^i(t), \quad (\bar{F}\bar{X})_{i,j}(t) = (\boldsymbol{\xi}_i^i(t))^{-1}\Delta\boldsymbol{\Phi}_j^i(t). \quad (8.40)$$

For time-invariant X, FX is defined by $\boldsymbol{y} = FX\boldsymbol{r}, \boldsymbol{y}(t) = \bar{F}\bar{X}\boldsymbol{r}(t)$, where the columns and individual elements of $\bar{F}\bar{X}$ are respectively

$$(\bar{F}\bar{X})_i = (\Xi_p^*\Xi_p)^{-1}\Xi_p^*\Delta\boldsymbol{\Phi}^i, \quad (\bar{F}\bar{X})_{i,j} = (\Xi_1^*\Xi_1)^{-1}\Xi_1^*\Delta\boldsymbol{\Phi}_j^i \quad (8.41)$$

where $\Xi_l : \mathbb{R}^l \to \mathscr{L}_2^l[0, T] : \boldsymbol{a} \mapsto \boldsymbol{b} : \boldsymbol{b} = \boldsymbol{\xi}_i^i(t)\boldsymbol{a}$.

Solution (8.41) corresponds to the 'line of best fit' when $\boldsymbol{\xi}_i^i$ is plotted against $\boldsymbol{\Phi}_j^i$. Hence the approach corresponds to approximating the response of the jth output to the single varying input, by a straight line, thus reducing the effect of noise in a transparent manner. This can be seen clearly when $\Delta\boldsymbol{r}_i^i$ is chosen to consist of straight line segments, as shown in Fig. 8.5 where for simplicity we set $H(s) = 1$. This provides a smooth input for the patient, while covering the necessary $\boldsymbol{r}_{i,width}$, ensuring sufficient dynamic excitation. For all choices of $\Delta\boldsymbol{r}_i^i$ the input applied to the physical system on the ith test is

$$\boldsymbol{z}_i^i(t) = \bar{X}_i\boldsymbol{r}_{a,i}(t) + \bar{X}_i\frac{\boldsymbol{r}_{i,width}}{2}\Delta\boldsymbol{r}_i^i(t) = \boldsymbol{z}_{a,i}(t) + \frac{\boldsymbol{z}_{i,width}}{2}\tilde{\bar{X}}_i\Delta\boldsymbol{r}^i(t) \quad (8.42)$$

and $\boldsymbol{z}_j^i = \boldsymbol{z}_{a,j}$ for $j \neq i$. Here $\tilde{\bar{X}}_i$ is the normalized vector $\bar{X}_i\|\bar{X}_i\|_\infty^{-1}$.

8.5 Case Study: Functional Hand and Wrist Motion

The subspace selection, identification and control design procedures are now tested in a clinically relevant setting. The electrode array is shown in Fig. 8.6b and comprises 4×6 elements printed on a polycarbonate substrate, using a hydrogel interface layer.

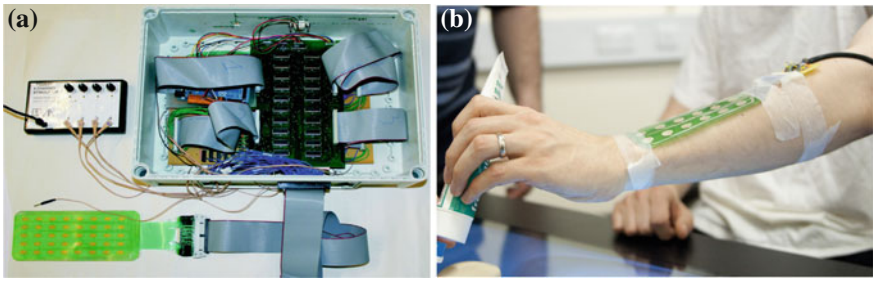

Fig. 8.6 **a** Electrode array (5 × 8 elements), multiplexor hardware and stimulator unit, and **b** electrode array (4 × 6 elements) positioned on participant's forearm while performing a task

It is manufactured by Tecnalia-Fatronik, San Sebastian, Spain, and is described in [4]. Each of the $n = 24$ array elements can be routed to one of four ES channels. Routing is achieved using custom made RS232 controlled multiplexor hardware, comprising an Arduino board and shift register array. As in the systems of Chaps. 5 and 7, the control system produces a 5 V 40 Hz square pulse train for each ES channel. These signals are then amplified by a modified commercial four channel stimulator (Odstock, UK). Two non-contact sensors (Kinect and PrimeSense) were used to measure wrist flexion/extensor, wrist abduction/adduction, and flexion of the metacarpophalangeal and proximal interphalangeal joints of each finger and the thumb, giving a total of $p = 12$ joint angles. The kinematic relationships, and details of the sensors and computations appear in Sect. 9.2.3.

To establish feasibility, tests were conducted on two unimpaired participants (denoted P1, P2) who were instructed to provide no voluntary effort. The array was positioned as shown in Fig. 8.6b, to cover wrist and finger extensor muscles including: extensor carpi radialis longus, extensor carpi radialis brevis, extensor digitorum, extensor pollicis longus, extensor pollicis brevis, extensor indius, and flexor digitorum profundus. At the beginning of each test session, the stimulator amplitudes were set by routing one channel to two adjacent elements of the array, outputting a 300 μs signal and slowly increasing the amplitude until a maximum comfortable level was reached. The amplitudes of the remaining channels were set to identical levels. The stimulation signal pulsewidth of each channel is the controlled variable and combines with the routing hardware to realise electrode array stimulation signal z, as shown in Fig. 8.1. Each test started from an initial wrist angle of approximately 20° flexion, 0° abduction, and finger joint angles of 35° flexion, 0° abduction.

8.5.1 Unrestricted Stimulation Space

Procedure 5 of Sect. 8.2 was first tested using an unrestricted subspace to establish baseline accuracy, setting $q = n$, $X = I$. In Step 2, Procedure 8 of Sect. 8.4

was employed to identify $M|_z X$. This involved sequentially applying the ramp input shown in Fig. 8.5 to each of the $n = 24$ array elements in turn, while the $p = 12$ angular outputs were recorded. The duration of each identification test was chosen as 5 s with a sampling time of $T_s = 0.01$ s. Proposition 8.1 was then used to design feedback controller K in Step 3. Here $\bar{K}(s)$ took the form of a PD controller with gains of $K_p = 1.6$, $K_d = 0.4$ so that $N_w(s)$ approximated a pure time delay of 0.7 s.

Three different reference postures were selected to verify the optimization procedure; "pointing" with the index finger, a "pinch" hand posture and an "open" hand posture. In order to clearly assess tracking accuracy, the reference was defined at all time points by selection of $P = I$. Each task incorporated specific finger movements as well as extension of the fingers and wrist, which comprise challenging movements for stroke patients to perform. This led to three reference signals, $\hat{\boldsymbol{\Phi}} \in \mathscr{L}_2^p[0, T]$, $T = 12$, with examples of the final gestures produced shown in Fig. 8.8. These postures each involve wrist angle extension of approximately 60° relative to the initial starting position, and extension of the two joint angles of each finger by 25° for one or more fingers. In addition, the open posture involved abduction of each finger by approximately 15°. Within Step 4 of Procedure 5, the ILC update of Proposition 8.2 was used, with $l = 0.4$, $\lambda = 0.7$.

Remark 8.2 Controller output z is the stimulation pulsewidth of the n elements of the array, which may all take different values. The current hardware cannot achieve this with only four independent channels, and hence constraints described in [12] were added to the controller to attain the closest approximation possible. When using a restricted subspace in the next section, these constraints can be translated to only appear in the calculation of subspace operator X. For example, specifying $q = 2$ and allowing each element of $\bar{X}(t)$ to be either 0 or one of two non-zero values means that each element of $z(t)$ can only ever be 0 or one of three non-zero values.

Tracking results are shown in Fig. 8.7a for the pointing task, and show the improvement produced by ILC compared with feedback action alone (i.e. when $k = 1$). To quantify the accuracy of successive input updates, percentage error was calculated across all joints for each posture using $100 \times \|\boldsymbol{e}_k\| \,/\, \|\boldsymbol{e}_0\|$, where $\boldsymbol{e}_0 = \hat{\boldsymbol{\Phi}} - \boldsymbol{\Phi}_0$, with $\boldsymbol{\Phi}_0$ the initial posture prior to stimulation. Results are shown in Table 8.1 for the first 3 iterations of each task, averaged across P1 and P2. Each execution of ILC reduces the error to approximately 40 %, yielding results with a mean joint angle error of typically less than 5°. Figure 8.8 shows the stimulation sites corresponding to z_3 across each task for P1. Tests were also performed using alternative initial hand positions, and gave rise to very similar final output positions in each case (although reduction in the normalized error occurred when the initial hand position was close to that of the reference posture). Results for the case of ILC applied with no feedback controller appear in [12]. The use of an iterative model-based update leads to significantly reduced error compared with the most accurate existing approaches in the literature, but incurs an identification test duration of 120 s per iteration.

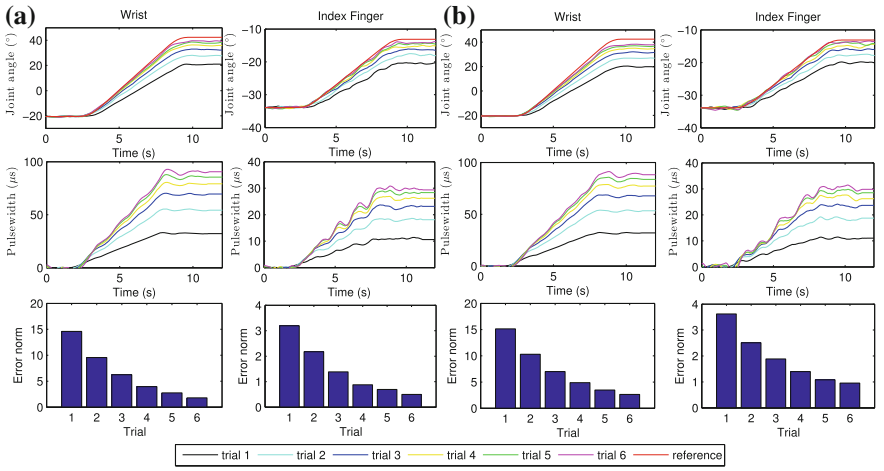

Fig. 8.7 P1 tracking results for pointing gesture, with **a** unrestricted and **b** restricted subspaces

Table 8.1 Unrestricted subspace: percentage error across all joints for $k = 1, 2, 3$

		Pointing	Pinching	Open
$100 \times \frac{\|\boldsymbol{e}_1\|}{\|\boldsymbol{e}_0\|}$	P1	26.1898	21.6141	14.7336
	P2	20.7930	29.1885	17.7463
$100 \times \frac{\|\boldsymbol{e}_2\|}{\|\boldsymbol{e}_0\|}$	P1	11.2145	10.4494	14.6097
	P2	13.0393	15.0268	12.4822
$100 \times \frac{\|\boldsymbol{e}_3\|}{\|\boldsymbol{e}_0\|}$	P1	3.7661	4.2790	4.3712
	P2	1.5297	4.0167	3.5955

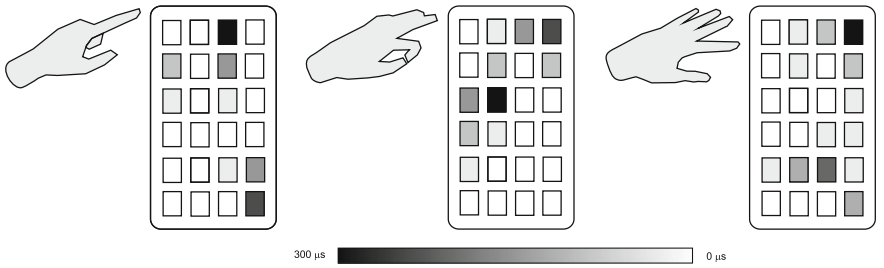

Fig. 8.8 Stimulation patterns for pointing, pinching and open hand gestures (z_3, $t = T$)

Table 8.2 Task and participant-specific restricted subspace, $q = 4$: percentage error across all joints for $k = 1, 2, 3$

		Pointing	Pinching	Open
$100 \times \frac{\|e_1\|}{\|e_0\|}$	P1	33.9884	27.9243	27.2419
	P2	38.1187	31.3543	23.9668
$100 \times \frac{\|e_2\|}{\|e_0\|}$	P1	14.4129	16.9458	19.1558
	P2	13.2719	15.0851	17.0341
$100 \times \frac{\|e_3\|}{\|e_0\|}$	P1	5.6186	4.5904	5.0830
	P2	3.8271	4.5765	6.0992

Table 8.3 Participant-specific restricted subspace $q = 6$: percentage error across all joints for $k = 1, 2, 3$

		Pointing	Pinching	Open
$100 \times \frac{\|e_1\|}{\|e_0\|}$	P1	35.8611	27.6188	28.0452
	P2	43.6825	36.8248	29.951
$100 \times \frac{\|e_2\|}{\|e_0\|}$	P1	23.5090	22.6162	22.1861
	P2	24.7642	23.7063	21.4247
$100 \times \frac{\|e_3\|}{\|e_0\|}$	P1	7.4743	6.3322	5.6863
	P2	5.2641	6.1649	6.2601

8.5.2 Stimulation Subspace

A restricted stimulation subspace is now employed in Step 1 of Procedure 5 to speed up the test procedure. For simplicity the subspace was constructed using Step (a) of Procedure 7. In particular, data sets z^1, z^2, z^3, and z^4 corresponded to each of the tests undertaken using the unrestricted subspace in Sect. 8.5.1. These were directly inserted as columns in $\bar{X}$ using (8.14), leading to $c = 4$. Each participant took a rest period of 30 min following the previous tests. Tracking results are shown in Fig. 8.7b for the pointing task, with error norm values given in Table 8.2. These show only a small reduction in accuracy, while the identification test time is reduced to 20 seconds per iteration. Similar convergence rates are observed to the previous tests since X has been chosen such that the reference belongs to $\text{im}(MX)$.

The previous results require a separate subspace for each task. To generate a single subspace for all three tasks, Step (f) in Procedure 7 was applied, using Proposition 8.3 to compute a single input space of dimension $q = 6$. In particular, Computational Procedure 6 was performed using Matlab function `nnmf`. Results are shown in Table 8.3. With only a small drop in accuracy this subspace covers a wide range of functional tasks, and corresponds to an identification test time of 30 s.

These results indicate that an identification time of approximately 2 min (comprising three identification routines, each followed by an ILC iteration to compute the new z_k) is sufficient to produce an input subspace that covers the required range of hand and wrist movements.

8.6 Conclusions

This chapter has applied the model structure of Chap. 2 and design framework of Chap. 6 to electrode array based stimulation. In particular, we have exploited a restricted stimulation subspace to yield model identification procedures suitable for clinical practice. We next embed the control structure in a rehabilitation system to evaluate its performance in assisting stroke patients to perform functional tasks.

References

1. L. Popović-Maneski, M. Kostic, G. Bijelic, T. Keller, S. Mitrovic, L. Konstantinovic, D.B. Popović, Multi-pad electrode for effective grasping: design. IEEE Trans. Neural Syst. Rehabil. Eng. **21**(4), 648–654 (2013)
2. S. Micera, T. Keller, M. Lawerence, M. Morari, D.B. Popović, Wearable neural prosthesis: restoration od sensory-motor function by transcutaneous electrical stimulation. IEEE Eng. Med. Biol. Mag. **29**, 64–69 (2010)
3. B.W. Heller, A.J. Clarke, T.R. Good, T.J. Healey, S. Nair, E.J. Pratt, Automated setup of functional electrical stimulation for drop foot using a novel 64 channel prototype stimulator and electrode array: results from a gait-lab based study. Med. Eng. Phys. **35**(1), 74–81 (2013)
4. N.M. Malešević, L.Z.P. Maneski, V. Ilić, N. Jorgovanović, G. Bijelić, T. Keller, D.B. Popović, A multi-pad electrode based functional electrical stimulation system for restoration of grasp. J. Neuroeng. Rehabil. **9**, 66 (2012)
5. S.B. O'Dwyer, D.T. O'Keeffe, S. Coote, G.M. Lyons, An electrode configuration technique using an electrode matrix arrangement for FES-based upper arm rehabilitation systems. Med. Eng. Phys. **28**, 166–176 (2006)
6. W. Tsang, K. Singh, E. Fiume, Helping hand: an anatomically accurate inverse dynamics solution for unconstrained hand motion, in *Proceedings of the 2005 ACM SIGGRAPH/Eurographics Symposium on Computer Animation* (2005), pp. 319–328
7. C.T. Freeman, D. Tong, K. Meadmore, Z. Cai, E. Rogers, A.M. Hughes, J.H. Burridge, Phase-lead iterative learning control algorithms for functional electrical stimulation based stroke rehabilitation. Proc. Inst. Mech. Eng. Part I: J. Syst. Control Eng. **225**(6), 850–859 (2011)
8. C.T. Freeman, P.L. Lewin, E. Rogers, Further results on the experimental evaluation of iterative learning control algorithms for non-minimum-phase plants. Int. J. Control **80**(4), 569–582 (2007)
9. Z. Cai, C.T. Freeman, P.L. Lewin, E. Rogers, Iterative learning control for a non-minimum phase plant based on a reference shift algorithm. Control Eng. Pract. **16**(6), 633–643 (2008)
10. D. Guillameta, J. Vitria, B. Schiele, Introducing a weighted non-negative matrix factorization for image classification. Pattern Recognit. Lett. **24**(14), 2447–2454 (2003)
11. A. d'Avella, P. Saltiel, E. Bizzi, Combinations of muscle synergies in the construction of a natural motor behavior. Neuroscience **6**(3), 300–308 (2003)
12. C.T. Freeman, Electrode array-based electrical stimulation using ILC with restricted input subspace. Control Eng. Pract. **23**(2), 32–43 (2014)

Chapter 9
Clinical Application: Fully Functional Stroke Rehabilitation

In this chapter electrode arrays are combined with single-pad electrodes to produce a rehabilitation system that supports functional task practice. Performance and usability of the system is then assessed with stroke participants in a clinical trial. The control system employs the electrode array control scheme developed in the last chapter within the general control framework developed in Chap. 6. This thereby demonstrates how arrays and single-pad electrodes can be transparently combined within the same control scheme.

The stroke rehabilitation system is the first to use model-based ES array controllers to support goal-oriented upper-limb task training. The system also embeds innovations in the stimulation hardware, sensing equipment and task display compared with the system described in Chap. 7. The major additions include:

1. A 24 element electrode array placed over the wrist and finger extensors to activate muscles such as extensor carpi radialis longus, extensor carpi radialis brevis, extensor digitorum, extensor pollicis longus, extensor pollicis brevis, extensor indicis, and flexor digitorum profundus.
2. A PrimeSense Carmine 1.09 (Apple Inc., California) depth camera that uses an RGB camera and infrared sensor to measure hand and wrist joint angles, reducing set-up time and removing constraints associated with contact-based sensors (e.g. the electro-goniometer used in Chap. 7).
3. A capacitive touch table (DISPLAX Inc., Portugal) that adds additional interactivity and motivation to the task display.

These new developments are intended to promote further reduction in upper limb motor impairments. The controllers can more precisely assist the functional task set of Chap. 7 to more fully support functional improvement [1]. The touch table promotes adherence through stimulating and motivating rehabilitation, as required in long term self-management. In combination with inexpensive non-contact depth sensors, this represents a significant step towards translation into the home environment. Note that more detailed results and in-depth analysis of the clinical feasibility study reported in this section appears in [2].

C. Freeman, *Control System Design for Electrical Stimulation in Upper Limb Rehabilitation*, DOI 10.1007/978-3-319-25706-8_9

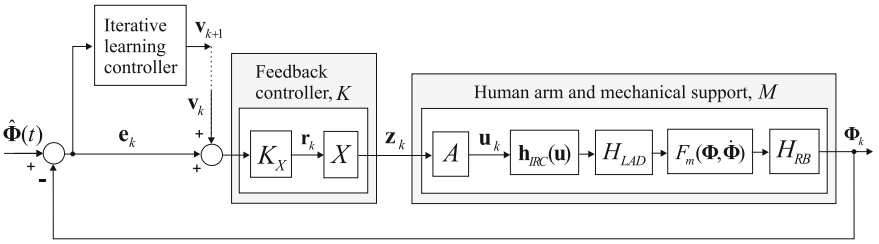

Fig. 9.1 Feedback and ILC control scheme for arbitrary electrode structures

9.1 General Integrated Control Framework

Before describing the system, analysis is presented which enables the array controllers developed in Chap. 8 to be transparently employed within the general design frameworks of Chaps. 4 and 6. To do this we generalize the control schematic shown in Fig. 9.1 to enable inclusion of arbitrary numbers of both single-pad and array electrode types. This results in the following control design procedure:

Procedure 9 (Embedding arrays within general robustness framework) Suppose N groups of single-pad electrodes or electrode arrays are used. Let the ith group contain n_i electrode elements, stimulating m_i muscles and have a specified subspace of dimension q_i. Then the system can be represented by Fig. 9.1 where operator A is defined by

$$A : \mathscr{L}_2^n[0,T] \to \mathscr{L}_2^m[0,T] : \boldsymbol{z} \mapsto \boldsymbol{u},\ \boldsymbol{u}_j = A_j \boldsymbol{z}_j,\ j = 1 \ldots N \tag{9.1}$$

where $m = \sum_{i=1}^N m_i$, $n = \sum_{i=1}^N n_i$, and operator $A_j : \mathscr{L}_2^{n_j}[0,T] \to \mathscr{L}_2^{m_j}[0,T]$ is given by (8.2), where for a group of single-pad electrodes, $n_j = m_j$ with $a_{i,l} = 1$ for $i = l$ and $a_{i,l} = 0$ otherwise. Similarly, operator X is defined as

$$X : \mathscr{L}_2^q[0,T] \to \mathscr{L}_2^n[0,T] : \boldsymbol{r} \mapsto \boldsymbol{z},\ \boldsymbol{z}_j = X_j \boldsymbol{r}_j,\ j = 1 \ldots N \tag{9.2}$$

where $q = \sum_{i=1}^N q_i$ and operator $X_j : \mathscr{L}_2^{q_i}[0,T] \to \mathscr{L}_2^{n_i}[0,T]$ has form (6.6) where for a group of single-pad electrodes, $q_j = n_j$, $\bar{X}_j = I$.

The signals associated with the jth group are $\boldsymbol{u}_{\mathscr{M}_j}, \boldsymbol{r}_{\mathscr{Q}_j}, \boldsymbol{z}_{\mathscr{N}_j}$ where

$$\mathscr{M}_j = \left\{1 + \sum_{i=1}^{j-1} m_i, \ldots, \sum_{i=1}^{j} m_i\right\}, \mathscr{N}_j = \left\{1 + \sum_{i=1}^{j-1} n_i, \ldots, \sum_{i=1}^{j} n_i\right\},$$
$$\mathscr{Q}_j = \left\{1 + \sum_{i=1}^{j-1} q_i, \ldots, \sum_{i=1}^{j} q_i\right\}.$$

If controllers K_X and L are chosen such that $b_{\bar{M}//\bar{C}}$ given by Theorem 6.4 (with $K = XK_X$) is finite, then from Theorem 4.5 robust stability of the system shown in Fig. 9.1 is guaranteed provided the modeling mismatch satisfies

$$\sup_{k \in \mathbb{N}_+} \left\| N|_{\bar{z}_1(k)} - M|_{\bar{z}(k)} \right\| < b_{\bar{M}//\bar{C}}^{-1} \tag{9.3}$$

where $M, N : z \mapsto \boldsymbol{\Phi}$ are the nominal and true generalized plant maps.

Design Procedure 9 shows that arrays can be incorporated in the control scheme simply by specifying consistent A and X structures. However, for each array, the component of model M linking array inputs and corresponding actuated joints must be identified experimentally on each iteration as described in Chap. 8. This can be achieved using the subspace identification approach of Sect. 8.3, but this approach should be extended to include all ES inputs, not just those of the array. Furthermore, because all joint angles may be affected by array stimulation, this procedure should in principle replace any use of an underlying model when using an electrode array.

In many cases each ES array assists joint angles that are not significantly affected by other stimulated muscles around an operating point (e.g. in the case of an array stimulating finger muscles). In this case a more pragmatic approach is to apply array identification Procedure 8 of Sect. 8.4 to the subset of joints known to be affected by array stimulation, and include only the array ES inputs. This hence preserves the simplicity and speed of the identification approach. It is then desirable to use a global model to capture the response of the remaining joints to single-pad stimulation, however this will be inaccurate if it omits the dynamics produced by the array (e.g. wrist and hand movement). A solution is to extend the global model to include the most significant source of interaction caused by the array in the form of a simplified lumped parameter representation with identifiable parameters (e.g. extend the arm model to include a lumped wrist representation).

The assumption of a subset of joints being locally dependent only on array ES inputs therefore leads to significant simplification. The next procedure specifies explicit robustness margins for this case to enable the designer to gauge applicability.

Theorem 9.1 (Robustness using partially decoupled design) *Assume a partially decoupled model in which the ith array block has dynamics $\boldsymbol{\Phi}_{\mathscr{P}_i} = M_i \boldsymbol{z}_{\mathscr{N}_i}$ (where with no loss of generality we assume $i = 1$), but the remaining joints use full model structure $\boldsymbol{\Phi}_{\bar{\mathscr{P}}_i} = M_{\dagger} \boldsymbol{z}$. Then applying the linearized design procedure of Chap. 4 or 6 with feedback and ILC structures*

$$K = \begin{bmatrix} K_i & 0 \\ K_{\dagger,i} & K_{\dagger} \end{bmatrix}, \quad L = \begin{bmatrix} L_i & 0 \\ L_{\dagger,i} & L_{\dagger} \end{bmatrix} \quad \text{such that} \quad \begin{cases} \|I - G_i L_i\| \le \gamma_i < 1 \\ \|I - G_{\dagger} L_{\dagger}\| \le \gamma_{\dagger} < 1 \end{cases}, \tag{9.4}$$

where $G_i = (I + M_i K_i)^{-1} M_i K_i$, $G_{\dagger} = (I + M_{\dagger} K_{\dagger})^{-1} M_{\dagger} K_{\dagger}$, robustly stabilizes the resulting closed-loop system if the true plant N satisfies

$$\sup_{k \in \mathbb{N}_+} \left\| N|_{\bar{z}_1(k)} - \begin{bmatrix} M_i|_{z(k)} & 0 \\ M_{\dagger,i}|_{z(k)} & M_{\dagger}|_{z(k)} \end{bmatrix} \right\| < \left\| \begin{bmatrix} \beta_{\bar{M}_i // \bar{C}_i} & 0 \\ \beta_{\bar{M}_{\dagger,i} // \bar{C}_{\dagger,i}} & \beta_{\bar{M}_{\dagger} // \bar{C}_{\dagger}} \end{bmatrix} \right\|^{-1} \tag{9.5}$$

where $M_{\dagger,i}|_z$, $M_{\dagger}|_z$ denote $M_{\dagger}$ linearised with respect to $\boldsymbol{z}_{\mathscr{N}_i}$, $\boldsymbol{z}_{\bar{\mathscr{N}}_i}$ respectively, $b_{\bar{M}_i // \bar{C}_i}$, $b_{\bar{M}_{\dagger} // \bar{C}_{\dagger}}$ are gain bounds on $[\bar{M}_i, \bar{C}_i]$, $[\bar{M}_{\dagger}, \bar{C}_{\dagger}]$ alone (computed using Theorem 4.6 with $\{M, K, L\} = \{M_i, K_i, L_i\}$, $\{M_{\dagger}, K_{\dagger}, L_{\dagger}\}$ respectively), and

$$\begin{aligned} & b_{M_{\dagger,i} // C_{\dagger,i}} \\ &= \left\| \begin{pmatrix} -I_{\dagger} K_{\dagger} & I_{\dagger} \\ \bar{I}_{\dagger} & M_{\dagger}|_z I_{\dagger} \end{pmatrix} \right\| \left\| \begin{pmatrix} -\bar{I}_i M_i|_z & \bar{I}_i \\ -I_i & -K_i \bar{I}_i \end{pmatrix} \right\| \left\{ \left\| \begin{pmatrix} M_{\dagger,i}|_z & 0 \\ 0 & K_{\dagger,i} \end{pmatrix} \right\| \left(1 + \frac{\left\| \begin{pmatrix} K_i \bar{I}_i \\ \bar{I}_i \end{pmatrix} L_i \right\|}{1 - \gamma_i} \right. \right. \\ & \left. \left. + \frac{\|K_{\dagger} L_{\dagger}\| \|(\bar{I}_{\dagger}, -\bar{I}_{\dagger} M_{\dagger}|_z)\|}{1 - \gamma_{\dagger}} \right) + \frac{\|K_{\dagger} L_{\dagger,i}\|}{1 - \gamma_i} + \frac{\|K_{\dagger} L_{\dagger}\| \|G_{\dagger,i} L_i + G_{\dagger} L_{\dagger,i}\|}{(1 - \gamma_i)(1 - \gamma_{\dagger})} \right\} \end{aligned} \tag{9.6}$$

where $G_{\dagger,i} = \bar{I}_{\dagger}(M_{\dagger,i}|_z K_i + M_{\dagger}|_z K_{\dagger,i})(I + M_{\dagger,i}|_z K_{\dagger,i})^{-1}$, $I_i = (I + K_i M_i|_z)^{-1}$, $\bar{I}_i = (I + M_i|_z K_i)^{-1}$, $I_{\dagger} = (I + K_{\dagger} M_{\dagger}|_z)^{-1}$ and $\bar{I}_{\dagger} = (I + M_{\dagger}|_z K_{\dagger})^{-1}$.

Moreover, design of K_i and L_i using Propositions 8.1 and 8.2 preserves the nominal properties of the electrode array dynamics $\boldsymbol{\Phi}_{\mathscr{P}_i} = M_i \boldsymbol{z}_{\mathscr{N}_i}$, $\boldsymbol{z}_{\mathscr{N}_i} = X_i \boldsymbol{r}_{\mathscr{Q}_i}$, $\boldsymbol{r}_{\mathscr{Q}_i} = K_i(\boldsymbol{v}_{\mathscr{P}_i} + \boldsymbol{e}_{\mathscr{P}_i})$ established in these propositions.

Proof Denote $M_1 = M_i|_z$, $M_2 = M_{\dagger,i}|_z$, $M_3 = M_{\dagger}|_z$, $K_1 = K_i$, $K_2 = K_{\dagger,i}$, $K_3 = K_{\dagger}$, $L_1 = L_i$, $L_2 = L_{\dagger,i}$, $L_3 = L_{\dagger}$, $I_j = (I + K_j M_j)^{-1}$, $\bar{I}_j = (I + M_j K_j)^{-1}$, $j = 1, 2, 3$. Then $M_j I_j K_j = I - \bar{I}_j = M_j K_j \bar{I}_j$, $K_j \bar{I}_j M_j = I - I_j = K_j M_j I_j$, and $M|_z = M$, where

$$M = \begin{bmatrix} M_1 & 0 \\ M_2 & M_3 \end{bmatrix}, \quad \text{so that} \quad KM = \underbrace{\begin{bmatrix} K_1 & 0 \\ K_2 & K_3 \end{bmatrix}}_{K} \begin{bmatrix} M_1 & 0 \\ M_2 & M_3 \end{bmatrix} = \begin{bmatrix} K_1 M_1 & 0 \\ K_2 M_1 + K_3 M_2 & K_3 M_3 \end{bmatrix}$$

and

$$(I + KM)^{-1} = \begin{bmatrix} (I + K_1 M_1)^{-1} & 0 \\ -(I + K_3 M_3)^{-1}(K_2 M_1 + K_3 M_2)(I + K_1 M_1)^{-1} & (I + K_3 M_3)^{-1} \end{bmatrix}$$

so from (4.60) the projection operator for the feedback case ($L = 0$) is

$$\Pi_{\bar{M}//\bar{K}} = \begin{pmatrix} I \\ M \end{pmatrix} (I + KM)^{-1}(I, K) = \begin{pmatrix} I_1 & 0 \\ -I_3(K_2 M_1 + K_3 M_2) I_1 & I_3 \\ M_1 I_1 & 0 \\ M_2 I_1 - M_3 I_3 (K_2 M_1 + K_3 M_2) I_1 & M_3 I_3 \end{pmatrix}$$
$$\begin{pmatrix} I_1 K_1 & 0 \\ I_3 K_2 - I_3(K_2 M_1 + K_3 M_2) I_1 K_1 & I_3 K_3 \\ M_1 I_1 K_1 & 0 \\ \big(M_2 - M_3 I_3 (K_2 M_1 + K_3 M_2)\big) I_1 K_1 + M_3 I_3 K_2 & M_3 I_3 K_3 \end{pmatrix}.$$

By reordering inputs and outputs, this can be partitioned by

$$\begin{bmatrix} \Pi_{\bar{M}_1//\bar{K}_1} & 0 \\ \Pi_{\bar{M}_2//\bar{K}_2} \Pi_{\bar{M}_3//\bar{K}_3} \end{bmatrix} \quad \text{where} \quad \Pi_{\bar{M}_1//\bar{K}_1} = \begin{pmatrix} I \\ M_1 \end{pmatrix} I_1(I, K_1),$$
$$\Pi_{\bar{M}_3//\bar{K}_3} = \begin{pmatrix} I \\ M_3 \end{pmatrix} I_3(I, K_3) \tag{9.7}$$

are the projection operators for $[\bar{M}_1, \bar{K}_1]$, $[\bar{M}_3, \bar{K}_3]$ alone, and

$$\Pi_{\bar{M}_2//\bar{K}_2} = \begin{bmatrix} -I_3(K_2 M_1 + K_3 M_2) I_1 & I_3(K_2 \bar{I}_1 - K_3 M_2 I_1 K_1) \\ (\bar{I}_3 M_2 - M_3 I_3 K_2 M_1) I_1 & \bar{I}_3 M_2 I_1 K_1 + M_3 I_3 K_2 \bar{I}_1 \end{bmatrix}$$
$$= \begin{pmatrix} -I_3 K_3 & I_3 \\ \bar{I}_3 & M_3 I_3 \end{pmatrix} \begin{pmatrix} M_2 & 0 \\ 0 & K_2 \end{pmatrix} \begin{pmatrix} I_1 & I_1 K_1 \\ -M_1 I_1 & \bar{I}_1 \end{pmatrix}. \tag{9.8}$$

Next consider the inclusion of ILC, with associated component of (4.50) given by:

$$\Pi_{\bar{M}//\bar{L}} \boldsymbol{w}(k+1) = \begin{pmatrix} I \\ M \end{pmatrix} K(I + MK)^{-1} L \sum_{i=0}^{k} (I - GL)^i (I + MK)^{-1}(-M, I) \boldsymbol{w}(k - i). \tag{9.9}$$

Using the identity $G = (I + MK)^{-1}MK = \begin{pmatrix} G_1 & 0 \\ G_2 & G_3 \end{pmatrix}$ where $G_1 = \bar{I}_1 M_1 K_1$, $G_3 = \bar{I}_3 M_3 K_3$, $G_2 = \bar{I}_3(M_2 K_1 + M_3 K_2)\bar{I}_1$, we can denote

$$\underbrace{\begin{pmatrix} \bar{L}_1 & 0 \\ \bar{L}_2 & \bar{L}_3 \end{pmatrix}}_{\bar{L}} := L \sum_{i=0}^{k} (I - GL)^i = \begin{pmatrix} L_1 & 0 \\ L_2 & L_3 \end{pmatrix} \sum_{i=0}^{k} \left(I - \begin{pmatrix} G_1 & 0 \\ G_2 & G_3 \end{pmatrix} \begin{pmatrix} L_1 & 0 \\ L_2 & L_3 \end{pmatrix} \right)^i$$

$$= \begin{pmatrix} L_1 & 0 \\ L_2 & L_3 \end{pmatrix} \sum_{i=0}^{k} \begin{pmatrix} I - G_1 L_1 & 0 \\ -(G_2 L_1 + G_3 L_2) & I - G_3 L_3 \end{pmatrix}^i$$

which equals

$$\begin{pmatrix} L_1 & 0 \\ L_2 & L_3 \end{pmatrix} \begin{pmatrix} \sum_{i=0}^{k} (I - G_1 L_1)^i & 0 \\ -\sum_{i=0}^{k} \sum_{j=0}^{i-1} (I - G_3 L_3)^{i-1-j} (G_2 L_1 + G_3 L_2)(I - G_1 L_1)^j & \sum_{i=0}^{k} (I - G_3 L_3)^i \end{pmatrix}.$$

Using this, (9.9) can then be written as

$$\begin{pmatrix} K_1 \bar{I}_1 & 0 \\ -K_3 \bar{I}_3 M_2 K_1 \bar{I}_1 + I_3 K_2 \bar{I}_1 & K_3 \bar{I}_3 \\ M_1 K_1 \bar{I}_1 & 0 \\ \bar{I}_3 M_2 K_1 \bar{I}_1 + M_3 I_3 K_2 \bar{I}_1 & M_3 K_3 \bar{I}_3 \end{pmatrix} \begin{pmatrix} \bar{L}_1 & 0 \\ \bar{L}_2 & \bar{L}_3 \end{pmatrix} \begin{pmatrix} -(\bar{I}_1 M_1)^\top & (\bar{I}_3 M_3 K_2 \bar{I}_1 M_1 - \bar{I}_3 M_2 I_1)^\top \\ 0 & -(\bar{I}_3 M_3)^\top \\ \bar{I}_1^\top & -(\bar{I}_3 (M_2 K_1 + M_3 K_2)\bar{I}_1)^\top \\ 0 & \bar{I}_3^\top \end{pmatrix}^\top.$$

By sequentially setting paired $\bar{L}$ components to zero, this can be expressed as

$$\begin{aligned} &\begin{pmatrix} 0 \\ I \\ 0 \\ M_3 \end{pmatrix} K_3 \bar{I}_3 \bar{L}_2 \bar{I}_1 \begin{pmatrix} -M_1 & 0 & I & 0 \end{pmatrix} + \begin{pmatrix} K_1 \\ I_3(K_2 - K_3 M_2 K_1) \\ M_1 K_1 \\ \bar{I}_3(M_2 K_1 + M_3 K_2) \end{pmatrix} \bar{I}_1 \bar{L}_1 \bar{I}_1 \begin{pmatrix} -M_1 & 0 & I & 0 \end{pmatrix} \\ &+ \begin{pmatrix} 0 \\ I \\ 0 \\ M_3 \end{pmatrix} K_3 \bar{I}_3 \bar{L}_3 \bar{I}_3 \begin{pmatrix} (M_3 K_2 M_1 - M_2) I_1 & -M_3 & (M_2 K_1 + M_3 K_2)\bar{I}_1 & I \end{pmatrix} \end{aligned} \tag{9.10}$$

Applying the same partitioning as in (9.12), (9.10) equals

$$\begin{pmatrix} 0 & 0 \\ \begin{pmatrix} K_3\bar{I}_3 \\ M_3K_3\bar{I}_3 \end{pmatrix}\bar{L}_2(-\bar{I}_1M_1, \bar{I}_1)\ 0 \end{pmatrix} + \begin{pmatrix} \begin{pmatrix} K_1\bar{I}_1 \\ M_1K_1\bar{I}_1 \end{pmatrix}\bar{L}_1(-\bar{I}_1M_1, \bar{I}_1) & 0 \\ \begin{pmatrix} -K_3\bar{I}_3 & I_3 \\ \bar{I}_3 & M_3I_3 \end{pmatrix}\begin{pmatrix} M_2 & 0 \\ 0 & K_2 \end{pmatrix}\begin{pmatrix} K_1\bar{I}_1 \\ \bar{I}_1 \end{pmatrix}\bar{L}_1(-\bar{I}_1M_1, \bar{I}_1)\ 0 \end{pmatrix}$$

$$+ \begin{pmatrix} 0 & 0 \\ \begin{pmatrix} K_3\bar{I}_3 \\ M_3K_3\bar{I}_3 \end{pmatrix}\bar{L}_3(\bar{I}_3, -\bar{I}_3M_3)\begin{pmatrix} M_2 & 0 \\ 0 & K_2 \end{pmatrix}\begin{pmatrix} -I_1 & -K_1\bar{I}_1 \\ -\bar{I}_1M_1 & \bar{I}_1 \end{pmatrix}\begin{pmatrix} I \\ M_3 \end{pmatrix}K_3\bar{I}_3\bar{L}_3\bar{I}_3(-M_3, I) & 0 \end{pmatrix}.$$

Recall that $\bar{L}_1 = \sum_{i=0}^{k}(I - G_1L_1)^i$, $\bar{L}_3 = \sum_{i=0}^{k}(I - G_3L_3)^i$,

$$\bar{L}_2 = L_2\sum_{i=0}^{k}(I - G_1L_1)^i - L_3\sum_{i=0}^{k}\sum_{j=0}^{i-1}(I - G_3L_3)^{i-1-j}(G_2L_1 + G_3L_2)(I - G_1L_1)^j. \tag{9.11}$$

Comparison with (9.9), and using (9.7), means that we can write

$$\Pi_{\bar{M}//\bar{C}}\boldsymbol{w}(k+1) = \underbrace{\begin{bmatrix} \Pi_{\bar{M}_1//\bar{K}_1} & 0 \\ \Pi_{\bar{M}_2//\bar{K}_2} & \Pi_{\bar{M}_3//\bar{K}_3} \end{bmatrix}}_{\Pi_{\bar{M}//\bar{K}}}\boldsymbol{w}(k+1) + \underbrace{\begin{bmatrix} \Pi_{\bar{M}_1//\bar{L}_1} & 0 \\ \Pi_{\bar{M}_2//\bar{L}_2} & \Pi_{\bar{M}_3//\bar{L}_3} \end{bmatrix}}_{\Pi_{\bar{M}//\bar{L}}}\boldsymbol{w}(k-i) \tag{9.12}$$

where $\Pi_{\bar{M}_1//\bar{L}_1}\boldsymbol{w}(k+1) = \begin{pmatrix} I \\ M_1 \end{pmatrix}K_1\bar{I}_1\bar{L}_1\bar{I}_1(-M_1, I)\boldsymbol{w}(k-i)$, $\Pi_{\bar{M}_3//\bar{L}_3}\boldsymbol{w}(k+1) = \begin{pmatrix} I \\ M_3 \end{pmatrix}K_3\bar{I}_3\bar{L}_3\bar{I}_3(-M_3, I)\boldsymbol{w}(k-i)$ are the projection operators for $[\bar{M}_1, \bar{C}_1]$, $[\bar{M}_3, \bar{C}_3]$ alone, and

$$\begin{aligned}
&\Pi_{\bar{M}_2//\bar{L}_2}\boldsymbol{w}(k-i) \\
&= \left\{\begin{pmatrix} K_3\bar{I}_3 \\ M_3K_3\bar{I}_3 \end{pmatrix}\bar{L}_2(-\bar{I}_1M_1, \bar{I}_1) + \begin{pmatrix} -K_3\bar{I}_3 & I_3 \\ \bar{I}_3 & M_3I_3 \end{pmatrix}\begin{pmatrix} M_2 & 0 \\ 0 & K_2 \end{pmatrix}\begin{pmatrix} K_1\bar{I}_1 \\ \bar{I}_1 \end{pmatrix}\bar{L}_1(-\bar{I}_1M_1, \bar{I}_1)\right. \\
&\qquad \left. + \begin{pmatrix} K_3\bar{I}_3 \\ M_3K_3\bar{I}_3 \end{pmatrix}\bar{L}_3(\bar{I}_3, -\bar{I}_3M_3)\begin{pmatrix} M_2 & 0 \\ 0 & K_2 \end{pmatrix}\begin{pmatrix} -I_1 & -K_1\bar{I}_1 \\ -\bar{I}_1M_1 & \bar{I}_1 \end{pmatrix}\right\}\boldsymbol{w}(k-i) \\
&= \begin{pmatrix} -I_3K_3 & I_3 \\ \bar{I}_3 & M_3I_3 \end{pmatrix}\left\{\begin{pmatrix} 0 & 0 \\ 0 & K_3 \end{pmatrix}\bar{L}_2 + \begin{pmatrix} M_2 & 0 \\ 0 & K_2 \end{pmatrix}\begin{pmatrix} K_1\bar{I}_1\ 0 \\ \bar{I}_1\ 0 \end{pmatrix}\bar{L}_1\right. \\
&\qquad \left. + \begin{pmatrix} 0 & 0 \\ 0 & K_3 \end{pmatrix}\bar{L}_3\begin{pmatrix} 0 & 0 \\ \bar{I}_3 & -\bar{I}_3M_3 \end{pmatrix}\begin{pmatrix} 0 & M_2 \\ K_2 & 0 \end{pmatrix}\right\}\begin{pmatrix} -\bar{I}_1M_1 & \bar{I}_1 \\ -I_1 & -K_1\bar{I}_1 \end{pmatrix}\boldsymbol{w}(k-i).
\end{aligned} \tag{9.13}$$

To bound $\|\Pi_{\bar{M}_2//\bar{L}_2}\|$ we follow the proof of Theorem 4.6, with the relation

$$\sum_{i=0}^{\infty}\Big\|\sum_{j=0}^{i-1}(I-G_3L_3)^{i-1-j}(G_2L_1+G_3L_2)(I-G_1L_1)^j\Big\|$$
$$\leq \|G_2L_1+G_3L_2\|\sum_{i=0}^{\infty}\|I-G_3L_3\|^i\sum_{i=0}^{\infty}\|I-G_1L_1\|^i \tag{9.14}$$

and summing each component of (9.13) we arrive at

$$\|\Pi_{\bar{M}_2//\bar{L}_2}\|\leq\beta_{\bar{M}_2//\bar{L}_2}=\left\|\begin{pmatrix}-I_3K_3 & I_3\\ \bar{I}_3 & M_3I_3\end{pmatrix}\right\|\left\|\begin{pmatrix}-\bar{I}_1M_1 & \bar{I}_1\\ -I_1 & -K_1\bar{I}_1\end{pmatrix}\right\|\left\{\frac{\|K_3L_2\|}{1-\gamma_1}\right.$$
$$\left.+\frac{\|K_3L_3\|\|G_2L_1+G_3L_2\|}{(1-\gamma_1)(1-\gamma_3)}+\left\|\begin{pmatrix}M_2 & 0\\ 0 & K_2\end{pmatrix}\right\|\left(\frac{\left\|\begin{pmatrix}K_1\bar{I}_1\\ \bar{I}_1\end{pmatrix}L_1\right\|}{1-\gamma_1}+\frac{\|K_3L_3\|\|(\bar{I}_3,-\bar{I}_3M_3)\|}{1-\gamma_3}\right)\right\}. \tag{9.15}$$

Hence from (9.12)

$$\|\Pi_{\bar{M}//\bar{C}}\|\leq\beta_{\bar{M}//\bar{C}}=\left\|\begin{bmatrix}\beta_{\bar{M}_1//\bar{C}_1} & 0\\ \beta_{\bar{M}_2//\bar{C}_2} & \beta_{\bar{M}_3//\bar{C}_3}\end{bmatrix}\right\|\quad\text{where}\quad\beta_{\bar{M}_j//\bar{C}_j}=\beta_{\bar{M}_j//\bar{K}_j}+\beta_{\bar{M}_j//\bar{L}_j},$$

with $\|\Pi_{\bar{M}_j//\bar{C}_j}\|\leq\beta_{\bar{M}_j//\bar{C}_j}$, $\|\Pi_{\bar{M}_j//\bar{L}_j}\|\leq\beta_{\bar{M}_j//\bar{L}_j}$. Adding bounds on (9.8) and (9.15) gives (9.6). Since $[M_i|_{z(k)},K_i]$ is independent of plant dynamics $\bar{M}_{\dagger}$, $\bar{M}_{\dagger,i}$, then nominal closed-loop properties $\boldsymbol{\Phi}_i=G_i\boldsymbol{v}_i$, $\boldsymbol{z}_i=M_i\boldsymbol{z}_i$ are preserved. □

Theorem 9 shows that a robust stability margin exists if K_i, L_i are designed to minimise $\beta_{\bar{M}_i//\bar{C}_i}$, $K_{\dagger}$, $L_{\dagger}$ are designed to minimise $\beta_{\bar{M}_{\dagger}//\bar{C}_{\dagger}}$, and $M_{\dagger,i}$, $K_{\dagger,i}$, $L_{\dagger,i}$, $G_{\dagger,i}$ are stable operators. In particular, condition (9.5) reveals the dual aims of the designer:

- Modeling: Include as accurate an interaction term $M_{\dagger,i}$ as possible (thereby reducing the left hand side of (9.5)). This means that the lumped parameter global model of the upper arm, $M_{\dagger}$, must include enough joints associated with the array(s) to capture the main interaction effects.
- Control: Following linearization, design feedback and ILC operators for the array and upper arm independently, minimizing $\beta_{\bar{M}_i//\bar{C}_i}$ and $\beta_{\bar{M}_{\dagger}//\bar{C}_{\dagger}}$ respectively. Following this, design the interaction operators $K_{\dagger,i}$, $L_{\dagger,i}$ to minimize the gain bound $\beta_{\bar{M}_{\dagger,i}//\bar{C}_{\dagger,i}}$ associated with the interaction dynamics (and hence maximize the right

hand side of (9.5)). The simplest approach is to set $K_{\dot{\imath},i} = L_{\dot{\imath},i} = 0$, which reduces bound (9.6) to

$$b_{M_{\dot{\imath},i}//C_{\dot{\imath},i}} = \left\|\begin{pmatrix} -I_{\dot{\imath}}K_{\dot{\imath}} & I_{\dot{\imath}} \\ \bar{I}_{\dot{\imath}} & M_{\dot{\imath}}|_z I_{\dot{\imath}} \end{pmatrix}\right\| \left\|\begin{pmatrix} \bar{I}_i M_i|_z & -\bar{I}_i \\ I_i & K_i \bar{I}_i \end{pmatrix}\right\| \|M_{\dot{\imath},i}|_z\| \times \left(1 + \frac{\left\|\begin{pmatrix} K_i \bar{I}_i \\ \bar{I}_i \end{pmatrix} L_i\right\|}{1-\gamma_i} + \frac{\|K_{\dot{\imath}}L_{\dot{\imath}}\|\|(\bar{I}_{\dot{\imath}}, -\bar{I}_{\dot{\imath}}M_{\dot{\imath}}|_z)\|}{1-\gamma_{\dot{\imath}}}\right)$$

However, this approach may lead to an unacceptable transient response as, for example, the wrist dynamics cause oscillations in the upper limb joints (which could have been damped by a suitable $K_{\dot{\imath},i} \neq 0$).

Theorem 9 motivates fusing a linearized global model, $M_{\dot{\imath}}|_z = [M_{\dot{\imath},i}|_z,\ M_{\dot{\imath},\dot{\imath}}|_z]$, with between-trial identification of array dynamics $M_i X|_{z(k)}$ using identification Procedure 8 of Sect. 8.4. If interaction term $M_{\dot{\imath},i}$ is negligible then the designer does not have to augment the global model to include joints associated with the array. This reduces the time necessary to identify parameters in the model, controller complexity and also the overall gain margin $b_{\bar{M}//\bar{C}}$. In this case Theorem 9 simplifies to:

Theorem 9.2 (Robustness using decoupling design) *Let a fully decoupled model be assumed in which the ith array block has dynamics $\boldsymbol{\Phi}_{\mathscr{P}_i} = M_i \boldsymbol{z}_{\mathscr{N}_i}$, and the remaining joints use $\boldsymbol{\Phi}_{\bar{\mathscr{P}}_i} = M_{\dot{\imath}} \boldsymbol{z}_{\bar{\mathscr{N}}_i}$. Then the system that results from applying the linearised design procedure of Chap. 4 or 6 with the feedback and ILC update structures*

$$K = diag\{K_i, K_{\dot{\imath}}\}, \quad L = diag\{L_i, L_{\dot{\imath}}\} \quad where \quad \begin{cases} \|I - G_i L_i\| \leq \gamma_i < 1, \\ \|I - G_{\dot{\imath}} L_{\dot{\imath}}\| \leq \gamma_{\dot{\imath}} < 1 \end{cases} \tag{9.16}$$

is robustly stable if

$$\sup_{k \in \mathbb{N}_+} \left\| N|_{\bar{z}_1(k)} - \begin{bmatrix} M_i|_{z(k)} & 0 \\ 0 & M_{\dot{\imath}}|_{z(k)} \end{bmatrix} \right\| < \left\| \begin{pmatrix} b_{\bar{M}_i, \bar{C}_i} & 0 \\ 0 & b_{\bar{M}_{\dot{\imath}}, \bar{C}_{\dot{\imath}}} \end{pmatrix} \right\|^{-1} \tag{9.17}$$

where without loss of generality we assume $i = 1$. Design of K_i and L_i using Propositions 8.1 and 8.2 preserves the nominal properties of the array dynamics $\boldsymbol{\Phi}_{\mathscr{P}_i} = M_i \boldsymbol{z}_{\mathscr{N}_i}$, $\boldsymbol{z}_{\mathscr{N}_i} = X_i \boldsymbol{r}_{\mathscr{Q}_i}$, $\boldsymbol{r}_{\mathscr{Q}_i} = K_i(\boldsymbol{v}_{\mathscr{P}_i} + \boldsymbol{e}_{\mathscr{P}_i})$ established in these propositions.

Proof The result immediately follows from setting $\bar{M}_{\dot{\imath},i} = 0$, $\bar{K}_{\dot{\imath},i} = 0$ and $\bar{L}_{\dot{\imath},i} = 0$ in the proof of Theorem 9.1. Note that, although interaction is embedded via computation of $M|_{z(k)}$ at the combined operating point, the linearized form then assumes no interaction between $\{z_i, \boldsymbol{\Phi}_i\}$ and $\{z_{\dot{\imath}}, \boldsymbol{\Phi}_{\dot{\imath}}\}$ in each trial. □

It is desirable to relate stability conditions (9.5) and (9.17) to specific components of the plant, e.g. to quantify levels of fatigue that may be tolerated. As in Propositions 3.4 and 4.1, this is easily achieved by inserting the forms

$$
\begin{aligned}
N|_{z_1} z &= \begin{pmatrix} N_i|_{z_1} \\ N_{\dot{\imath}}|_{z_1} \end{pmatrix} z = \begin{pmatrix} (H_{RB}F_m)_i|_{w_1} H_{LAD} \boldsymbol{h}_{IRC}|_{z_1} \\ (H_{RB}F_m)_{\dot{\imath}}|_{w_1} H_{LAD} \boldsymbol{h}_{IRC}|_{z_1} \end{pmatrix} z, \\
M|_z z &= \begin{bmatrix} M_i|_{z(k)} & 0 \\ M_{\dot{\imath},i}|_{z(k)} & M_{\dot{\imath}}|_{z(k)} \end{bmatrix} z = \begin{pmatrix} \overline{(H_{RB}F_m)}_i H_{LAD} \bar{\boldsymbol{h}}^i_{IRC} & 0 \\ \overline{(H_{RB}F_m)}_{\dot{\imath}} H_{LAD} \bar{\boldsymbol{h}}^i_{IRC} & \overline{(H_{RB}F_m)}_{\dot{\imath}} H_{LAD} \bar{\boldsymbol{h}}^{\dot{\imath}}_{IRC} \end{pmatrix} z, \\
M|_z z &= \begin{bmatrix} M_i|_{z(k)} & 0 \\ 0 & M_{\dot{\imath}}|_{z(k)} \end{bmatrix} z = \begin{pmatrix} \overline{(H_{RB}F_m)}_i H_{LAD} \bar{\boldsymbol{h}}^i_{IRC} & 0 \\ 0 & \overline{(H_{RB}F_m)}_{\dot{\imath}} H_{LAD} \bar{\boldsymbol{h}}^{\dot{\imath}}_{IRC} \end{pmatrix} z,
\end{aligned}
$$

where $\bar{\boldsymbol{h}}^i_{IRC} = \frac{\partial}{\partial z_{\mathcal{N}_i}} \boldsymbol{h}_{IRC}(z)$ and $\boldsymbol{h}^{\dot{\imath}}_{IRC} = \frac{\partial}{\partial z_{\mathcal{N}_i}} \boldsymbol{h}_{IRC}(z)$, into the left hand side of (9.5) and (9.17) respectively.

In the next section the control design framework is applied within a clinical feasibility trial with stroke participants.

9.2 System Description and Set-Up

The rehabilitation system comprises the five components shown in Fig. 9.2. Participants sit on a perching stool in front of the touch table, and a SaeboMAS arm support (Saebo Inc., Charlotte) is used to de-weight their upper extremity according to individual need. Surface electrodes are positioned on the anterior deltoid and triceps, and an electrode array is placed over the common extensor complex of the forearm. The PrimeSense is used in combination with another depth camera (Kinect, Microsoft Washington) to measure the position of joint centres within the shoulder, elbow and wrist. Data from these sensors are fed into the control algorithm hardware and software, which updates the ES control signals for each muscle group to assist performance of functional tasks. The therapist uses an operator monitor displaying a graphical user interface (GUI) to select appropriate tasks and monitor training progression. The therapist also has an over-ride stop button which can be used to terminate trials with immediate effect.

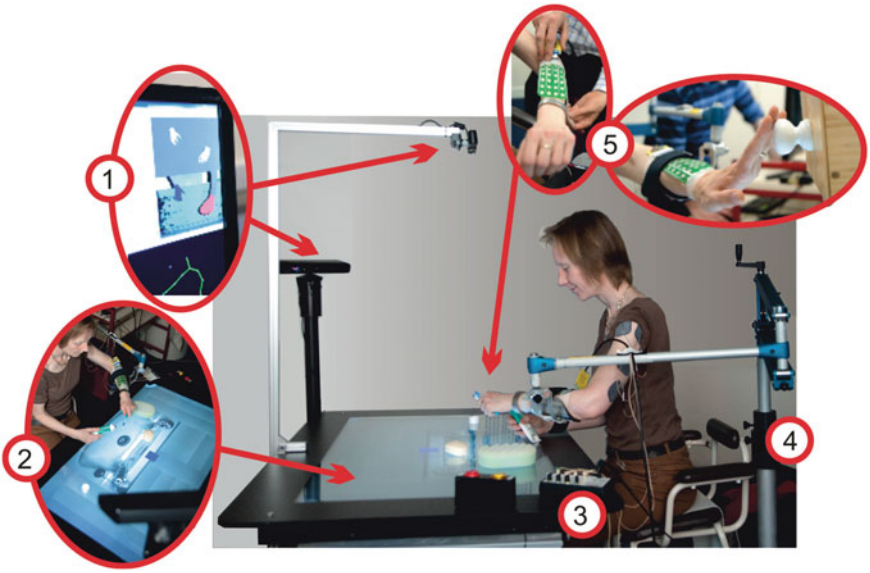

Fig. 9.2 System components: (*1*) Motion tracking hardware, (*2*) interactive touch table display, (*3*) ES controller and multiplexor hardware, (*4*) SaeboMAS and perching stool, and (*5*) electrode-array

9.2.1 Task Design

Figure 9.3 shows the four main images displayed by the touch table; a default image, a bathroom sink, a coffee table, and a chopping board. The same task set as in Chap. 7 is employed to provide a varied range of functional activities: closing a drawer, switching a light switch, stabilizing an object, pressing a button and repositioning an object relevant to each image (e.g. a tube of toothpaste). The light switch is located at two different heights (low and high) and there are four table-mounted positions at which the virtual buttons can be located or real objects repositioned both in the sagittal plane and towards the frontal plane (45° across body, 45° to the hemiplegic side or in line with the shoulder) as illustrated in Fig. 9.3. The objects are placed at different percentages of arm length (60, 75, and 90 %) from the participant's glenohumeral joint as shown in Fig. 9.3a). The table was positioned at a distance of 45 % arm length from the glenohumeral joint and 35 cm below the arm when the arm was held 90° horizontal to the shoulder.

9.2.2 System Software

The software and data flow is shown schematically in Fig. 9.4. The system software undertakes tracking of the participant's movement in real-time, extraction of

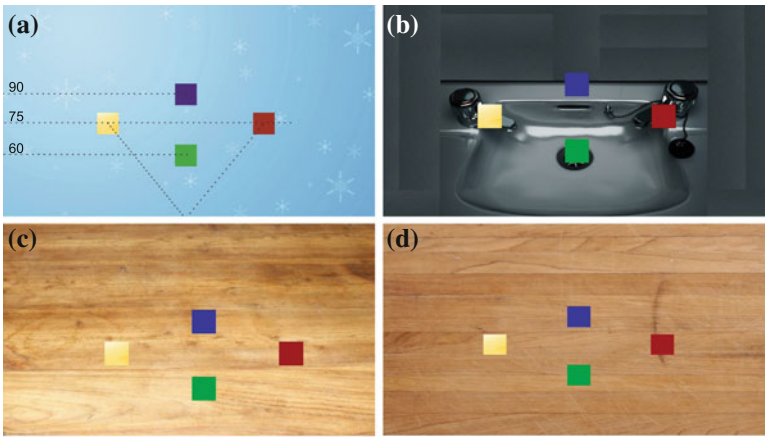

Fig. 9.3 Task design and graphical backgrounds: **a** default (overlaid with task placement geometry), **b** bathroom sink, **c** coffee table and **d** chopping board

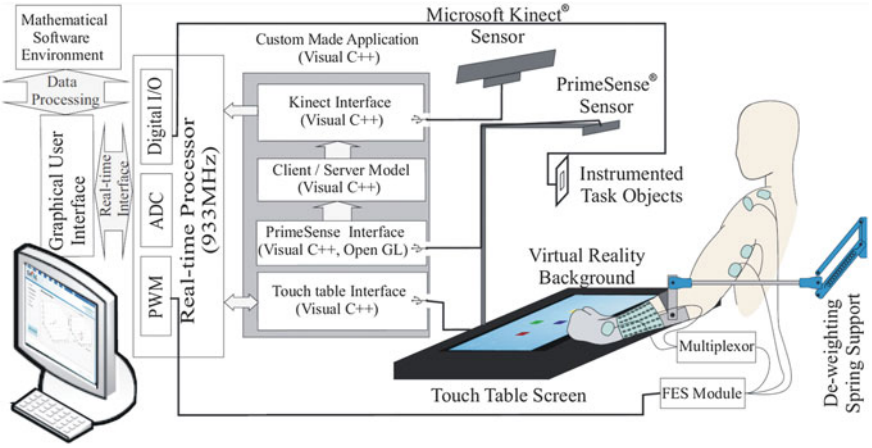

Fig. 9.4 Software signal flow diagram

kinematic variables, and subsequent implementation of ES control schemes. A custom made C++ application interfaces with Kinect middle-ware (Skeletal Viewer), which in turns receives data from PrimeSense via a Client/Server (Transmission Control Protocol (TCP)) connection with its associated middle-ware (3Gear Systems). This application directly communicates with real-time hardware (dSPACE ds1103), which handles all data processing and control implementation, and interfaces with the touch table and graphical user interface via direct hardware access. Communication with the touch table employs Snowflake software (NUITEQ Inc., Sweden) which controls the task display and touch feedback. The GUI oversees communication with the system inputs and outputs and is responsible for customizing

control parameters, implementing the ES control, collecting and storing position data, selecting the task to be performed and reviewing performance after each session. The real-time hardware generates pulse-width modulated (PWM) signals for each ES channel, together with RS232 serial data to control the electrode array. Digital inputs and outputs are also used to interface with the instrumented task objects.

9.2.3 Motion Tracking

Recently various low-cost position sensors have emerged that are suitable for home-use by patients with minimal assistance. A Kinect was employed in Chap. 7 to measure shoulder and arm joint angles, and a goniometer measured wrist flexion and abduction. To collect a comprehensive set of hand/wrist angles we now exchange the goniometer for the PrimeSense which provides joint centre position data for the wrist and fingers, from which joint angles can be extracted as described next.

Figure 9.5 shows the assumed kinematic model, which integrates a hand and wrist description into the model described in Sect. 7.1. The Kinect is used to capture joint centre locations $(x_i, y_i, z_i)^\top$ for the shoulder, elbow and wrist, $i = 1, 2, 3$ respectively. The PrimeSense captures joint centre locations $(x_i, y_i, z_i)^\top$ for the hand

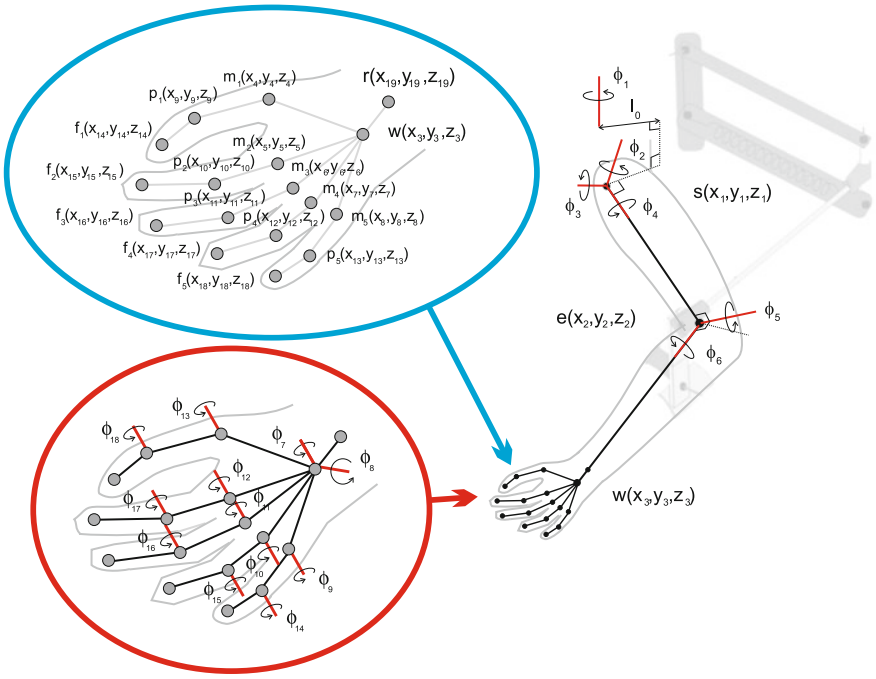

Fig. 9.5 Human arm joint centre locations and kinematic model variables

and wrist, $i = 3, \ldots, 19$, respectively. As previously, joint angles $\phi_1, \ldots, \phi_5$ denote the orientation of the upper arm and forearm segments, with joint axes chosen to align with motion elicited by ES. The procedure used to define $\phi_1, \ldots, \phi_5$ is described in [3], together with the mapping $\left((x_1, y_1, z_1)^\top, \ldots, (x_3, y_3, z_3)^\top\right) \mapsto (\phi_1, \ldots, \phi_5)$. The position vectors $(x_i, y_i, z_i)^\top$ are denoted $\boldsymbol{s}$, $\boldsymbol{e}$, $\boldsymbol{w}$ and $\boldsymbol{r}$ for the shoulder ($i = 1$), elbow ($i = 2$), wrist ($i = 3$) and root ($i = 19$) respectively with $\boldsymbol{m}$, $\boldsymbol{p}$ and $\boldsymbol{f}$ similarly denoting the metacarpophalangeal (MCP) joint positions, proximal interphalangeal (PIP) joint positions and fingertip positions respectively. Note that the model does not include the distal interphalangeal joints due to their limited range of movement. Using these data, forearm rotation, wrist flexion/extension and abduction/adduction joint angles are then computed respectively by

$$\phi_6 = \cos^{-1}\left(\frac{((\boldsymbol{s}-\boldsymbol{e})\times(\boldsymbol{e}-\boldsymbol{w}))\cdot((\boldsymbol{r}-\boldsymbol{w})\times(\boldsymbol{w}-\boldsymbol{m}_3))}{\|(\boldsymbol{s}-\boldsymbol{e})\|\|(\boldsymbol{e}-\boldsymbol{w})\|\|(\boldsymbol{r}-\boldsymbol{w})\|\|(\boldsymbol{w}-\boldsymbol{m}_3)\|}\right),$$

$$\phi_7 = \cos^{-1}\left(\frac{(\boldsymbol{r}-\boldsymbol{w})\cdot(\boldsymbol{w}-\boldsymbol{m}_3)}{\|\boldsymbol{r}-\boldsymbol{w}\|\|\boldsymbol{w}-\boldsymbol{m}_3\|}\right),\ \phi_8 = \cos^{-1}\left(\frac{((\boldsymbol{r}-\boldsymbol{w})\times(\boldsymbol{w}-\boldsymbol{m}_3))\cdot(\boldsymbol{m}_5-\boldsymbol{m}_3)}{\|(\boldsymbol{r}-\boldsymbol{w})\|\|(\boldsymbol{w}-\boldsymbol{m}_3)\|\|\boldsymbol{m}_5-\boldsymbol{m}_3\|}\right).$$

MCP joints angles, ϕ_9 to ϕ_{13}, and PIP joints, ϕ_{14} to ϕ_{18}, are similarly computed by

$$\phi_{14-i} = \cos^{-1}\left(\frac{(\boldsymbol{w}-\boldsymbol{m}_i)\cdot(\boldsymbol{m}_i-\boldsymbol{p}_i)}{\|(\boldsymbol{w}-\boldsymbol{m}_i)\|\|(\boldsymbol{m}_i-\boldsymbol{p}_i)\|}\right),\ \phi_{19-i} = \cos^{-1}\left(\frac{(\boldsymbol{p}_i-\boldsymbol{f}_i)\cdot(\boldsymbol{p}_i-\boldsymbol{f}_i)}{\|(\boldsymbol{p}_i-\boldsymbol{f}_i)\|\|(\boldsymbol{p}_i-\boldsymbol{f}_i)\|}\right),$$

respectively for $i = 1, \ldots, 5$. Although there is evidence that simultaneous use of the Kinect and PrimseSense cameras can cause interference, this has been found to have little effect on measurement and is strongly correlated with the distance between sensors and observed object [4]. To examine sensor efficacy, joint error has been recorded during repeated tests performed using the proposed training task set, and performance then quantified through comparison with an electro-goniometer. A minimum mean joint error of less than 10° has been established with the Kinect placed at 45° on the opposite side of the impaired arm at a −20° pitch angle in sitting mode, and the PrimeSense positioned 700 mm above the touch-table.

9.2.4 Stimulation Hardware

As in Chap. 7, two single pad ES electrode pairs are positioned over the anterior deltoid and triceps muscles. In addition, the electrode array is placed on the forearm to actuate wrist and hand extensor muscles as in Chap. 8. The key movements produced using the electrode array are shown in Fig. 9.6 and comprise open-hand and pinching movements for grasping and releasing objects, and a pointing movement for switching lights and pushing buttons.

The electrode array (Tecnalia-Fatronik, San Sebastian, Spain) comprises 4×6 elements printed on a polycarbonate substrate, using a hydrogel interface layer. Four stimulation channels are produced by the control hardware, each comprising a 5 V,

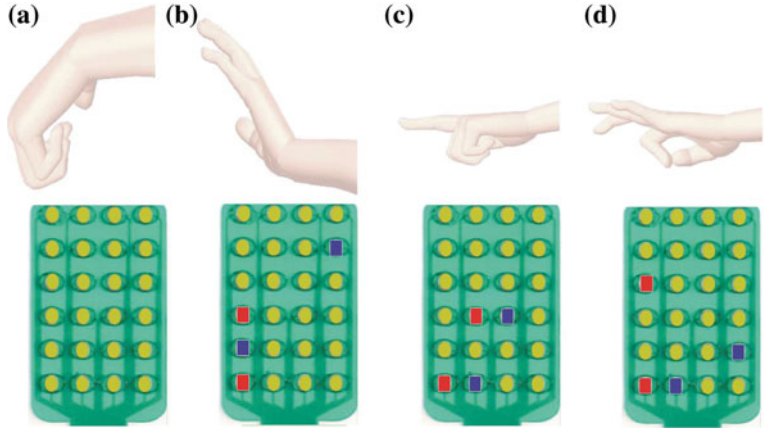

Fig. 9.6 Experimental hand gestures and identified array elements (*left hand view*): **a** Starting, **b** Open hand, **c** Pointing, and **d** Pinch gestures

40 Hz pulse train, where pulse-width is the controlled variable (0–300μs). These are then fed to a four channel stimulator (Odstock Medical Ltd., Salisbury, UK) which amplifies the voltage of each channel to a fixed level determined at the beginning of each session by applying a 300 μs signal to the stimulation site and slowly increasing a dial on the stimulator until the maximum comfortable level is achieved. When setting the voltage amplitude of an array channel, the stimulation site comprises two adjacent array elements located over the wrist and hand extensors.

9.2.5 Control Design

Theorems 9.1 and 9.2 provide two choices with which to design a control scheme integrating arrays and single-pad electrodes. For simplicity we select the simpler design procedure of Theorem 9.2 which assumes locally decoupled dynamics about an updated operating point. The underlying assumption of weak local interaction between the upper arm and wrist/hand is motivated by the inertial and Coriolis coupling between arm segments and the hand being negligible compared with the coupling due to spasticity and inherent stiffness of the muscular tendon structure.

As described, the system has $n = 26$ electrode sites, $q = 4$ stimulation channels, and $p = 17$ joints. The first two electrode sites, first two channels, and first five joints are associated with the single-pad electrodes, giving $n_1 = 2, n_2 = 24, q_1 = 2, q_2 = 2, p_1 = 5$ and $p_2 = 12$. Following Procedure 9 we therefore set $A_1 = I$ and $X_1 = I$ in the forms of A and X given by (9.1) and (9.2) respectively. At the beginning of each treatment session the subspace X_2 is identified for each participant using Procedure 7 of Sect. 8.3 which involves using past experience and known muscle geometry. The operator X_2 maps the two array stimulation channel signals,

$\boldsymbol{r} \in \mathscr{L}_2^{q_2}[0, T]$, to the stimulation appearing at the array elements, $\boldsymbol{z} \in \mathscr{L}_2^{n_2}[0, T]$. Physically this routing is achieved via custom-made RS232 controlled multiplexor hardware, comprising an Arduino board and shift register array, which interface with a relay bank.

The decoupled design of Theorem 9.2 means that joints $\boldsymbol{\Phi}_{\mathscr{P}_1} = [\phi_1, \ldots, \phi_5]^\top$ are controlled only using stimulation input $\boldsymbol{r}_{\mathscr{Q}_1} = \boldsymbol{z}_{\mathscr{N}_1} = [u_1, u_2]^\top$, with model M_1 matching that used in Chap. 7. Hence exactly the same feedback and ILC controllers as designed for the upper arm in Chap. 7 can be used. In addition, joints $\boldsymbol{\Phi}_{\mathscr{P}_2} = [\phi_6, \ldots, \phi_{17}]^\top$ are controlled using only array stimulation $\boldsymbol{r}_{\mathscr{Q}_2} = [u_3, u_4]^\top$, $\boldsymbol{z}_{\mathscr{N}_2} = X_2 \boldsymbol{r}_{\mathscr{Q}_2}$, with linearized model $M_2|_{z(k)}$ matching that employed in Chap. 8. Hence the specialized feedback and ILC control implementations of Propositions 8.1 and 8.2 can be employed and maintain their nominal properties.

Remark 9.1 If were desired to implement the partially decoupled design of Theorem 9.1, the necessary steps would be to: (1) augment the upper limb model with a lumped parameter representation of the wrist, (2) use it to compute the linearized interaction component $M_{2,1}|_{z(k)}$ appearing in M, and (3) use M to design a controller which includes the interaction term $K_{2,1}$ in its structure. This augmented control action allows the upper arm stimulation to respond to changes in the wrist position.

9.3 Results

The system has been tested with both unimpaired and stroke participants. Following ethical approval, 6 participants (2 unimpaired and 4 stroke) were recruited with demographic characteristics for the latter given in Table 9.1. At the beginning of each session they were set-up at the workstation, which took 15 min and comprised:

1. Participant placement as described in Sect. 9.2,
2. Electrode-array and single electrode placement and setting of comfortable stimulation amplitude for each channel as described in Sect. 9.2.4,
3. Array stimulation subspace identification as described in Procedure 7 of Sect. 8.3.

Table 9.1 Stroke participant demographic characteristics

Participant	Gender	Age (years)	Side of paresis	Time since stroke (months)
1	M	54	L	35
2	M	51	L	64
3	F	47	L	60
4	M	43	L	96
Average		48.75		63.75

Each unimpaired participant attended a single session, in which they used the system to perform the tasks described in Sect. 2.1. They were instructed to provide no voluntary effort, and were not shown the task. Each stroke participant attended 17 intervention sessions. The inclusion criteria were the same as in Chap. 7. The set-up procedure also followed steps (1)–(3) above, and was followed by 60 min practising of a subset of ES-assisted functional reach and grasp tasks dictated by clinical need. At the beginning and end of each intervention session, each stroke participant completed two tasks without ES assistance (high light switch and button pressing tasks). The same clinical assessments as used in the previous clinical trial and described in Sect. 7.1.1 were used. The assessments were conducted according to standard protocol, by qualified physiotherapists who were independent of the study. Data collection was carried out by a team of experienced researchers.

9.3.1 Unimpaired Participants

The hand and wrist identification procedure of Sect. 8.4 should ideally be repeated between trials to identify model component $M_2|_{z(k)}$ within Theorem 9.2, which assumes the structure $\bar{H}(s)F$. However, due to the dominant effect of spasticity and stiffness outweighing variation in operating point conditions, satisfactory results were obtained by performing a single identification test at the start of each participant's experimental session.

The upper arm feedback and ILC controllers K_1 and L_1 were calculated as in Chap. 7. In particular, K_1 took the form of a PD controller about both the shoulder and elbow joints, with proportional gains between 2 and 3 and derivative gains of 0.1. ILC operator L_1 took the form of a phase-lead ILC update.

Then array control operators K_2 and L_2 were computed using Propositions 8.1 and 8.2 respectively. In particular, $\bar{K}(s)$ took the form of a PD controller, with proportional gains between 1 and 1.2 and derivative gains between 0.3 and 0.5. These were chosen so that $N_w(s)$ in Proposition 8.1 approximated a pure delay.

Parameters required to represent each task were extracted in separate tests with 12 unimpaired participants, as reported in [5]. These were used to define extended task operator P which, due to the decoupled design, had components of the form $P_j = \text{diag}\{P_{1,j}, P_{2,j}\}$, $j = 1, \ldots, S$. Since both subsystems use the same ILC structure, we can express the update as

$$\boldsymbol{v}_{k+1}(t) = \boldsymbol{v}_k(t) + \begin{bmatrix} l_1(P_{1,j})^\dagger & 0 \\ 0 & l_2(P_{2,j}(FX_2)^\perp)^\dagger \end{bmatrix} \begin{bmatrix} (\boldsymbol{e}_k)^e_{\mathscr{P}_1}(t+\lambda_1) \\ (\boldsymbol{e}_k)^e_{\mathscr{P}_2}(t+\lambda_2) \end{bmatrix}, \quad t \in [t_{j-1}, t_j], \quad j = 1, \ldots, S, \quad k = 0, 1, \ldots \tag{9.18}$$

where $l_1, l_2 > 0$ are gains and $\lambda_1, \lambda_2 > 0$ phase-leads. In practice, suitable parameters were $l_1 = 0.3$ and $\lambda_1 = 0.8s$, $l_2 = 0.3$ and $\lambda_2 = 0.8s$.

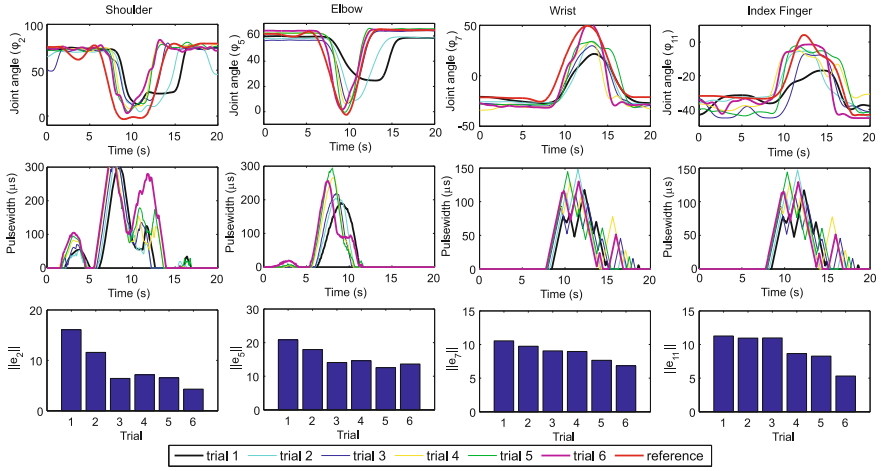

Fig. 9.7 Tracking results for unimpaired Participant 1 during far reach task

Tests comprised 6 trials of each of the far reaching and low light switch tasks. SaeboMAS support was set according to participant needs. Results for Participant 1, as illustrated by Fig. 9.7, confirm improved tracking between trials $k = 1$ and $k = 6$ with summary performance measures given in Table 9.2. Here the virtual reference $\hat{\boldsymbol{\Phi}} = G\boldsymbol{v}_\infty$ is used to provide a clear measure of error at each time point $t \in [0, T]$. Although all wrist and hand axes were controlled, results for ϕ_7 and ϕ_{11} (wrist and index finger extension) are shown as 42 % of the functional movements of the hand involve the four fingers moving together [6].

The effect of fatigue and moderate to severe spasticity was addressed by re-tuning the feedback control parameters, and reducing learning gains l_1, l_2 to sacrifice convergence speed for robustness. Results confirm satisfactory accuracy and feasibility of the system.

Table 9.2 Unimpaired participants assisted results

	Task	Trial no	Norm of error			
			$\|\hat{\phi}_2 - \phi_2\|$	$\|\hat{\phi}_5 - \phi_5\|$	$\|\hat{\phi}_7 - \phi_7\|$	$\|\hat{\phi}_{11} - \phi_{11}\|$
Participant 1	Far reaching	1	8.54	8.72	12.76	8.51
		6	3.45	6.34	6.55	5.02
	Low light switch	1	9.95	11.33	6.12	3.73
		6	4.33	3.68	4.95	3.02
Participant 2	Far reaching	1	12.09	6.86	8.49	7.05
		6	7.92	4.68	4.90	4.99
	Low light switch	1	7.30	7.03	19.58	12.38
		6	2.03	6.42	6.60	8.17

9.3.2 Stroke Participants

For each stroke participant the set-up procedure steps (1)–(3) were performed at the beginning of each of the 17 intervention sessions, using the same identification procedure and control structures as the unimpaired case. However, due to time constrains the arm model identification process was not repeated each session unless performance was deemed unsatisfactory. The four chronic participants each completed the intervention over a 6–8 week period.

9.3.2.1 Assisted Tracking Performance

When assisted by ES, each participant was supported by both the SaeboMAS and ES according to their clinical need. The level of gravitational support was varied between tasks based on physiotherapist observations and participant voluntary action. For all participants the level reduced over the intervention. As shown in Figs. 9.8 and 9.9, improvements were seen in mean tracking accuracy for all four joints as was the case with unimpaired participants. The results demonstrate the success of the control system for improving movement accuracy during reaching and grasping tasks. Summary performance measures are given in Table 9.3 and confirm that tracking accuracy increased between the first and last ILC trials. For example, the norm of tracking error for all joints (last column) reduced on average to less than half, attaining an accuracy on trial $k = 6$ which confirms that the overall movement was performed to a satisfactory level of precision to support functional movement. Since the first trial ($k = 1$) corresponds to $\boldsymbol{\nu}_k = 0$, these results clearly show the improvement compared with using feedback controllers alone.

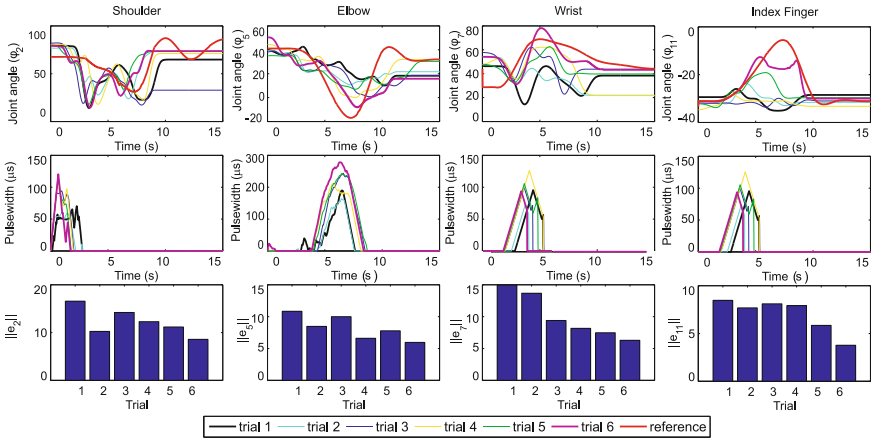

Fig. 9.8 Tracking results for Stroke Participant 1 during ES-Assisted drawer closing task

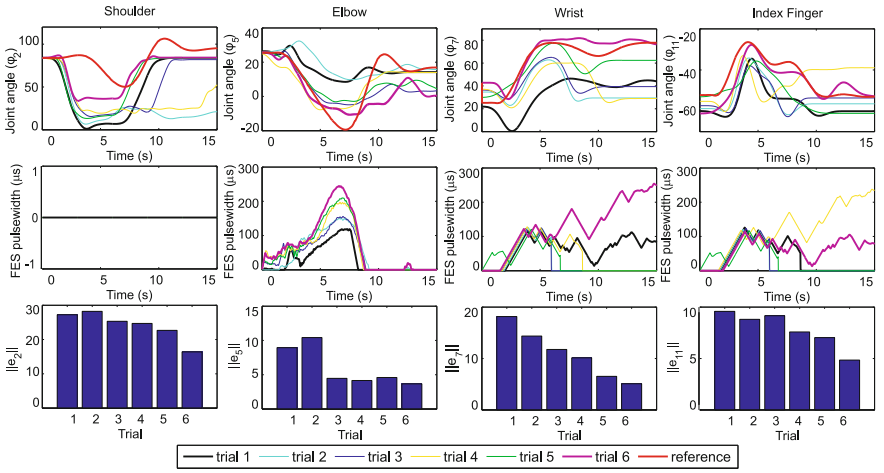

Fig. 9.9 Tracking results for Stroke Participant 4 during ES-Assisted low light task

Table 9.3 ES-assisted tracking results for stroke participants taken mid-way during intervention (session 9)

	Task	Trial no	Norm of error				
			$\|\hat{\phi}_2 - \phi_2\|$	$\|\hat{\phi}_5 - \phi_5\|$	$\|\hat{\phi}_7 - \phi_7\|$	$\|\hat{\phi}_{11} - \phi_{11}\|$	$\|\hat{\boldsymbol{\Phi}} - \boldsymbol{\Phi}\|$
Participant 1	Drawer closing	1	16.6	10.8	14.9	8.47	192.8
		6	10.1	7.42	6.28	4.9	72.74
Participant 2	Far reaching	1	24.9	9.94	9.77	7.78	196.68
		6	19.1	5.01	5.36	6.52	89.12
Participant 3	Near reaching	1	16	5.42	30.4	12.5	186.84
		6	12	3.24	13.5	6.21	105.88
Participant 4	High light switch	1	25.3	8.68	12.9	9.55	217.96
		6	37.6	5.37	5.42	5.52	125.64

9.3.2.2 Unassisted Tracking Performance

During ES-unassisted tasks each participant was only supported by the SaeboMAS. The level of support was set by the physiotherapist at a constant level during the first treatment session according to each participant's needs. The range of movement, defined as the difference between maximum and minimum joint angles, was calculated for each ES-unassisted task. Results in Table 9.4 demonstrate improved range of movement at all four stimulated joints over the intervention. In particular mean improvements over the course of the intervention were 5° in shoulder flexion (high light switch), 13° in elbow extension (contralateral reach), 42° in wrist extension (near reach), and 34° in index finger extension (far reach). As in Chap. 7 and prior

Table 9.4 Stroke participant clinical assessment data

Participant	Action Research Arm Test		Fugl-Meyer		ES-Unassisted Range of Movement							
					ϕ_2		ϕ_4		ϕ_6		ϕ_{11}	
	Base-Line	Post-	Base-Line	Post-	Base-Line	Post-	Base-Line	Post-	Base-Line	Post-	Base-Line	Post-
P1	8	9	26	33	6	14	30	33	30	50	11	23
P2	6	5	28	28	7	13	10	23	65	130	15	42
P3	7	3	30	35	2	16	16	29	59	73	6	44
P4	10	13	23	38	3	8	30	35	40	76	32	45
ttest p-value			0.0596		0.0054		0.0041		0.0322		0.0364	

studies [7–9], one-tailed t-tests were applied to best-fit linear regression slopes of range of movement against session number, and yielded p-values <0.05 in all cases.

9.3.2.3 Clinical Outcome Measures

As in the previous clinical applications, the primary outcome measures were the motor component of the FMA and the ARAT, with maximum scores of 66 and 57 respectively. Scores are shown in Table 9.4 with improvements seen in both; for two participants the ARAT and for three participants the FMA improved. A paired t-test was applied to the FMA scores but the p-value of 0.0596 is not deemed significant.

9.4 Discussion

The system detailed in this chapter was motivated by evidence that shoulder and elbow training only improves motor impairment in the shoulder and elbow [7, 8], as reflected in the clinical case-studies of Chaps. 5 and 7. Similarly, training of the wrist and finger extensors has been found to only improve hand function [10]. However, when these muscle groups are trained simultaneously, significant improvements are observed, with participants reporting greater capacity to perform everyday tasks at home, such as opening drawers, stabilizing and moving objects, and pressing light switches [9]. Unfortunately the majority of systems reported in the literature stimulate too few muscles and use non-selective, large electrodes. They also do not employ position feedback or model-based control algorithms. This leads to inadequate support during functional activities.

The aim of this study is to establish the feasibility of combining state-of-the-art technologies to enable people with stroke to practice goal-oriented functional tasks. The system developed in this chapter incorporates VR, ES hardware, advanced sensing, control and passive support. Compared with previous systems, this demonstrates a substantial development in the scope of technology for upper-limb rehabilitation. It also shows that the integrated control scheme provides fine finger movements during

training of everyday tasks by employing a model of the hand and wrist, and learning from past experience. While the study confirmed acceptance and positive outcomes, limitations included the small sample size, absence of a control group or follow-up (due to time constraints).

9.5 Conclusions

The control framework has been demonstrated within a rehabilitation system which supports functional task training, with assistance provided by a combination of single-pad electrodes and an electrode array. As the first upper-limb system to employ model-based controllers to assist shoulder, elbow and hand movement, it has established the feasibility of the control framework for clinical use. The next chapter describes subsequent challenges that must be addressed in order to translate this technology into the home environment.

References

1. J.M. Veerbeek, E. van Wegen, R. van Peppen, P.J. van der Wees, E. Hendriks, M. Rietberg, G. Kwakkel, What is the evidence for physical therapy poststroke? A systematic review and meta-analysis. PLoS ONE **9**(2), e87987 (2014)
2. M. Kutlu, C.T. Freeman, E. Hallewell, A.M. Hughes, D.S. Laila, Upper-Limb Stroke Rehabilitation using Electrode-Array Based Functional Electrical Stimulation with Sensing and Control Innovations. Medical Engineering and Physics (2015) (In Press)
3. C.T. Freeman, D. Tong, K. Meadmore, Z. Cai, E. Rogers, A.M. Hughes, J.H. Burridge, Phase-lead iterative learning control algorithms for functional electrical stimulation based stroke rehabilitation. Proc. Inst. Mech. Eng.—Part I: J. Syst. Control Eng. **225**(6), 850–859 (2011)
4. R.M. Martin, M. Lorbach, O. Brock. Deterioration of depth measurements due to interference of multiple RGB-D sensors. In *IEEE/RSJ International Conference on Intelligent Robots and Systems (IROS 2014)*, pp. 4205–4212. IEEE (2014)
5. C.T. Freeman, T. Exell, K.L. Meadmore, E. Hallewell, A.-M. Hughes, Computational models of upper limb motion during functional reaching tasks for application in FES based stroke rehabilitation. Biomed. Eng. J. **60**(3), 179–191 (2015)
6. J.N. Ingram, K.P. Körding, I.S. Howard, D.M. Wolpert, The statistics of natural hand movements. Exp. Brain Res. **188**(2), 223–236 (2008)
7. A.M. Hughes, C.T. Freeman, J.H. Burridge, P.H. Chappell, P. Lewin, E. Rogers, Feasibility of iterative learning control mediated by functional electrical stimulation for reaching after stroke. J. Neurorehabil. Neural Repair **23**(6), 559–568 (2009)
8. K.L. Meadmore, A.-M. Hughes, C.T. Freeman, Z. Cai, D. Tong, J.H. Burridge, E. Rogers, Functional electrical stimulation mediated by iterative learning control and 3*d* robotics reduces motor impairment in chronic stroke. J. Neuroeng. Rehabil. **32**(9), 1–11 (2012)
9. K.L. Meadmore, T. Exell, E. Hallewell, A.-M. Hughes, C.T. Freeman, M. Kutlu, V. Benson, E. Rogers, J.H. Burridge, The application of precisely controlled functional electrical stimulation to the shoulder, elbow and wrist for upper limb stroke rehabilitation: a feasibility study. J. Neuroeng. Rehabil. **11**, 105 (2014)
10. G. Mann, P.N. Taylor, R. Lane, Accelerometer-triggered electrical stimulation for reach and grasp in chronic stroke patients: a pilot study. Neurorehabil. Neural Repair **25**, 774–781 (2011)

Chapter 10
Conclusions and Future Research Directions

The ES control framework developed in this book is applicable to a wide range of musculoskeletal systems combined with passive/robotic support devices, and can incorporate an arbitrary number of single-pad or electrode arrays positioned over appropriate muscles to assist movement. Utility has been illustrated in a series of clinical feasibility studies which have trained increasingly functional tasks. Implementation has culminated in the system described in Chap. 9, which embeds a motivating training environment, a varied task set, with ES assistance supplied to muscle groups that are aligned with clinical need. Figure 10.1 shows the control structure of Fig. 9.1, as expressed in the lifted notation and augmented by exogenous disturbances, $\boldsymbol{u}_0, \boldsymbol{y}_0$.

The ultimate goal of this rehabilitation technology is to translate into patients' homes, where it can be used without direct supervision from a therapist over longer training periods. Further developments are required to facilitate this, and include:

1. Lengthy and often fatiguing model identification tests (that may require a therapist to administer) must be reduced or eliminated.
2. Control scheme parameter tuning must automatically compensate for physiological changes such as fatigue, spasticity and change in electrode position.
3. ES hardware must be easy to don and doff, and incorporate as few components and wires as possible.
4. Patient-specific motor re-learning models are necessary to enable tasks and treatment modalities to be automatically chosen to maximize long-term treatment outcomes.
5. Expensive components (e.g. dSPACE, touch table, SaeboMAS) should be replaced with affordable alternatives (e.g. embedded 'system on chip' hardware, tablet/smart TV/smartphone, Bakx Magic Arm/Focal Meditech Balancer/Sammons Preston Stable Slide).

C. Freeman, *Control System Design for Electrical Stimulation in Upper Limb Rehabilitation*, DOI 10.1007/978-3-319-25706-8_10

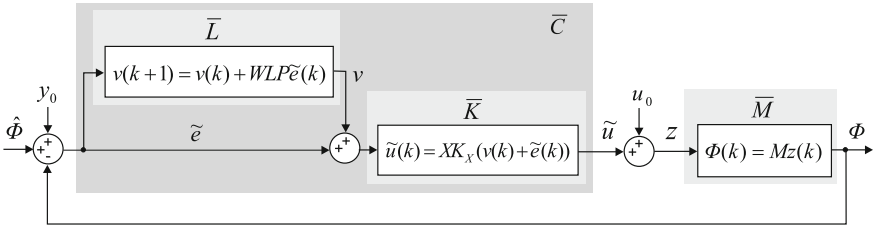

Fig. 10.1 General feedback and ILC control scheme in lifted framework with external disturbance

These developments are aligned with the needs of patients, carers and healthcare professionals that have been identified in [1], and in questionnaires reported in [2]. The next section describes an approach which has potential to address points (1) and (2), and the subsequent section provides a route to address point (3).

10.1 Elimination of Identification and Manual Controller Tuning

The control design framework developed in this book involves obtaining a plant model description, $M|_{z(k)}$, that captures the plant dynamics about the operating point, $z(k)$, corresponding to the kth task attempt. The feedback and ILC controllers K and L are then computed using this model. In the case of single-pad electrodes, feedback controller K may alternatively be designed using a global model, M, but L must still be designed using the linearized model $M|_{z(k)}$.

While this provides a powerful framework to enable ES to support functional movements, the need to identify the underlying model is a significant limitation. For example, in the studies of Chaps. 7 and 9 identification took approximately 15 min and was conducted only at the start of each treatment session. Similarly, time constraints also meant that identification of an array model between trials was not undertaken, and incurred further reduction in tracking accuracy. This was also the reason the fully decoupled design of Theorem 9.2 was used instead of the partially decoupled design of Theorem 9.1. A further issue is the presence of fatigue and spasticity which can rapidly change the stimulated arm dynamics leading to degraded levels of performance. It is therefore desirable to reduce, or ideally remove, the need for model identification, while at the same time adapting the controller to maintain satisfactory performance.

An obvious solution is to expand the framework to automatically chose the 'best' model that matches observed input-output data from a bank of possible models that are specified by the designer before the experiment or treatment session begins. Such a framework, however, requires carefully selection of the candidate model set, controller properties and switching in order to preserve robust stability bounds (as specified by tracking performance bound (4.43) of Theorem 4.5).

A suitable framework has recently become available in the form of estimation based multiple model switched adaptive control (EMMSAC) developed in [3, 4]. EMMSAC uses a bank of Kalman filters to assess the performance of a set of candidate plant models, and the controller corresponding to the most suitable plant model is then switched into closed-loop. Distinct from other switched multiple model approaches, robust performance bounds for EMMSAC are invariant to the size of the set of possible models chosen by the designer. This means that adding more candidate models does not degrade the resulting closed-loop performance properties. Feasibility of using EMMSAC for ES-based upper limb rehabilitation was established in [5], where it was employed to assist participants perform isometric tracking tasks using ES, while supported by a robotic arm. Results with five unimpaired participants showed that it is possible to eliminate model identification while employing closed-loop ES controllers that maintain high performance in the presence of rapidly changing system dynamics. The axiomatic framework of EMMSAC places no restriction on control structure or plant uncertainty form, but delivers explicit guarantees for robust performance. A comprehensive framework for extension to ILC has recently been formulated in [6] and is termed estimation based multiple model ILC (EMMILC). Experimental results confirm further increased tracking performance due to the addition of ILC.

Acting in the lifted space, EMMILC employs exactly the same lifted structure that has been used extensively in this book to perform stability analysis. However, instead of a single model and controller pair $\{\bar{M}, \bar{C}\}$ defined by (4.34)–(4.36) we now define n pairs $\{\bar{M}_i, \bar{C}_i\}_{i=1,\ldots,n}$ before the experiment or treatment session begins. Note that for simplicity they and the true plant, $\bar{N}$, are assumed to be LTI. For each model $\bar{M}_i$ in our candidate model set $G := \{\bar{M}_i\}_{i=1,\ldots,n}$ we implement an estimator $NE(\bar{M}_i)$ which uses observations $(\tilde{\boldsymbol{u}}, \tilde{\boldsymbol{e}})^\top$ to generate a residual $r_i[k]$ at the end of trial k. The size of $r_i[k]$ corresponds to the norm of the minimum disturbance needed to explain the observed signals if $\bar{M}_i$ was the true plant ($r_i[k]$ can readily be computed using a Kalman filter running over $t \in [0, T]$ on trial k). These values are fed to the minimization operator H, which returns the index, q_f, of the plant with minimal residual. The free switching signal q_f is then delayed long enough to prevent instability effects caused by rapid switching, and thereby ensure overall convergence of the closed-loop signals. For this purpose we implement a delay operator D which ensures that a delay of Δ iterations must elapse before another is permitted. The signal q then determines the controller choice $\bar{C}_{q(k)}$ (corresponding to the selected plant) which is switched into closed-loop. Together these components comprise the switching operator $S = DH(NE, G)$ shown in Fig. 10.2. The table summarizes the structural requirements that specify the switching algorithm illustrated in Fig. 10.2, where restriction operator $\mathscr{R}_k \boldsymbol{v} := (\boldsymbol{v}(0), \ldots, \boldsymbol{v}(k))$.

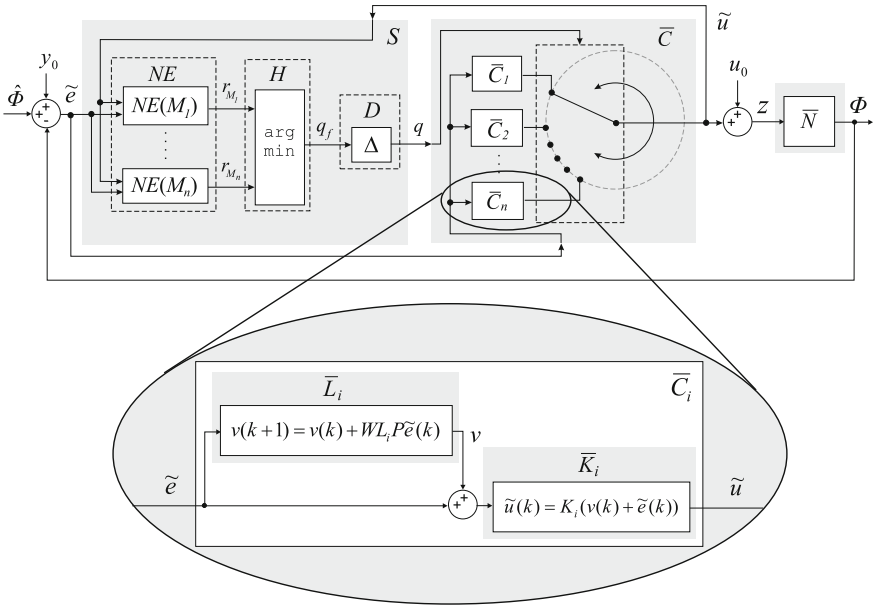

Fig. 10.2 EMMILC structure: switch $S = DH(NE, G)$ outputs switching signal q to determine which atomic controller choice $\bar{C}_{q(k)}$ to switch into closed-loop. With no switching (q fixed), this corresponds to the framework of Chap. 6

$$\text{Controller:} \quad \bar{C} : \tilde{\boldsymbol{e}} \mapsto \tilde{\boldsymbol{u}} : \tilde{\boldsymbol{u}}(k) = \bar{C}_{q(k)}\left[\begin{cases} 0 & \text{if} \quad i < k_s \\ \tilde{\boldsymbol{e}}(k) & \text{if} \quad i \geq k_s \end{cases}\right](k)$$

$$\text{Estimator:} \quad NE : r_i[k] = \inf\left\{\left\| \begin{matrix} \boldsymbol{u}_0 \\ \boldsymbol{y}_0 \end{matrix} \right\| : \mathscr{R}_k(\boldsymbol{y}_0 + \boldsymbol{\Phi} - \tilde{\boldsymbol{e}}) = \mathscr{R}_k \bar{M}_i(\boldsymbol{u}_0 - \tilde{\boldsymbol{u}})\right\}$$

$$\text{Minimizer:} \quad H : q_f(k) := \min_{1 \leq i \leq n} r_i[k], \ \forall k \in \mathbb{N}$$

$$\text{Delay:} \quad D : q(k) := \begin{cases} q_f(k) & \text{if } k - k_s(k) \geq \Delta \\ q(k_s(k)) & \text{else,} \end{cases} \qquad k_s(k) := \max\{i \leq k, \ q(i) \neq q(i-1)\}$$

The comprehensive nature of the axiomatic EMMILC framework of [6] means that there are numerous possible design options with which to specify each controller and estimator. A possible procedure that is appropriate to ES-based rehabilitation is outlined below:

Procedure 10 (EMMILC design procedure)

- Select an uncertainty set $U \in \bar{\mathscr{M}}$ we seek to control. This is the smallest set that contains the true plant description $\bar{N}$. Here $\bar{\mathscr{M}}$ is the set of all lifted LTI models $\mathscr{L}_2^m[0, T] \times \mathbb{N} \to \mathscr{L}_2^p[0, T] \times \mathbb{N}$ (which can be directly generated from their non-lifted counterparts $\mathscr{L}_2^m \to \mathscr{L}_2^p$).

- Select a candidate model set, $G \subset \bar{\mathscr{M}}$, which satisfies the condition

$$\exists\, \bar{M}_i \in G \quad \textit{such that} \quad \delta(\bar{M}_i, \bar{N}) < \delta_{\max}.$$

  This specifies a maximum distance of $\delta_{\max}$ between models, measured using the gap metric (precise computation of $\delta_{\max}$ is given in [6]).
- Associate each model $\bar{M}_i$ with a stabilizing controller $\bar{C}_i$ using a control design procedure $\bar{C}_i = \Omega \bar{M}_i$. If hardware allows, then each controller can be computed individually. Alternatively we can select a minimal set of controllers that stabilizes each element in U (computed using robust stability bound (4.42)), and associate multiple estimators with the same controller.

Recall that robust performance bounds computed using (4.43) for the case of a fixed controller $\bar{C}$ determine how closely the true plant maintains its operating point in the presence of external disturbance. These bounds take the form

$$\|\Pi_{\bar{N}//\bar{C}}\| \begin{pmatrix} \mathbf{0} \\ \hat{\boldsymbol{\Phi}} \end{pmatrix} \leq b$$

with explicit values of $b < \infty$ computed in Sects. 4.4 and 6.4. From (4.42), these hold provided the model is sufficiently close to the true plant $\bar{N}$, thereby quantifying robust stability. EMMILC provides the following equivalent condition which holds across the entire uncertainty space U.

Theorem 10.1 *EMMILC design using Procedure 10 stabilizes the true closed-loop system* $[\bar{N}, \bar{C}]$*, and delivers the tracking performance bound*

$$\|\Pi_{\bar{N}//\bar{C}}\| \begin{pmatrix} \mathbf{0} \\ \hat{\boldsymbol{\Phi}} \end{pmatrix} \leq b_{\max}$$

where $\bar{C} = \Omega \bar{N}$*, with finite values of* $\delta_{\max}$ *and* $b_{\max}$ *computed in [6] as a function of* U *and control design procedure* Ω*.*

Proof The analysis in [6] is applicable to the system of Fig. 10.1, but uses the simpler controller structure $\bar{C} = \bar{L}$ in place of $\bar{C} = \bar{K}(I + \bar{L})$. We hence must verify the EMMILC controller assumptions (defined in [6]) hold for this case. Consider Fig. 10.1 and substitute $K = XK_X$ and $L = WLP$. First note the update relationship

$$\begin{aligned} \tilde{\boldsymbol{u}}(k+1) &= K\boldsymbol{v}(k+1) + K\tilde{\boldsymbol{e}}(k+1) \\ &= K(\boldsymbol{v}(k) + L\tilde{\boldsymbol{e}}(k)) + K\tilde{\boldsymbol{e}}(k+1) \\ &= \tilde{\boldsymbol{u}}(k) + K(L-I)\tilde{\boldsymbol{e}}(k) + K\tilde{\boldsymbol{e}}(k+1) \end{aligned}$$

$$= \tilde{\boldsymbol{u}}(k) + K(L-I)\big(\hat{\boldsymbol{\Phi}} + (-M, I)\boldsymbol{w}_0(k) - M\tilde{\boldsymbol{u}}(k)\big) + K\big(\hat{\boldsymbol{\Phi}} + (-M, I)\boldsymbol{w}_0(k+1) - M\tilde{\boldsymbol{u}}(k+1)\big).$$

Therefore

$$\begin{aligned}(I + KM)\tilde{\boldsymbol{u}}(k+1) &= \big(I + K(I-L)M\big)\tilde{\boldsymbol{u}}(k) + KL\hat{\boldsymbol{\Phi}} \\ &\quad + K(L-I)(-M, I)\boldsymbol{w}_0(k) + K(-M, I)\boldsymbol{w}_0(k+1) \\ \Rightarrow \tilde{\boldsymbol{u}}(k+1) &= \big(I - (I+KM)^{-1}KLM\big)\tilde{\boldsymbol{u}}(k) + (I+KM)^{-1}KL\hat{\boldsymbol{\Phi}} \\ &\quad + (I+KM)^{-1}K(L-I)(-M, I)\boldsymbol{w}_0(k) \\ &\quad + (I+KM)^{-1}K(-M, I)\boldsymbol{w}_0(k+1)\end{aligned}$$

so that

$$\begin{aligned}\tilde{\boldsymbol{u}}(k) &= \big(I - (I+KM)^{-1}KLM\big)^j\tilde{\boldsymbol{u}}(k-j) \\ &\quad + \sum_{i=1}^{j}\big(I - (I+KM)^{-1}KLM\big)^{i-1}(I+KM)^{-1} \\ &\quad \times K\Big\{(L-I)(-M, I)\boldsymbol{w}_0(k-i) + (-M, I)\boldsymbol{w}_0(k+1-i) + L\hat{\boldsymbol{\Phi}}\Big\}. \qquad (10.1)\end{aligned}$$

We next use relation $\sum_{i=1}^{k}(I - XLM)^i X = X\sum_{i=1}^{k}(I - LMX)^i$ to give

$$\begin{aligned}\tilde{\boldsymbol{u}}(k) &= \big(I - (I+KM)^{-1}KLM\big)^j\tilde{\boldsymbol{u}}(k-j) \\ &\quad + (I+KM)^{-1}K\sum_{i=1}^{j}\big(I - LM(I+KM)^{-1}K\big)^{i-1} \\ &\quad \times \Big\{(L-I)(-M, I)\boldsymbol{w}_0(k-i) + (-M, I)\boldsymbol{w}_0(k+1-i) + L\hat{\boldsymbol{\Phi}}\Big\} \\ &= \big(I - (I+KM)^{-1}KLM\big)^j\tilde{\boldsymbol{u}}(k-j) + (I+KM)^{-1}K\sum_{i=1}^{j}\big(I - LG\big)^{i-1} \\ &\quad \times \Big\{(L-I)(-M, I)\boldsymbol{w}_0(k-i) + (-M, I)\boldsymbol{w}_0(k+1-i) + L\hat{\boldsymbol{\Phi}}\Big\}. \qquad (10.2)\end{aligned}$$

Now $\tilde{\boldsymbol{u}}(0) = K\tilde{\boldsymbol{e}}(0) = K(I+MK)^{-1}\big(\hat{\boldsymbol{\Phi}} + (-M, I)\boldsymbol{w}_0(0)\big)$ so this can be written as

$$\begin{aligned}\tilde{\boldsymbol{u}}(k) &= \big(I - (I+KM)^{-1}KLM\big)^k\tilde{\boldsymbol{u}}(0) + (I+KM)^{-1}K\sum_{i=1}^{k}\big(I - LG\big)^{i-1} \\ &\quad \times \Big\{(L-I)(-M, I)\boldsymbol{w}_0(k-i) + (-M, I)\boldsymbol{w}_0(k+1-i) + L\hat{\boldsymbol{\Phi}}\Big\}\end{aligned}$$

$$
\begin{aligned}
&= \big(I - (I + KM)^{-1}KLM\big)^k K(I + MK)^{-1}\big(\hat{\boldsymbol{\Phi}} + (-M, I)\boldsymbol{w}_0(0)\big) \\
&\quad + (I + KM)^{-1}K \\
&\quad \times \sum_{i=1}^{k} \big(I - LG\big)^{i-1}\Big\{(L - I)(-M, I)\boldsymbol{w}_0(k - i) \\
&\qquad\qquad + (-M, I)\boldsymbol{w}_0(k + 1 - i) + L\hat{\boldsymbol{\Phi}}\Big\}.
\end{aligned}
$$

We then use the relationship $(I - XLM)^k X = X(I - LMX)^k$ to give

$$
\begin{aligned}
\tilde{\boldsymbol{u}}(k) &= (I + KM)^{-1}K\big(I - LG\big)^k\big(\hat{\boldsymbol{\Phi}} + (-M, I)\boldsymbol{w}_0(0)\big) + (I + KM)^{-1}K \\
&\quad \times \sum_{i=1}^{k} \big(I - LG\big)^{i-1}\Big\{(L - I)(-M, I)\boldsymbol{w}_0(k - i) + (-M, I)\boldsymbol{w}_0(k + 1 - i) + L\hat{\boldsymbol{\Phi}}\Big\}
\end{aligned}
$$

which can be written as

$$
\begin{aligned}
\tilde{\boldsymbol{u}}(k) &= (I + KM)^{-1}K\sum_{i=1}^{k} \big(I - LG\big)^{i-1}L(I + MK)^{-1}(-M, I)\boldsymbol{w}_0(k - i) \\
&\quad + (I + KM)^{-1}K \times (-M, I)\boldsymbol{w}_0(k) \\
&\quad + (I + KM)^{-1}K\Big[\big(I - LG\big)^k + \sum_{i=1}^{k} \big(I - LG\big)^{i-1}L\Big]\hat{\boldsymbol{\Phi}},
\end{aligned}
$$

and so the operating point bias on $\tilde{\boldsymbol{u}}$ is given by

$$
\bar{\boldsymbol{u}}(k) = (I + KM)^{-1}K\Big[\big(I - LG\big)^k + \sum_{i=1}^{k} \big(I - LG\big)^{i-1}L\Big]\hat{\boldsymbol{\Phi}}. \tag{10.3}
$$

Hence (10.2) can be written as

$$
\begin{aligned}
\tilde{\boldsymbol{u}}(k) &= \big(I - (I + KM)^{-1}KLM\big)^j\tilde{\boldsymbol{u}}(k - j) + \bar{\boldsymbol{u}}(j) + (I + KM)^{-1}K\sum_{i=1}^{j} \big(I - LG\big)^{i-1} \\
&\quad \times \Big\{(L - I)(-M, I)\boldsymbol{w}_0(k - i) + (-M, I)\boldsymbol{w}_0(k + 1 - i)\Big\} - (I + KM)^{-1}K\big(I - LG\big)^j\hat{\boldsymbol{\Phi}} \\
&= \big(I - (I + KM)^{-1}KLM\big)^j\tilde{\boldsymbol{u}}(k - j) + \bar{\boldsymbol{u}}(j) + (I + KM)^{-1}K\sum_{i=1}^{j} \big(I - LG\big)^{i-1} \\
&\quad \times L(I + MK)^{-1}(-M, I)\boldsymbol{w}_0(k - i) + (I + KM)^{-1}K(-M, I)\boldsymbol{w}_0(k) \\
&\quad - (I + KM)^{-1}K(I - LG)^j(-M, I)\boldsymbol{w}_0(k - j) - (I + KM)^{-1}K\big(I - LG\big)^j\hat{\boldsymbol{\Phi}}.
\end{aligned}
$$

Convergence of $\tilde{\boldsymbol{u}}$ with respect to the operating point is hence

$$\begin{aligned}\tilde{\boldsymbol{u}}(k)-\bar{\boldsymbol{u}}(k) &= \big(I-(I+KM)^{-1}KLM\big)^{j}\Big[\tilde{\boldsymbol{u}}(k-j)-\bar{\boldsymbol{u}}(k-j)\Big]-\bar{\boldsymbol{u}}(k)\\ &\quad+\big(I-(I+KM)^{-1}KLM\big)^{j}\bar{\boldsymbol{u}}(k-j)+\bar{\boldsymbol{u}}(j)+(I+KM)^{-1}K\sum_{i=1}^{j}\big(I-LG\big)^{i-1}\\ &\quad\times L(I+MK)^{-1}(-M,I)\boldsymbol{w}_0(k-i)+(I+KM)^{-1}K(-M,I)\boldsymbol{w}_0(k)\\ &\quad-(I+KM)^{-1}K(I-LG)^{j}(-M,I)\boldsymbol{w}_0(k-j)-(I+KM)^{-1}K\big(I-LG\big)^{j}\hat{\boldsymbol{\Phi}}.\end{aligned}$$

Now note that

$$\begin{aligned}&\bar{\boldsymbol{u}}(j)-\bar{\boldsymbol{u}}(k)+\big(I-(I+KM)^{-1}KLM\big)^{j}\bar{\boldsymbol{u}}(k-j)-(I+KM)^{-1}K\big(I-LG\big)^{j}\hat{\boldsymbol{\Phi}}\\ &=(I+KM)^{-1}K\Bigg\{\Big[(I-LG)^{j}+\sum_{i=1}^{j}(I-LG)^{i-1}L\Big]\\ &\qquad-\Big[(I-LG)^{k}+\sum_{i=1}^{k}(I-LG)^{i-1}L\Big]\\ &\qquad+(I-LG)^{j}\Big[(I-LG)^{k-j}+\sum_{i=1}^{k-j}(I-LG)^{i-1}L\Big]-\big(I-LG\big)^{j}\Bigg\}\hat{\boldsymbol{\Phi}}\\ &=(I+KM)^{-1}K\Bigg\{\sum_{i=1}^{j}(I-LG)^{i-1}L-\sum_{i=1}^{k}(I-LG)^{i-1}L\\ &\qquad+\sum_{i=1}^{k-j}(I-LG)^{i-1}L\Bigg\}\hat{\boldsymbol{\Phi}}=0\end{aligned}$$

so that we obtain the relation

$$\begin{aligned}\tilde{\boldsymbol{u}}(k)-\bar{\boldsymbol{u}}(k) &= \big(I-(I+KM)^{-1}KLM\big)^{j}\Big[\tilde{\boldsymbol{u}}(k-j)-\bar{\boldsymbol{u}}(k-j)\Big]\\ &\quad+(I+KM)^{-1}K\sum_{i=1}^{j}\big(I-LG\big)^{i-1}L(I+MK)^{-1}(-M,I)\boldsymbol{w}_0(k-i)\\ &\quad+(I+KM)^{-1}K(-M,I)\boldsymbol{w}_0(k)-(I+KM)^{-1}K(I-LG)^{j}(-M,I)\boldsymbol{w}_0(k-j).\end{aligned}\tag{10.4}$$

The corresponding operating point for $\tilde{\boldsymbol{e}}$ is given by $\bar{\boldsymbol{e}}(k)=\hat{\boldsymbol{\Phi}}-M\bar{\boldsymbol{u}}(k)$ and using

$$\tilde{\boldsymbol{e}}(k)=\boldsymbol{y}_0(k)+\hat{\boldsymbol{\Phi}}-M(\boldsymbol{u}_0(k)+\tilde{\boldsymbol{u}}(k))$$

convergence of $\tilde{\boldsymbol{e}}(k)$ with respect to the operating point follows

$$\tilde{\boldsymbol{e}}(k) - \bar{\boldsymbol{e}}(k) = \boldsymbol{y}_0(k) - M\boldsymbol{u}_0(k) - M\tilde{\boldsymbol{u}}(k) + M\bar{\boldsymbol{u}}(k) = (-M, I)\boldsymbol{w}_0(k) - M(\tilde{\boldsymbol{u}}(k) - \bar{\boldsymbol{u}}(k)). \tag{10.5}$$

Combining (10.4) and (10.5) gives

$$\begin{aligned}\begin{pmatrix}\tilde{\boldsymbol{u}}(k) - \bar{\boldsymbol{u}}(k)\\ \tilde{\boldsymbol{e}}(k) - \bar{\boldsymbol{e}}(k)\end{pmatrix} &= \begin{pmatrix} I\\ -M\end{pmatrix}(\tilde{\boldsymbol{u}}(k) - \bar{\boldsymbol{u}}(k)) + \begin{pmatrix} 0\\ (-M, I)\end{pmatrix}\boldsymbol{w}_0(k) = \begin{pmatrix} K\\ I\end{pmatrix}(I + MK)^{-1}\\ &\quad \times (-M, I)\boldsymbol{w}_0(k) + \begin{pmatrix} I\\ -M\end{pmatrix}\Big\{\big(I - (I + KM)^{-1}KLM\big)^j\Big[\tilde{\boldsymbol{u}}(k-j) - \bar{\boldsymbol{u}}(k-j)\Big]\\ &\quad + (I + KM)^{-1} \times K\Big\{\sum_{i=1}^{j}\big(I - LG\big)^{i-1}L(I + MK)^{-1}(-M, I)\boldsymbol{w}_0(k-i)\\ &\quad - (I - LG)^j(-M, I)\boldsymbol{w}_0(k-j)\Big\}\Big\}.\end{aligned}$$

Let $\|I - (I + KM)^{-1}KLM\| < \gamma_1$, then we can bound

$$\begin{aligned}|\boldsymbol{w}_2(k) - \bar{\boldsymbol{w}}_2(k)| &= |(\tilde{\boldsymbol{u}}(k) - \bar{\boldsymbol{u}}(k), \tilde{\boldsymbol{e}}(k) - \bar{\boldsymbol{e}}(k))^\top|\\ &\le \|(I, M)^\top\|\gamma_1^j|\tilde{\boldsymbol{u}}(k-j) - \bar{\boldsymbol{u}}(k-j)|\\ &\quad + \|(K, I)^\top(I + MK)^{-1}(-M, I)\||\boldsymbol{w}_0(k)|\\ &\quad + \|(I, M)^\top(I + KM)^{-1}K\|\sum_{i=1}^{j}\gamma^{i-1}\|L(I + MK)^{-1}(-M, I)\||\boldsymbol{w}_0(k-i)|.\end{aligned}$$

Hence, recalling that $K = XK_X$ and $L = WLP$, we define

$$\begin{aligned}b_1 &= \|(I, M)^\top(I + KM)^{-1}K\|\|L(I + MK)^{-1}(-M, I)\|,\\ b_2 &= \|(K, I)^\top(I + MK)^{-1}(-M, I)\|\end{aligned}$$

in the M_α and M_β structures defined in Proposition 3 of [6], which yield

$$\|\boldsymbol{w}_2|I_3\|_{\bar{\boldsymbol{w}}_2} \le \gamma_1^{|I_2|}\|(I, M)^\top\|\|M_\alpha(|I_3|)\|\|\boldsymbol{w}_2|I_1\|_{\bar{\boldsymbol{w}}_2} + \|M_\beta(|I_2|, |I_3|)\|\|\boldsymbol{w}_0|_{I_1\cup I_2\cup I_3}\|.$$

where intervals I_1, I_2, and I_3 are defined in [6]. The terms M_α and M_β are then used to calculate values of delay Δ and gap distance $\delta_{\max}$ such that robust stability bound (10.1) holds [6]. Since terms b_1 and b_2 appear explicitly within the fixed controller robust stability margin of Theorem 4.6, they are necessarily finite, and hence give rise to a finite value of $b_{\max}$ satisfying (10.1). Therefore EMMILC can always guarantee robust stability over the entire uncertainty space U specified by the designer. □

Application of EMMILC therefore enables the control framework developed in this book to be used autonomously in patient's own homes without the presence of an engineer to perform identification tests or tune controller parameters. However,

future work is needed to extend the current isometric arm implementation of [5] to encompass the full arm structure of (2.6). Following this, future research will involve constructing a suitable set of candidate models which captures all possible variation in the underlying stimulated arm dynamics.

10.2 Wearable ES Technology

In terms of assistive technology development, the highest priority for stroke participants and carers has been identified as 'ease of set-up' followed by 'comfort' and 'durability' [1]. Wearable ES technology which exploits intrinsic properties of fabric is a central component in realizing this requirement. Manufacturing suitable electrode arrays directly on an appropriate fabric is the most direct method of producing a flexible, breathable, and light weight device. However, no fabrication technique has so far realized such an electrode array economically. Embroidery has been used to manufacture smart fabric type electrode pads and electrode wiring on fabric for neuroprosthetic applications [7]. However, this required expensive high quality custom made silver sputtered yarns produced using plasma vapor sputtering since commercial metal coated yarns (e.g. silver coated Nylon 66 'ShieldX') showed low uniformity due to the degradation of the conductive yarn surface during the embroidery process [8].

Weaving and knitting have been used in fabricating smart fabrics for various wearable electronic applications (e.g. sensing, display, health monitoring, power generating) [9–11]. However, these methods are also not suitable for fabricating a wearable ES array. Weaving and knitting approaches impose limitations on the design of the array because the conductive path is constrained to follow the physical location of the yarns within the fabric. There is also a lack of homogeneity in the resistance of the conductive pattern due to the imprecise gaps between the conductive yarns.

A flexible and breathable fabric electrode array (FEA) has, however, recently been demonstrated and is shown in Fig. 10.3b. This is fabricated entirely by screen printing the active electrode array directly onto a standard fabric. Screen printing is a straightforward and cost effective fabrication method which facilitates significant design freedom in terms of pattern geometries [12, 13]. It is a well established technology in both the textile and printed electronic fields.

The printed FEA has required the development of bespoke polymer based screen printable pastes that can be processed in a manner compatible with textiles. These materials are now commercially available from Smart Fabric Inks Ltd, UK (see http://www.fabinks.com for details). A carbon loaded silicone rubber has been applied to form the electrodes which enable dry contact via the conductive pad-skin interface and avoids the need to use the hydrogel that is typically required by existing electrodes [14]. The materials with skin contact used in the FEA are biocompatible.

The performance of the FEA has been compared to that of the leading alternative, which comprises the flexible array on polycarbonate with a hydrogel layer (Fatronik-Tecnalia, Spain) used in Chap. 8 and shown in Fig. 10.3a. The FEA can

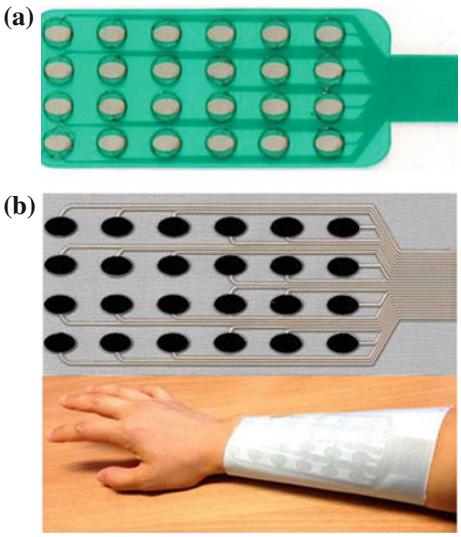

Fig. 10.3 **a** Flexible polycarbonate array from Fatronik-Tecnalia, and **b** Fabric electrode array

produce comparable angular joint movement compared to the polycarbonate array; in addition, FEA has significant improvement on the flexibility, breathability and comfort. Critical postures of daily life have been achieved by stimulation of an optimized selection of electrode elements.

To quantify the difference in accuracy using the two electrode array types, results in Chap. 8 have been repeated with two new participants. Each participant used both the fabric array and the polycarbonate array under identical conditions, with a rest period in between tests. The results are shown in Table 10.1 for each task. The ILC procedure gives rise to results with a mean joint angle error of typically less than 7 % of the initial value. It can also be seen that the FEA is able to produce slightly superior results when compared with the flexible polycarbonate array. Full details of the electrode manufacture and experimental test results appear in [15].

These results hence lay the foundation for development of wearable ES rehabilitation technology embedded in normal clothes. One possible realization of a wearable ES sleeve is shown in Fig. 10.4, where the ES electronics are mounted within the

Table 10.1 Percentage error, $100 \times \|\boldsymbol{e}_3\|/\|\boldsymbol{e}_0\|$, across all joints using each array type

Array Type	Particpant	Pointing	Pinch	Open hand
FEA	P1	5.29	5.33	6.18
	P2	3.55	6.97	5.45
Polycarbonate array	P1	6.81	7.73	7.90
	P2	4.46	6.86	6.51

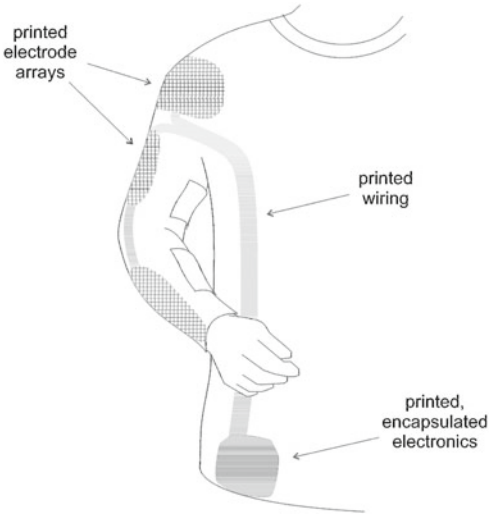

Fig. 10.4 Possible design of wearable clothing

clothing using encapsulation. This system could then be used in conjunction with a tablet computer running software which directs stroke participants in performing training movements using suitable audio-visual prompts.

10.3 Wider Application Domains and Greater Scope

Precise control of ES to assist movement has rich potential to aid recovery in neurological conditions such as cerebral palsy, head injury, Parkinson's disease, and Spinal Cord Injury (SCI). For example, 50–60 % of the 100,000 UK Multiple Sclerosis patients have impaired hand/arm function and could benefit from ES or robot assisted technology. This was illustrated in Chap. 7 which described an MS Society-funded pilot study confirming the feasibility of applying ES and robotic assistance for upper limb rehabilitation. The same technology can also be directly utilized for restoration of lower-limb function, with researchers from Technischen Universität Berlin, ETH Zürich, University of Washington and University of California having all employed ILC to control ES applied to the lower extremity.

The control framework developed has assumed that the patient repeatedly attempts the same task for the purpose of rehabilitation. However the combination of ES and robotics also has rich potential to function in a purely assistive manner, i.e. acting as an orthosis to help perform a one-off task specified by the user that may take place anywhere in or out-side their home. This firstly poses a challenge in terms of sensing their movement, since static depth cameras may be inappropriate. Greater emphasis then falls on fusing wearable inertial measurement systems, body-mounted depth sensors, or biopotential signals to predict movement indirectly.

Biopotential signals (e.g. electromyographic (EMG), electroencephalographic (EEG)) can also be used within the underlying modeling and control framework to predict the user's intended movement, and is a rich area of current research. They also have great potential to improve the accuracy of the control systems developed in this book since they provide a mechanism to account for the user's voluntary contribution to the task completion (which affects the controller operating point). In terms of measuring suitable signals, the array technology described in Sect. 10.2 can be used in conjunction with electronic filtering to extract EMG signals from the relevant muscles.

As well as expanding the underlying models, more flexibility can be embedded within the ILC framework of Chap. 6. For example, it is possible for learning to still take place during repeated but non-identical tasks, which would enable more varied tasks to be used in training. Such tasks would increase user motivation during therapy, as well as unlock the potential for wider assistive utility. When used in an assistive manner, it is also possible to embed a model of the task employed within the EMMILC framework, so that the estimator bank not only matches the plant model, but also chooses the task that most closely fits the user's intention. Another possible expansion of the generalized ILC framework of Chap. 6 is to enable the point-to-point times $\{t_i\}$ to also be updated automatically to minimize a cost function, or to more closely match the user's voluntary intention. Feasibility of the former case has recently been established in [16].

Perhaps the most challenging area of future research is to develop computational models of patients' sensorimotor re-learning during therapy. These models are required to capture changes in arm impairment as a function of (1) parameters governing the rehabilitation modalities (e.g. gains/weights determining task and control action), and (2) underlying patient physiology. Suitably optimized, they would then enable rehabilitation systems to automate the treatment modalities applied to maximize long-term recovery, and hence ensure clinical effectiveness without relying on the continued presence of a therapist. Starting points in this area include the fitting of linear state-space models to the recovery process reported in [17].

References

1. A.-M. Hughes, J.H. Burridge, S.H. Demain, C.E. Ellis-Hill, C. Meagher, L. Tedesco-Triccas, R. Turk, I. Swain, Translation of evidence-based assistive technologies into stroke rehabilitation: users' perceptions of the barriers and opportunities. BMC Health Serv. Res. **14**, 124 (2014)
2. K.L. Meadmore, A.-M. Hughes, C.T. Freeman, V. Benson, J.H. Burridge, Participant feedback in the evaluation of novel stroke rehabilitation technologies. J. Rehabil. Robot. **1**, 82–92 (2013)
3. D. Buchstaller, M. French, Robust stability and performance for multiple model adaptive control: Part I—the framework. IEEE Trans. Autom. Control (2015) (In Press)
4. D. Buchstaller, M. French, Robust stability and performance for multiple model adaptive control: Part II—gain bounds. IEEE Trans. Automa. Control (2015) (In Press)
5. O.W. Brend, C.T. Freeman, M. French, Multiple model adaptive control of functional electrical stimulation. IEEE Trans. Control Syst. Technol. **23**(5), 1901–1913 (2015)

6. C.T. Freeman, M. French, Estimation based multiple model iterative learning control, in *54th IEEE Conference on Decision and Control*, (2015) (In Press)
7. T. Keller, M. Lawrence, A. Kuhn, Textile neuroprosthesis garment for functional electrical stimulation, in *International Workshop on Functional Electrical Stimulation*, Krems, Austria (2007), pp. 107–110
8. M. Lawrence, Transcutaneous electrode technology for neuroprostheses, Ph.D. thesis, ETH Zurich, 2009
9. A. Lymberis, R. Paradiso, Smart fabrics and interactive textile enabling wearable personal applications: R&d state of the art and future challenges, in *30th Annual International IEEE EMBS Conference*, Vancouver, British Columbia, Canada (2008), pp. 5270–5273
10. K. Cherenack, C. Zysset, T. Kinkeldei, N. Münzenrieder, G. Tröster, Woven electronic fibers with sensing and display functions for smart textiles. Adv. Mater. **22**, 5178–5182 (2010)
11. K. Cherenack, L.V. Pieterson, Smart textiles: challenges and opportunities. J Appl. Phys. **112**, 091301 (2012)
12. M. Zirkl, A. Sawatdee, U. Helbig, M. Krause, G. Scheipl, E. Kraker, P.A. Ersman, D. Nilsson, D. Platt, P. BodÃű S. Bauer, G. Domann, B. Stadlober, An all-printed ferroelectric active matrix sensor network based on only five functional materials forming a touchless control interface. Adv. Mater. **23**, 2069–2074 (2011)
13. Y. Kim, H. Kim, H.J. Yoo, Electrical characterization of screen-printed circuits on the fabric. IEEE Trans. Adv. Packag. **33**, 196–205 (2010)
14. M.R. Neuman, Biopotential electrodes, in *The Biomedical Engineering Handbook*, ed. by J.D. Bronzino, 2nd edn (CRC Press, Boca Raton, 1999), pp. 889–900
15. K. Yang, C.T. Freeman, R.N. Torah, S.P. Beeby, J. Tudor, Screen printed fabric electrode array for wearable functional electrical stimulation. Sens. Actuators A: Phys. **213**, 108–115 (2014)
16. Y. Chen, B. Chu, C.T. Freeman, Point-to-point iterative learning control with optimal tracking time allocation, in *54th IEEE Conference on Decision and Control* (2015) (In Press)
17. S. Balasubramaniam, A robust and sensitive metric for quantifying movement smoothness. IEEE Trans. Rehabil. Eng. **59**(8), 2126–2136 (2012)